

CHEMIA

**STUDIA UNIVERSITATIS BABEŞ-BOLYAI
CHEMIA**

1/2022

EDITORIAL BOARD OF STUDIA UNIVERSITATIS BABEȘ-BOLYAI CHEMIA

ONORARY EDITOR:

IONEL HAIDUC – Member of the Romanian Academy

EDITOR-IN-CHIEF:

LUMINIȚA SILAGHI-DUMITRESCU

EXECUTIVE EDITOR:

CASTELIA CRISTEA

EDITORIAL BOARD:

PAUL ȘERBAN AGACHI, Babeș-Bolyai University, Cluj-Napoca, Romania

LIVAIN BREAU, UQAM University of Quebec, Montreal, Canada

HANS JOACHIM BREUNIG, Institute of Inorganic and Physical Chemistry,
University of Bremen, Bremen, Germany

JEAN ESCUDIE, HFA, Paul Sabatier University, Toulouse, France

ION GROSU, Babeș-Bolyai University, Cluj-Napoca, Romania

EVAMARIE HEY-HAWKINS, University of Leipzig, Leipzig, Germany

FLORIN DAN IRIMIE, Babeș-Bolyai University, Cluj-Napoca, Romania

FERENC KILAR, University of Pecs, Pecs, Hungary

BRUCE KING, University of Georgia, Athens, Georgia, USA

ANTONIO LAGUNA, Department of Inorganic Chemistry, ICMA,
University of Zaragoza, Zaragoza, Spain

JURGEN LIEBSCHER, Humboldt University, Berlin, Germany

KIERAN MOLLOY, University of Bath, Bath, UK

IONEL CĂTĂLIN POPESCU, Babeș-Bolyai University, Cluj-Napoca,
Romania

CRISTIAN SILVESTRU, Babeș-Bolyai University, Cluj-Napoca, Romania

[http://chem.ubbcluj.ro/~studiachemia/;](http://chem.ubbcluj.ro/~studiachemia/)
http://www.studia.ubbcluj.ro/serii/chemia/index_en.html

**YEAR
MONTH
ISSUE**

**Volume 67 (LXVII) 2022
MARCH
1**

S T U D I A

UNIVERSITATIS BABEȘ–BOLYAI

CHEMIA

1

ISSUE DOI:10.24193/subbchem.2022.1

STUDIA UBB EDITORIAL OFFICE: B.P. Hasdeu no. 51, 400371 Cluj-Napoca, Romania,
Phone + 40 264 405352

CUPRINS – CONTENT – SOMMAIRE – INHALT

ENIKO COVACI, TIBERIU FRENTIU, Greenness and Whiteness Profiles of UV/VIS Photochemical Vapor Generation Capacitively Coupled Plasma Microtorch Optical Emission Spectrometry Method for Mercury Determination and Speciation in Food and Water	7
IOANA-NICOLETA LINCA, SILVIA IMRE, IOAN TOMUȚĂ, AMELIA TERO-VESCAN, There Are No Perfect Analytical Methods - Optimization Study of a Pharmacopoeia Method for Clopidogrel Analysis	27
STEFAN PETROVIĆ, JELENA MRMOŠANIN, ALEKSANDRA PAVLOVIĆ, SLAĐANA ALAGIĆ, SNEŽANA TOŠIĆ, GORDANA STOJANOVIĆ, The Influence of Agricultural Soil Preparation Methods on the Pseudo-Total Element Content Determined by ICP-OES	43

HORIA F. POP, COSTEL SÂRBU, A Powerful Supervised Fuzzy Method. Characterization, Authentication and Traceability of Roman Pottery.....	61
ELISABETA CRISTINA TIMIS, Improvements Necessary for a River Pollutant Transport Model to Obtain a Better Performance	75
DRAGAN DJORDJEVIC, MARIJA KODRIC, RADICA KRSTIC, SUZANA DJORDJEVIC, Kinetic Considerations of Textile Dyes Adsorption from Water on a Sorbent from Cellulosic Waste.....	89
NAZIFE ASLAN, ORHAN ATAKOL, NILGÜN ŞEN, A Novel Schiff Bases/Multiwalled Carbon Nanotube Based Adsorbents To Remove ²¹⁰ Pb From Water.....	107
DAN CRISTIAN DANIELESCU, ADRIAN EUGEN CIOABLĂ, VASILE PODE, Study Concerning Performances of two Types of Prehydrolyzed Polymer in Comparison with Aluminum Sulphate as a Coagulant for Waste Water	125
RABAH ALI KHALIL, SHAYMA'A HASHIM ABDULRAHMAN, Newly Developed Statistically Intensive Qsar Models for Biological Activity of Isatin Derivatives	139
SLAĐANA MEDIĆ PAP, DARIO DANOJEVIĆ, SVETLANA GLOGOVAC, MARIJANA PEIĆ TUKULJAC, DALIBOR ŽIVANOV, DEJAN PRVULOVIĆ, Antioxidant Response of Tomato to Late Blight (<i>Phytophthora infestans</i>) Infection Depending on Symptoms Intensity .	153
KEZBAN YILDIZ DALGINLI, CANAN GULMEZ, EMINE ATAKISI, ONUR ATAKISI, Lactoferrin Modulates Increased Liver DNA Damage by Reducing Serum Cytokine, Hecpidin and Iron Levels in Lipopolysaccharide-Induced Endotoxemia In Rats.....	165
SANDA-ILEANA CIMPEAN, IOANA AMBROSIE, MADALINA MOLDOVAN, ADA DELEAN, DOINA PRODAN, CRISTINA PREJMEREAN, MARIOARA MOLDOVAN, MARIA TOMOAIA-COTISEL, LOREDANA COLCERIU-BURTEA, Testing of New Experimental Giomers: Water Sorption, Conversion Degree, Radiopacity, Microstructure and Biological Behavior.....	177
DANICA DIMITRIJEVIĆ, DANIJELA KOSTIĆ, DUŠAN PAUNOVIĆ, MILAN MITIĆ, JOVANA KRSTIĆ, IVANA RAŠIĆ MIŠIĆ, BILJANA ARSIĆ, Antimicrobial Activity and the Quantitative Analyses of Phenolic Compounds and Heavy Metals of Red Mulberry Extracts (<i>Morus Rubra</i> L.) from Serbia	195

MARIANA ADINA MATICA, FINN LILLELUND AACHMANN, ANNE TØNDERVIK, HÅVARD SLETTA, VASILE OSTAFE, Preparation, Physico-Chemical Characterization and Antibacterial Properties of Chitosan and Chitosan–Nisin Membranes	209
TAMARA-RITA OVÁRI, GABRIEL KATONA, GABRIELLA SZABÓ, LIANA MARIA MURESAN, Electrochemical Evaluation of the Relationship Between the Thermal Treatment and the Protective Properties of Thin Silica Coatings on Zinc Substrates	227
ADRIAN PATRUT, ROXANA T. PATRUT, VICTOR BOCOS-BINTINTAN, ILEANA-ANDREEA RATIU, LASZLO RAKOSY, GEORGE ZDROB, EUFROSINA VANCA, KARL F. VON REDEN, Radiocarbon Investigation of Two Old Elms from Romania.....	245
IOANA ALINA POPESCU, SORIN-AUREL DORNEANU, ROXANA MARIA TRUȚĂ, PETRU ILEA, Recent Research Related to Li-Ion Battery Recycling Processes – A Review	257
LUCIAN CRISTIAN POP, GABRIEL BARTA, LIVIU COSMIN COTET, KLARA MAGYARI, MONICA BAIA, LUCIAN BARBU TUDORAN, RODICA UNGUR, DAN VODNAR, LUCIAN BAIA, VIRGINIA DANCIU, Antimicrobial Activity of Graphene Oxide-coated Polypropylene Surfaces.....	281

Studia Universitatis Babes-Bolyai Chemia has been selected for coverage in Thomson Reuters products and custom information services. Beginning with V. 53 (1) 2008, this publication is indexed and abstracted in the following:

- Science Citation Index Expanded (also known as SciSearch®)
- Chemistry Citation Index®
- Journal Citation Reports/Science Edition

GREENNESS AND WHITENESS PROFILES OF UV/VIS PHOTOCHEMICAL VAPOR GENERATION CAPACITIVELY COUPLED PLASMA MICROTORCH OPTICAL EMISSION SPECTROMETRY METHOD FOR MERCURY DETERMINATION AND SPECIATION IN FOOD AND WATER

ENIKO COVACI^{a,b,*}, TIBERIU FRENTIU^{a,b}

ABSTRACT. The aim of the study was the evaluation of greenness and whiteness profiles of UV/Vis photo-induced cold vapor generation (UV/Vis-PVG) capacitively coupled plasma microtorch optical emission spectrometry methods for Hg determination and speciation as CH_3Hg^+ and Hg^{2+} . Sample preparation for CH_3Hg^+ determination in fish tissue consisted of an extraction in HBr–toluene–aqueous L-cysteine solution and UV-PVG in 0.6 mol L^{-1} HCOOH. Total Hg was determined in food samples following ultrasound assisted extraction in concentrated HCOOH and UV-PVG. Hg speciation was based on extraction in HCOOH and UV/Vis selective derivatization of total Hg/ Hg^{2+} . The greenness profile was assessed by National Environmental Methods Index, Analytical Eco-Scale, Green Analytical Procedure Index and Analytical Greenness Metric, while the whiteness profile was evaluated using the Red–Green–Blue (RGB) 12 algorithm. The methods, based on miniaturized instrumentation, were characterized by a higher greenness and whiteness compared to the traditional SnCl_2 cold vapor generation inductively coupled plasma optical emission spectrometry, SnCl_2 cold vapor generation atomic fluorescence spectrometry, and sometimes than that of thermal decomposition atomic absorption spectrometry. This study is a novelty because, to the best of our knowledge, is the first approach of this kind for Hg determination and speciation based on optical emission spectrometry using a fully miniaturized instrumentation.

Keywords: greenness and whiteness profile, mercury speciation, capacitively coupled plasma microtorch

^a Babes-Bolyai University, Faculty of Chemistry and Chemical Engineering, 11 Arany Janos str., RO-400028, Cluj-Napoca, Romania

^b Babes-Bolyai University, Research Center for Advanced Analysis, Instrumentation and Chemometrics, ANALYTICA, 11 Arany Janos str., RO-400028, Cluj-Napoca, Romania

* Corresponding author: eniko.covaci@ubbcluj.ro

INTRODUCTION

Several national and international organizations, such as the United States Environmental Protection Agency (1970) [1] and the World Commission on Environment and Development (1983) [2] have been established with the aim to develop an appropriate legislative framework to prevent and reduce environmental pollution. Anastas and Warner introduced for the first time in 1998 the concept of Green Chemistry or Sustainable Chemistry, and laid down its 12 principles [3]. Namiesnik and his coworkers introduced for the first time the concept of Green Analytical Chemistry (GAC) in 2012 [4]. The 12 GAC principles provide the reduction or complete elimination of reagents for sample preparation, preservation and analysis, decrease of energy consumption, efficient waste treatment and increase operator safety [4]. Numerous analytical methods have been developed, which were considered green by the authors, but unfortunately without clearly defined metrics for evaluation. Therefore, the assessment was often subjective and not properly justified [5, 6]. As a consequence, several objective procedures for the greenness profile have been developed, such as the National Environmental Methods Index (NEMI) [7], the pictogram developed by Raynie *et al.* [8], Analytical Eco-Scale (AES) [9], Green Analytical Procedure Index (GAPI) [10], Hexagon pictogram [11], Analytical Method Greenness Score (AMGS) [12] and the Analytical Greenness metric (AGREE) [13]. The greenness evaluation procedures were applied mainly for chromatographic methods, in which a significant number of reagents are used, and less for non-chromatographic methods [14–20]. These procedures are based on the establishment of the green profile, usually on some economic and sample preparation aspects and do not take into account other important aspects of the analytical methods, such as analytical performance, level of utility and applicability, which should be as wide as possible.

Due to these shortcomings, Nowak and his coworkers recently introduced the White Analytical Chemistry (WAC) concept and its 12 principles [21], based on Red (analytical performance), Green (green chemistry) and Blue (practical aspects) principles, known as the RGB 12 procedure, for the evaluation of the analytical methods in a global manner [6, 21, 22].

The aim of the study was the assessment of greenness and whiteness profiles of 3 methods based on UV/Vis photochemical vapor generation capacitively coupled microtorch optical emission spectrometry (UV/Vis-PVG- μ CCP-OES) for total Hg determination and its speciation as CH_3Hg^+ and Hg^{2+} in food and water samples. The multiple metrics, based on NEMI, AES, GAPI and AGREE were applied for greenness profile, while the RGB 12 approach

was used for whiteness profile assessment. The procedure was applied for CH_3Hg^+ speciation in fish tissue samples by UV-PVG- μCCP -OES using the selective extraction in HBr–toluene–aqueous L-cysteine solution, in comparison with the thermal decomposition atomic absorption spectrometry (TD-AAS) method, recommended by the European Commission for CH_3Hg^+ determination in such foods [23, 24]. The second method, UV-PVG- μCCP -OES was evaluated for total Hg determination in water and diverse food, such as fish tissue, animal meat and organs, vegetables, fruits and food supplements, in comparison with SnCl_2 cold vapor generation capacitively coupled microtorch optical emission spectrometry (SnCl_2 -CVG- μCCP -OES), SnCl_2 cold vapor generation inductively coupled plasma atomic emission spectrometry (SnCl_2 -CVG-ICP-OES), SnCl_2 cold vapor generation atomic fluorescence spectrometry (SnCl_2 -CVG-AFS) and TD-AAS based on direct solid sampling. The greenness and whiteness profile of UV/Vis-PVG- μCCP -OES method was assessed for Hg speciation as CH_3Hg^+ and Hg^{2+} in fish samples. Details of sample preparation, analytical performances and operating conditions of the miniaturized instrumentation with the plasma microtorch were already published [24–27]. Therefore, the novelty of this study consists in the evaluation for the first time of the greenness and whiteness profiles in an integrated approach for several non-chromatographic methods, developed in our laboratory, for Hg determination and speciation using optical emission spectrometry, based on a cost-effective and fully miniaturized instrumentation, in which the core is a low power and low Ar consumption capacitively coupled plasma microtorch interfaced with a low resolution microspectrometer.

RESULTS AND DISCUSSION

Greenness profile of the UV/Vis-PVG- μCCP -OES methods according to the NEMI procedure

According to Table 1, the UV-PVG- μCCP -OES method, used for CH_3Hg^+ determination in fish tissue samples based on a double liquid-liquid extraction in the HBr–toluene–L-cysteine system, presents a greenness score of only 25% (1 green quadrant), similar with the TD-AAS method, due to the use of persistent, bioaccumulative and toxic (PBT) solvents (toluene), use of corrosive and hazardous reagents (HBr), and due to the generation of large amount of waste, 95 mL and 51 mL, respectively. Anyway, this sample preparation procedure was established in an inter-laboratory study and is recommended by the European Commission for the determination of CH_3Hg^+

[23], because it is easy to apply and does not require complicated instrumentation, such as the TD-AAS, specially designed for Hg determination. The original UV-PVG- μ CCP-OES method for total Hg determination, developed in our laboratory, in fish tissue and food by ultrasound assisted extraction in concentrated HCOOH and UV photochemical vapor generation (UV-PVG) in 0.6 mol L^{-1} HCOOH has a greenness score of 75% (3 green quadrants), due to the fact that it does not use PBT and corrosive reagents, and does not generate waste in a large quantity. The same greenness score was obtained by the same UV-PVG- μ CCP-OES method for total Hg determination in water using UV-PVG in 0.6 mol L^{-1} HCOOH. The classical methods, SnCl_2 -CVG-ICP-OES and SnCl_2 -CVG-AFS, have a lower greenness score ($\sim 50\%$), because they require a complete sample digestion in $\text{HNO}_3 - \text{H}_2\text{O}_2$ system, uses HCl as medium for SnCl_2 cold vapor generation and generate a higher amount of waste (50–60 mL). The conclusion is also valid in the case of the SnCl_2 -CVG- μ CCP-OES method, although it uses the same miniaturized instrumentation, because the sample preparation procedure is paramount to the characteristics of the instrumentation. In these circumstances, the TD-AAS method, based on direct solid sampling for Hg determination has a greenness score of 100%, because it allows the determination of Hg in fresh or dry sample, and thus the sample preparation is simple. Instead, there may be issues with sensitivity and reproducibility.

The UV/Vis-PVG- μ CCP-OES specially designed for Hg speciation as CH_3Hg^+ and Hg^{2+} in fish tissue, based on ultrasound assisted sample extraction in concentrated HCOOH and selective UV/Vis-PVG of $\text{CH}_3\text{Hg}^+/\text{Hg}^{2+}$ in 0.6 mol L^{-1} HCOOH has a greenness score of 75%. On the other hand, the use of TD-AAS method for Hg speciation presents a score of only 25%, due to the hazardous and corrosive reagents used in the double liquid-liquid extraction in HBr–toluene–L-cysteine system.

The study revealed the limitation of the NEMI approach in the evaluation of the greenness profile of a method, because this procedure considers only the sample preparation protocol (type and amount of reagents, and waste generated), and does not take into account the economic aspects and instrument miniaturization, important aspects in the state-of-the-art development of cost-effective and highly sensitive methods. However, it is clear that regardless of the instrumentation, the use of ultrasound assisted sample extraction in concentrated HCOOH and UV-PVG derivatization, in which only HCOOH is used, has a higher degree of greenness, compared to the classical HNO_3 and H_2O_2 extraction methods and the conventional SnCl_2 derivatization in HCl medium.

Table 1. Greenness profile of the UV/Vis-PVG- μ CCP-OES methods for Hg determination and speciation in food and water using the NEMI procedure [7], in comparison with classical methods

Species determined (sample)	Method				
	UV-PVG- μ CCP-OES	TD-AAS	SnCl ₂ -CVG-ICP-OES	SnCl ₂ -CVG-AFS	SnCl ₂ -CVG- μ CCP-OES
CH ₃ Hg ⁺ (fish tissue)			-	-	-
Total Hg (food)					
Total Hg (water)		-	-	-	-
Hg speciation as CH ₃ Hg ⁺ and Hg ²⁺ (fish tissue)*			-	-	-

* Hg speciation as CH₃Hg⁺ and Hg²⁺ by μ CCP-OES was achieved by UV/Vis-PVG- μ CCP-OES

Greenness profile of the UV/Vis-PVG- μ CCP-OES methods according to the AES procedure

The AES procedure ensures a more advanced assessment of the greenness profile of an analytical method, as it takes into account not only the reagents use and waste generated, but also economic aspects, such as energy consumption and professional risk of the operator. The results presented in Table 2, highlights that the UV-PVG- μ CCP-OES method, developed for CH₃Hg⁺ determination presents an AES score of 61%, similar to that of TD-AAS (62%), due to the same sample preparation protocol (double liquid-liquid extraction in HBr–toluene–L-cysteine) and similar energy consumption of around 0.2 kWh.

The UV-PVG- μ CCP-OES method, developed for total Hg determination in vegetables and foods of animal origin, presents an excellent greenness score of 78%, *versus* 66% in the case of the traditional method SnCl₂-CVG-ICP-OES. This score could be attributed to the use of a single reagent (HCOOH) for extraction and derivatization, while in the case of SnCl₂-CVG-ICP-OES a complete sample digestion with HNO₃ and H₂O₂ and derivatization with SnCl₂ is mandatory. Furthermore, additional penalty points are assigned to the ICP-OES instrument due to the high energy demand, which is about 200 times higher than that of the miniaturized UV-PVG- μ CCP-OES set-up. Also, UV-PVG- μ CCP-OES method has a higher degree of greenness, compared to SnCl₂-CVG-AFS method, in which case a complete sample digestion was necessary.

Table 2. Greenness profile of the UV/Vis-PVG- μ CCP-OES methods for Hg determination and speciation in food and water using the AES procedure [9], in comparison with classical methods

Species determined (sample)	AES criteria	Methods penalty points/AES score				
		UV-PVG- μ CCP-OES	TD-AAS	SnCl ₂ -CVG-ICP-OES	SnCl ₂ -CVG-AFS	SnCl ₂ -CVG- μ CCP-OES
CH₃Hg⁺ (fish tissue)	Reagents	27	28	-	-	-
	Instrumentation, professional risk, waste	12	12	-	-	-
	AES score	61	62	-	-	-
Total Hg (food)	Reagents	13	8	23	22	21
	Instrumentation, professional risk, waste	9	1	11	10	10
	AES score	78	91	66	68	69
Total Hg (water)	Reagents	7	-	-	-	-
	Instrumentation, professional risk, waste	5	-	-	-	-
	AES score	85	-	-	-	-
Hg speciation as CH₃Hg⁺ and Hg²⁺ (fish tissue)*	Reagents	13	28	-	-	-
	Instrumentation, professional risk, waste	9	12	-	-	-
	AES score	78	62	-	-	-

* Hg speciation as CH₃Hg⁺ and Hg²⁺ by μ CCP-OES was achieved by UV/Vis-PVG- μ CCP-OES

The TD-AAS method has the highest greenness score (91%), according to the AES procedure, as the total Hg determination is based on the direct solid sampling without further preparation. In the case of this method, only 8 and 1 penalty points were attributed to the use of O₂ for sample decomposition and to the energy consumption for sample drying by lyophilization, respectively. Because the UV-PVG- μ CCP-OES method has a slightly lower AES score, it could be considered as a viable alternative to TD-AAS.

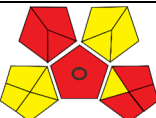









Furthermore, the UV-PVG- μ CCP-OES set-up enables Hg speciation as CH₃Hg⁺ and Hg²⁺ in fish tissue samples after extraction in HCOOH and UV/Vis-PVG in 0.6 mol L⁻¹ HCOOH with and without *on-line* preconcentration of the Hg vapor on a gold filament microcollector. On the other hand, the SnCl₂-CVG-ICP-OES and SnCl₂-CVG-AFS methods, are not appropriate to be used for this purpose, because they do not include the *on-line* preconcentration device, necessary for Hg²⁺ determination.

Also, the UV/Vis-PVG- μ CCP-OES method has a higher score of AES compared to the TD-AAS method, due to the sample preparation considerations presented in the previous procedures.

Greenness profile of the UV/Vis-PVG- μ CCP-OES methods according to the GAPI procedure

According to Table 3, the UV-PVG- μ CCP-OES method used for total Hg determination in water samples is the greenest one, because it could be observed 3 green triangles in different pentagons, attributed to the sample preparation (no extraction), amount of reagents and energy consumption. The TD-AAS method has the highest greenness profile for Hg determination directly in solid samples, because it has the most pentagons colored in green. All the methods based on the miniaturized μ CCP-OES system with or without *on-line* Hg vapor preconcentration show a lower profile of greenness.

Table 3. Greenness profile of the UV/Vis-PVG- μ CCP-OES methods for Hg determination and speciation in food and water using the GAPI procedure [10], in comparison with classical methods










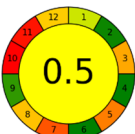
Species determined (sample)	Method				
	UV-PVG- μ CCP-OES	TD-AAS	SnCl ₂ -CVG-ICP-OES	SnCl ₂ -CVG-AFS	SnCl ₂ -CVG- μ CCP-OES
CH ₃ Hg ⁺ (fish tissue)			-	-	-
Total Hg (food)					
Total Hg (water)		-	-	-	-
Hg speciation as CH ₃ Hg ⁺ and Hg ²⁺ (fish tissue)*			-	-	-

* Hg speciation as CH₃Hg⁺ and Hg²⁺ by μ CCP-OES was achieved by UV/Vis-PVG- μ CCP-OES

Greenness profile of the UV/Vis-PVG- μ CCP-OES methods according to the AGREE procedure

The results presented in Table 4 show that the UV-PVG- μ CCP-OES method used for CH_3Hg^+ determination, has a greenness score of only 55%, similar to the TD-AAS method (50%), due to the reagents and solvents used in the sample preparation protocol for the two methods. However, the AGREE calculator sets the scores for each of the 12 criteria, and therefore it could be identified those which determines the greenness profile. Consequently, it could be observed that the sample amount, number of steps in the sample preparation protocol and energy consumption has the highest greenness score.

Table 4. Greenness profile of the UV/Vis-PVG- μ CCP-OES methods for Hg determination and speciation in food and water using the AGREE procedure [13], in comparison with classical methods

Species determined (sample)	Method				
	UV-PVG- μ CCP-OES	TD-AAS	SnCl_2 -CVG-ICP-OES	SnCl_2 -CVG-AFS	SnCl_2 -CVG- μ CCP-OES
CH_3Hg^+ (fish tissue)			-	-	-
Total Hg (food)					
Total Hg (water)		-	-	-	-
Hg speciation as CH_3Hg^+ and Hg^{2+} (fish tissue)*			-	-	-

* Hg speciation as CH_3Hg^+ and Hg^{2+} by μ CCP-OES was achieved by UV/Vis-PVG- μ CCP-OES

The UV-PVG- μ CCP-OES method for total Hg determination in food and water with or without *on-line* cold vapor preconcentration was found to have a good greenness profile (65%), compared to SnCl_2 -CVG-ICP-OES (44%) and SnCl_2 -CVG-AFS (49%). The results are in agreement with the lower energy consumption of the μ CCP-OES instrumentation, and simpler sample preparation (ultrasound assisted extraction in HCOOH) in comparison with total sample digestion, required in the case of the classical methods. Also, a significant improvement of the greenness degree (15%) can be observed if UV-PVG derivatization is connected to a miniaturized instrumentation with a microplasma source, compared to the classical derivatization assisted by SnCl_2 and HCl medium coupled with classical spectral instrumentation based on optical emission and atomic fluorescence spectrometry. Consequently, the UV-PVG- μ CCP-OES method for total Hg determination following HCOOH extraction and UV-PVG approach could be considered a viable alternative in terms of sample preparation and derivatization. The TD-AAS method presented the highest degree of greenness, namely 79%. On the other hand, UV/Vis-PVG- μ CCP-OES method for Hg speciation has a higher greenness profile (65%), compared to the TD-AAS method (50%), because the method developed on the miniaturized instrumentation is based only on the selective derivatization of Hg species, while the TD-AAS is based on the double selective liquid-liquid extraction.

Whiteness profile of the UV/Vis-PVG- μ CCP-OES methods according to the RGB 12 procedure

As shown in Figures 1 and 2, the UV/Vis-PVG- μ CCP-OES methods present similar or higher whiteness profile, compared to those of reference methods. The significant differences were found to be in the case of methods developed for total Hg determination using ultrasound assisted extraction in HCOOH and UV-PVG in $0.6 \text{ mol L}^{-1} \text{ HCOOH}$ medium. The developed methods and those of reference can be ordered in a descending manner according to their whiteness profile as follows: UV-PVG- μ CCP-OES (95%) > TD-AAS (87%) \approx SnCl_2 -CVG- μ CCP-OES (81%) > SnCl_2 -CVG-AFS (75%) >> SnCl_2 -CVG-ICP-OES (60%). This ordering is in accordance with the RGB levels, which include the 12 principles and consider the analytical performance, operating conditions, mode of operation, applicability, etc. Therefore, the miniaturized UV-PVG- μ CCP-OES instrumentation present the highest redness score in terms of scope of application (R1) and analytical performance (R2), such as the best LOD and LOQ, compared to traditional methods.

The higher whiteness profile is also determined by the higher greenness profile due to the lower toxicity of HCOOH used for sample extraction and UV/Vis-PVG, a lower amount of reagents, a lower amount of generated waste, but mainly by the instrumentation with a lower energy and Ar consumption (G1–G3 criteria).



Figure 1. Visualization of the redness, greenness, blueness and whiteness profiles of the UV/Vis-PVG-μCCP-OES methods, in comparison with traditional methods for Hg determination and speciation, according to the RGB 12 algorithm [21]

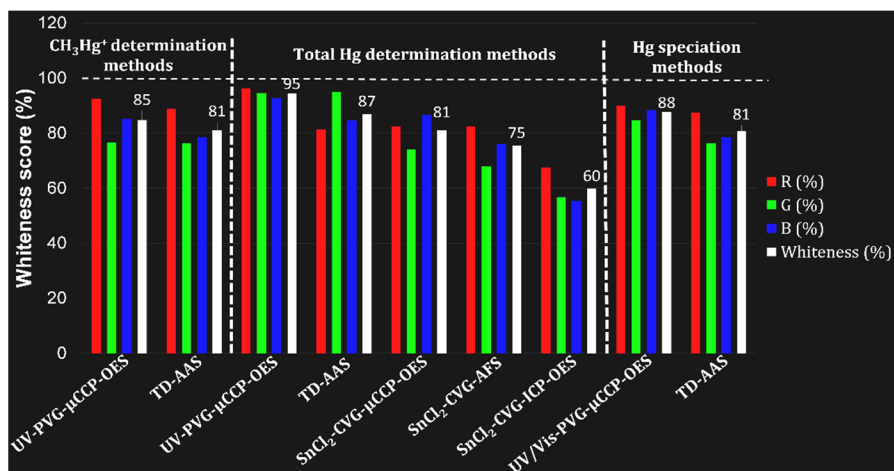


Figure 2. Comparison of the redness, greenness, blueness and whiteness profiles of the methods, obtained by the RGB 12 algorithm [21]

The better whiteness profile of the method based on miniaturized instrumentation is in agreement with the better blueness score, mainly due to the cost-effective fully miniaturized instrumentation (B1 criteria), which is almost ten times cheaper compared to ICP-OES, and the simplicity of its operation (B4 criteria). It could be observed that the UV/Vis-PVG-μCCP-OES method for Hg speciation have a higher whiteness profile (88%), compared to that of TD-AAS (81%). This feature can be explained by the ultrasound assisted extraction in HCOOH and UV/Vis-PVG selective derivatization of total Hg/Hg²⁺ species, compared to the procedure based on double liquid-liquid extraction in the HBr–toluene–L-cysteine system, used for selective extraction of CH₃Hg⁺ for the determination of TD-AAS. Consequently, the greenness and blueness profiles of the methods based on microplasma source have higher scores (85% and 88%, respectively), than that for the TD-AAS method (76% and 78%, respectively). The redness profile of the UV/Vis-PVG-μCCP-OES and TD-AAS methods have similar scores (90% and 88%, respectively) as a result of the similar analytical performances of the two methods.

CONCLUSIONS

The greenness profile of the UV/Vis-PVG-μCCP-OES methods for Hg determination and speciation as CH₃Hg⁺ and Hg²⁺ were evaluated by four procedures, namely NEMI, AES, GAPI and AGREE. Each of these unique

approaches have proven to be limited, but by combining them it has been possible to highlight which method has the greenest profile and which steps of the analytical method are responsible for improving its greenness degree. The greenness profiles of the new methods were characterized by scores in the range of 25–75% according to NEMI procedure, 61–85% according to AES procedure and 55–65% according to AGREE procedure, compared to scores of 25–68% obtained for SnCl_2 -CVG-ICP-OES and SnCl_2 -CVG-AFS as reference methods. On the other hand, the UV-PVG- μ CCP-OES usually exhibits very high greenness scores. However, the lowest greenness score was obtained for CH_3Hg^+ determination, based on a double liquid-liquid extraction in the HBr -toluene-L-cysteine system and determination by UV-PVG- μ CCP-OES and TD-AAS. It was also highlighted a higher greenness of the methods based on ultrasound assisted extraction in HCOOH combined with UV/Vis-PVG for total Hg determination and its speciation. The evaluation of whiteness profile by the RGB 12 procedure of the UV/Vis-PVG- μ CCP-OES methods highlighted their advantage in terms of analytical performance and economic aspects due to the miniaturized and cost-effective instrumentation, low Ar and energy consumption.

EXPERIMENTAL SECTION

Sample preparation for Hg determination and speciation as CH_3Hg^+ and Hg^{2+}

The sample preparation for determination of methylmercury in fish tissue by UV-PVG- μ CCP-OES and TD-AAS methods was based on a double liquid-liquid selective extraction, developed by the European Commission [23, 24]. Amounts of 0.2 g fish tissue sample was extracted with 10 mL HBr 47% and 0.5 mL distilled water, then CH_3Hg^+ species were selectively extracted twice in 20 mL and 15 mL toluene, respectively, and finally re-extracted in 6 mL 1% (w/v) aqueous L-cysteine solution. For quantification by UV-PVG- μ CCP-OES, aliquot volumes of 1–5 mL were diluted to 50 mL and brought in 0.6 mol L^{-1} HCOOH medium for the UV-PVG of CH_3Hg^+ . In the case of TD-AAS method, CH_3Hg^+ was determined in 1% (w/v) L-cysteine solution, without derivatization.

Sample preparation for total Hg determination in food samples (fish tissue, vegetables, fruits, food supplements, meat and organs) by UV-PVG- μ CCP-OES was based on an ultrasound assisted extraction of 0.2 g sample in 98–100% HCOOH for 3 h at 50°C , followed by UV-PVG in 0.6 mol L^{-1} HCOOH medium. The Hg determination in fish tissue samples was carried out without preconcentration, while in other foods the *on-line* preconcentration of

Hg cold vapor on a gold filament microcollector was applied. In water samples the total Hg was determined by derivatization in 0.6 mol L^{-1} HCOOH, without any further sample preparation [26].

Sample preparation for Hg, CH_3Hg^+ and Hg^{2+} determination by UV/Vis-PVG- μCCP -OES was also based on ultrasound assisted extraction in HCOOH and selective UV/Vis-PVG in 0.6 mol L^{-1} HCOOH [27].

Sample preparation for total Hg determination in fish tissue by SnCl_2 -CVG-ICP-OES, SnCl_2 -CVG-AFS and SnCl_2 -CVG- μCCP -OES consisted of a microwave assisted digestion in 8 mL 60% (w/w) HNO_3 and 2 mL 30% (w/w) H_2O_2 , and dilution to 50 mL in 5% (v/v) HCl. A solution of SnCl_2 in HCl was used as derivatization reagent [25, 26].

Instrumentation

The UV/Vis-PVG- μCCP -OES instrumentation (Babes-Bolyai University, Cluj-Napoca, Romania) consist of a fully miniaturized set-up, containing a continuous flow photochemical vapor generator equipped with a high-power UV lamp (500 W), a gas-liquid separator, a Nafion tube for Hg cold vapor drying, a low power (10–15 W) and low Ar consumption (100 mL min^{-1}) capacitively coupled plasma microtorch, a low-resolution CCD microspectrometer (QE65 Pro or Maya2000 Pro, Ocean Optics, Dunedin, USA) for signal registration and data processing [24, 26, 27]. A preconcentration step on a gold filament microcollector, mounted between the gas-liquid separator and the Nafion tube was used for the determination of total Hg in food samples with low concentration (vegetables, fruits, water, etc.). The operating mode consisted of Hg cold vapor trapping on the gold filament at room temperature from 25 mL aliquot sample, thermal desorption after electrical heating (5 V, 1.8 A) and recording several episodic spectra at 253.652 nm [26]. For the CH_3Hg^+ and Hg^{2+} speciation the UV/Vis-PVG- μCCP -OES instrumentation with and without cold vapor preconcentration and UV-PVG for total Hg (UV lamp turned on) and Vis-PVG for Hg^{2+} species (UV lamp turned off) [27].

For total Hg determination by SnCl_2 -CVG- μCCP -OES, the experimental set-up was similar, but in this case the plasma microtorch was interfaced with a HGX-200 cold vapor generator (Teledyne CETAC, Nebraska, USA), instead of the photochemical vapor generator [26].

For comparative determinations by TD-AAS an Automated Direct HG Analyzer Hydra-C Teledyne Leeman Instruments (Hudson, USA) was used [24]. A Spectro CIROS^{CCD} spectrometer (Spectro, Kleve, Germany) interfaced with a HGX-200 cold vapor generator was used for SnCl_2 -CVG-ICP-OES determination. A Hydra-AF Mercury Analyzer (Teledyne Leeman Instruments, USA) was used for SnCl_2 -CVG-AFS determinations [26].

The working conditions of the UV/Vis-PVG- μ CCP-OES and reference methods are presented in Table 5, while figures of merit in Table 6 [24–27].

Table 5. Working conditions for Hg determination and speciation as CH_3Hg^+ and Hg^{2+} by UV/Vis-PVG- μ CCP-OES and reference methods

Method (species determined)	Working conditions
UV/Vis-PVG-μCCP-OES with or without preconcentration (total Hg and CH_3Hg^+ speciation) [24, 26, 27]	Derivatization reagent: 0.6 mol L^{-1} HCOOH at 10 mL min^{-1} Sample throughput: 20 analyses/hour Plasma power: 15 W Argon flow rate: 100 mL min^{-1} Amount of waste: 95 mL for CH_3Hg^+ determination and 35 mL for total Hg and Hg^{2+} determination
SnCl_2-CVG-ICP-OES (total Hg) [26]	Sample flow rate: 5 mL min^{-1} Derivatization reagent: 20% (w/v) SnCl_2 stabilized in 15% (v/v) HCl at 2 mL min^{-1} Sample throughput: 10 analyses/hour Plasma power: 1400 W Argon flow rate: 1500 mL min^{-1} Amount of generated waste: 62 mL
SnCl_2-CVG-AFS (total Hg) [26]	Sample flow rate: 5 mL min^{-1} Derivatization reagent: 2% (w/v) SnCl_2 stabilized in 10% (v/v) HCl at 1 mL min^{-1} Sample throughput: 12 analyses/hour Argon flow rate: 150 mL min^{-1} Amount of generated waste: 55 mL
SnCl_2-CVG-μCCP-OES (total Hg) [26, 26]	Sample flow rate: 3.5 mL min^{-1} Derivatization reagent: 20% (w/v) SnCl_2 stabilized in 15% (v/v) HCl in 1 mL min^{-1} Sample throughput: 20 analyses/hour Plasma power: 15 W Argon flow rate: 150 mL min^{-1} Amount of generated waste: 53 mL
TD-AAS (CH_3Hg^+ and total Hg) [24]	Amount of sample: 0.2 g or 0.2 mL Sample throughput: 6 analyses/hour Oxygen flow rate: 300 mL min^{-1} Amount of generated waste: 51 mL for CH_3Hg^+ determination and insignificant for total Hg determination by direct solid sampling

Table 6. Figures of merit for total Hg determination and speciation as CH_3Hg^+ and Hg^{2+} by UV/Vis-PVG- μCCP -OES and reference methods

Determined Hg species /Method	Calibration range (µg L ⁻¹)	Precision ¹	Accuracy ²	LOD		LOQ		Ref.
				(ng L ⁻¹)	(µg kg ⁻¹)	(ng L ⁻¹)	(µg kg ⁻¹)	
<i>CH₃Hg⁺</i>								
UV-PVG-µCCP-OES	0–5 (n=7)	2.7–9.4	99 ± 8	7	2	21	6	[24]
TD-AAS	0–25 ng	3.5–10.4	99 ± 9	-	-	5	15	[24]
<i>Total Hg</i>								
UV-PVG-µCCP-OES without preconcentration	0–1 (n=6)	2.6–12.7	101 ± 7	3.5	9	10.5	36	[26]
UV-PVG-µCCP-OES with preconcentration	0–0.1 (n=6)	3.0–12.8	101 ± 12	0.1	0.3	0.25	0.75	[26]
TD-AAS	0–25 ng	2.6–8.1	99 ± 7	-	0.2	-	0.6	[27]
SnCl ₂ -CVG-ICP-OES	0–10 (n=6)	1.6–10.3	100 ± 7	19	57	5	15	[26]
SnCl ₂ -CVG-AFS	0–1 (n=6)	2.7–5.7	102 ± 6	5	15	12.5	38	[26]
SnCl ₂ -CVG-µCCP-OES	0–1 (n=6)	1.3–8.5	100 ± 7	3.5	10.5	9	27	[26]
<i>Hg speciation as CH₃Hg⁺ and Hg²⁺</i>								
UV-PVG-µCCP-OES (Total Hg)	0–1 (n=7)	2.6–10.2	99 ± 6	3.5	9	10.5	27	[27]
Vis-PVG-µCCP-OES (Hg ²⁺)	0–10 (n=7)	2.0–13.4	99 ± 9	1.9	4.8	5.7	14	[27]

¹ Precision is expressed as Relative Standard Deviation (%)

² Accuracy is expressed as Pooled Recovery ± Confidence Interval (%) for 95% confidence level and n=5 complete analysis

Procedures used for evaluation of greenness and whiteness profiles

In the NEMI procedure, developed by the Methods and Data Comparability Board (MDBC) the greenness profile is shown by the aid of a four-quadrant circle, in which every quadrant represents different aspects of the analytical method, corresponding to the type and amount of reagents (3 quadrants) and amount of generated waste (1 quadrant) [7]. Each quadrant is colored in green if the corresponding criteria is met, otherwise it is left blank. The greenness criteria for reagents are not met if they are persistent, bioaccumulative and toxic, according to the Toxics Release Inventory (TRI) list (criterion 1, PBT), are found on the Recovery Conservation Act (RCA)'s D, F, P and U hazardous waste lists (criterion 2), reagents used are corrosive (pH <2 and >12) (criteria 3), and the fourth quadrant is associated with the amount of generated waste (> 50 g or >50 mL) (criterion 4) [7].

The AES procedure, developed by Galuszka *et al.* [9], is based on the assignment of 100 points to a completely green profile for a method, from which different penalty points (PP) are deducted according to the amount of reagents, their hazard to human health and environment (according to their pictograms and signal words), energy consumption, occupational hazard and the amount of generated waste. Methods with an AES score > 75 are considered excellent green, between 75 and 50 acceptable green and < 50 inadequately green.

The GAPI procedure, which is a combined method between the NEMI and AES procedures, consists of a pictogram with 5 pentagons, describing the following aspects: (1) collection, preservation, transportation and storage of samples; (2) sample preparation in terms of scale of extraction, solvents/reagents used in the protocol and additional treatment; (3) amount of reagents and solvents, health hazard and safety hazard; (4) instrumentation, in terms of energy consumption, occupational hazard, amount of waste and waste treatment; and (5) method type, such as direct or indirect measurement. Each section of the five pentagons is colored in red, yellow and green according to its greenness profile. In the central pentagon a circle is drawn if the procedure is suitable for quantification, or if this circle is not present the procedure is appropriate only for qualitative identification. The GAPI procedure was described by Plotka-Wasyłka [10].

The AGREE procedure, developed by Pena-Pereira *et al.* [13], is a calculator written in python, which takes into account the criteria from the 12 principles of GAC, presented as different color, red, yellow, green in geometric sections around of a central circle, in which the general greenness score of the method is presented as value and color, respectively. Also, in each of the 12 segments a value between 0 and 1 and a color is assigned, according to its greenness score. The general greenness score of a method is calculated as average of the 12 principles scores. A method is completely green if the overall score is equal to 1. The following 12 principles are considered in the evaluation of the green profile of a method: (1) type of sampling (remote sensing, *in-field* sampling, *at-line*, *on-line*, *off-line*, etc.); (2) amount of sample required for analysis; (3) positioning of the analytical device (*off-line*, *at-line*, *on-line* or *in-line*); (4) number of major, distinct steps in the sample preparation procedure; (5) degree of method automation and miniaturization of the sample preparation procedure; (6) derivatization reagents; (7) amount of generated waste; (8) number of analytes determined during one analysis and number of samples analyzed per hour; (9) energy consumption; (10) type of reagents used (no reagents, all/some/none of the reagents are from bio-based sources); (11) amount of toxic reagents and solvents used in the analysis and (12) threats to which the operator and the environment is

exposed (toxic to aquatic life, bioaccumulative, persistent, highly flammable, highly oxidizable, explosive and corrosive reagents). The AGREE calculator was described by Pena-Pereira *et al.* [13].

The whiteness profile was assessed using the RGB 12 algorithm, developed by Nowak *et al.* [21], based on the 12 principles of WAC, which are divided into 3 parts, each corresponding to a different aspect of the analytical method. The first group contains the “red” principles, which includes aspects of the analytical performance (R1: scope of application; R2: LOD and LOQ; R3: precision and R4: accuracy). The second group contains the “green” principles, and includes reagents toxicity, generated waste and energy consumption (G1: toxicity of reagents; G2: number and amount of reagents and waste; G3: energy and other media; and G4: direct impacts to human health and environment). Finally, the third group contains the “blue” principles, such as aspects related to analytical efficiency and practical/economic criteria (B1: cost-efficiency; B2: time-efficiency; B3: requirements of the method, such as sample amount, advanced equipment, personal qualification, etc.; and B4: operational simplicity). The RGB 12 algorithm consists in the calculation of a score between 0 and 100 for the RGB profile by the analyst in an objective manner. The 0 score for RGB procedure represents the worst results, while a score of 100 is associated to the best redness, greenness and blueness profiles. The profile of the RGB procedure is appreciated depending on the red, green and blue colors shade. An excel worksheet was developed by Nowak *et al.* [21], in which the parameters for the red, green and blue profiles are entered, which do not have to be linearly dependent. The shade of each color is set automatically in the program according to the red, green and blue score of the method.

ACKNOWLEDGMENTS

This work was supported by a grant of the Romanian National Authority for Scientific Research and Innovation, CNCS/CCCDI-UEFISCDI, (Contract no. 93PED/2017), Project number PN-III-P2-2.1-PED-2016-0135, within PNCDI III.

This work was also supported by a grant of Romanian Ministry of Education and Research, National Council for the Financing of Higher Education, Project number CNFIS-FDI-2021-0061.

REFERENCES

1. J.A. Linthorst; *Found. Chem.*, **2010**, *12*, 55-68.
2. B.A. de Marco; B.S. Rechelo; E.G. Totoli; A.C. Kogawa; H.R.N. Salgado; *Saudi Pharm. J.*, **2019**, *27*, 1-8.
3. J.C. Warner; P.T. Anastas; *Green chemistry: Theory and Practice*, Oxford University Press, New York, US, **1998**.
4. Galuszka; Z. Migaszewski; J. Namiesnik; *TrAC, Trends Anal. Chem.*, **2013**, *50*, 78-84.
5. M. de la Guardia; S. Garrigues. *Challenges in Green Analytical Chemistry*, 2nd ed., The Royal Society of Chemistry, Cambridge, UK, **2020**.
6. J.A. Tickner; M. Becker; *Curr. Opin. Green Sustain. Chem.*, **2016**, *1*, 1-4.
7. L.H. Keith; L.U. Gron; J.L. Young; *Chem. Rev.*, **2007**, *107*, 2695-2708.
8. J.J.D. Douglas Raynie; *Green assessment of chemical methods*. In: 13th Annual Green Chemistry and Engineering Conference, Maryland, **2009**.
9. Galuszka; Z.M. Migaszewski; P. Konieczka; J. Namiesnik; *TrAC, Trends Anal. Chem.*, **2012**, *37*, 61-72.
10. J. Plotka-Wasyłka; *Talanta*, **2018**, *181*, 204-209.
11. Ballester-Caudet; P. Campins-Falco; B. Perez; R. Sancho; M. Lorente; G. Sastre; C. Gonzalez; *TrAC, Trends Anal. Chem.*, **2019**, *118*, 538-547.
12. M.B. Hicks; W. Farrell; C. Aurigemma; L. Lehmann; L. Weisel; K. Nadeau; H. Lee; C. Moraff; M. Wong; Y. Huang; P. Ferguson; *Green Chem.*, **2019**, *21*, 1816-1826.
13. F. Pena-Pereira; W. Wojnowski; M. Tobiszewski; *Anal. Chem.*, **2020**, *92*, 10076-10082.
14. M. Sajid; M. Asif; I. Ihsanullah; *Microchem. J.*, **2021**, *169*, article number 106565.
15. Gutierrez-Serpa; R. Gonzalez-Martin; M. Sajid; V. Pino; *Talanta*, **2021**, *225*, article number 122053.
16. K.P. Kannaiah; A. Sugumaran; H.K. Chanduluru; S. Rathinam; *Microchem. J.*, **2021**, *170*, article number 106685.
17. M. Gamal; I. A. Naguib; D.S. Panda; F.F. Abdallah; *Anal. Methods*, **2021**, *13*, 369-380.
18. H.M. Marzouk; E.A. Ibrahim; M.A. Hegazy; S.S. Saad; *Biomed. Chromatogr.*, **2021**, *35*, article number e5132.
19. D. Mohamed; M.M. Fouad; *Microchem. J.*, **2020**, *157*, article number 104873.
20. S. Rathinam; L.K. Santhana; *Processes*, **2021**, *9*, article number 1272.
21. P.M. Nowak; R. Wietecha-Poslusznny; J. Pawliszyn; *TrAC, Trends Anal. Chem.*, **2021**, *138*, article number 116223.
22. M. Tobiszewski; *Anal. Methods*, **2016**, *8*, 2993-2999.

23. S.G.J. Calderon; F. Cordeiro; B. de la Calle. Determination of methylmercury in seafood by direct mercury analysis: standard operating procedure, JRC Technical Reports, European Commission, Institute for Reference Materials and Measurements, Geel, Belgium, February 2013 (<https://ec.europa.eu/jrc/sites/default/files/Full%20JRC%20Technical%20report%20SOP.pdf>) (Accessed 13 January 2022).
24. E. Covaci; M. Senila; M. Ponta; E. Darvasi; D. Petreus; M. Frentiu; T. Frentiu; *Talanta*, **2017**, *170*, 464-472.
25. E. Covaci; M. Senila; M. Ponta; E. Darvasi; M. Frentiu; T. Frentiu; *Food Control*, **2017**, *82*, 266-273.
26. E. Covaci; M. Senila; C. Tanaselia; S.B. Angyus; M. Ponta; E. Darvasi; M. Frentiu; T. Frentiu; *J. Anal. At. Spectrom.*, **2018**, *33*, 799-808.
27. E. Covaci; S.B. Angyus; M. Senila; M. Ponta; E. Darvasi; M. Frentiu; T. Frentiu; *Microchem. J.*, **2018**, *141*, 155-162.

THERE ARE NO PERFECT ANALYTICAL METHODS - OPTIMIZATION STUDY OF A PHARMACOPOEIA METHOD FOR CLOPIDOGREL ANALYSIS

IOANA-NICOLETA LINCA^a, SILVIA IMRE^{a,b*}, IOAN TOMUȚĂ^c,
AMELIA TERO-VESCAN^d

ABSTRACT. Clopidogrel is a chiral compound, (+)-(S)-enantiomer has antiplatelet activity, while (-)-(R)-clopidogrel is considered an impurity of the active substance. The development of HPLC methods for optical purity analysis involves the use of expensive chiral columns and the methodologies could be different in the two well recognized compendia, European (Ph.Eur.) and United States (USP) Pharmacopoeias. The aim of this study was to optimise the chiral chromatographic assay of clopidogrel and its impurities from tablets taking into consideration the official pharmacopoeia provision by testing the influence of the variation of different chromatographic parameters on the relative retention times of clopidogrel and official impurities in order to achieve the separation performance parameters described in USP43. HPLC-UV enantioseparation of clopidogrel was performed on a column with ovomucoid as a stationary phase chiral selector and phosphate – acetonitrile mixtures as mobile phase. The official relative retention of clopidogrel and its A and C impurities could not be achieved in this study, neither by applying a classical optimization methodology nor by using the experimental design methodology which raises the issue of reviewing the pharmacopoeia provisions. A comparative discussion between the two different approaches regarding chiral separation of clopidogrel in Ph.Eur. and USP is provided.

Keywords: clopidogrel, chiral separation, HPLC, ovomucoid, enantioseparation.

^a Department of Analytical Chemistry and Drug Analysis, Faculty of Pharmacy, George Emil Palade University of Medicine, Pharmacy, Science, and Technology of Targu Mures, 38 Gheorghe Marinescu street, RO-540142, Targu Mures, Romania

^b Center of Advanced Medical and Pharmaceutical Research, George Emil Palade University of Medicine, Pharmacy, Science, and Technology of Targu Mures, 38 Gheorghe Marinescu street, RO-540142, Targu Mures, Romania

^c Department of Pharmaceutical Technology and Biopharmacy, Faculty of Pharmacy, Iuliu Hatieganu University of Medicine and Pharmacy, 41 Victor Babes street, RO-400012, Cluj-Napoca, Romania

^d Department of Chemistry and Medical Biochemistry, Faculty of Medicine in English, George Emil Palade University of Medicine, Pharmacy, Science, and Technology of Targu Mures, 38 Gheorghe Marinescu street, RO-540142, Targu Mures, Romania

* Corresponding author: silvia.imre@umfst.ro

INTRODUCTION

Clopidogrel (CLPD) is an antiplatelet agent, an inhibitor of P2Y₁₂, commonly used in the secondary prevention of cardiovascular disease including transient ischemic attack, stroke or peripheral artery disease [1]. Although modern P2Y₁₂ inhibitors such as prasugrel and ticagrelor are marketed, CLPD still has financial advantages over them and unlike aspirin, clopidogrel has the advantage of being used in patients at high risk of bleeding [2]. CLPD is a prodrug transformed into its active metabolites (2-oxo-CLPD and CLPD thiol) mainly via CYP2C19, but also with the participation of other enzyme systems CYP1A2, CYP2B6 and CYP3A, its active metabolites bind irreversibly to the receptor P2Y₁₂ in blood platelets, preventing their aggregation [3].

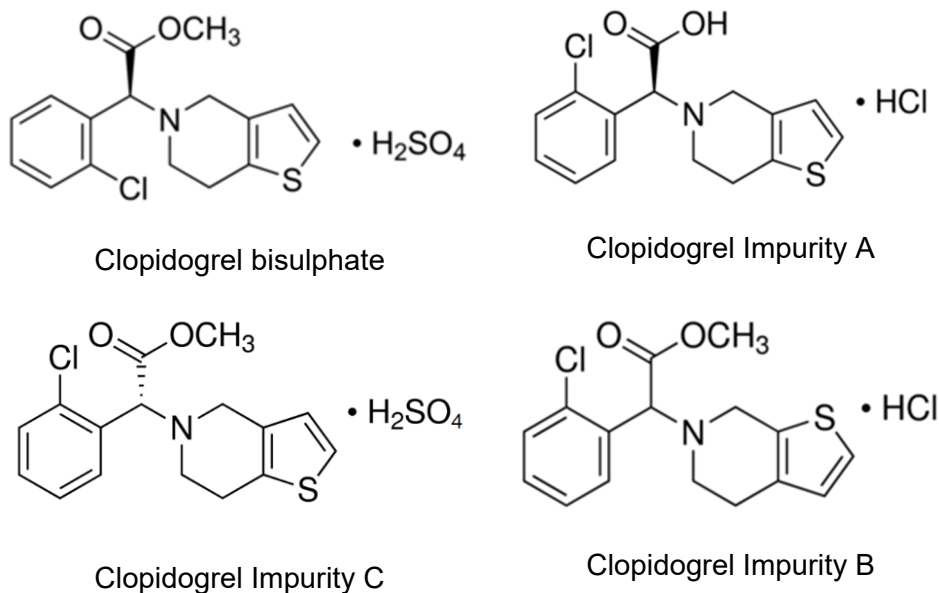


Figure 1. Chemical structures of CLPD and chemically related impurities specified in pharmacopoeias (USP, Ph. Eur. 10.5)

CLPD contains an asymmetric carbon atom and presents optical isomerism, but only the (+)-(S) enantiomer has antiplatelet activity, while the (-)-(R) enantiomer lacks this pharmacological effect. Additionally, in animal studies, it was observed that the (-)-(R) enantiomer triggered seizures at high doses [4,5], therefore, it is considered an impurity of (+)-(S)-CLPD [6].

Considering the chirality of CLPD, the possibility of enantiomerism, as well as the activation of the compound *in vivo*, a special interest is given to its impurities, including those from the active substance synthesis or other classes of compounds resulting from degradation processes which are described in the literature as well [7,8]. According to monographs from United States Pharmacopoeia 43st Edition (USP43) and the European Pharmacopoeia 10.5 (Ph. Eur. 10.5), the impurities of interest are: carboxylic acid form impurity A (IMP A), positional stereo isomer impurity B (IMP B) and a chiral isomer of clopidogrel impurity C (IMP C) (Figure 1).

Pharmaceutical impurities are compounds present in the final product that are not drug nor excipient. Impurity profiling is a condition *sine qua non* for the quality of a substance and also for the registration process as imposed by regulatory authorities, including the Food and Drug Administration (FDA) or European Medicines Agency (EMA), and according to pharmacopoeia provisions such as United States Pharmacopoeia (USP) or European Pharmacopoeia (Ph. Eur.) [9-11].

Considering the tests imposed by regulating authorities to pharmaceutical manufacturers in terms of quality and quantity of active substance in raw material or pharmaceutical forms, the relatively large number of samples analyzed but also the costs imposed by these analyzes (expensive and short-lifespan chiral columns in the analysis of impurities, reducing the volume of solvents that are not environmentally friendly or adaptation of the HPLC systems to specific working conditions), the methods described in pharmacopoeias are in general well optimized.

Our study aims to combine the classical approach by applying the USP43 HPLC method for the determination of CLPD and its impurities and Quality by Design (QbD) method in order to achieve the suitability criterion regarding the relative retention by respecting the accepted limits of variation for different chromatographic parameters and, nevertheless, to find out how appropriate is the optimization under these regulations in the case of CLPD.

RESULTS AND DISCUSSIONS

Influence of several chromatographic parameters on the efficiency and selectivity of CLPD determination

First, the chromatographic conditions described by the USP43 method for the determination of CLPD in raw material and tablets were reproduced: ovomucoid column (150x4.6 mm, 5 μ m), mobile phase composition 75% phosphate 10 mM, 25% ACN, flow 1 mL/min, column temperature 25 $^{\circ}$ C,

wavelength 220 nm, injection volume 10 μ L. In these chromatographic conditions IMP A, CLPD and IMP C had the unadjusted relative retention (RRT) (retention time ratio) of 0.683, 1 and 1.504, respectively (Figure 2).

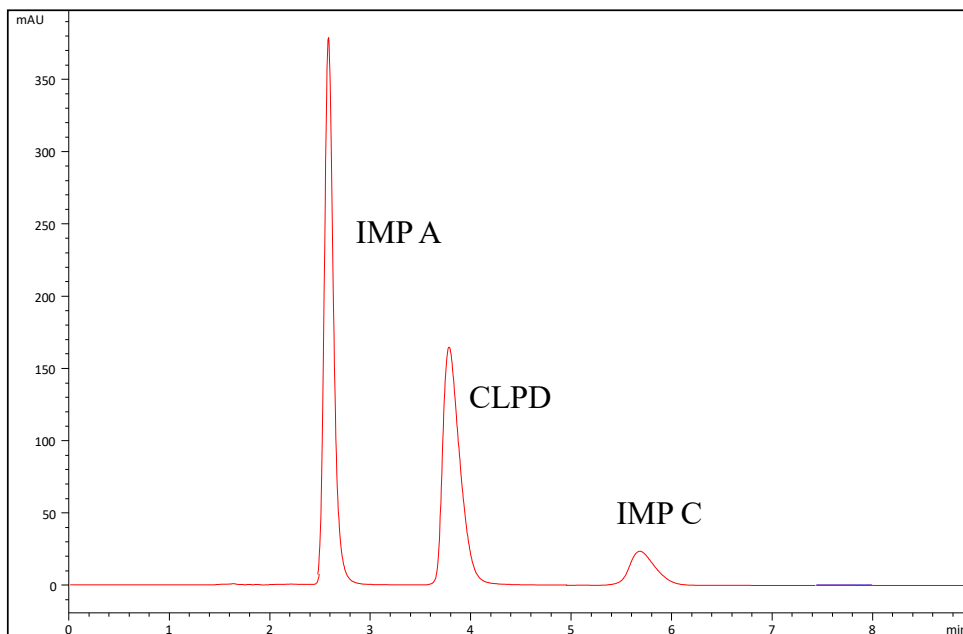


Figure 2. Chromatogram of a mixture consisted of IMP A (100 μ g/mL) $R_t = 2.586$ min, CLPD (100 μ g/mL) $R_t = 3.785$ min and IMP C $R_t = 5.695$ min (unknown concentration) in the mobile phase. Chromatographic conditions as stated in USP43 clopidogrel tablets monography

According to the official USP43 monography of CLPD tablets, RRT should be 0.5 (IMP A), 1 (CLPD) and 2 (IMP C), respectively. Consequently, changes in chromatographic conditions were performed but in respect of the limits imposed by pharmacopoeia (see Table 4), however other chromatographic conditions were modified to larger limits, such as phosphate salt concentration. Changes in experimental chromatographic conditions produced minor changes in the retention time of IMP A, therefore it was tested whether a drastic change in phosphate concentration of aqueous mobile phase to values of twice and half from the official limit in the mobile would modify the capacity factor of this substance to obtain the $RRT = 0.5$.

In order to obtain a $RRT = 0.5$ for IMP A, first, an attempt was made to obtain an appropriate mixture between aqueous component (10 mM potassium dihydrogen phosphate) of the mobile phase and the organic

component. Different conditions were tested on a standard binary mixture of IMP A and CLPD. As seen in Figure 3.a, at 25°C, an increased percent of phosphate increases the resolution of the peaks, with a consecutive decrease in the symmetry T of the CLPD peak, while the symmetry T of IMP A peak does not seem to be influenced (Table 1).

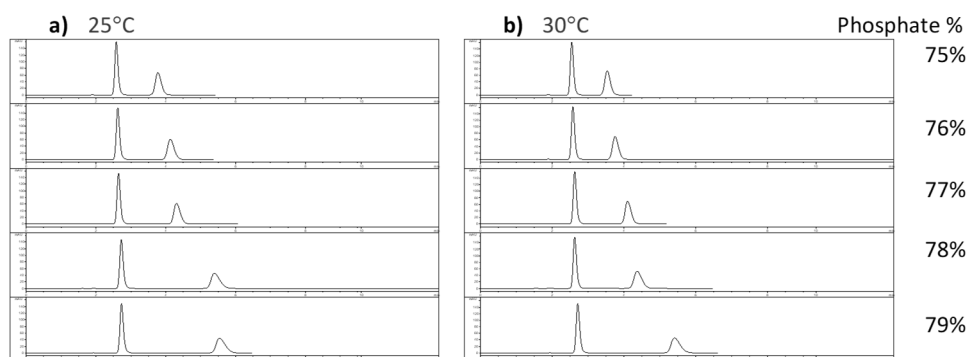


Figure 3. The influence of 10 mM phosphate percent (75%, 76%, 77%, 78% and 79%) in the mobile phase on the separation of IMP A and CLPD (standard aqueous mixture of CLPD and IMP A, 100 µg/mL each analyte) at a) 25°C and b) 30°C.

The other chromatographic conditions correspond to USP43 provisions.

Increasing the temperature of the chromatographic column to 30°C did not improve the symmetry of the peaks when using similar compositions of the mobile phase (Figure 3.b and Table 2). The RRT = 0.5 for IMP A was obtained for a percentage in the mobile phase of 78% phosphate at 25°C and a percentage of 79% at 30°C.

Table 1. The influence of phosphate percent in the mobile phase and the column temperature on the separation and symmetry of IMP A and CLPD peaks. The other chromatographic parameters were set according to USP43 provisions

Phosphate 10 mM (V/V)*	25 °C			30 °C		
	RRT IMPA	T _{IMP A}	T _{CLPD}	RRT IMP A	T _{IMP A}	T _{CLPD}
75%	0.684	0.763	0.746	0.720	0.758	0.768
76%	0.635	0.761	0.720	0.690	0.760	0.742
77%	0.614	0.762	0.703	0.640	0.760	0.716
78%	0.505	0.764	0.627	0.600	0.756	0.672
79%	0.492	0.762	0.616	0.501	0.764	0.622

* isocratic conditions, ACN up to 100% (V/V) in the composition of the mobile phase

The influence of flow rate and decreasing of column temperature on the separation of IMP A and CLPD was tested by maintaining the other chromatographic parameters as specified in USP43. Two tests were performed at 20°C, one at a flow rate of 1 mL/min where RRT IMP A = 0.67 min and the second, at 1.5 mL/min where RRT IMP A = 0.652 min, which indicates that the 50% flow rate increases and a lower temperature of separation with 5 units do not significantly influence the RRT of IMP A in comparison with the results obtained in USP43 conditions.

In terms of absolute retention time, IMP A is not significantly influenced by modifying the proportion between the aqueous and organic phase, by a change with 5°C of the column temperature, or by a 50% increase in mobile phase flow. The observed RRT variations were due to the sensitivity of CLPD retention to these chromatographic condition changes.

Taking into consideration the previous results, univariate or multivariate modifications of the reference chromatographic conditions in the USP43 were made, using a three component mixture of CLPD, IMP A and IMP C, respectively. The results are presented cumulatively in Table 2. In addition to varying the chromatographic conditions between the limits accepted by USP43, a double and a half concentration level of phosphate in the mobile phase, and the replacement of a part of ACN with MeOH were also tested. The chromatographic conditions modifications take into consideration the stability of ovomucoid column, very sensitive to degradation at high organic content in mobile phase.

Table 2. The RRT of IMP A and IMP C by uni- or multivariate changes of the reference USP43 chromatographic conditions

Mobile phase - phosphate, % (V/V)			Mobile phase - ACN, % (V/V)	Mobile phase – MeOH, % (V/V)	Flow, mL / min	t, °C	RRT	
10 mM	20 mM	5 mM					IMP A	IMP C
75	0	0	25	0	1	25	0.684	1.485
0	75	0	25	0	1	25	0.506	1.510
0	0	75	25	0	1	25	0.753	1.477
82.5	0	0	17.5	0	1	25	0.302	2.131
0	75	0	20	5	1	25	0.514	1.693
80	0	0	20	0	1	30	0.421	1.896
80	0	0	20	0	1.5	35	0.510	1.586
75	0	0	25	0	1	20	0.670	1.590
75	0	0	25	0	1.5	20	0.652	1.630

Despite these adjustments, the relative retention times as according to the reference and, in the same time, an acceptable symmetry for CLPD and IMP C could not be achieved; higher percent of phosphate in the mobile phase A, although lead to RRT values close to reference, caused an improper tailing phenomenon of CLPD and IMP C peaks (Figure 4).

Absolute retention times of IMP A vary in a range of 0.6 min under the selected conditions, while for CLPD and IMP C changes of up to 15 min (for IMP C) were observed. For IMP A, the capacity factor k' and the retention on the column were little influenced by the experimental conditions. For CLPD and IMP C, improving the selectivity leads to a decrease in the separation efficiency under the tested conditions (asymmetric and wide peaks).

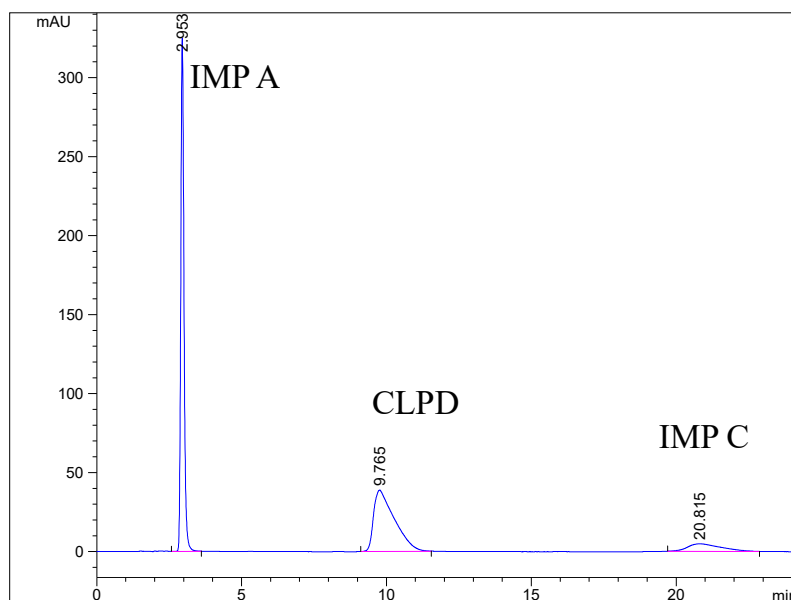


Figure 4. Chromatogram of a standard mixture of IMP A, CLPD and IMP C at 25°C, with a mobile phase consisting in 82.5% phosphate, 17.5% ACN, 1 ml/min, 220 nm

Increasing the percentage and concentration of phosphate leads to increased selectivity. Increasing the temperature reduces the separation between IMP A and CLPD, and between CLPD and IMP C, respectively; lowering the temperature has the opposite effect. Replacing a part of the ACN in the mobile phase with MeOH increases the separation between peaks, as it was accepted.

Optimizing chromatographic conditions through experimental design

All the experimental results obtained by varying different chromatographic parameters were used in an experimental design software Modde verse 12 to optimize the method with the main objective achieving the relative retention times for IMP A and C as mentioned in USP43. Calculations were performed and the proposed conditions are shown in Figure 5. The chromatogram obtained in these conditions is presented in Figure 6.

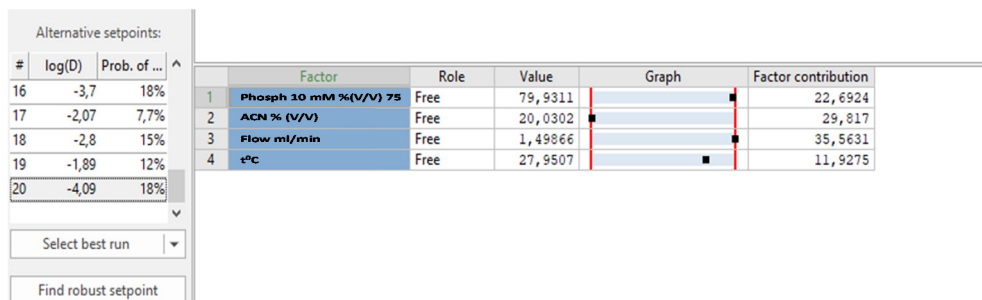


Figure 5. Optimization of the chromatographic conditions by experimental design

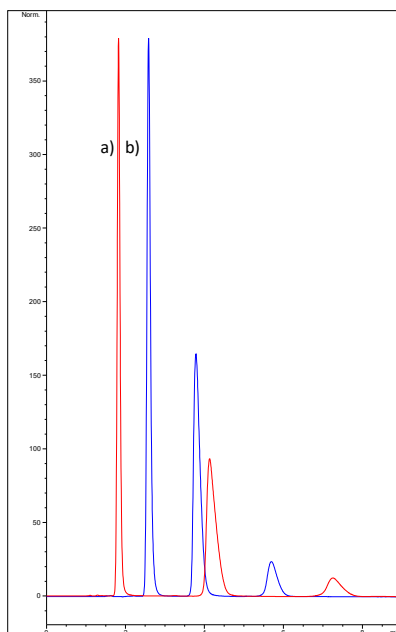


Figure 6. a) Experimental design conditions; b) USP43 conditions.

The absolute retention times were: $t_{R \text{ IMP A}} = 1.826$ min, $t_{R \text{ CLPD}} = 4.13$ min, $t_{R \text{ IMP C}} = 7.253$ min, and the relative retention $RRT \text{ IMP A} = 0.442$, $RRT \text{ CLPD} = 1$ and $RRT \text{ IMP C} = 1.756$, respectively.

The comparative analysis of the two chromatograms, a decrease of the peak symmetry of IMP C was observed in the proposed conditions compared to USP43 method. The results were not satisfactory, probably due to the limited number of experimental input data.

Estimating the CLPD and IMP A content in pharmaceutical products

The USP43 method for CLPD determination was tested for the analysis of the active substance and IMP A from two types of tablets (sample 1 and 2) available on the Romanian market, as IMP A was the only impurity available in measurable quantities.

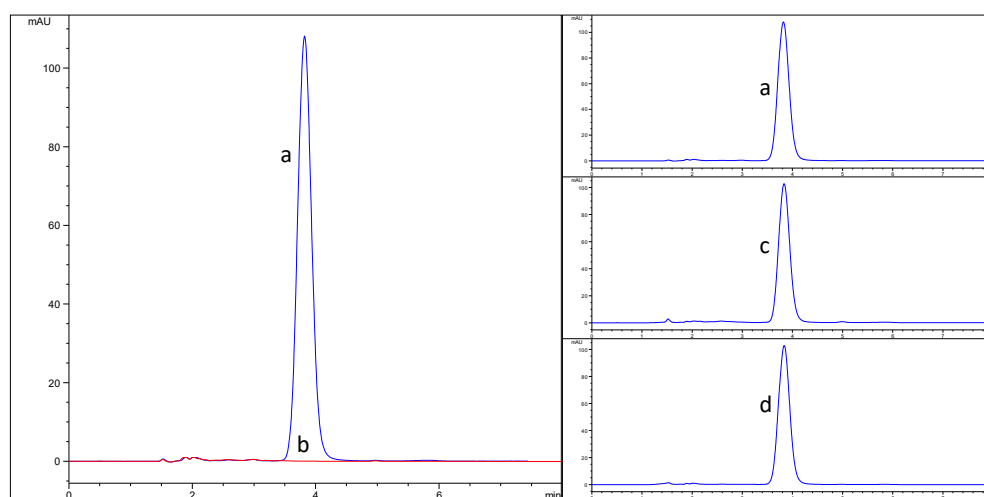


Figure 7. Chromatograms: a) CLPD standard solution (100 $\mu\text{g/mL}$ in MeOH); b) Mobile phase; c) Sample 1 solution; d) Sample 2 solution. Chromatographic conditions: 75% phosphate 10 mM, 25% ACN, 1 mL/min, 25°C, 220 nm, injected volume 10 μL

The results obtained after the analysis of the two commercial tablets (containing 75 mg CLPD bisulphate) under official conditions of USP43 are presented in Table 3.

Table 3. The estimated content of active pharmaceutical ingredient and IMPA A of two commercial CLPD tablets

	CLPD, mg/tablet	Limits of acceptance USP43, mg/tablet	IMP A, %	IMP A limit of acceptance, USP43
Sample 1	71.89	67.5 ÷ 82.5	0.042	1.2%
Sample 2	73.29		0.013	

As it can be seen, the tablets follow the regulations in terms of active pharmaceutical ingredient and IMP A content. The experiment provides an estimate as method was not validated, but demonstrates on one hand the applicability of method itself and on the other hand the validity of the approach in the respective laboratory.

Comparison of different approaches of chiral HPLC resolution for clopidogrel in the context of official provisions

The United States Pharmacopoeial Convention (USP Convention) meets at 5-year intervals to add monographs to new substances introduced in therapy or to review existing monographs, usually due to advances in analytical techniques based on the recommendations of the Council of Experts. [12].

The most frequently used methods in the analysis of active substance and impurities in raw materials or pharmaceutical forms in the case of chiral molecules such as CLPD are high-performance liquid chromatography (HPLC) and ultrahigh-performance liquid chromatography (UPLC) with UV detection, and involve the use of chiral stationary phases (carbohydrate-based columns - amylose and cellulose derivatives, protein-based columns - α 1-acid glycoprotein (AGP), albumin or vancomycin etc) [13-15], while for determinations of CLPD from biological samples HPLC coupled with a mass spectrometer (HPLC-MS) technique is used [16-18]. In the monographs regarding CLPD from Ph. Eur. 10.1 cellulose derivatives of silica are stipulated for chiral liquid chromatography tests, while the USP43 states the use of a protein derivatized silica, i.e. ovomucoid, for the assay of CLPD bisulfate and the tablets containing the same salt, and also for the determination of the related compounds in CLPD tablets [10,11]. The latter compendium also requires a polysaccharide column (a cellulose derivatized silica) for the determination of R enantiomer of CLPD. In the Japanese Pharmacopoeia (JPh17) a cellulose chiral column is stipulated for the determination of the optical isomer from the drug substance but an ovomucoid column is required when analyzing CLPD tablets [19].

In the case of determinations of compounds such as CLPD, the use of chiral columns involves high costs, therefore optimizing the methods of analysis especially in case of injection of high volumes of samples to detect low concentrations of chemically related impurities that can lead to premature destruction of a chromatographic column is extremely important. In literature there are many cases in which changes of analytical methods have been proposed that would bring improvements such as shortening the analysis time or prolonging the life of the column by using "milder" solvents, temperature applied to the column, mobile phase flow etc. For example, determination of somatropin through isoelectric focusing was changed with capillary zone electrophoresis in the January 2006 European Pharmacopoeia Supplement 5.3, because of a study elaborated by several laboratories [20].

Another example, the latest edition of Ph. Eur. uses heptane and ethanol, a mobile phase typical for normal phase chromatography to determine CLPD, which would imply the need to purchase an HPLC system equipped with tubing resistant to these solvents. Moreover, these solvents are toxic to the environment, while the USP method involves the use of more environmentally friendly solvents. In addition, in the case of the USP method of CLPD, the analysis time is shorter (under 10 minutes compared to 25 minutes in Ph. Eur. 10.1), but the column costs involved are higher [10,11].

In British Pharmacopoeia 2016 edition, in the CLPD Hydrogen Sulfate monograph it is recommended for the analysis of CLPD impurities by reversed-phase HPLC the use of a stationary phase end-capped octadecylsilyl silica gel type, and as mobile phase a mixture of MeOH and 0.96 g/L sodium pentanesulfonate monohydrate solution adjusted to pH 2.5 with phosphoric acid, ACN and MeOH, a flow rate of 1 mL/min and 30°C column temperature. To test the presence of chiral impurities, HPLC analysis is recommended on a silica gel column and a mobile phase containing ethanol and heptane, similar to the method in Ph. Eur. 10.1 [21].

The concept of QbD was introduced in 2004 by the U.S. Food and Drug Administration (FDA) and approved in 2005 by the International Conference on Harmonization (ICH) refers primarily to analytical methods for controlling the quantity and quality of the active substance. QbD is mainly applied to liquid chromatography analyzes (HPLC or UHPLC) usually in reversed phase and with UV detection to determine the active substance and impurities [22]. This concept can remove the influence that different variables can have on the results of the chromatographic analysis [23]. In the present study, the optimizing of USP43 method for determining CLPD, the QbD method produced results similar to those obtained in the laboratory in terms of modifying the main chromatographic parameters to obtain an efficient separation.

Limitations of the described experimental study

The limitations could be summarised as follows:

- Failed to work with all three official USP43 impurities;
- The method was not validated;
- The classical variation of the experimental conditions, within the limits provided by the compendial norms, did not allow the achievement of the separation conditions provided by the USP43 monograph;
- The aim was only to optimize the selectivity of the method, expressed by relative retention times, without taking into account the symmetry of the peak (which varies significantly on the ovomucoid column with the variation of chromatographic parameters).

CONCLUSIONS

HPLC analysis with chiral stationary phases is a common approach in pharmacopoeias, especially for enantiomeric purity tests, having major importance for substances used in therapy as a pure optical isomer.

The present study achieved relative retention times of CLPD and its IMP A and C only close to those specified in USP43, both by applying a classical optimization methodology and by using experimental design, which indicates the need of a possible revision of the official CLPD determination conditions.

EXPERIMENTAL SECTION

Chemicals and reagents

CLPD bisulfate, IMP A and IMP C were USP standards. HPLC-grade acetonitrile (ACN) and methanol (MeOH) were purchased from VWR Chemicals and J.T. Baker, respectively, and were used as solvents for standard solutions preparation. Pure potassium dihydrogen phosphate was purchased from Merck, Germany and was used for the preparation of the HPLC mobile phase. Distilled, deionized water was produced by a Direct-Q5 Millipore (Millipore SA, France) water system.

Chromatographic conditions

The HPLC stereoselective method of CLPD was performed on an Agilent 1100 Series System (Agilent Technologies, USA) equipped with a UV detector. As a chiral stationary phase, an Ultron OVM was used (150x4.6 mm

column, 5 μm particles, Shinwa Chemical/Agilent Technologies). The chiral selector consisted of ovomucoid glycoprotein immobilized on an aminopropyl silane-derivatized silica column. Different mobile phases were tested, containing different proportions of the aqueous component as phosphate buffer and various proportions of organic modifiers (methanol and acetonitrile). Concentrations of 5 mM, 10 mM, and 20 mM potassium dihydrogen phosphate in ultrapure water were tested as an aqueous mobile phase.

Samples, stock and standard solutions preparation

Stock solutions of 1000 $\mu\text{g/mL}$ CLPD and IMP A in MeOH were prepared by weighting appropriate amounts with the aid of an AB 54 S Metter-Toledo, Switzerland, analytical balance, both solutions were then diluted to a concentration level of 100 $\mu\text{g/mL}$ with MeOH. A stock solution with unknown concentration of IMP C was prepared by same method, as the small amount of standard available could not be weighed. A mixture of CLPD (100 $\mu\text{g/mL}$), IMP A (100 $\mu\text{g/mL}$) and IMP C was prepared with ultrapure water. Another standard mixture of CLPD and IMP A in MeOH was prepared as specified in USP43; the solution obtained had concentration levels of 40 $\mu\text{g/mL}$ CLPD and 250 $\mu\text{g/mL}$ IMP A. The latter mixture was diluted with the mobile phase according to the monograph and concentration levels of 1 $\mu\text{g/mL}$ for CLPD and 6.25 $\mu\text{g/mL}$ for IMP A were obtained.

CLPD tablets from two different producers, available on the Romanian market, were purchased and samples were prepared according to the USP43 monograph by weighing and grinding 20 tablets. A quantity of the ground tablet powder, corresponding to the average weight of one tablet, was suspended in 50 mL of MeOH using ultrasonic baths T700/H (Elma, Switzerland). The solution obtained was then diluted as specified and filtered through a syringe filter with proper porosity.

Reference chromatographic conditions (USP43):

- Ultron OVM column 150x4.6 mm, 5 μm (Agilent Technologies);
- Column temperature: 25°C;
- Mobile phase consisting of a mixture of ACN and potassium dihydrogen phosphate 10 mM;
- Flow rate: 1 mL/min;
- Sample temperature: 20°C;
- Injection volume: 10 μL ;
- Detection: 220 nm.

Optimization of chromatographic conditions

The changes applied to the chromatographic conditions are limited and must vary between specific ranges according to Ph. Eur. 10.1 [10] and USP43 [11] (see Table 4).

Table 4. Adjustments that can be applied to the isocratic elution in HPLC analysis as stated by USP43 and Ph. Eur. 10

Variable	USP43	Ph. Eur. 10
Composition of the mobile phase, the minor component	$\pm 30\%$ relative percent or $\pm 10\%$ absolute values (the widest range is chosen)	$\pm 30\%$ relative percent or $\pm 2\%$ absolute values (the widest range is chosen)
pH of the aqueous phase component	± 0.2 pH	± 0.2 pH (or ± 1.0 pH in analysis of non-ionizable substances)
Salt concentration in the buffer mobile phase component	$\pm 10\%$	$\pm 10\%$
Mobile phase flow rate	$\pm 50\%$; (higher limit is acceptable when changing the column size)	$\pm 50\%$; (higher limit is acceptable when changing the column size)
Column temperature	± 10 °C	± 10 °C

Experimental data acquisition and processing

Chromatographic data were obtained by the HPLC system software: Chemstation RevA 10.02[1757]. Optimization of the analytical method through experimental design was performed on a Modde vers 12 software.

CONFLICTS OF INTEREST

The authors declare no conflict of interest.

REFERENCES

1. G. Patti; G. Micieli; C. Cimminiello; L. Bolognese; *Cardiovasc. Ther.*, **2020**, article ID 8703627.
2. N. Sarafoff; R.A. Byrne; D. Sibbing; *Curr. Pharm. Des.*, **2012**, 18, 5224-5239.
3. <https://www.rxlist.com/search/rxl/clopidogrel%20bisulfate> (Last accessed date 24.10.2021)
4. C.R. Tynes; B. Livingston; H. Patel; J.J. Arnold; *J. Pediatr. Pharmacol. Ther.*, **2014**, 19, 25–29.

5. M. Lestari; Clopidogrel Bisulfate. In *Profiles of Drug Substances, Excipients and Related Methodology*, H.G. Brittain, Academic Press, **2010**, Volume 35, Chapter 2, pp. 71-115.
6. Y. Gomez Y; E. Adams; J. Hoogmartens; *J. Pharm. Biomed. Anal.*, **2004**, 34, 341-348.
7. A. Mohan; M. Hariharan; E. Vikraman; G. Subbaiah; B.R. Venkataraman; D. Saravanan; *J. Pharm. Biomed. Anal.*, **2008**, 47, 183 - 189.
8. E.S. Elzanfaly; H.E. Zaazaa; A.T. Soudi; M.Y. Salem; *Chem. Pap.*, **2015**, 69, 1541–1547.
9. International Conference on Harmonisation of Technical Requirements for Registration of Pharmaceuticals for Human Use (ICH) Impurities in New Drug Products ICH Topic Q3B(R2). Available at <https://www.ema.europa.eu/en/ich-q3b-r2-impurities-new-drug-products#current-effective-version-section> (Last accessed date 24.10.2021).
10. Clopidogrel bisulfate monograph, *European Pharmacopoeia 10.1*, EDQM, Council of Europe, **2020** (electronic version).
11. Clopidogrel hydrogen sulfate monograph, Clopidogrel tablets monograph, *USP 43-NF 38*, United States Pharmacopeial Convention, **2021** (electronic version).
12. R.L. Williams; *AAPS J.*, **2006**, 8, E661-664.
13. R. Petkovska; C. Cornett; A. Dimitrovska; *Maced. J. Chem. Chem. En.*, **2008**, 27, 53-64.
14. K. Nikolic; B. Ivkovic; Z. Besovic Z et al; *Chirality*, **2009**, 21, 878–885.
15. R. Ferretti; L. Zanitti; R. Cirilli R; *J. Sep. Sci.*, **2018**, 41, 1208-1215.
16. J. Kavitha; K.S. Kokilambigai; R. Seetharaman; R.R. Harini; A.A. Kaaviya; P. Sowndaravel; K.S. Lakshmi; *Crit. Rev. Anal. Chem.*, **2018**, 48, 119-131.
17. M. Karazniewicz-Lada; D. Danielak; F. Glowka; *J. Liq. Chrom. Rel. Tech.*, **2014**, 37, 620-633.
18. R.N. Rao; K.G. Prasad; P.B. Priya; S. Bijarji; *Chirality*, **2014**, 26(2): 102-107.
19. Clopidogrel bisulfate monograph, Clopidogrel tablets monograph, *Japanese Pharmacopoeia XVII ed.*, Tokyo: Society of Japanese Pharmacopoeia, **2016**, 736-739.
20. S. Storms; A. Feltus; A. Barker; M.-A. Joly; M. Girard; *Pharmeur. Sci. Notes.*, **2009**, 1, 25-36.
21. Clopidogrel Hydrogen Sulfate monograph, *British Pharmacopoeia*, volume 1, **2016**, I-606.
22. T. Tome; N. Žigart; Z. Časar; A. Obreza; *Org. Process. Res. Dev.*, **2019**, 23, 1784-1802.
23. R. Peraman; K. Bhadraya; Y.P. Reddy; *Int. J. Anal. Chem.*, **2015**, Article ID 868727.

THE INFLUENCE OF AGRICULTURAL SOIL PREPARATION METHODS ON THE PSEUDO-TOTAL ELEMENT CONTENT DETERMINED BY ICP-OES

STEFAN PETROVIĆ^{a,*}, JELENA MRMOŠANIN^a,
ALEKSANDRA PAVLOVIĆ^a, SLAĐANA ALAGIĆ^b,
SNEŽANA TOŠIĆ^a, GORDANA STOJANOVIĆ^a

ABSTRACT. The five agricultural soil preparation methods for the purpose of determining the pseudo-total content of 20 elements (Al, As, Ca, Cd, Co, Cr, Cu, Fe, Hg, K, Mg, Mn, Mo, Na, Ni, P, Pb, S, Si and Zn) in 4 soil samples taken from different plots of soils in the vicinity of Vranje (Southern Serbia) was applied in this paper. The following methods were used: digestion with aqua regia and hydrogen-peroxide with heating at temperature 190 °C, digestion with aqua regia and hydrogen-peroxide in combination with ultrasound with heating at temperature 95 °C, digestion with reverse aqua regia and hydrogen-peroxide with heating at temperature 190 °C, and digestion with nitric acid and hydrogen-peroxide under reflux with heating at temperature 95 °C, and digestion with perchloric acid with heating at temperature 190 °C. The results were statistically processed using an ANOVA test. The results obtained by this study show that the amount of extracted elements from the soil is influenced by several different factors including the following: soil type, soil content and chemical form of the elements.

Keywords: *soil, digestion methods, macro and microelements, inductively coupled plasma optical emission spectrometry, ANOVA*

INTRODUCTION

Soil, as the main habitat of humans, plants, and animals, is a highly specific component of the biosphere, which consists of mineral constituents, organic matter or humus, living organisms, air, water, and which regulates the natural cycles of these components. Soil acts as a natural buffer that

^a University of Niš, Faculty of Sciences and Mathematics, Višegradska 33, 18 000 Niš, Serbia

^b University of Belgrade, Technical Faculty, Vojske Jugoslavije 12, 19210 Bor, Serbia

* Corresponding author: stefan.petrovic@pmf.edu.rs

controls the transport of chemical elements and substances into the atmosphere and hydrosphere, but it also represents a geochemical reservoir of contaminants. The most crucial role of soil is its productivity, which is responsible for the survival of mankind. Although the average content of elements in soil mostly stems from the parent material (rock), anthropogenic factors also contribute significantly to the total content in the soil [1,2].

Plants need elements for natural growth and development. Some elements present in larger amounts are harmful to the plant and they cause visible effects on it (leaf chlorosis, smaller growth, smaller yield). It is necessary to monitor soil contamination, especially that caused by heavy metals, in order to maintain a healthy environment. Heavy metals are naturally found in soils formed by the geological processes of change, erosion, and alteration. Heavy metals are not biodegradable, they accumulate in the environment and come from chemical and metallurgical industry, mining, traffic, domestic and commercial activities, waste incineration plants, industrial wastewater, sewage sludge, poor quality fertilizers, pesticides, fungicides, or as a result of anthropogenic activities in general. Deforestation, soil erosion, extraction processes from natural resources, climate change, precipitation, floods, as well as wet and dry atmospheric deposition also affect soil composition. The contents of Cd, Cr, Cu, Pb, and Zn are the best indicators of human influence. Mn is also known to easily migrate into the environment. The overuse of pesticides and fertilizers in agriculture causes the increase in the concentration of macro and microelements in agricultural soil. The presence of heavy metals in soil affects the quality of food and groundwater, microorganism activity, and plant development [3-7].

The total metal concentration in soil does not necessarily correspond to the amount of metals that are bioavailable to plants. Clay minerals, hydrated metal oxides (mostly Fe, Mn, and Al), as well as organic matter, are considered the most important components of soil, and it is exactly these components that dictate the bioavailability of elements. Moreover, physical, chemical, and biological characteristics of soil (soil texture, redox potential, pH, buffer capacity, cation exchange capacity, organic matter amount, clay amount, sulfate, carbonate, and hydroxide amount, soil humidity and temperature, and the microorganisms inhabiting it) also affect the migration and bioavailability of elements. In addition, the uptake of elements by plants is also affected by plant type, age, plant parts, growth period, element stability, and the element transfer factor [4,8,9]. The chemical form of the metals in soil can largely affect their behavior, toxicity, bioavailability, as well as the chemical reactions they participate in, which further influences the motion of this metal among the parts of the complex ecosystem (water, air, biota, and soil/sediments). Heavy metals can be retained by some soil components, so as to precipitate or coprecipitate as sulfides, carbonates, oxides, or hydroxides [10].

Soil sample preparation as an analytical step is very important and it often participates in the obtained results with the largest error, which is why the selection of sample preparation method is one of the most important factors that influence the validity of the obtained results. Several methods, more or less different, with different efficiency of so-called element extraction, different duration of the process and, most importantly, different requirements for laboratory equipment have been described in the literature. An important criterion when choosing the method is whether certain information about the total element concentration (*total content*), element concentration apart from the one mainly related to the silicate fraction (*pseudo-total content*) or about the amount of bioavailable elements is needed.

The efficiency of a soil preparation method depends on the nature of the element, matrix content, and decomposition conditions. During the selection of optimal soil preparation conditions, the mass of the sample, the composition of oxidizing agents and mixtures, the final volume, as well as the physical parameters (temperature, ultrasonic wave intensity, etc.) are varied. There are no universal methods, and the goal is to achieve extraction maximum, work minimum, agent minimum, and the highest environmental protection. The recovery values of pseudo-total and total digestion vary depending on the mineral content, origin of the soil, digestion method, and the tested element. A method is considered satisfactory if about 90% of the element gets extracted [5,11].

The so-called wet digestion is one of the most commonly used methods for determining the total and pseudo-total content. It enables high sample decomposition, i.e., the decomposition of organic matter by heating the samples in the presence of strong oxidizing agents (HNO_3 , HCl , HClO_4 , HF , H_2O_2 , etc.) or their mixtures, where one agent serves for the decomposition and the other forms water-soluble complex salts with the elements that are being tested. Sulfuric acid is rarely used because of its construction of insoluble PbSO_4 and BaSO_4 and hydrofluoric acid due to its high aggressiveness. If the procedure is carried out in a closed system, the addition of HF degrades the silicate matrix, which leads to the so-called total digestion [12]. However, HF may also form insoluble precipitates with Al , Ca , Fe , and Mg , as well as coprecipitates with Rb , Sr , Y , Ba , Th , and U . Wet digestion can be carried out in open or closed vessels (autoclaves), using ultrasound or in microwave ovens. Wet digestion in open systems lasts pretty long and requires greater amounts of the solvent. It can also come to the loss of volatile analytes, and there is also a risk of soil contamination. Microwave digestion as a contemporary method of sample preparation, where the preparation time is shorter and the amount of the solvent is smaller, is commonly used for the

analysis of smaller amounts of analytes. The mixture of conc. HCl and conc. HNO₃ (3:1, v/v, so-called *aqua regia*) has been most commonly used [2,4,6,7,11-15]. This mixture is one of the most aggressive solvents with a greater sample decomposition effect compared to individual acids. What is varied is the amount of the mixture, time, temperature, as well as whether the procedure is carried out in an open or closed system. This is a very effective method for the extraction of heavy metal pseudo-total content in soil and it is most commonly used in the European Union. It is often used as a standard method for the preparation of reference soil samples in some countries (the UK and France). Nitric acid oxidizes hydrochloric acid producing various oxidating, highly reactive products, chlorine and nitrosyl-chloride. It dissolves even precious metals, but does not dissolve silicates completely. Nitrosyl-chloride dissolves sulfides, sulfosalts, selenides, tellurides, arsenides, while the present chlorides as a complexing reagent make this method highly effective.

In terms of other solvents, either individual or in a mixture, the following ones are used: aqua regia with the addition of HClO₄ [11,16]; aqua regia with the addition of H₂O₂ using microwave digestion [17]; the mixture of conc. HCl and conc. HNO₃ (1:3, v/v) in an open system [18]; the mixture of conc. HCl and conc. HNO₃ of different ratios in a microwave oven [11]; the mixture of conc. HCl, conc. HNO₃ and conc. HF (9:3:2, v/v/v) in a microwave oven [19]; dilute nitric acid (1:1, v/v) in an open system with the addition of H₂O₂ [11]; conc. nitric acid in a microwave oven (USEPA Method 3051A) [10,20]; boiled 2M HNO₃ [3]; nitric acid and hydrogen-peroxide with microwave digestion (USEPA Method 3050a) [21]; HNO₃ and HF in an oven (3:2, v/v) [5]; 20% nitric acid [6]; nitric and hydrofluoric acid [22]; nitric acid and hydrogen-peroxide [23,24].

Samples are often burned in an oven (the so-called dry process) with the aim of decomposing organic matter, after which the dry residue is treated with a solvent or solvent mixture [6]. The procedure of the so-called sequential extraction is also not uncommon: of exchangeable elements with magnesium-nitrate, carbonates with sodium-acetate, oxides with hydroxylamine and hydrochloric acid, organic matter with hydrogen-peroxide and residues with hydrogen-peroxide, hydrofluoric, nitric and perchloric acid [25].

There are a number of papers in the literature where different extraction procedures were carried out with the aim of assessing phytoavailable amounts i.e. the amounts of elements that are available to plants for adoption: Cd, Cu, Pb, and Zn with potassium-nitrate [15]; K, Ca, and Mg with ammonium-acetate; Fe, Zn, Mn, and Cu with DTPA [4]; K with ammonium-acetate; Zn, Cu, Cd, and Ni with DTPA [26]; Cu, Zn, and Cd with sodium-nitrate; P and K with water saturated with carbon-dioxide; Mg with calcium-chloride [3]; Na,

K, Ca, and Mg with ammonium-acetate [2]; K, Mg, and Na with ammonium-acetate, S with calcium-chloride, P with sodium-bicarbonate, Fe, Zn, Mn, and Cu with DTPA, B with hot water [27]; Ca and Mg with potassium-chloride; P, K, Fe, Zn, Mn, and Cu with a mixture of dilute HCl and H₂SO₄ [20]; different fractions of arsenic with ammonium-chloride, ammonium-fluoride, sodium-hydroxide, sulfuric acid [21]; Co, Cd, Cr, Pb, and Ni with ammonium-chloride, calcium-chloride, strontium-chloride, DTPA [10]; heavy metals with ammonium-acetate [6].

In this paper the efficiency of five accessible and most commonly used methods of soil sample preparation for determining the pseudo-total content of elements using inductively coupled plasma optical emission spectrometry (ICP-OES) was investigated.

RESULTS AND DISCUSSION

The validation process of the applied ICP-OES methods included the linearity of the calibration curve, the correlation coefficients, the limit of detection (LOD) as well as possible matrix interferences (Table 1). The calibration lines on several wavelengths were constructed for each element. The selection of the analytical emission line was made based on the calibration line parameters (maximum relative emission intensities, the correlation coefficients, the limit of detection), as well as based upon the tables of known interferences, baseline shifts and the background correction (the highest signal-to-background ratio) which was manually selected for the quantitative measurements. The limit of detection was calculated using the 3σ criterion [28]. The possible matrix interferences were examined by comparing the calibration slopes of the external calibration lines to the slope of the standard addition method lines [29]. The ratio $\text{Slope}_{\text{cal}}/\text{Slope}_{\text{sam}}$ values closer to 1 indicate a negligible matrix effect at the selected wavelengths that is the matrix has less effect on the quantitative determination of the elements. The obtained results for the ME are from -5.12 % to 1.21%, which indicates that the selected wavelengths can be used because they are at a satisfactory level of influence of the samples matrix.

Table 1. The parameters of the selected analytical lines

Element	λ (nm)	LOD (ppm)	r	Linear range (ppm)	Ratio $\text{Slope}_{\text{cal}}/\text{Slope}_{\text{sam}}$	ME* (%)
Al	396.152	0.0077919	1	0-100	1.0065	0.65
As	189.042	0.0035719	1	0-1	0.9702	-2.98
Ca	396.847	0.0445667	0.9998	0-100	1.0057	0.57
Cd	226.502	0.0002784	1	0-1	1.0104	1.04
Co	228.616	0.0002645	1	0-1	0.9981	-0.19
Cr	267.716	0.0004410	1	0-1	1.0101	1.01
Cu	324.754	0.0003766	0.9999	0-1	1.0074	0.74
Fe	259.941	0.0028537	0.9999	0-100	1.0097	0.97
Hg	184.950	0.0001166	1	0-0,025	0.9919	-0.81
K	766.491	0.0122200	0.9999	0-100	0.9897	-1.03
Mg	279.553	0.0002343	1	0-10	0.9488	-5.12
Mn	257.611	0.0001789	0.9997	0-1	1.0011	0.11
Mo	202.095	0.0009466	0.9999	0-1	1.0121	1.21
Na	589.592	0.0070642	1	0-100	1.0100	1.00
Ni	231.604	0.0005709	0.9999	0-1	1.0074	0.74
P	177.495	0.0006585	0.9999	0-100	0.9864	-1.36
Pb	220.353	0.0088547	1	0-1	0.9955	-0.45
S	180.731	0.0088103	1	0-100	0.9973	-0.27
Si	251.612	0.0137430	0.9996	0-100	1.0067	0.67
Zn	206.200	0.0003018	0.9992	0-1	1.0093	0.93
<p>*ME = $\left(\frac{I_1}{I_2} - 1\right) \times 100\%$; I_1 – the intensity of the selected line in the standard solution; I_2 – the intensity of the selected line spiked standard solution</p>						

THE INFLUENCE OF AGRICULTURAL SOIL PREPARATION METHODS
ON THE PSEUDO-TOTAL ELEMENT CONTENT DETERMINED BY ICP-OES

The 5 methods listed above (M1-M5) were applied for the purpose of preparing the 4 agricultural soil samples (1-4). The obtained results concerning the content of the elements that were tested are given in Tables 2, 3, and 4.

Table 2. Mean content \pm SD (mg kg^{-1}) of the elements extracted using different sample preparation methods

	Al	As	Cd	Ca	Cr	Co	Cu
1M1	8767 \pm 40	5.6 \pm 0.2 ^a	1.15 \pm 0.02	2745 \pm 6	21.9 \pm 0.2 ^a	11.0 \pm 0.2	18.8 \pm 0.1
1M2	6046 \pm 50	3.4 \pm 0.2	0.93 \pm 0.03 ^{a,b}	2300 \pm 50	30.72 \pm 0.01	10.3 \pm 0.2	23.09 \pm 0.08
1M3	12849 \pm 40	5.5 \pm 0.2 ^a	0.80 \pm 0.02	1975 \pm 30	21.85 \pm 0.06 ^a	9.92 \pm 0.08	25.1 \pm 0.5
1M4	20306 \pm 40	6.58 \pm 0.08 ^b	0.96 \pm 0.02 ^{a,c}	2928 \pm 30	31.8 \pm 0.2	12.23 \pm 0.08 ^a	37.8 \pm 0.2
1M5	13868 \pm 80	6.6 \pm 0.2 ^b	0.95 \pm 0.02 ^{b,c}	2612 \pm 9	27.12 \pm 0.03	12.18 \pm 0.06 ^a	39.3 \pm 0.2
2M1	7194 \pm 30 ^a	3.6 \pm 0.1 ^b	0.81 \pm 0.03	2050 \pm 8 ^a	14.65 \pm 0.08	8.2 \pm 0.2 ^a	17.6 \pm 0.2
2M2	9751 \pm 30	5.0 \pm 0.2	0.55 \pm 0.01 ^a	2023 \pm 20 ^a	15.81 \pm 0.08	7.76 \pm 0.08	25.1 \pm 0.3
2M3	6748 \pm 30	3.6 \pm 0.2 ^b	0.49 \pm 0.02	1684 \pm 20	11.2 \pm 0.2	6.20 \pm 0.08	23.3 \pm 0.2
2M4	11329 \pm 40	4.2 \pm 0.2 ^a	0.56 \pm 0.02 ^a	2377 \pm 20	16.67 \pm 0.08	8.24 \pm 0.06 ^a	36.7 \pm 0.2
2M5	7266 \pm 40 ^a	4.5 \pm 0.2 ^a	0.62 \pm 0.02	2127 \pm 20	13.97 \pm 0.08	7.2 \pm 0.2	28.1 \pm 0.2
3M1	10712 \pm 50 ^b	4.32 \pm 0.06 ^{a,c}	1.38 \pm 0.04	3030 \pm 5	24.58 \pm 0.09	11.01 \pm 0.08	29.9 \pm 0.3
3M2	10711 \pm 40 ^b	4.8 \pm 0.2	0.563 \pm 0.006 ^{a,b}	2119 \pm 20 ^a	20.36 \pm 0.08 ^a	8.86 \pm 0.03	38.7 \pm 0.2
3M3	8872 \pm 30 ^a	3.8 \pm 0.2 ^{b,e}	0.60 \pm 0.02 ^{a,c}	1810 \pm 20	16.05 \pm 0.03	7.22 \pm 0.03	34.8 \pm 0.3
3M4	12434 \pm 50	4.1 \pm 0.2 ^{b,c,d}	0.59 \pm 0.02 ^{b,c}	2087 \pm 20 ^a	19.73 \pm 0.03	8.1 \pm 0.2	45.2 \pm 0.3
3M5	8802 \pm 40 ^a	3.9 \pm 0.3 ^{a,d,e}	1.28 \pm 0.03	2398 \pm 6	20.4 \pm 0.02 ^a	9.2 \pm 0.2	46.3 \pm 0.3
4M1	8474 \pm 40	4.71 \pm 0.08 ^{a,c}	0.87 \pm 0.02 ^c	7749 \pm 40	16.26 \pm 0.08 ^{c,d,e}	8.5 \pm 0.08	22.54 \pm 0.08
4M2	12933 \pm 40	6.5 \pm 0.2	0.61 \pm 0.02 ^a	12258 \pm 40	17.1 \pm 0.2 ^{a,b,d}	8.2 \pm 0.2	35.4 \pm 0.2 ^a
4M3	7905 \pm 40	5.1 \pm 0.2	0.642 \pm 0.008 ^{a,b}	8833 \pm 30	11.71 \pm 0.08	7.04 \pm 0.06	29.17 \pm 0.06
4M4	11081 \pm 60	4.8 \pm 0.2 ^{b,c}	0.66 \pm 0.02 ^b	12867 \pm 40	15.64 \pm 0.08 ^{b,e,f}	7.87 \pm 0.08	89 \pm 3
4M5	6594 \pm 50	5.0 \pm 0.2 ^{a,b}	0.88 \pm 0.03 ^c	12415 \pm 60	15 \pm 3 ^{a,c,f}	7.52 \pm 0.03	36.6 \pm 0.3 ^a

*the amounts of an element marked with the same letters within one and the same sample (by column) do not significantly differ statistically; a is always less than b; b is always less than c, etc.; the greater the value of the letters a, b, c, etc. the less the obtained results differ

Table 3. Mean content \pm SD (mg kg^{-1}) of the elements extracted using different sample preparation methods

	Fe	Pb	Mg	Mn	Ni	K	Na
1M1	28747 \pm 60	12.3 \pm 0.2 ^c	4067 \pm 20	592 \pm 2 ^{a,b}	20.5 \pm 0.1	4375 \pm 8	555 \pm 2
1M2	32552 \pm 80	12.3 \pm 0.4 ^{b,c}	4844 \pm 3	601 \pm 4 ^a	26.1 \pm 0.2 ^a	6632 \pm 30 ^a	88 \pm 2
1M3	30736 \pm 90	12.71 \pm 0.08 ^b	5289 \pm 9	584 \pm 7 ^b	26.0 \pm 0.3 ^a	6154 \pm 20	134 \pm 2
1M4	35921 \pm 50	17.9 \pm 0.2 ^a	6248 \pm 30	675 \pm 4	26.7 \pm 0.2	7431 \pm 20	172.2 \pm 0.8
1M5	33868 \pm 50	18.25 \pm 0.08 ^a	5832 \pm 20	646 \pm 2	29.1 \pm 0.2	6643 \pm 50 ^a	145 \pm 2
2M1	13514 \pm 70 ^a	15.7 \pm 0.2	2297 \pm 5 ^a	506 \pm 2 ^b	13.3 \pm 0.1 ^a	2693 \pm 8 ^a	530 \pm 4
2M2	13351 \pm 30	17.4 \pm 0.2	4000 \pm 20	531 \pm 4 ^a	20.3 \pm 0.4	3095 \pm 30	82 \pm 2
2M3	11370 \pm 40	18.1 \pm 0.2	2049 \pm 20	505 \pm 5 ^b	13.2 \pm 0.3 ^a	3018 \pm 30	130 \pm 2
2M4	13589 \pm 70 ^a	22.6 \pm 0.1	2444 \pm 30	597 \pm 2	19.2 \pm 0.5	3321 \pm 20	226 \pm 2
2M5	12584 \pm 80	19.9 \pm 0.2	2261 \pm 8 ^a	528 \pm 2 ^a	17.5 \pm 0.3	2660 \pm 7 ^a	121 \pm 2
3M1	30594 \pm 70	8.5 \pm 0.2 ^a	4539 \pm 7	557 \pm 2	20.8 \pm 0.2	4799 \pm 6	479 \pm 2
3M2	24688 \pm 80	9.4 \pm 0.2 ^b	4052 \pm 20	461 \pm 3	24.4 \pm 0.1	4421 \pm 9	82 \pm 3
3M3	23947 \pm 90	8.71 \pm 0.08 ^a	3917 \pm 30	467.5 \pm 0.9	19.4 \pm 0.3	3529 \pm 9	95 \pm 2
3M4	25184 \pm 60	9.4 \pm 0.2 ^b	4159 \pm 10	495.5 \pm 0.8 ^a	18.8 \pm 0.2	4165 \pm 10	123 \pm 1
3M5	25500 \pm 60	11.8 \pm 0.2	3766 \pm 4	495 \pm 2 ^a	17.96 \pm 0.08	4038 \pm 5	145.4 \pm 0.8
4M1	13045 \pm 80 ^a	19.9 \pm 0.4	2704 \pm 5 ^a	552 \pm 2	15.13 \pm 0.08 ^a	2613 \pm 1	864 \pm 2
4M2	15455 \pm 60	22.04 \pm 0.05	3320 \pm 30	640 \pm 3	18.0 \pm 0.2	3172 \pm 20	228 \pm 2 ^a
4M3	12568 \pm 80	24.7 \pm 0.4	2662 \pm 30 ^a	622 \pm 4	14.8 \pm 0.2 ^a	2222 \pm 10	184 \pm 3
4M4	14329 \pm 70	28.5 \pm 0.2	2931 \pm 40	631 \pm 2	23.4 \pm 0.2	2864 \pm 20	269 \pm 2
4M5	12895 \pm 60 ^a	20.7 \pm 0.2	2360 \pm 8	581 \pm 2	13.68 \pm 0.05	2135 \pm 6	226.3 \pm 0.8 ^a

*the amounts of an element marked with the same letters within one and the same sample (by column) do not significantly differ statistically; a is always less than b; b is always less than c, etc.; the greater the value of the letters a, b, c, etc. the less the obtained results differ

The obtained results were statistically processed using the *one-dimensional variance analysis* method (*One-way ANOVA*) with the application of the *Tukey post-hoc test* for the purpose of finding the contents which do not exhibit a statistically significant difference, i.e., for the purpose of establishing for which element(s) and in which sample(s) the different soil preparation methods do not statistically differ. Based on the obtained results, in general, it can be concluded that there are no regularities neither per sample nor per

THE INFLUENCE OF AGRICULTURAL SOIL PREPARATION METHODS
ON THE PSEUDO-TOTAL ELEMENT CONTENT DETERMINED BY ICP-OES

the methods applied or the element tested, which suggests that the efficiency of the element extraction with the application of these methods is affected by a number of different factors. It is evident that the smallest statistically significant difference, as a result of the application of different methods, can be found in the contents of the following elements: As, Cd, Pb, Cr, Mn and Ni, while most of the statistically significant differences can be found among the contents of macroelements.

Table 4. Mean content \pm SD (mg kg⁻¹) of the elements extracted using different sample preparation methods

	Zn	Mo	P	Si	S	Hg
1M1	95.7 \pm 0.3	0.49 \pm 0.03 ^a	727 \pm 2 ^a	140 \pm 2	326 \pm 2 ^a	0.0574 \pm 0.0003
1M2	100.4 \pm 0.5 ^a	3.30 \pm 0.05	726 \pm 4 ^a	422 \pm 4	461.2 \pm 0.8	0.3286 \pm 0.0004
1M3	100.7 \pm 0.3 ^a	<LOD	623 \pm 3	14.7 \pm 0.5	312 \pm 2	0.0651 \pm 0.0006
1M4	158.6 \pm 0.3	0.53 \pm 0.02 ^a	781 \pm 3	66 \pm 2	329 \pm 3 ^a	0.0333 \pm 0.0002
1M5	155.4 \pm 0.6	0.78 \pm 0.02	812 \pm 3	440 \pm 2	381 \pm 2	0.1214 \pm 0.0006
2M1	89.7 \pm 0.6	0.37 \pm 0.03	797 \pm 2	96 \pm 2	299 \pm 2	0.0522 \pm 0.0003
2M2	96.1 \pm 0.3	0.48 \pm 0.03	959 \pm 3	538 \pm 3	384 \pm 2	0.0505 \pm 0.0001
2M3	92.1 \pm 0.3	<LOD	785 \pm 5	19.6 \pm 0.4	324 \pm 2	0.0287 \pm 0.0002
2M4	150.0 \pm 0.3	1.942 \pm 0.008	885 \pm 3	49.2 \pm 0.3	367 \pm 2 ^a	0.0374 \pm 0.0002
2M5	115.6 \pm 0.3	<LOD	904 \pm 3	555 \pm 2	363 \pm 3 ^a	0.1227 \pm 0.0005
3M1	113.6 \pm 0.3	0.39 \pm 0.02	760 \pm 2	67 \pm 1	296 \pm 2	0.0766 \pm 0.0001
3M2	80.4 \pm 0.3	0.51 \pm 0.02 ^a	730 \pm 4	297 \pm 2	209 \pm 2 ^a	0.1162 \pm 0.0002
3M3	84.3 \pm 0.5	0.30 \pm 0.02	592 \pm 3	14.4 \pm 0.2	227 \pm 3	0.0268 \pm 0.0003
3M4	107.3 \pm 0.3	0.48 \pm 0.04 ^a	626 \pm 3	79 \pm 2	207 \pm 2 ^a	0.0313 \pm 0.0004
3M5	132.2 \pm 0.3	<LOD	696 \pm 1	409.9 \pm 0.8	337 \pm 2	0.189 \pm 0.002
4M1	102.5 \pm 0.6	0.40 \pm 0.03	2113 \pm 4	53.1 \pm 0.8	596 \pm 2	0.0818 \pm 0.0003
4M2	130.3 \pm 0.3	0.78 \pm 0.02	2821 \pm 3	491 \pm 3	826 \pm 2	0.0224 \pm 0.0002
4M3	112.6 \pm 0.6	<LOD	2384 \pm 3	17.6 \pm 0.4	651.2 \pm 0.8	0.0275 \pm 0.0002
4M4	321.4 \pm 0.3	2.01 \pm 0.02	2584 \pm 4 ^a	151.1 \pm 0.8	787 \pm 3	0.0520 \pm 0.0003
4M5	147.4 \pm 0.3	0.62 \pm 0.01	2586 \pm 2 ^a	641 \pm 2	697 \pm 2	0.0747 \pm 0.0001

*the amounts of an element marked with the same letters within one and the same sample (by column) do not significantly differ statistically; a is always less than b; b is always less than c, etc.; the greater the value of the letters a, b, c, etc. the less the obtained results differ

In order to compare the efficiency of the applied methods more easily, relative content deviations in those samples where the M2, M3, M4, and M5 methods were applied in relation to the samples where the M1 method was applied are given in Tables 5 and 6:

$$rel.deviation = \frac{X_{MN} - X_{M1}}{X_{M1}} \times 100\% \quad (1)$$

where X_{M1} is the mean element content (mg kg^{-1}) in the sample prepared using method M1; X_{MN} is the mean element content (mg kg^{-1}) in the sample prepared using methods M2, M3, M4, and M5.

Table 5. Relative deviation (%) of the content of the tested elements in the samples prepared using methods M2, M3, M4, and M5 in relation to method M1

Element	sample-1				sample-2			
	M2	M3	M4	M5	M2	M3	M4	M5
Al	-31.03	46.56	131.62	58.18	35.55	-6.20	57.49	1.00
As	-39.29	-1.79	17.50	18.23	38.09	-1.17	16.87	25.66
Cd	-18.73	-30.08	-16.37	-17.34	-32.88	-39.26	-30.58	-24.23
Ca	-16.22	-28.06	6.66	-4.83	-1.29	-17.87	15.94	3.75
Cr	39.97	-0.43	44.97	23.57	7.93	-23.87	13.79	-4.63
Co	-6.06	-9.89	11.08	10.65	-5.18	-24.24	0.76	-12.26
Cu	22.62	33.18	100.88	108.94	43.13	32.76	109.16	59.86
Fe	13.23	6.92	24.96	17.81	-1.21	-15.87	0.55	-6.89
Pb	0.53	3.61	45.65	48.73	10.58	15.43	43.97	26.28
Mg	19.12	30.06	53.64	43.41	74.10	-10.82	6.40	-1.58
Mn	1.45	-1.29	13.97	9.17	4.92	-0.24	18.02	4.26
Ni	27.22	26.77	30.13	42.08	52.89	-0.32	44.67	31.76
K	51.59	40.66	69.84	51.84	14.91	12.05	23.32	-1.25
Na	-84.11	-75.78	-68.98	-73.96	-84.57	-75.53	-57.29	-77.23
Zn	4.86	5.16	65.63	62.31	7.11	2.71	67.25	28.83
Mo	576.38	/	8.58	58.92	31.25	/	431.37	/
P	-0.17	-14.40	7.41	11.61	20.43	-1.51	11.06	13.52
Si	202.23	-89.45	-53.02	214.77	461.77	-79.50	-48.69	479.72
S	41.53	-4.14	0.91	17.02	28.72	8.67	22.86	21.58
Hg	472.69	13.44	-42.00	111.53	-3.14	-45.06	-28.38	135.08

The positive and negative deviation values in the tables express the percentage of how much more or less of an element was extracted using the given method (M2-M5) in relation to the method M1. The analysis of the obtained results shows that the greatest extraction efficiency is achieved by pseudo-total extraction with nitric acid under reflux (M4) for the largest number of the elements tested in sample 1 (Al, Ca, Cr, Co, Fe, Mg, Mn, K, and Zn). In terms of efficiency, the method with aqua regia using ultrasound (M5) follows, which is mostly used for the extraction of As, Cu, Pb, Ni, P, and Si. Better contact between the sample and the reagent applied using reflux and ultrasound must have contributed to that. In terms of sample 2, the highest efficiency was also noticed in the case of the M4 method applied for the following elements: Al, Ca, Cr, Co, Cu, Fe, Pb, Mn, K, Zn, and Mo. Then follows the M2 method with aqua regia for As, Mg, Ni, P, Si, and S. Sample 3 was specific in that the reverse aqua regia method proved most effective for Cd, Ca, Cr, Co, Fe, Mg, Mn, K, Na, and P. This method turned out to be the best for Cd and Na in samples 1 and 2, as well as for Na, Co, and Hg in sample 4. Then follows the M5 method for Cu, Pb, Zn, Si, S, and Hg. The greatest variability in method efficiency was noticed in sample 4 where two of the methods stood out: the M2 method proved best for the extraction of the following elements: Al, As, Cr, Fe, Mg, Mn, K, P, and S, while the M4 method proved most favorable for the following elements: Ca, Cu, Pb, Ni, Zn, and Mo.

Even with these variabilities observed, some general conclusions can be drawn. It is characteristic for Na that the M1 method was best for all of the examined samples, while the results of the analyses concerning Si showed that the most favorable method was M5, where aqua regia was used as a very aggressive and destructive reagent with the application of ultrasound. Comparing the concentration values for Si obtained using methods M2 and M5 which utilize aqua regia as a reagent, it can be observed that the greatest amounts of this mineral were extracted by these methods, with the concentration values obtained using ultrasound which provided a better phase contact being slightly higher. It is widely known that mineral acids like HCl, HNO₃, and HClO₄, which are generally used for element extraction both individually and in combination with one another, do not dissolve the silicate fraction of the sample, or dissolve it very little. During the experimental execution of soil preparation after the digestion had been conducted, a certain amount of silicate fraction remained, which is why the amount of Si in the tested samples does not represent the total content of this mineral. Al, Cd, Ca, Cu, Fe, Pb, and Zn were best extracted by method M4 in most of the samples, As and S by method M2, and Hg by method M5. Similar behavior in terms of for which sample which method proved best was observed in the following groups of elements: Cr, Co, Mn, and K; Cu, Pb, and Zn; Ca and Fe, which suggests the same chemical form in which these elements are present in the tested samples.

Table 6. Relative deviation (%) of the content of the tested elements in the samples prepared using methods M2, M3, M4, and M5 in relation to method M1

Element	sample-3				sample-4			
	M2	M3	M4	M5	M2	M3	M4	M5
Al	-0.01	-17.17	16.08	-17.84	52.62	-6.71	30.77	-22.18
As	11.57	-12.22	-5.14	-8.87	38.30	9.15	1.06	5.63
Cd	-59.07	-56.39	-56.79	-7.32	-29.48	-25.93	-23.61	0.95
Ca	-30.06	-40.25	-31.13	-20.86	58.19	13.98	66.04	60.21
Cr	-17.17	-34.71	-19.75	-16.86	5.33	-27.96	-3.79	-6.78
Co	-19.56	-34.47	-26.48	-16.58	-3.23	-17.07	-7.25	-11.38
Cu	29.52	16.41	51.34	54.81	56.93	29.41	292.82	62.56
Fe	-19.30	-21.73	-17.68	-16.65	18.48	-3.66	9.85	-1.14
Pb	10.19	2.62	10.46	38.91	10.87	24.03	43.31	4.03
Mg	-10.73	-13.70	-8.38	-17.03	22.78	-1.54	8.42	-12.70
Mn	-17.13	-16.04	-11.01	-11.17	15.91	12.66	14.31	5.30
Ni	17.42	-6.46	-9.66	-13.51	19.14	-2.24	54.53	-9.61
K	-7.87	-26.45	-13.21	-15.84	21.39	-14.99	9.61	-18.29
Na	-82.93	-80.22	-74.24	-69.66	-73.63	-78.69	-68.84	-73.80
Zn	-29.20	-25.79	-5.56	16.40	27.14	9.92	213.59	43.86
Mo	28.96	-24.27	22.91	/	95.63	/	401.00	55.88
P	-3.90	-22.10	-17.59	-8.38	33.50	12.79	22.26	22.37
Si	341.66	-78.56	18.31	510.17	824.73	-66.82	184.32	1105.60
S	-29.62	-23.52	-30.02	13.79	38.51	9.22	31.96	16.84
Hg	51.70	-65.04	-59.13	147.13	-72.59	-66.40	-36.41	-8.65

Based on the presented results, it is evident that the pseudo-total element extraction using concentrated perchloric acid did not prove most efficient for any element in any sample, which is why this method is not suitable for the preparation of these types of soil. Another reason for this is that hydrogen-peroxide, which is normally recommended for the additional decomposition of the present organic matter, was not used in this method.

Apart from the papers cited in the introduction in which different soil preparation methods were used, the results concerning the efficiency of different methods are also present in the literature. For instance, *Safarova et al.* [11] tested the extraction efficiency of Cd, Pb, Co, Ni, Zn, Mn, Cu, and Hg from solid samples (soil, rocks, sediments, and industrial waste) using the different methods. The obtained results showed that the different efficiency of the applied methods depended on the applied soil sample. Based on the

results obtained from the study, the authors concluded that there was no universal method for the decomposition of different samples and that the selection of the preparation method depended on the nature of the element, composition of the sample or matrix, decomposition conditions, equipment availability, and the urgency of the analysis. They also noticed that there were no significant differences between the open system decomposition and microwave digestion for the following elements: Pb, Cu, Fe, Zn, and Mn as well as the microwave digestion and the digestion in an autoclave were the methods of the highest efficiency. *Santos and Alleoni* [12] applied the EPA 3051 method and the aqua regia method to determine the pseudo-total concentration of Cd, Co, Cr, Cu, Ni, Pb, and Zn in soil samples. Based on the results obtained, they concluded that the aqua regia method was far more efficient than the USEPA 3051 method in terms of the amount of Co, Ni, Pb, and Zn extracted, while these two methods did not differ significantly concerning the extraction of Cr and Cu. *Oliviera et al.* [30] concluded that the extraction with aqua regia was a satisfactory method for the purpose of assessing the phytoavailable amounts of elements, as well as the elements that can be excreted into natural waters. *Florian* [31] noticed that the aqua regia method was more suitable for the digestion of samples when it comes to the determination of trace elements which are potentially hazardous for the environment. Also, the comparison of 3050A and 3050BA methods showed that the 3050B method resulted in a better recovery of Ag, As, Ba, Be, Co, Cu, Sb, and V, and that the 3050A method resulted in a better recovery of Cd, Cr, Mo, Ni, Pb, Sb, and Zn. Also, there was no difference between the microwave digestion and the digestion on a heating surface for Cu, Pb, Zn, Cr, and Ni [23].

The observed variability concerning the efficiency of different methods in this paper and in the papers of other authors might be the result of a number of different factors: soil type, quantitative and qualitative soil composition (metals, non-metals, and organic matter), pH value of soil solution, electrical conductivity, chemical form in which the elements are (oxides, sulfates, carbonates, sulfides, complexes etc.).

CONCLUSION

The results concerning the determination of the tested elements' content in agricultural soils prepared by different methods have shown that there is no universal method, i.e., that the efficiency of the element extraction depends on its nature, on the chemical form in which it occurs, on the

composition of the soil i.e., soil type, etc. In most cases, the method with nitric acid and reflux and with aqua regia and ultrasound have shown the highest efficiency, while the method with perchloric acid has shown the lowest efficiency. It is also evident that the smallest statistically significant difference, as a result of the application of different methods, can be found in the contents of the following elements: As, Cd, Pb, Cr, Mn and Ni, while most of the statistically significant differences can be found among the contents of macroelements.

MATERIALS AND METHODS

Samples and reagents

In the fall of 2018, four soil samples were taken from different agricultural plots of soil near Vranje and each of them was prepared using different soil preparation methods for the purpose of assessing the extraction efficiency of the elements that were tested.

A shovel was used for soil sampling and the samples were taken at a depth of 15 to 20 cm from the surface of around 100 cm². A representative sample was made from each of the four agricultural plots of soil by taking a sample from five different places along the length of the plot and those samples were later homogenized, sifted through a sieve, and stored in polyethylene bags. Just before preparation, the samples were dried in the oven at 95 °C to constant weight. The dried samples were laid aside in desiccators to cool, after which approximately 1 g of each sample was measured.

The following chemicals were used for the preparation of soil samples: 65% HNO₃ (Sigma-Aldrich, SAD); 37% HCl (Sigma-Aldrich, SAD); 30% H₂O₂ (Macron, SAD); 70% HClO₄ (Sigma-Aldrich, USA). The following standards were used for the construction of a calibration line: multielement standard ULTRA SCIENTIFIC #2: Al, As, Ba, Be, Bi, Cd, Ca, Ce, Cr, Co, Cu, Ga, In, Fe, Pb, Li, Mg, Mn, Ni, K, Rb, Se, Na, Sr, Tl, U, V, and Zn (10 µg cm⁻³), multielement standard ULTRA SCIENTIFIC #4: B, Ge, Mo, Nb, P, Re, Si, S, Ta, Ti, W, and Zr (10 µg cm⁻³) (USA). 99.996% purity argon was used for the operation of ICP-OES. Deionized water ($\kappa=0.05$ µS cm⁻¹) was used for the purposes of preparing the solutions and washing the laboratory dishes.

Instruments

Inductively coupled plasma optical emission spectrometer ICP-OES (Arcos Spectro, Germany); analytical balance (METTLER TOLEDO, Switzerland); ultrasonic bath (Bandelin SONOREX Digital 10 P, Sigma, USA); drying oven (LLG LABWARE uniOVEN 150, Germany); deionizator TKA MicroMed Wasseraufbereitungssysteme GmbH, Germany); stirrers (LLG LABWARE uniSTIRRER, Germany); automatic variable pipette (Transferpette S (0.5-5 cm³), Germany).

The following operating conditions of the ICP-OES instrument were used: analysis pump rate 2 mL min⁻¹, RF power 1300 W, nebulizer gas flow rate 0.89 L/min, coolant gas flow rate 12 L min⁻¹, auxiliary gas flow rate 0.8 L min⁻¹, axial and radial plasma view mode.

Methods of pseudo-total metal extraction from soil

Pseudo-total metal extraction from soil using reverse aqua regia (M1)

Approximately 1 g of each sample was measured and moved to an Erlenmeyer flask. 12 cm³ of conc. HNO₃ and 4 cm³ of conc. HCl (HNO₃:HCl = 3:1, v/v) were added. The contents of the flasks were heated in a sand bath at a temperature of about 190 °C. In the end, 2 cm³ of 30% H₂O₂ were added to each flask, after which the contents were cooled and filtrated using filter paper (black ribbon). The filtrate was collected in normal 50 cm³ vessels [18,23].

Pseudo-total metal extraction from soil using aqua regia (M2)

Approximately 1 g of each sample was measured and moved to an Erlenmeyer flask. 12 cm³ of conc. HCl and 4 cm³ of conc. HNO₃ were added to each Erlenmeyer flask. The contents of the flasks were heated in a sand bath at a temperature of about 190 °C for an hour, after which 2 cm³ of 30% H₂O₂ was added and heated until the foaming stopped. The mixture was cooled and filtrated through filter paper (black ribbon), while the filtrate was collected in a normal 50 cm³ vessel [17].

Pseudo-total metal extraction from soil using concentrated perchloric acid (M3)

Approximately 1 g of each sample was measured and moved to an Erlenmeyer flask. 18 cm³ of conc. perchloric acid were poured over the soil, after which the content was heated at a temperature of 190 °C for an hour. The mixture was cooled and filtrated through filter paper (black ribbon), and the filtrate was collected in a normal 50 cm³ vessel [11].

Pseudo-total metal extraction from soil under reflux (M4)

Approximately 1 g of each sample was measured and moved to a round-bottom flask. Then, 10 cm³ of 1:1 (v/v) of nitric acid were added and magnet and reflux condenser were put. The mixtures were refluxed for 10 – 15 minutes at a temperature of 95 °C (without boiling) with stirring. The mixture was partially cooled, after which 5 cm³ of conc. HNO₃ were added to it, the reflux condenser was placed again, and the mixture was refluxed for another 30 minutes. The final step was repeated one more time to ensure better oxidation of the sample. The mixture was then evaporated to a small volume (approximately 5 cm³) without boiling (95 °C) and the reflux condenser was taken out. The mixture was cooled, after which 2 cm³ of cold deionized water and 3 cm³ of 30% hydrogen peroxide were added to it for the total oxidation of the sample. The flask containing the mixture was carefully heated with stirring but without the reflux condenser, while special attention was paid not to lose the mixture during its foaming. After the foaming had stopped, another 1 cm³ of 30% hydrogen peroxide was carefully added to the mixture, and the procedure was repeated until the foaming caused by the recent addition of hydrogen peroxide stopped. The cooled mixture was then filtrated using filter paper (black ribbon), and the filtrate was collected in a normal 50 cm³ vessel [23].

Pseudo-total metal extraction from soil using aqua regia in combination with ultrasound (M5)

Approximately 1 g of each sample was measured and moved to an Erlenmeyer flask. 12 cm³ of conc. HCl and 4 cm³ of conc. HNO₃ were poured over the measured soil. The Erlenmeyer flask was put inside an ultrasonic bath which had previously been heated to the temperature of 95 °C. It took an hour for the process of extraction, after which the sample was cooled. 3 cm³ of 30% hydrogen peroxide were added to the cooled sample. In order to ensure the total oxidation, another 1 cm³ of 30% hydrogen peroxide was added, and the procedure was repeated until the foaming caused by the recent addition of hydrogen peroxide stopped. It is important to avoid losing the mixture during its foaming, which is why the reaction mixture was heated gradually and carefully. The cooled mixture was then filtrated using filter paper (black ribbon) and the filtrate was collected in a normal 50 cm³ vessel [11].

ACKNOWLEDGEMENT

This research was financially supported by the project of the Ministry of Education, Science and Technological Development of Republic of Serbia (Agreement No 451-03-9/2021-14/200124).

REFERENCES

1. A. Kabata-Pendias; H. Pendias; *Trace elements in soils and plants*, 3rd ed.; Boca Raton London, New York Washington, **2001**
2. E. Vavoulidou, E. J. Avramides; P. Papadopoulos; A. D. Nagref; *Water. Air. Soil Pollut.*, **2004**, 4, 631–640
3. E. Fässler; B. H. Robinson; W. Stauffer; S. K. Gupta; A. Papritz; R. Schulin; *Agric. Ecosyst. Environ.*, **2010**, 136, 49–58
4. Y. Bulent; A. Senay; C. Harun; S. Halis; *African J. Agric. Res.*, **2014**, 9, 465–472
5. C. Voica; A. Dehelean; A. Iordache; I. Geana; *Rom. Reports Phys.*, **2012**, 64, 221–231
6. A. Dumčius; D. Paliulis; J. Kozlovskā-Kędziora; *Ekologija*, **2011**, 57, 30–38
7. M. Ahmadi; R. Akhbarizadeh; N. J. Haghighifard; G. Barzegar; S. Jorfi; *J. Environ. Heal. Sci. Eng.*, **2019**, 17, 657–669
8. J.E. Fergusson; *The Heavy Elements: Chemistry, Environmental Impact, and Health Effects*, 1st ed.; Pergamon Press, Oxford, **1991**
9. M. Secer; A. Bodur; Ö.L. Elmaci; S. Delibacak; N. Iqbal; *Int. J. water*, **2002**, 2, 197–211
10. C. Aydinalp; A.V. Katkat; *Plant, Soil Environ.*, **2004**, 50, 212–217
11. V.I. Safarova; G.F. Shaidullina; T.N. Mikheeva; F.K. Kudasheva; N.R. Nizamutdinova; *Inorg. Mater.*, **2011**, 47, 1512–1517
12. S.N. Dos Santos; L.R.F. Alleoni; *Water. Air. Soil Pollut.*, **2013**, 224, 1–16
13. M. Biro; D. Kavšek; J. Karasiński; P. Szwarczewski; E. Bulska; D.B. Vončina; *Cent. Eur. J. Chem.*, **2014**, 12, 687–699
14. B.A. Zarcinas; C.F. Ishak; M.J. McLaughlin; G. Cozens; *Environ. Geochem. Health*, **2004**, 26, 343–357
15. K.-H. Baek; H.-H. Kim; J.-S. Park; B. Bae; Y.-Y. Chang; I.-S. Lee; *Korean J. Ecol.*, **2004**, 27, 231–237
16. S. Zhao; Z. Shen; L. Duo; *Environ. Sci. Pollut. Res.*, **2014**, 22, 5263–5270
17. W. Addis; A. Abebaw; *Cogent Chem.*, **2017**, 3, 1–12
18. W.J.S. Mwegoha; C. Kihampa; *African J. Environ. Sci. Technol.*, **2010**, 4, 763–769
19. M. Senila; O. Cadar; L. Senila; A. Becze; M. Roman; B. Angyus; G. Bruj; *Studia UBB Chemia*, **2021**, 66, 105–116
20. P.B. Corguinha; G.A. de Souza; V.C. Gonçalves; C. de A. Carvalho; W.E.A. de Lima; F.A.D. Martins; C.H. Yamanaka; E.A.B. Francisco; L.R.G. Guilherme; *J. Food Compos. Anal.*, **2014**, 37, 143–150
21. O. Fayiga; L.Q. Ma; Q. Zhou; *Environ. Pollut.*, **2007**, 147, 737–742
22. United States Environmental Protection Agency (USEPA), <https://www.epa.gov/sites/production/files/2015-12/documents/3052.pdf>, (accessed 3 March 2021)

23. United States Environmental Protection Agency (USEPA),
<https://www.epa.gov/sites/production/files/2015-06/documents/epa-3050b.pdf>,
(accessed 3 March 2021)
24. United States Environmental Protection Agency (USEPA),
<https://www.epa.gov/sites/production/files/2015-12/documents/3051a.pdf>,
(accessed 3 March 2021)
25. V. Suthar; K.S. Memon; M. Mahmood-UI-Hassan; *Environ. Monit. Assess.*, **2014**, *186*, 3957–3968
26. A. Papadopoulos; C. Prochaska; F. Papadopoulos; N. Gantidis; E. Metaxa; *Environ. Manage.*, **2007**, *40*, 719–726
27. R.M. Nair; D. Thavarajah; P. Thavarajah; R.R. Giri; D. Ledesma; R.Y. Yang; P. Hanson; W. Easdown; J.d.A. Hughes; J.D.H.D. Keatinge; *J. Food Compos. Anal.*, **2014**, *39*, 23–32
28. J. Uhrovčík; *Talanta*, **2014**, *119*, 178–180
29. M.E. Ghanjaoui; M.L. Cervera; E.I. Rhazi; M. de la Guardia; *Food Chem.*, **2011**, *125*, 1309–1313
30. S.A. Oliveira; S.R.L. Tavares; C.F. Mahler; **2008**
31. D. Florian; R.M. Barnes; G. Knapp; *Fresenius J. Anal. Chem.*, **1998**, *362*, 558–565

A POWERFUL SUPERVISED FUZZY METHOD. CHARACTERIZATION, AUTHENTICATION AND TRACEABILITY OF ROMAN POTTERY

HORIA F. POP^a, COSTEL SÂRBU^{b*}

ABSTRACT. A supervised fuzzy method is described and efficiently applied for the first time in this study. The advantages of the new approach for the characterization and classification of various Roman potteries on the basis of their mineral composition has been explored. The new classification robust approach allows more relevant conclusions to be drawn, finding more specific groups and a better characterization of Roman potteries using their degrees of membership to each fuzzy partition and solving in this way some discrepancies. The efficiency of the supervised fuzzy method was also estimated by the values of quality performance features obtained applying different fuzzy quality criteria and highly illustrative graphs. The parameters of the prototype (class centre) illustrate much better than, for example, arithmetic mean the specific characteristics of each class, and the degrees of membership allow a rationale comparison of the similarity and differences of Roman pottery samples investigated.

Keywords: supervised fuzzy method, prototypes, fuzzy quality criteria, Roman pottery, spectrometry

INTRODUCTION

It is well known and widely accepted that data analysis (data science) has reached a new level when chemometric methods have been starting to be efficiently applied [1-5]. These methods offer the best alternative for graphical visualization or finding the natural existing groups and relationships between objects (samples, cases) and/or their characteristics (variables). The most commonly used methods are cluster analysis (CA), principal component analysis (PCA), discriminant analysis (DA), and others more or less sophisticated methods [6-8].

^a Department of Computer Science, Faculty of Mathematics and Computer Science, Babeş-Bolyai University, 400084-Cluj-Napoca, Romania

^b Department of Chemistry, Faculty of Chemistry and Chemical Engineering, Babeş-Bolyai University, 400084-Cluj-Napoca, Romania

* Corresponding author: costelsarbu@ubbcluj.ro

Cluster analysis and classification are two important tasks which occur daily in everyday life. The goal of cluster analysis is to find meaningful groups in data [9]. Generally two types of algorithm are distinguished, these being hierarchical and non-hierarchical or relocation (partitioning) clustering. Both methods require the calculation of a (dis)similarity matrix. This (dis)similarity which is really a measure of the proximity of the pair of objects (points) in the p -dimensional characteristic space, defined by the p properties measured for each individual, is usually expressed in terms of the Euclidean, Mahalanobis, Manhattan or Chebychev distance between the two points. Either the number of clusters to be generated can be specified in advance, or it may be optimized by the algorithm itself according to certain criteria.

The problem of classification (also called discriminant analysis) involves classifying objects into classes when there is already information about the nature of the classes. This information often comes from a data set of objects that have already been classified by experts or by other means. Classification aims to determine which class new objects belong to and develops automatic algorithms for doing so. Typically, this involves assigning new observations to the class whose objects they most closely resemble in some sense [7].

Classification is said to be a “supervised” problem in the sense that it requires the supervision of experts to provide some examples of the classes. Clustering, in contrast, aims to divide a set of objects into groups without any examples of the “true” classes, and so is said to be an “unsupervised” problem [7].

In classical cluster analysis and classification each object must be assigned to exactly one cluster or class. This is a source of ambiguity and error in cases of outliers or overlapping clusters and affords a loss of information. This kind of vagueness and uncertainty can, however, be taken into account by using the theory of fuzzy sets [10]. A fuzzy set or a fuzzy subset is a collection of ill-defined and not-distinct objects with un-sharp boundaries in which the transition from membership to non-membership in a subset of a reference set is gradual rather than abrupt.

The theory of fuzzy set is basically a theory of graded concepts. It is an extreme generalization of ordinary set theory [11] and is basically designed to handle the concept of partial truth. A central concept of fuzzy set theory is that it is permissible for an element to belong partly to a fuzzy set. It provides an adequate conceptual framework as well as a powerful mathematical tool to model the real-world problems which are often obscure and indistinct [12-16].

The data arising from fuzzy systems are in general, soft, with no precise boundaries. Fuzziness of this type can often be used to represent situations in the real world better than the rigorous definitions of crisp set

theory [11]. Fuzzy sets can be particularly useful when dealing with imprecise statements, ill-defined data, incomplete observations or inexact reasoning. There is often fuzziness in our everyday world as, for example, varying signal heights in spectra from the same substance, or varying patterns in pattern recognition studies [12-16].

The goal of the present study is to define and apply a new methodology for Roman potteries characterization and classification, improving in this way the approach proposed by Mirti and al. [17]. The new classification robust approach used here allows more relevant conclusions to be drawn, finding more specific groups and a better characterization of Roman potteries using their degrees of membership to each fuzzy partition and solving in this way some discrepancies. The efficiency of the supervised fuzzy method was also estimated by the values of quality performance features obtained applying different fuzzy quality criteria [13, 18, 19] and highly illustrative graphs.

RESULTS AND DISCUSSION

Step 1. First we started to run the data set including 16 samples (training set) accurately assigned to three groups (according to their stylistic features and results obtained using different multivariate methods applied to spectroscopic data) as the authors of the original study indicated [17]. The input and output partitions, namely the degrees of membership (DOMs), are shown in Table 1. The supervised fuzzy c-means (SFCM) produced 3 fuzzy partitions (groups), which were all represented by a prototype (a cluster centre with the parameters corresponding to the fuzzy robust means of the original spectral concentrations for 16 terra sigillata samples weighted by DOMs corresponding to each partition). To compare the fuzzy partitions and the similarity and differences of samples, we have to analyse both the characteristics of the prototypes corresponding to the three fuzzy partitions (A1–A3) obtained by applying SFCM and DOMs of samples corresponding to all fuzzy partitions. The results presented in Table 1 and 2 and also Figure 1 clearly illustrate the most specific characteristics of each fuzzy partition and their (dis)similarity and point out the samples assigned according to their DOMs.

The fuzzy partition A1, for example, has a moderate concentration of Al (18.25%) but the highest concentration of Fe (8.87%) and Mg (7.85%) and the smallest concentration of Ca (2.46%). This partition contains all the samples assigned by Mirti and al. [17] to the group I with very high DOMs within the range 0.964-0.997.

Table 1. The input and output partitions (DOMs) of the training set (n=16)

No	Symbol	Site	Position	Input partitions			Output partitions		
				A1	A2	A3	A1	A2	A3
1	A2	PPS	N-W	1	0	0	0.977	0.010	0.013
2	A8	PPS	N-W	1	0	0	0.964	0.017	0.020
3	A8b	PPS	N-W	1	0	0	0.997	0.001	0.002
4	B1	PPS	N or C	0	0	1	0.019	0.038	0.944
5	B4	PPS	N-W	1	0	0	0.995	0.002	0.003
6	B12	PPS	N-W	1	0	0	0.987	0.006	0.007
7	B13	PPS	N-W	1	0	0	0.979	0.009	0.012
8	B14	PPS	N-W	1	0	0	0.985	0.006	0.009
9	B15	PPS	N or C	0	0	1	0.049	0.141	0.810
10	B21	PPS	N or C	0	0	1	0.023	0.058	0.919
11	W2	PP	G	0	1	0	0.095	0.206	0.700
12	W3	PP	G	0	1	0	0.006	0.972	0.022
13	W4	PP	G	0	1	0	0.010	0.955	0.035
14	W5	PP	G	0	1	0	0.036	0.115	0.849
15	W6a	PP	G	0	1	0	0.008	0.962	0.030
16	W6b	PP	G	0	1	0	0.030	0.126	0.844

PPS= Porta principalis sinistra; PP= Porta Praetoria;

G= Gaulish production; N-W= north-western; N or C= north or central

Table 2. The coordinates (fuzzy means) of the prototypes corresponding to different partitions (%)

Partition	Al ₂ O ₃	Fe ₂ O ₃	CaO	MgO	Na ₂ O	K ₂ O	TiO ₂	MnO
n = 16								
A1	18.25	8.87	2.46	7.85	1.61	3.71	0.98	0.13
A2	21.58	5.81	9.98	1.16	0.14	3.88	0.80	0.07
A3	16.52	6.70	10.54	3.25	1.00	3.06	0.83	0.13
n = 21								
A1	18.41	8.92	2.40	8.10	1.54	3.65	0.92	0.13
A2	21.41	5.80	9.64	1.20	0.17	3.82	0.82	0.07
A3	16.54	6.66	10.27	3.21	0.99	3.03	0.84	0.13
n = 24								
A1	19.61	8.04	2.76	5.74	1.39	3.34	0.85	0.11
A2	20.74	5.74	5.40	1.56	0.76	3.29	0.78	0.06
A3	14.91	6.28	11.88	2.99	0.87	2.92	0.73	0.11

The fuzzy partition A2, with the highest concentration for Al (21.58%), and also a high concentration for Ca (9.98%) but with the smallest concentration for Fe (5.81%), Mg (1.16%) and Na (0.14%), includes only three samples from the group II, as it was indicated by Mirti and al. [17], namely W3, W4 and W6a with the following very high DOMs: 0.972, 0.955 and 0.962. The other three samples namely W2, W5 and W6b were assigned to A3 with relatively high DOMs: W2 (0.700), W5 (0.849) and W6b (0.844).

The fuzzy partition A3 includes the three samples moved from A2 and the three samples B1 (0.944), B15 (0.810) and B21 (0.919) assigned to group III by Mirti and al. [17]. This partition is characterized by the highest concentration of Ca (10.54%), the smallest concentration of Al (16.52%) and the intermediate concentration for Fe (6.70%) and Mg (3.25%).

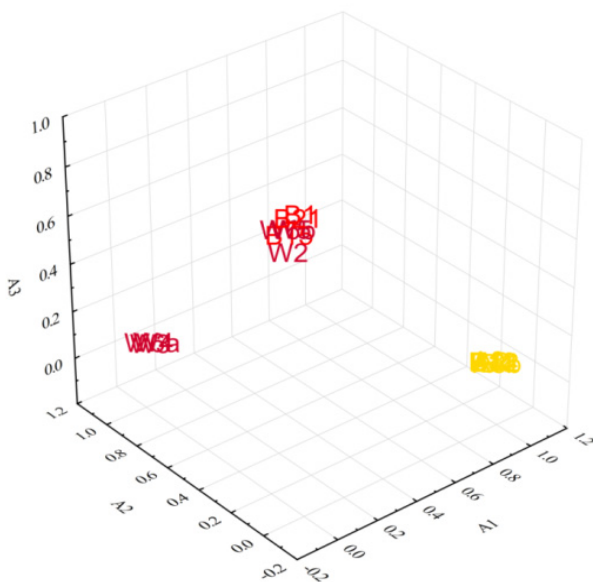


Figure 1. 3-D scatterplot of DOMs corresponding to A1, A2 and A3 (n = 16)

All of the above statements concerning the efficiency of SFCM are well supported also by 2D and 3D scatterplot of DOMs corresponding to the three partitions (very compact groups) (Figure 1) and the values of the fuzzy clustering validity indices considered (Table 3): partition coefficient-PC (optimal/maximum value = 1); partition entropy-PE (optimal/minimum value = 0); Backer-Jain index-BJI (optimal/maximum value = 1) and Xie-Beni index-XBI (optimal/minimum value = 0).

Table 3. The clustering validity indices values

Fuzzy partition	Clustering validity index			
	PC	PE	BJI	XBI
n = 16	0.8739	0.2604	0.9071	0.0623
n = 21	0.8329	0.3277	0.8506	0.1415
n = 5	0.7016	0.5429	0.6701	0.3702
n = 45	0.6792	0.5660	0.7101	0.4381
n = 24	0.5448	0.7743	0.5872	0.3555

Step 2. Considering now the results obtained at the first step we will use the output partition of the training set as an input partition to predict the assignments of the five uncertain samples indicated in Table 4 and Table 5. All five samples are assigned to A1 but with quite different DOMs: B2 (0.985), W1a (0.927), W1b (0.911), B3 (0.671) and B16 (0.381). The case of B16 is quite interesting because its DOMs to the three partitions are practically equal, and this aspect illustrates in fact a large difference of B16 from the samples assigned to A1, A2 and A3 with very high DOMs (Table 4 and Figure 2). We have to remark also the slight modification of the characteristics of prototypes and the values of fuzzy clustering validity indices ($n = 21$) comparing with data corresponding to the training data set ($n = 16$), presented also in Table 2 and 3.

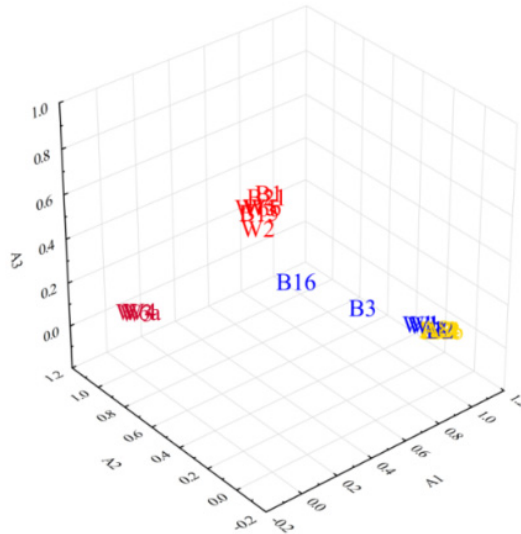


Figure 2. 3-D scatterplot of DOMs corresponding to A1, A2 and A3 ($n = 21$)

Table 4. The input and output partitions of the predicting set (n=21)

No	S*	Site	P*	Input partitions			Output partitions		
				A1	A2	A3	A1	A2	A3
1	A2	PPS	N-W	0.977	0.010	0.013	0.977	0.010	0.013
2	A8	PPS	N-W	0.964	0.017	0.019	0.964	0.017	0.019
3	A8b	PPS	N-W	0.997	0.001	0.001	0.997	0.001	0.002
4	B1	PPS	N or C	0.019	0.038	0.943	0.019	0.038	0.944
5	B4	PPS	N-W	0.995	0.002	0.004	0.995	0.002	0.003
6	B12	PPS	N-W	0.987	0.006	0.007	0.987	0.006	0.007
7	B13	PPS	N-W	0.979	0.009	0.012	0.979	0.009	0.012
8	B14	PPS	N-W	0.985	0.006	0.009	0.985	0.006	0.009
9	B15	PPS	N or C	0.049	0.141	0.810	0.049	0.141	0.810
10	B21	PPS	N or C	0.023	0.058	0.919	0.023	0.058	0.919
11	W2	PP	G	0.095	0.205	0.700	0.095	0.206	0.700
12	W3	PP	G	0.006	0.972	0.022	0.006	0.972	0.022
13	W4	PP	G	0.010	0.955	0.035	0.010	0.955	0.035
14	W5	PP	G	0.036	0.115	0.849	0.036	0.115	0.849
15	W6a	PP	G	0.008	0.961	0.030	0.008	0.962	0.030
16	W6b	PP	G	0.030	0.126	0.844	0.030	0.126	0.844
17	B2	PPS	?	-	-	-	0.985	0.007	0.008
18	B3	PPS	?	-	-	-	0.671	0.177	0.152
19	B16	PPS	?	-	-	-	0.381	0.293	0.326
20	W1a	PP	?	-	-	-	0.927	0.031	0.042
21	W1b	PP	?	-	-	-	0.911	0.041	0.048

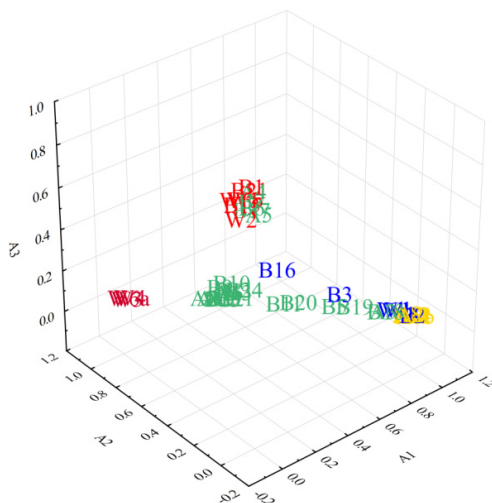
Symbol; PPS= Porta principalis sinistra; PP= Porta Praetoria; G= Gaulish production; N-W= north-western; N or C= north or central; ? = uncertain; P= position

Step 3. In order to identify the origin of the 24 common ware samples, we used the results obtained at step 1 and 2 as input partition presented in Table 5 and the spectral data. The final results are shown in Table 5. Considering the DOMs of the 24 samples to the three partitions the following conclusions can be formulated. Six common ware samples are assigned to partition A1, four with relatively high DOMs: A3 (0.878), B5 (0.701), B18 (0.886), B19 (0.767), and two samples with small DOMs: B11 (0.531) and B20 (0.571). Thirteen samples (A6, A7, A9, A10, A11, A12, A13, B8, B9, B10, B22, B23, B24) are assigned to partition A2 with relatively small and quite similar DOMs within the range (0.501-0.685). Five samples (A4, A5, B6, B7, B17) are assigned to partition A3 with relatively high DOMs within the range (0.744-0.911). The similarity and differences of the considered common wares with terra sigillata is also well illustrated in Figure 3.

Table 5. The input and output partitions of the predicting set (n = 45)

No	S*	Site	P*	Input partitions			Output partitions		
				A1	A2	A3	A1	A2	A3
1	A2	PPS	N-W	0.977	0.010	0.013	0.977	0.010	0.013
2	A8	PPS	N-W	0.964	0.017	0.019	0.964	0.017	0.019
3	A8b	PPS	N-W	0.997	0.001	0.002	0.997	0.001	0.002
4	B1	PPS	N or C	0.019	0.038	0.944	0.019	0.038	0.944
5	B4	PPS	N-W	0.995	0.002	0.003	0.995	0.002	0.003
6	B12	PPS	N-W	0.987	0.006	0.007	0.987	0.006	0.007
7	B13	PPS	N-W	0.979	0.009	0.012	0.979	0.009	0.012
8	B14	PPS	N-W	0.985	0.006	0.009	0.985	0.006	0.009
9	B15	PPS	N or C	0.049	0.141	0.810	0.049	0.141	0.810
10	B21	PPS	N or C	0.023	0.058	0.919	0.023	0.058	0.919
11	W2	PP	G	0.095	0.205	0.700	0.095	0.206	0.700
12	W3	PP	G	0.006	0.972	0.022	0.006	0.972	0.022
13	W4	PP	G	0.010	0.955	0.035	0.010	0.955	0.035
14	W5	PP	G	0.036	0.115	0.849	0.036	0.115	0.849
15	W6a	PP	G	0.008	0.962	0.030	0.008	0.962	0.030
16	W6b	PP	G	0.030	0.126	0.844	0.030	0.126	0.844
17	B2	PPS	?	0.985	0.007	0.008	0.985	0.007	0.008
18	B3	PPS	?	0.671	0.177	0.152	0.671	0.177	0.152
19	B16	PPS	?	0.381	0.293	0.326	0.380	0.293	0.326
20	W1a	PP	?	0.927	0.031	0.042	0.927	0.031	0.042
21	W1b	PP	?	0.911	0.041	0.048	0.911	0.041	0.048
22	A3		C	-	-	-	0.878	0.095	0.028
23	A4		C	-	-	-	0.037	0.052	0.911
24	A5		C	-	-	-	0.132	0.124	0.744
25	A6		C	-	-	-	0.291	0.639	0.071
26	A7		C	-	-	-	0.252	0.685	0.064
27	A9		C	-	-	-	0.310	0.619	0.072
28	A10		C	-	-	-	0.307	0.617	0.076
29	A11		C	-	-	-	0.352	0.570	0.078
30	A12		C	-	-	-	0.292	0.642	0.066
31	A13		C	-	-	-	0.325	0.553	0.123
32	B5		C	-	-	-	0.701	0.249	0.050
33	B6		C	-	-	-	0.087	0.120	0.793
34	B7		C	-	-	-	0.064	0.094	0.842
35	B8		C	-	-	-	0.305	0.559	0.136
36	B9		C	-	-	-	0.264	0.576	0.160
37	B10		C	-	-	-	0.285	0.514	0.201
38	B11		C	-	-	-	0.531	0.420	0.050
39	B17		C	-	-	-	0.095	0.131	0.774
40	B18		C	-	-	-	0.886	0.087	0.027
41	B19		C	-	-	-	0.767	0.177	0.056
42	B20		C	-	-	-	0.571	0.361	0.067
43	B22		C	-	-	-	0.322	0.609	0.068
44	B23		C	-	-	-	0.316	0.622	0.063
45	B24		C	-	-	-	0.351	0.501	0.148

S* = Symbol; P* = Position; PPS= Porta principalis sinistra; PP= Porta Praetoria; G= Gaulish production; N-W= north-western; N or C= north or central



determined by spectroscopic methods is shown in Table 2. Pottery represents the most abundant category of portable material culture to come down to us from the Roman world, and it is thus by no means either surprising or inappropriate that pottery studies have enjoyed a position of some prominence in Roman archaeology [23-25]. Terra sigillata pottery is the most famous fine ware of the Roman period. It is characterized by the redness of its body (or paste) and slip (or gloss), similar to the colour of the clay (terra), and by the use of stamps (sigilla) in some cases. Sigillata production can be seen as the industrial activity of specialized workshops. This pottery appeared at first in the mid-first century BC in Italy. Augusta Praetoria (Arezzo) was probably the first important production centre. From the Augustan period (27 BC – 14 AD), sigillata's success had ensured its spread within and outside the Italian Peninsula and branches were established in Pisa and in the south of Gaul. By visual examination of fragments collected at different sites and according to the results obtained applying various multivariate methods, such as hierarchical cluster analysis (HCA), PCA, non-linear mapping (NLM), including also soft independent modelling of class analogy (SIMCA) and K nearest neighbors (KNN), the authors assigned, with more or less accuracy, the majority of considered samples to three main groups. Some discrepancies and uncertain assignments were also mentioned [17].

Supervised fuzzy method

This new method is twofold, composed by a first, learning step and a subsequent prediction step. The underlying assumption is that there is a data set available, previously known and analysed. We are able to construct a fuzzy cluster substructure of that given data set. The method used here might vary, and the assumed cluster shape might vary as well. Once the fuzzy cluster substructure of the given data set is known, the fuzzy partition associated to this data set forms the basis for the prediction step.

Consider a new data set with data items not yet clustered and associated to the fuzzy cluster substructure of the original known data. The purpose of the prediction step is to run a limited fuzzy clustering procedure able to embed these new data items into the fuzzy partition that is already available. At this point, the same method as in the first step is used, but with two major modifications. On one side, all the data items, from both steps, are used in the computation of the class prototypes. On the other side, only the fuzzy membership degrees of the new data items are set and updated along the execution of the method. The fuzzy memberships of the original data items, as computed in the learning step, are kept constant.

Learning step: fuzzify the input classes

Consider a data set $X = \{x^1, \dots, x^n\}$, with $x^j \in \mathbf{R}^s$ for all values of j . Consider a given crisp c -partition of X , (*i.e.*, a partition formed by c classes), where the value of c is predefined. Consider a given fuzziness constant $m > 1$. The purpose of this phase is to fuzzify the input partition and construct a fuzzy c -partition that best corresponds to the cluster structure of the data set. In the particular case of spherical prototypes, this procedure is the Fuzzy c -Means algorithm (FCM) [20,21].

We consider the classes A_i having a particular geometrical shape, and, as such, characterized by a prototype L_i of a certain kind. We are denoting by $D(x^j, L_i)$ the dissimilarity between the data item x^j and the prototype L_i . Depending on the shape of the classes, the dissimilarity D will be defined accordingly.

We aim to minimize the objective function

$$J(P, L) = \sum_{i=1}^c \sum_{j=1}^n A_i(x^j)^m \cdot D(x^j, L_i).$$

As explained by Bezdek [21], the procedure works by constructing a double Picard iterative process that consecutively minimizes the two functions $J(P, \cdot)$ and $J(\cdot, L)$. The procedure follows:

- S1. Set $l = 0$;
- S2. Initialize fuzzy partition $P^{(0)} = \{A_1, \dots, A_c\}$ to be the given crisp c -partition of X ;
- S3. Compute the prototypes L_i that minimize $J(P^{(l)}, \cdot)$;
- S4. Compute the fuzzy partition $P^{(l+1)}$ that minimizes $J(\cdot, L)$, as follows:

$$A_i^{(l+1)}(x^j) = \frac{1}{\sum_{k=1}^c \left(\frac{D(x^j, L_i)}{D(x^j, L_k)} \right)^{\frac{1}{m-1}}};$$

- S5. Compare $P^{(l+1)}$ with $P^{(l)}$. If they are close enough, then STOP, else increase l by 1 and GOTO S3.

For a proof of the minimization in step S4 see Bezdek [21].

The closeness of two fuzzy partitions is evaluated in step S5 using a distance. A good choice is the distance induced by the L_∞ norm, *i.e.*, if the larger difference between two consecutive fuzzy membership degrees is smaller than certain ε , then stop the procedure.

As discussed above, the choice for the geometrical shape of the classes influences the prototypes and the relationships leading to the minimization of $J(P^{(l)}, \cdot)$ in step S3. For instance, let us assume that the classes have spherical shape. This leads to the prototypes L_i being points in the space \mathbf{R}^s of the data set. Consequently, we define the dissimilarity as

$$D(x^j, L_i) = d(x^j, L_i)^2 = \|x^j - L_i\|^2$$

where d is the Euclidean distance in the space \mathbf{R}^s . It follows that the prototypes L_i that minimize $J(P^{(l)}, \cdot)$ at step S3 above are determined as follows [21]:

$$L_i = \frac{\sum_{j=1}^n A_i(x^j)^m \cdot x^j}{\sum_{j=1}^n A_i(x^j)^m}.$$

For examples of other geometrical prototypes, see Bezdek et al. [22] and Höppner et al. [13].

Following the results discussed by Dunn [20] and Bezdek [21], the method described above converges to a local optimum. Let us remember that our problem is to fuzzify a given crisp partition, such that it matches the best cluster structure of the data. The local optimum found in the vicinity of the initial crisp partition, as determined by this method, is, actually, the desired result.

Prediction step: assign fuzzy values to new items

Consider a data set $X = \{x^1, \dots, x^n\}$, with $x^j \in \mathbf{R}^s$ for all values of j . Consider known the fuzzy partition $P = \{A_1, \dots, A_c\}$ corresponding to the cluster structure of X as determined in the previous step. Consider a data set $Y = \{x^{n+1}, \dots, x^{n+p}\}$ we need to predict their fuzzy membership degrees to the given fuzzy partition P . The procedure is an extension of the procedure indicated in [21].

Under the same assumptions as above, we will proceed as follows:

- S1. Set $l = 0$;
- S2. Initialize fuzzy partition $P^{(0)} = \{A_1, \dots, A_c\}$ to be the given fuzzy partition P ;
- S3. Compute the prototypes L_i that minimize $J(P^{(l)}, \cdot)$;
- S4. Compute the fuzzy partition $P^{(l+1)}$ that minimizes $J(\cdot, L)$, as follows:

$$A_i^{(l+1)}(x^j) = \frac{1}{\sum_{k=1}^c \left(\frac{D(x^j, L_i)}{D(x^j, L_k)} \right)^{\frac{1}{m-1}}}, \text{ for } j = n+1, \dots, n+p.$$

S5. Compare $P^{(l+1)}$ with $P^{(l)}$. If they are close enough, then STOP, else increase l by 1 and GOTO S3.

At the step S4, only the fuzzy membership degrees of the data items in Y are updated. The values of the data items in X are not touched, as we are interested in predicting the fuzzy memberships for the newly available data items. The same discussion on the choice of prototypes L and dissimilarity D as above is, of course, valid at this point and the same reasoning on the local optima as above is also valid.

REFERENCES

1. D.L. Massart, B.G.M. Vandeginste, S.N. Deming, Y. Michotte, L. Kaufman, *Chemometrics: a Textbook*, Elsevier, Amsterdam, **1988**.
2. J.W. Einax, H. Zwaniger, S. Geiß, *Chemometrics in Environmental Analysis*, John Wiley & Sons Ltd, Chichester, UK, **1997**.
3. R.G. Brereton, *Applied Chemometrics for Scientists*, John Wiley & Sons Ltd, Chichester, UK, **2007**.
4. M. Otto, *Chemometrics. Statistics and Computer Application in Analytical Chemistry*, third ed., Wiley-VCH, Weinheim, **2017**.
5. R.G. Brereton, *Chemometrics: Data Driven Extraction for Science*, second ed., John Wiley & Sons Ltd, Chichester, UK, **2018**.
6. B. Nisbet, G. Miner, K. Yale, *Handbook of Statistical Analysis and Data Mining Applications*, second ed., Academic Press, Elsevier Inc., **2018**.
7. C. Bouveyron, G. Celeux, T.B. Murphy, A.E. Raftery, *Model-based Clustering and Classification for Data Science*, University Printing House, Cambridge, **2019**.
8. S. Borra, R. Thanki, N. Dey, *Satellite Image Analysis: Clustering and Classification*, Springer Nature, Singapore Pte Ltd., **2019**.
9. C. Hennig, M. Meila, F. Murtagh, R. Rocci, R. (Eds), *Handbook of Cluster Analysis*, CRC Press, Boca Raton, New York, **2016**.
10. L.A. Zadeh, *Inf. Control*, **1965**, 8, 338–353.
11. D.A. Simovici, C. Djeraba, *Mathematical Tools for Data Mining: Set Theory, Partial Orders, Combinatorics*, second ed., Springer-Verlag, London, UK, **2014**.
12. D.H. Rouvray, (Ed), *Fuzzy Logic in Chemistry*, Academic, San Diego, **1997**.

13. F. Höppner, R.K. Klawonn, R. Kruse, T. Runkler, *Fuzzy Cluster Analysis: Methods for Classification, Data Analysis and Image Recognition*, John Wiley & Sons, Chichester, UK, **1999**.
14. H.F. Pop, C. Sârbu, O. Horovitz, D. Dumitrescu, *J. Chem. Inf. Comput. Sci.*, **1996**, 36, 465-482.
15. Y. Jin, L. Wang, (Eds), *Fuzzy Systems in Bioinformatics and Computational Biology*, Springer-Verlag, Heidelberg, **2009**.
16. T-C.T. Chen, K. Honda, *Fuzzy Collaborative Forecasting and Clustering*, Springer Nature, Switzerland AG, **2020**.
17. P. Mirti, V. Zelano, R. Aruga, E. Ferrara, L. Appolonia, *Archaeometry*, 32 **1990**, 32, 163-175.
18. C. Sârbu, K. Zehl, J.W. Einax, *Chemometr. Intell. Lab. Syst.*, **2007**, 86, 121-129.
19. C. Sârbu, J. W. Einax, *Anal. Bioanal. Chem.*, **2008**, 390, 1293-1301.
20. J.C. Dunn, *J. Cybern.*, **1973**, 3, 32-57.
21. J.C. Bezdek, *Pattern Recognition with Fuzzy Objective Function Algorithms*, Plenum Press, New York, **1981**.
22. J.C. Bezdek, C. Coray, R. Gunderson, J. Watson, *SIAM J. Appl. Math.*, **1981**, 40, 339-372.
23. D.P.S. Peacock, *Pottery in the Roman World: an Ethnoarchaeological Approach*, Long Man, New York, **1982**.
24. J.T. Peña, *Roman Pottery in the Archaeological Record*, Cambridge University Press, UK, **2007**.
25. A. Shiyab, A. Al-Shorman, N. Turshan, M. Tarboush, F. Alawneh, A. Rahabneh, *J. Archaeol. Sci. Rep.*, **2019**, 25, 100-115.

IMPROVEMENTS NECESSARY FOR A RIVER POLLUTANT TRANSPORT MODEL TO OBTAIN A BETTER PERFORMANCE

ELISABETA CRISTINA TIMIS^a*

ABSTRACT. A wealth of field facts, including the high human pressure on rivers, the eutrophication danger and the complexity of in-river phenomena (causing difficulties in water quality modelling) revealed the need to offer reliable tools for the pollutant transport modelling and for the understanding and estimation of the complex in-river pollutant behaviour. This paper presents an application of ADModel (a detailed advection dispersion pollutant transport model) for the case of River Swale (UK), in order to show why an improved representation (a) of the hydrodynamic river characteristics and (b) of the pollutant transformations; is very important for the advection-dispersion models, as it generates a major gain in the modelling skills (e.g. prediction improvement) and on the understanding of in-river phenomena. ADModel obtained good results during calibration against field measurements of concentration, showing that an improved version (using detailed representation of the river stretch and pollutant transformations) facilitates a better model performance and a wider applicability, including the identification of additional phenomena along the river stretch, of importance in ordinary situations and also during un-controlled pollution situations.

Keywords: *ADModel, in-river pollutant transport model, river water quality, phosphorus prediction, rating equations.*

INTRODUCTION

Fresh water is a vital resource under constant pressure due to pollution and climate change. Even if significant counteraction is being conducted these latest decades, there is a need for continuous and careful

^a *Babeş-Bolyai University, Faculty of Chemistry and Chemical Engineering, Department of Chemical Engineering, Computer Aided Process Engineering Research Centre, 11 Arany Janos str., RO-400028, Cluj-Napoca, Romania,*

** Corresponding author: elisabeta.timis@ubbcluj.ro*

water resources management in order to slow down their future deterioration [1, 2]. Models for the transport of pollutants along rivers are very useful in this endeavour, especially when applied for the key determinants of river water quality, such as phosphorus (P) compounds. There is a large number of studies on the modelling of P compounds, because they are significant driving forces for the eutrophication [3]. In this respect it is important to mention the main tendency to focus on catchment and multi-catchment scale models [3, 4], while detailed models (at high time and space resolution, such as ADModel) are the subject of less studies, e.g. [5 to 8], probably due to the need for large amount of experimental data and a high workload spent for their development. It is known that measuring P species at high time and space resolution is expensive and not commonplace, therefore there are situations where monitoring is not available or where extensive data sets are unreliable [8]. Modelling is still very much needed for those un-monitored situations and also in cases where data are scarce. Details on how to treat such challenging cases by means of knowledge management and other process systems engineering techniques are extensively discussed and illustrated elsewhere [10], while a recent example of integrating already existing models for a river basin lacking detailed measurements is also available [8].

In addition, the importance of ecosystem processes, together with the ecosystem status, as indicators of ecological health is increasingly being recognised [11]; and there is much scope for detailed modelling studies to add to this growing body of research.

This work is related to aspects of the detailed modelling of the advective dispersive pollutant transport in rivers such as: the proper representation of river parameters (e.g., river bed shape), the description of pollution sources discharging effluent into the river, and the identification of an adequate pollutant transformations model. Generally, the greatest attention is given to the latter aspect, as the good understanding of pollutant dynamics (needed for the further pollutant transport modelling task) involves on one side information on the river channel parameters, discharge and concentrations monitoring data, and on the other side details on kinetics and rate-determining controls on the processes comprised in the transformations model (emphasized also in [12]). It is also important to remark that all the effort should be rewarded by the results of detailed models via (1) the improved capacity with respect to details offered within the simulation results; (2) the opportunity to explore in-river phenomena at high time and space resolution with the help of simulations; and (3) the possibility to include such models in software to control the reduction of pollutants concentration right

during their discharge in the river, [13, 14]. ADModel, presented in this research, offers these opportunities and proved to open possibilities further research. ADModel has been first presented in 2010 [5] and calibrated with respect to nitrogen compounds, [7].

This paper is part of the recent research (including [15]), aiming at an improved version of ADModel with respect to phosphorous compounds, in order to facilitate better prediction accuracy and a wider use of the model. On the other hand, the additional improvements related to the representation of hydrodynamic aspects along the river stretch facilitate increased prediction accuracy of ADModel in general (for all considered nutrient species, not only P components), facilitating the further application of ADModel to other pollutant species.

RESULTS AND DISCUSSION

The present section points the ADModel's improvements and presents a discussion on the results.

A. Improvements in representing the river stretch

Rating equations are employed in the water quality models for the modelling of water depth as function of the water flow along the river channel. The reason for using such models is that monitoring of water flow is carried out along rivers with higher frequency (e.g. intensive automatic measurements may be implemented in some locations) compared to the water depth (e.g. measured on a monthly basis or occasionally during intensive campaigns).

Two approaches for the rating equations at monitoring sites have been proposed. The simple approach (denominated "old rating" and represented using blue stars in **Figure 1** and **Figure 2**) considers a single rating equation at each monitoring site, employed to express the non-linear dependency of water depth on discharge for all flow ranges. The detailed approach (denominated "new rating" and represented using black crosses in **Figure 1** and **Figure 2**) considers the adjustment of rating equations at each site, in order to provide different values of the rating equation's coefficients for low flows and high flows.

The demarche is based on the available discharge and water depth field data, which has been split into two independent data sets: a development set and an evaluation set. The evaluation of the old and new rating coefficients

against experimental data reveals better estimation performance for the new approach, when different sets of coefficients are employed for the low discharge and high discharge respectively (see **Figure 1** and **Figure 2**).

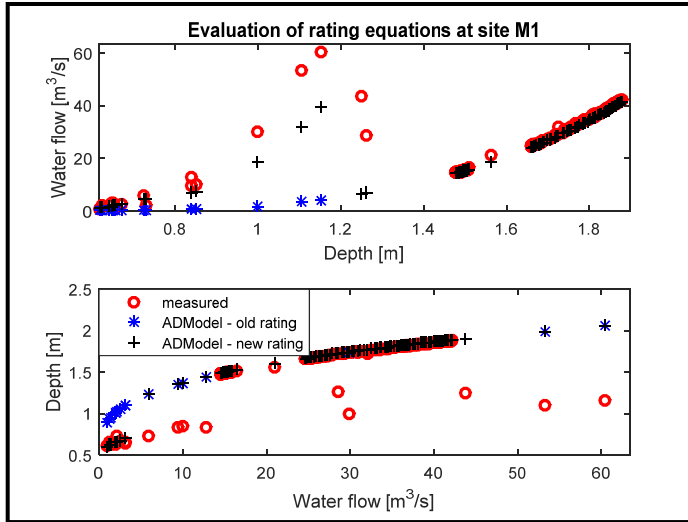


Figure 1. Rating equations improvement at the upstream (site M1) end of the river stretch

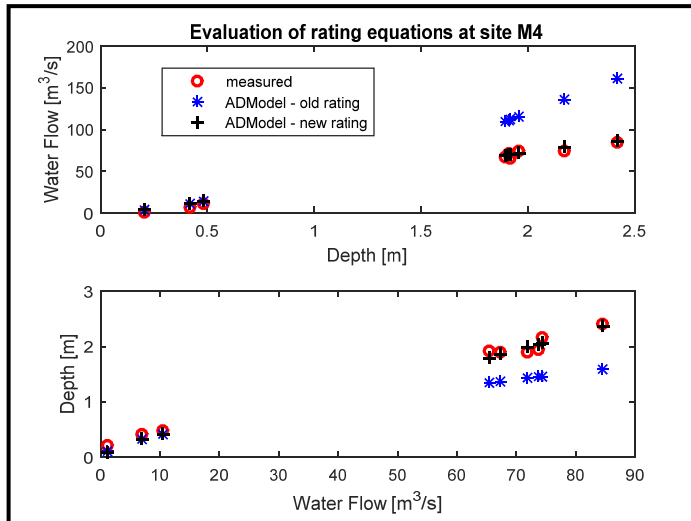


Figure 2. Rating equations improvement at the downstream (M4 in 1b) end of the river stretch

B. Improvements in representing the SRP and OP transformations

ADModel results including concentration time series (conservative and non-conservative simulations) are presented against the concentrations measurements in Figure 3 (corresponding to the three transformations model) and Figure 4 (corresponding to the five vs. three transformations model).

Predictions of the initial non-conservative ADModel (Figure 3) follow the shape of the conservative model predictions for the most of the points, while they should be closer to the measurements. These results reveal the need to include additional transformations in the model and/or improve the dynamic representation of the existing ones. SRP concentrations are overestimated during the most of the time, showing evidence that SRP sinks (not considered at all in this ADModel version) should be included in the model, as they have significant contribution to the SRP variability. Therefore, the adsorption and the uptake of SRP are included in the five transformations version of ADModel. OP is, in the most occasions underestimated for the higher range of concentrations (over 0.4 mg/L), while it is overestimated for the lower range of concentrations. In this case there is a need of representing better the transformation rates of sedimentation and re-suspension in order to cater for the variability of these phenomena in relation with the water flow and seasonality.

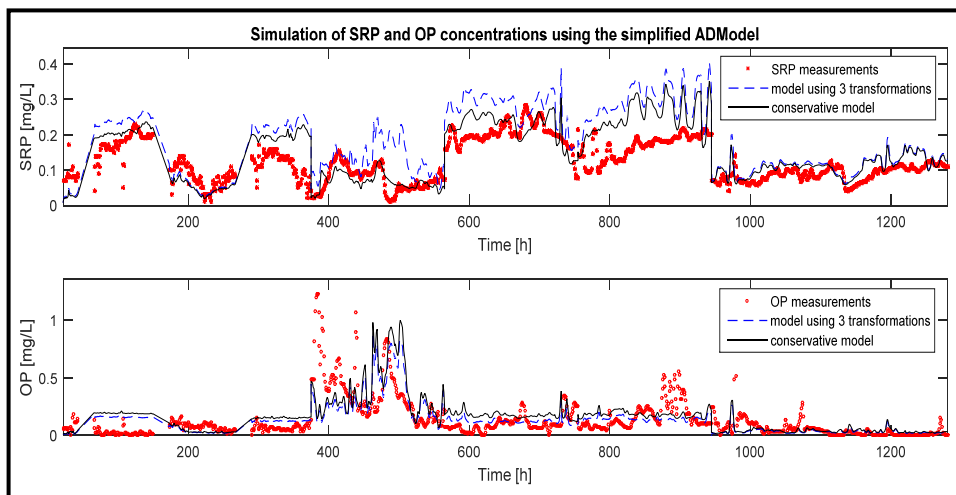


Figure 3. Results of ADModel for the simulation of SRP (upper plot) and OP (lower plot) against field data. ADModel is using the initial, simpler approach for the transformation rates.

The results of ADModel employing the more complex five transformations approach show improvement in predictions (see Figure 4), especially with respect to SRP, for which the NS criteria value is 0.48 (compared to 0.07 and -1.05 corresponding to the conservative ADModel and to the simpler 3 transformations ADModel, respectively, as shown in Figure 4). There is no evident tendency of significant underestimating or overestimating correlated to specific ranges of SRP concentrations. On the other hand, there is little improvement in the prediction of OP concentrations, for which the NS criteria value is 0.20 (compared to 0.05 and 0.18 corresponding to the conservative ADModel and to the simpler 3 transformations ADModel respectively). The OP larger concentrations are underestimated, while the OP lower concentrations are overestimated.

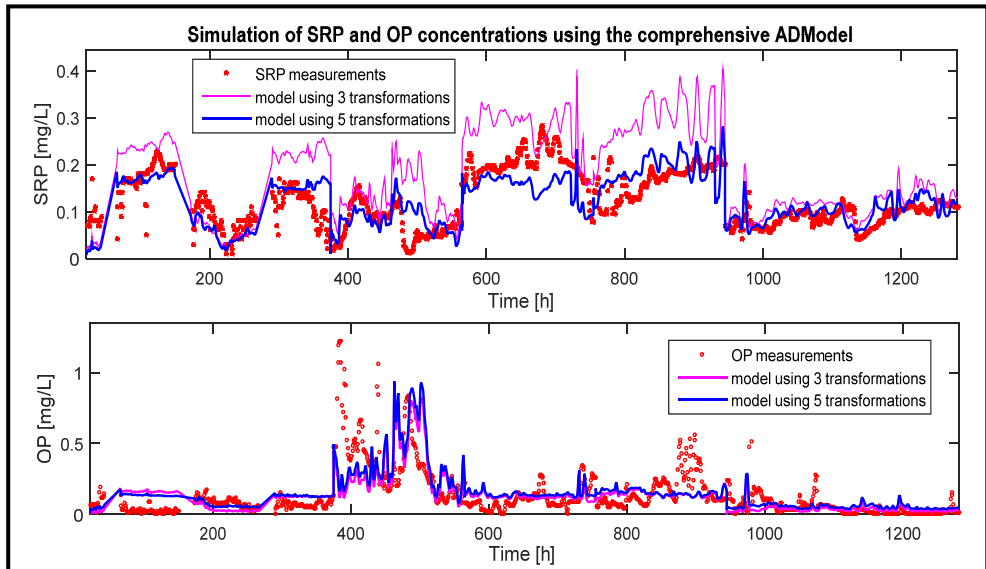


Figure 4. Results of ADModel for the simulation of SRP (upper plot) and OP (lower plot) against field data. ADModel is using the improved approach for the transformation rates.

A representation of all NS coefficient values for ADModel runs is available in Figure 5.

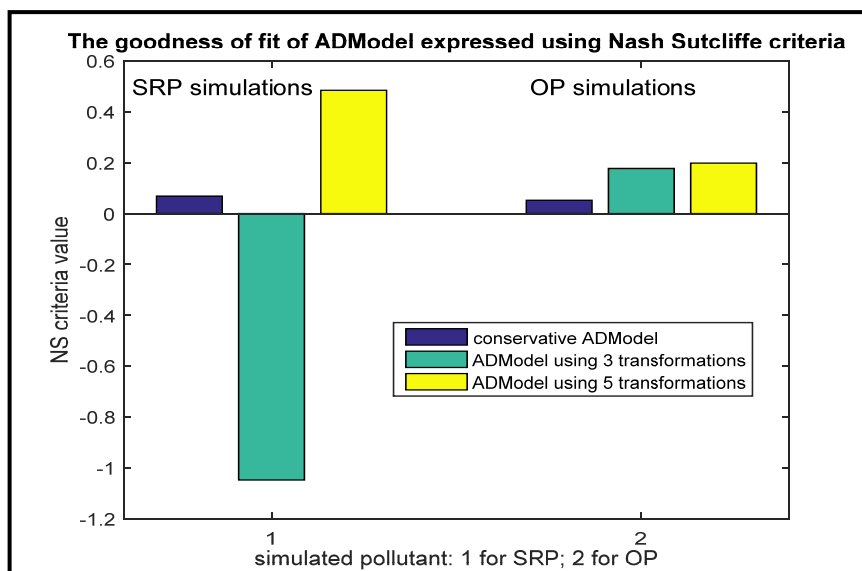


Figure 5. Nash Sutcliffe coefficient values for the simulations of SRP and OP against field data.

A further analysis on the model results has been conducted in order to search for answers in the correlations of the experimental data and simulated data to the controlling factors of the transformation rates. Its visual representation is available in Figure 6. Its findings show that for the lower SRP concentrations the overestimations can be mainly related with (1) the largest valued of the water flow; and (2) the highest values of the seasonality factor (corresponding to late spring), which may indicate the need to improve the representation of the SRP uptake by plants, as in that period this activity is higher compared to other periods. The underestimation of higher SRP concentrations is correlated with (1) flows lower than 50 m³/s; (2) seasonality factor around 0.5 (corresponding to the mid-spring); and (3) temperatures above 15 °C and also between 7 and 10 °C, which may indicate a need of higher mineralization rates during those periods. Such increased rates could be obtained with the help of a better estimated OP concentration, which is also generally underestimated during those periods. Though, for the OP the larger underestimations occur at flows between 50 m³/s and 100 m³/s; lower to mid values of the seasonality factor (under 0.5, corresponding to the beginning of winter to the early mid-spring), and temperatures above 7 °C.

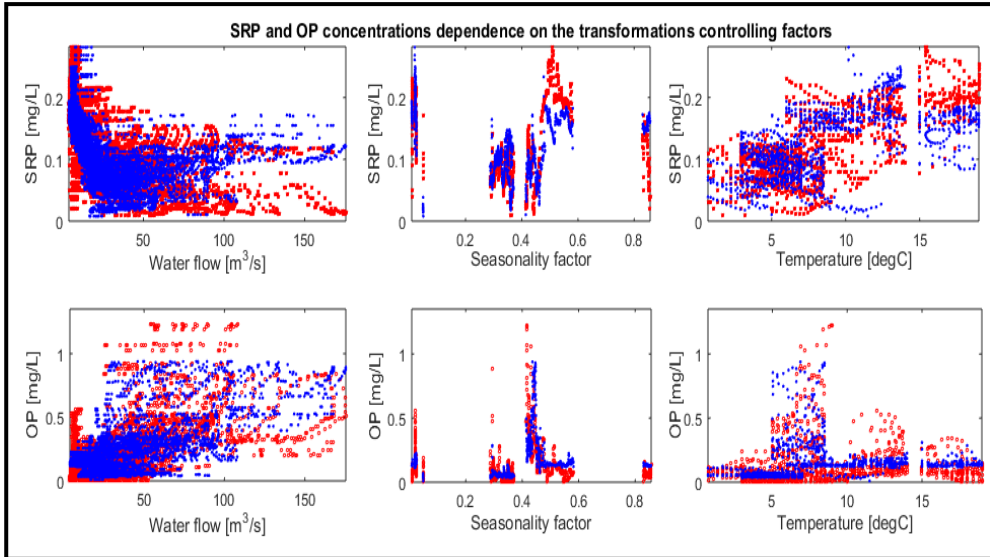


Figure 6. The concentrations of SRP and OP depending on the water flow, seasonality and temperature: simulated with the improved ADModel (blue markers) and measured (red markers).

The multiple forms of phosphorus undergo multiple transformations during in-river transport, including a continuous internal “recycling” process which involves transformations of one form into another. These interdependencies between components, the transfers between phases and the other transformations are complex and play a key role in formulating water quality models. Results show that for this case study a more detailed model for the P transformations enables ADModel to make better prediction of P components during their transport along the reach of River Swale, compared to the simpler approaches, especially for the SRP.

Further investigations with respect to OP transformations need to be conducted in order to improve the representation of already included transformations and also to include additional transformations, such as the excretion by living organisms and the respiration of living organisms. It is worth mentioning that additional field data is also needed for the implementation of such further improvements.

CONCLUSIONS

The present paper discussed the case study of ADModel, a powerful advection-dispersion model for the detailed prediction of OP and SRP along a stretch of River Swale (UK). Transformations are the main key factors influencing the SRP and OP transport along the river, especially for the present case study. Therefore, five empirical models (correlating transformation rates to temperature, water flow and seasonality) have been offered for a more comprehensive representation of the phenomena. ADModel including these five transformations has been compared against simpler approaches: (1) a conservative ADModel and (2) ADModel including three transformations.

Simulation results show that an improved representation of transformations leads to better results of ADModel. There are small improvements of the prediction performance associated to OP (NS criteria increased from 0.18 to 0.20) and significant improvements of the prediction performance associated to SRP (NS criteria increased from -1.05 to 0.48). The results of this research enable to conduct further work using ADModel [18], namely the investigation of additional in-stream phenomena: unidentified transformations or unknown additional in-stream sources and sinks of OP and SRP.

A main benefit of ADModel consists of its practical use in multiple directions: (a) prediction of SRP and OP concentrations along the river stretch in normal and abnormal (e.g. accidental release) of pollutant discharge in the river; (b) prospections related to the river stretch response in case of the modification of pollution load due to multiple types of phosphorus sources in the river catchment (e.g. dynamics of agricultural activities or animal farms, increased population, changes in the waste water treatment plants); and (c) the opportunity to include ADModel in pollution counteraction tools (e.g. software based on model predictive control).

EXPERIMENTAL SECTION

A. The river stretch and field data

Among the widely investigated forms of Phosphorous there are three measurable components (SRP - Soluble Reactive Phosphorus, TDP - Total Dissolved Phosphorus and TP - Total Phosphorus), while two others can be derived from the first three (PP - Particulate Phosphorus and DHP - Dissolved Hydrolysable Phosphorus, consisting of Dissolved Organic P, Polymeric P and Colloid). The Organic Phosphorus (OP) consists of PP and Dissolved Organic P. The three forms of measurable P are available for the River Swale in the form of time series and the species included in ADModel are OP and SRP.

The findings have been validated with the help of field data including measurements of river bed characteristics, water flow time series, water depth time series and concentration time series for the P compounds at up to four sites (noted with M1, corresponding to the upstream end of the stretch, to M4, corresponding to the downstream end of the stretch) along the river stretch (54km long), collected at a resolution from 15 minutes (for the water flow) to 3 hours (for concentrations).

Employed field data is available online, [16].

B. The method: ADModel description

ADModel is a detailed advection-dispersion mathematical model for the pollutant transport along rivers, based on the analytical solution (equations 1 and 2) of the general one-dimensional advection-dispersion equation identified for the continuous discharge of pollutants [17] in the case of the initial and boundary conditions specified in equations 3, 4 and 5:

$$c(x,t) = c_0 + \frac{(c_s - c_0)}{2} \left[\operatorname{erfc} \left(\frac{x - V_x t}{\sqrt{4D_x t}} \right) + \exp \left(-\frac{x V_x}{D_x} \right) \operatorname{erfc} \left(\frac{x + V_x t}{\sqrt{4D_x t}} \right) \right] \quad (1)$$

$$\operatorname{erfc}(x) = 1 - \operatorname{erf}(x) = 1 - \frac{1}{\sqrt{2\pi}} \int_{-\infty}^x e^{-t^2/2} dx \quad (2)$$

$$\begin{aligned} c_0 &= c(x,0) & x > 0; \quad t &= 0 \\ c_{s0} &= c(x_s,0) & x = x_s; \quad t &= 0 \\ c_s &= c(x_s,t) & x = x_s; \quad t &> 0 \end{aligned} \quad (3, 4, 5)$$

where c [mg/L] is the concentration along the river stretch (x [m]) in time (t [s]); c_0 [mg/L] is the initial concentration along the stretch assuming nonzero initial condition throughout the river; c_s [mg/L] is the concentration at source during the release; c_{s0} [mg/L] is the initial concentration at the source (x_s [m]); and; V_x [m/s] is the mean water flow velocity along the river; D_x [m/s] is the longitudinal dispersion coefficient; erf is the error function; erfc is the complementary error function.

Pollutant species transformations have been added to the equation. Initially ADModel has considered three transformations involving SRP and OP (mineralization, sedimentation and re-suspension, presented in Table 1), as they are employed in QUESTOR [5]. QUESTOR is a water quality modelling framework for river networks, capable to simulate also SRP and OP at daily step, previously calibrated also for the monitoring M1 and M4,

which are involved in the present research. The unassertive ADModel results when employing the three transformations approach, discussed later on during this paper, motivated the improvement of transformations representation, in order to (1) include two additional types of processes (uptake and adsorption) and (2) identify a different formulation of transformation rates in order to ensure their dynamics according to the change of controlling factors (see Table 1).

The controlling factors considered by the three transformations model are the water flow and water temperature, as the flow influences sedimentation and re-suspension while temperature influences mineralization. An additional controlling factor (seasonality) has been added, because phosphorous transformations vary among the times of the year (e.g. living organisms lifecycle involving phosphorus compounds is affected by the seasons of the year). The seasonality influence on the transformation rates is expressed via the seasonality factor, a continuous function, taking values between 0 (early winter) and 1 (early summer).

Further on during the calibration of ADModel empirical transformation models have been proposed for the estimation of each transformation rate, in order to make ADModel applicable for a wide range of field situations.

Table 1. ADModel configurations with respect to SRP and OP transformations model.

Transformations	Simple three transformations ADModel, [5]	Comprehensive five transformations ADModel, [15]
Mineralization	Transformation of OP to SRP First order with respect to OP Depending on temperature	Transformation of OP to SRP First order with respect to OP Depending on water temperature
Sedimentation	Consumption of OP Zero order with respect to SRP. Constant rate	Consumption of OP First order with respect to SRP Depending on water flow
Re-suspension	Source of OP Zero order with respect to OP Constant rate	Source of OP Zero order with respect to OP Depending on water flow and seasonality
Uptake	Not included	Consumption of SRP Zero order with respect to SRP Depending on water flow and seasonality
Net adsorption	Not included	Including adsorption as consumption of SRP and desorption as source of SRP First order with respect to SRP Depending on temperature

The Nash Sutcliffe (NS) coefficient, [5], has been employed as criteria for the assessment of the model's goodness of fit during all simulations, comparing estimated concentrations with measurements. The possible range of the NS coefficient is between minus infinity and one. The closer the NS value is to 1 the better the agreement between the estimates and field data is and the model is more performant.

ACKNOWLEDGMENTS

This research did not receive any specific grant from funding agencies in the public, commercial, or not-for-profit sectors. The author would like to thank Michael Hutchins and Mike Bowes for their knowledge of nutrient dynamics in the Swale River basin. The Environment Agency and Yorkshire Water has provided data for model testing.

REFERENCES

1. M.G. Hutchins; R.J. Williams; C. Prudhomme; M.J. Bowes; H., Brown; A.J. Waylett; M. Loewenthal; *Hydrol Sci J.*; **2016**, *61*, 16, 2818-2833.
2. H. Koraqi; I., Luzha; F. Tërmkolli; *Studia U Babes-Bol. Che.*; **2016**, *LXI*, 4, 267 – 276.
3. B.J. Robson; *Environ Model Softw.*; 2014, *61*,339-359.
4. S. Giri, *Env. Pollut.*; **2021**, *271*, 116332.
5. E.C. Ani; M.G. Hutchins; A. Kraslawski; P.Ş. Agachi; *River Res Appl.*, **2011**, *27*, 1216-1236.
6. E.C. Ani; G. Wallis; A. Kraslawski; P.Ş. Agachi; *Comput. Aided Chem. Eng.*; **2009**, *26*, 731-736.
7. Ani E.C.; M.G. Hutchins; A. Kraslawski; P.Ş. Agachi; Assessment of pollutant transport and river water quality using mathematical models, *Rev Roum Chim.*; **2010**, *55*, 4, 285-291.
8. E.C. Ani; V.M. Cristea; P.Ş. Agachi; A. Kraslawski; *Rev. Chim.*; **2010**, *61*, 1108-1112.
9. B.H. Hoang; H.A. Hien; N.T.N. Dinh; N.A. Thao; P.T.T. Ha; J. Kandasamy; T.V. Nguyen; *Ecohydrol. Hydrobiol.*; **2019**, *19*, 210–223.
10. E.C. Ani; V.M. Cristea; P.Ş. Agachi; *Chem. Eng. Trans.*; **2011**, *24*, part 3, 1075-1080.
11. C.Von Schiller; V. Acuña; I. Aristi; M. Arroita; A. Basaguren; A. Bellin; L. Boyero; A. Butturini; A. Ginebreda; E. Kalogianni; A. Larrañaga; B. Majone; A. Martínez; S. Monroy; I. Muñoz; M. Paunović; O. Pereda; M. Petrovic; J. Pozo; S. Rodríguez-Mozaz; D. Rivas; S. Sabater; F. Sabater; N. Skoulikidis; L. Solagaistua; L. Vardakas; A. Elosee; *Sci. Total Environ.*; **2017**, *596-597*, 465-480.

12. E.C. Timis (Ani); M.V. Cristea; P.Ş. Agachi; *Rev. Chim.*, **2015**, 66, 9, 1495-1503.
13. E.C. Timis (Ani); M.V. Cristea; P.Ş. Agachi; *Environ. Res. Eng. Manag.*, **2012**, 11, 1, 13-20.
14. V.M. Cristea; *J. Environ. Manage.*, **2013**, 128, 828–836.
15. E.C. Timis; [software] ADModel for phosphorus compounds, *HydroShare*, **2020**, doi.org/10.4211/hs.ec5a38dcb26f4e0a855bb9c1010fa083
16. M.G. Hutchins; E.C. Timis; [dataset] Field data for the development of ADModel, *HydroShare*, **2020**, doi.org/10.4211/hs.858aaf445ca645f5948a7bd73c16cdd6
17. M.T. van Genuchten; W.J. Alves; *United States Department of Agriculture, Technical Bulletin*, **1982**, 1661.
18. E.C. Timis; M.G. Hutchins; M.V. Cristea; *J. Hydrol.*, **2022**, submitted for publication after minor revisions.

KINETIC CONSIDERATIONS OF TEXTILE DYES ADSORPTION FROM WATER ON A SORBENT FROM CELLULOSIC WASTE

DRAGAN DJORDJEVIC^{a*}, MARIJA KODRIC^a, RADICA KRSTIC^a,
SUZANA DJORDJEVIC^b

ABSTRACT. The synthesis of a new sorbent based on waste cotton cellulose and kinetics of adsorption of reactive textile dye from aqueous solution are the subject of the study in this manuscript. The sorbent is made of waste cotton fibbers collected from the textile plants for spinning yarn and weaving fabrics after being physically and chemically modified. Qualitative and quantitative characterization of the sorbent shows that carbon is dominant in the chemical composition. The sorbent used is a relatively finely divided material with heterogeneous porous particles, generally below 300 μm in size. Maximum adsorption capacity and the rate constant of the pseudo-second order generally depend on the amount of the cellulose-based sorbent, the initial dye concentration and the temperature. A new kinetic model based on the results of adsorption capacity and pseudo second order rate constant was defined. The low value of the activation energy means that the adsorption is mostly of a physical nature. Thermodynamic parameters, change of free Gibb's energy, change of enthalpy and change of entropy, as well as activation energy according to the standard equation confirm the adequacy of the new kinetic model of dye adsorption.

Keywords: *adsorption, reactive dye, pseudo-second order, cellulose-based sorbent, new kinetic model, thermodynamic parameters.*

INTRODUCTION

The textile industry is a significant exploiter of synthetic dyes used for dyeing and printing textiles in factory plants. Unfortunately, some of those dyes are carcinogenic and mutagenic because they were derived hazardous

^a University of Nis, Faculty of Technology in Leskovac, Bulevar oslobođenja 124, 16000 Leskovac, Serbia

^b Higher Technological and Artistic Professional School Leskovac, Vilema Pušmana 17, 16000 Leskovac, Serbia

* Corresponding author: drag_64@yahoo.com

chemicals. In addition, the spillage of dyed liquid waste into the receiving waters affects their aesthetic nature, interferes with the transmission of sunlight and reduces photosynthetic activity, which jointly disturbs the natural balance by affecting the waters of the world and the food chain [1].

Development of new systems for treatment of synthetic dyes in wastewater, as well as the improvement of the existing ones, is closely related to the industrial and technological development. The main goal of any treatment method or procedure is to visually remove the dye first, and then to remove the dye residues until it is safe to release them into the watercourses or their reuse. It is usually the application of one or a combination of several procedures of physical, chemical and biological nature. Procedures that follow the nature and the natural way of removing pollutants are prioritized [2, 3].

Sorbents are used for wastewater treatment, which enable the control of sorption and desorption processes. Natural sorbents, such as clay, loam and ash have an insufficient, small specific particle surface of $200 \text{ m}^2\cdot\text{g}^{-1}$ and sorbents based on granulated activated carbon and synthetic sorbents have a particle surface up to $2000 \text{ m}^2\cdot\text{g}^{-1}$. The effect of adsorption on wastewater treatment is exceptional. Therefore, adsorption is usually applied for final fine water treatment [4-6].

The design and the scope of the adsorption system requires knowledge of the adsorption equilibrium, as well as the adsorption kinetics. Progress in understanding kinetics is limited by the theoretical complexity of the adsorption mechanism to a large extent. Many models of various complexities have been developed for predicting the sorption speed of adsorbate on a sorbent. Pseudo-first order and pseudo-second order models are the two most used empirical models in liquid adsorption studies [7].

Most of the papers are focused on the research of new materials that serve as sorbents in adsorption processes. Kinetic studies in those papers, in which the experimental data are fitted with suitable models, serve only as supplements in the assessment of the suitability of the sorbents. In an ideal case, the model should discover the speed limitation mechanism, with minimum complexity, and extrapolate the results to the operating conditions that are of interest [8, 9].

Specific research deals with the formation of a new sorbent based on waste cotton textiles and the adsorption of reactive dye kinetics in its own manner. Namely, a new kinetic model was proposed based on the analysis of parameters of importance, on mutual comparison, as well as on the assumptions about the relations that can be seen from the experimental results. Such research has not been the subject of study recently, nor have papers been presented related to a specific sorbent and a new model of kinetics.

RESULTS AND DISCUSSION

According to the applied procedure, the yield after modification of waste cotton fibbers into a cellulose-based sorbent ranged between 40-45%. Yield was calculated based on the differences in the mass of raw fiber and the final product–sorbent.

The surface morphology of the obtained cellulose-based sorbent is shown in micrograph, in Figure 1. The sorbent used is a relatively finely divided material with heterogeneous porous particles, of dispersed shape and form, generally below 300 μm in size. There are pronounced cracks, cavities and channels present in the depths of larger particles that represent the basis of the material micro porosity.

Apart from that, high porosity is characteristic for similar sorbents, and it is enabled precisely by the presence of particles of very irregular shapes, a high degree of amorphization and many voids in the structure. It is assumed that the dye molecules easily penetrate the interior of the particles through these pores and channels, where they are adsorbed on numerous internal active centres. The porous structure of the particle surface facilitates the diffusion of dye into the interior of the pores, which has been noted in other studies as well [10,11].

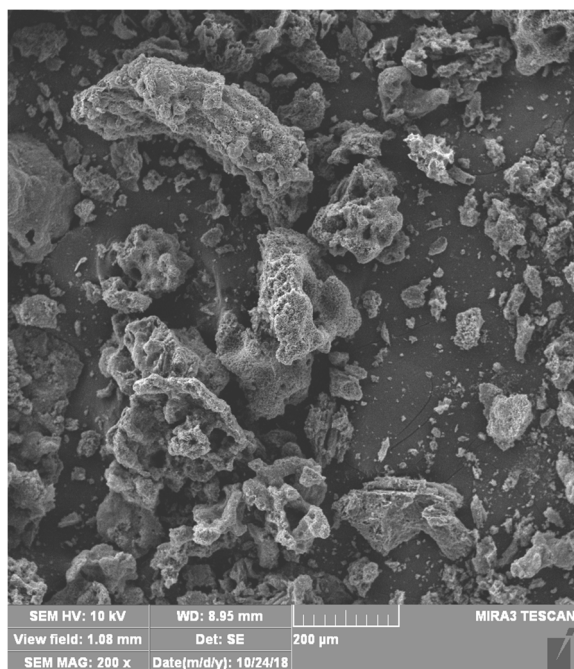


Figure 1. Micrograph of the applied cellulose-based sorbent

Table 1 shows the results of the quantitative composition of the sorbent, i.e., the percentage of one element in relation to the sum of all detected elements (EDS analysis). Based on the data, it can be concluded that carbon is dominant, while the greater presence of oxygen can be related to oxides of aluminium, silicon or aluminosilicate. However, since there is very little aluminium and silicon, it is assumed that the sorbent ability to react with oxygen from air is dominant.

Similar sorbents, active carbons exposed to air, are subject to adsorption of atmospheric oxygen, which results in an increase of the number of surface functional groups, such as phenolic, lactonic, carboxylic, etc. The presence of sulphur is interesting, which occurs, for instance, in the structure of active carbons in the elementary form, as well (usually up to 5 %) in the form of organic or inorganic compounds. Carbon complexes with sulphur, in the structure of active carbons, are very stable and they cannot be removed even at temperatures higher than 1100 °C, unless a reducing atmosphere of hydrogen is present [11,12].

Table 1. Cellulose-based quantitative sorbent composition based on EDS analysis

Spectrum	C	O	Na	Al	Si	S	Ca	Total
Mean	67.26	29.05	2.98	0.03	0.00	0.51	0.17	100.00
Std. deviation	1.44	2.02	0.47	0.04	0.00	0.27	0.10	-
Max.	69.53	31.15	3.49	0.09	0.00	0.72	0.29	-
Min.	65.84	26.04	2.41	0.00	0.00	0.22	0.07	-

Figure 2 shows the dependence of the percentage of dye removed (%Removal) and the adsorption capacity (q_t) on the initial dye concentration (C_0) during the 60-minute adsorption on a sorbent of mass 1 g. The % Removal decreases nonlinearly as the initial dye concentration increases, while the q_t increases linearly with increasing C_0 .

In Table 2, comparative results of published research papers are shown for the degree of dye removal from aqueous solutions through the sorbent based on similar waste cellulosic material.

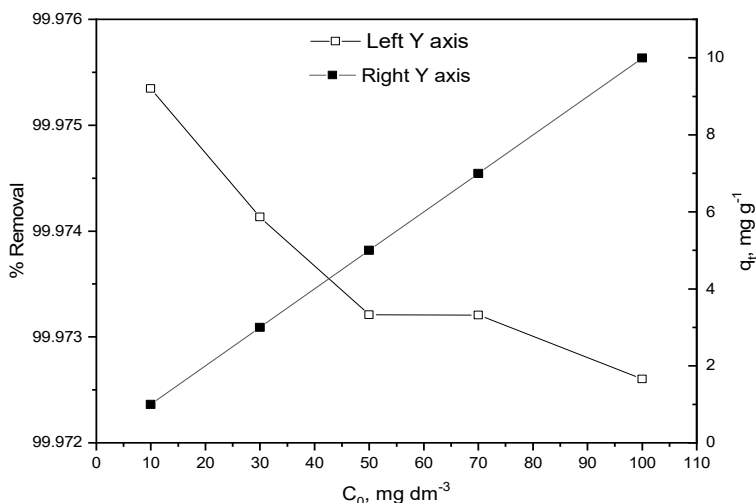


Figure 2. Influence of initial dye concentration on %Removal and q_t

Table 2. Comparative data for the degree of dye removal in different studies

Dye	Sorbent	%Removal	References
Reactive Blue 2	Based on waste cellulose	99	This research
Methylene blue	Activated carbon derived from pyrolysis of <i>Vetiveria zizanioides</i>	79	[13]
Congo red		69	
Reactive Blue 19	Agricultural waste of corn silk	84	[14]
Reactive Red 218		85	
Bezaktiv Red S-Max	Activated carbons from jujube stones	55	[15]
	Activated carbons from palm rachis	92	
Crystal violet	Elephant grass-based lignin	97	[16]

Figure 3 shows the examination results of reactive dye sorption kinetics on a cellulose-based sorbent for different amounts of sorbent and initial adsorbate concentrations in accordance with the pseudo-second order model. This model includes all phases of adsorption, such as the external diffusion, adsorption and internal diffusion in particles, since a pseudo model is in question. Since the reaction takes place in the adsorbed layer on the surface of the sorbent, the reaction rate depends on the concentration of the reactants in the layer on the sorbent surface.

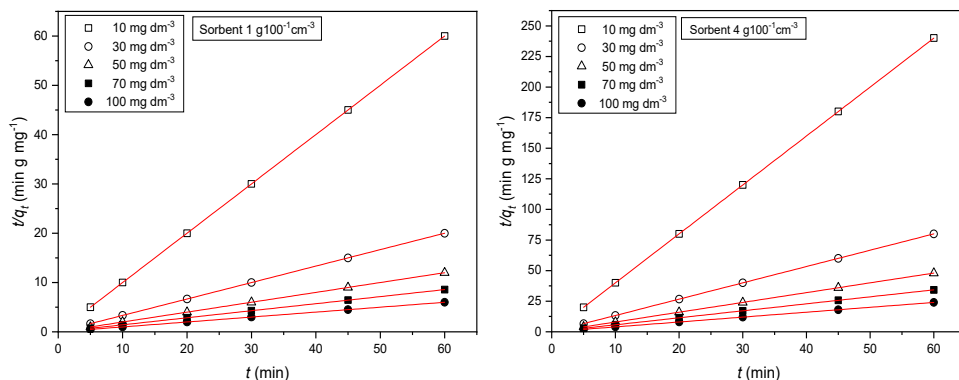


Figure 3. Reactive dye adsorption kinetics (pseudo-second order) at 20 °C for minimum and maximum amount of sorbent

Table 3 shows the results of kinetic parameters of the reactive dye adsorption for the smallest and largest amount of cellulose-based sorbent. The applicability or validity of the pseudo-second order kinetic model was valorized by the coefficient of determination. Since this parameter has a maximum value ($R^2=1$), it can be concluded that full functionality is achieved when the model can be fully used to describe the process of the reactive dye adsorption on a cellulose-based sorbent. In addition, the differences between the parameters $q_{e,cal}$ and $q_{e,exp}$ are minimal for this model, or practically insignificant. Similar results were obtained for the medium amounts of sorbent and for treatments at 40 and 60 °C.

Furthermore, according to the data from Table 3, the rate constant of the pseudo-second order depends on the initial dye concentration in the solution and the amount of sorbent.

Table 3. Kinetic parameters for reactive dye adsorption on cellulose-based sorbent

Sorbent amount g	Initial dye concentration mg·dm ⁻³	$q_{e,exp}$ mg·g ⁻¹	Pseudo-second order, 20 °C		
			k_2 g·mg ⁻¹ ·min ⁻¹	$q_{e,cal}$ mg·g ⁻¹	R^2
1	10	0.9997	248.88	0.9998	1
	30	2.9992	82.35	2.9993	1
	50	4.9987	49.81	4.9987	1
	70	6.9981	34.92	6.9984	1
	100	9.9973	24.61	9.9980	1
4	10	0.2499	920.68	0.2500	1
	30	0.7499	310.89	0.7499	1
	50	1.2498	204.55	1.2498	1
	70	1.7496	153.36	1.7497	1
	100	2.4995	107.43	2.4996	1

Similar research confirms the above, namely the use of cheap and ecological bio-sorbents from agricultural cellulosic waste (lignocellulosic waste, activated carbons, textile sludge) has shown to be efficient for the adsorption of reactive dye from water. The kinetic pseudo-second order model stands out as the basic model in describing the sorption rate of the reactive textile dye [10,15, 17].

There is an interesting relationship between the adsorption capacity, that is the rate constant of the pseudo-second order from the amount of cellulose-based sorbent, initial dye concentration and temperature.

The analysis of the results of experimental studies of the dye adsorption kinetics of cellulose-based sorbent showed that the maximum adsorption capacity q_e and the rate constant of the pseudo-second order k_2 generally depend on the amount of the cellulose-based sorbent, the initial dye concentration and the temperature. Figure 4 illustrates the dependence of the adsorption capacity from the initial concentration at various sorbent amounts of the cellulose-based sorbent at a constant temperature (20 °C) with fitted straight lines. Identical dependence was detected at other temperatures (40 and 60 °C), so these relations are not shown in the graph.

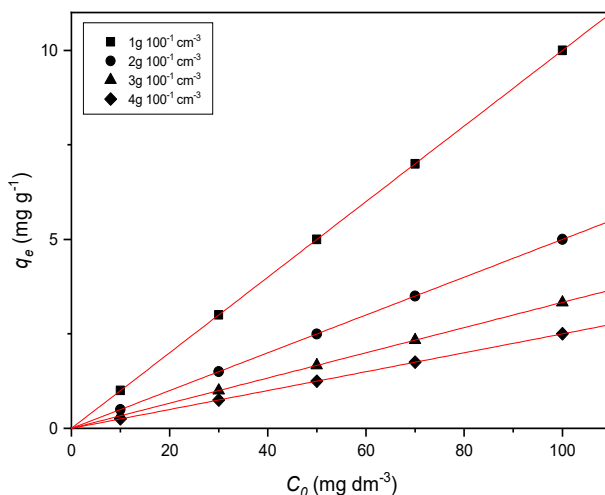


Figure 4. Dependence of the adsorption capacity on initial dye concentrations for different amounts of sorbent at 20 °C

According to the results shown in Figure 4, the maximum adsorption capacity increases linearly along with increasing the initial dye concentration, and the slope of the fitted lines decreases along with increasing the sorbent amount. The values of the slope of the fitted lines at different sorbent amounts

at temperatures 20, 40 and 60 °C were calculated by the linear regression method and they are presented in Table 4. The data from this table indicate that the adsorption capacity does not depend on the temperature. The influence of temperature on adsorption is interesting. Namely, as the temperature increases, the speed of the chemical reaction increases, so if the process of suppression is hemi-sorption, then the sorption capacity will be higher at a higher temperature (equilibrium could occur). But if the process is physical adsorption, then higher temperatures could have negative adsorption results. Also, it should be considered that the temperature can chemically change the sorbent and its adsorption sites, as well as the adsorption activity. Better adsorption at higher temperatures may also indicate the endothermic nature of this process.

Table 4. The influence of sorbent amount and temperature on slope values fitted straight lines

Sorbent amount g·100·l·cm ⁻³	Slope, dm ³ ·g ⁻¹		
	20 °C	40 °C	60 °C
1	0.09997	0.09997	0.09998
2	0.04999	0.04999	0.04999
3	0.03333	0.03333	0.03333
4	0.02499	0.02500	0.02500

Figure 5 shows a graph of the dependence of the slope or the proportionality constant on the sorbent amount, w . As in graph from Figure 5, the fitted straight lines completely coincide for various temperatures, while the slope value of these fitted lines decreases with the increase of the sorbent amount.

The following dependence between the maximum capacity of adsorption and the initial concentration exists:

$$q_e = \text{Slope} \cdot C_0 \quad (1)$$

The proportionality constant or slope from the equation (1), depends on the sorbent mass, w :

$$\text{Slope} = f(w) \quad (2)$$

Since the logarithmic scale of the abscissa and ordinates is shown in the graph of Figure 5, then:

$$\text{Slope} = k \cdot w^m \quad (3)$$

$$\log(\text{Slope}) = \log(k) + m \cdot \log(w) \quad (4)$$

where: K – is the proportionality constant (from the graph in Figure 5).

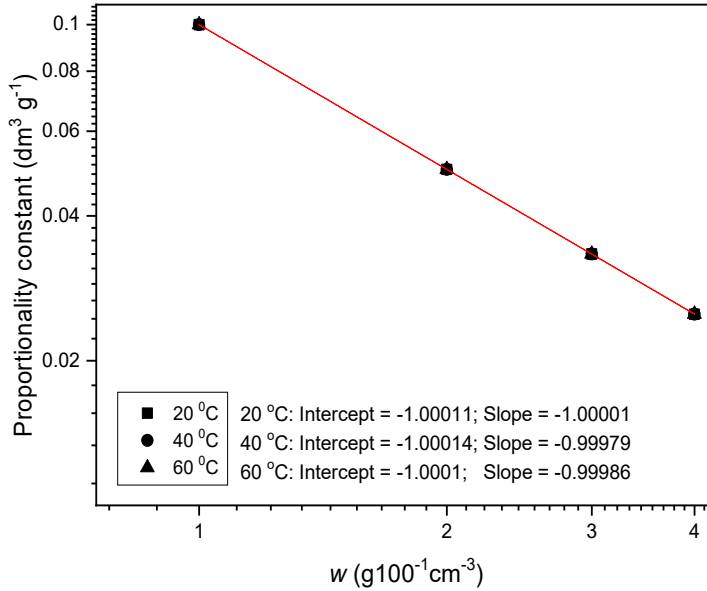


Figure 5. Dependence of the proportionality constant (slope) of fitted straight lines on the sorbent amount for all temperatures

Furthermore, numerous slope and segment values for all temperatures obtained by the linear regression method are entered in the graph of Figure 5. It can be noticed that these numerous values overlap to a large extent. After rounding the digits, without major errors, it can be said that the segment and the slope have the same numerical value, -1 each (the segment has a numerical value -1, the slope has a numerical value of -1), for all temperatures:

$$\log(\text{Slope}) = -1 - 1 \cdot \log(w) \quad (5)$$

$$\log(\text{Slope}) = -1 + \log\left(\frac{1}{w}\right) \quad (6)$$

$$\text{Slope} = 0.1 \cdot \frac{1}{w} \quad (7)$$

After the transformation of equation (1) the following is obtained:

$$q_e = \frac{0.1}{w} \cdot C_0 \quad \text{i.e.} \quad q_e = 0.1 \cdot \frac{C_0}{w} \quad (8)$$

The graph in Figure 6 illustrates the dependence of the pseudo-second order rate constant from the initial concentration at different amounts of cellulose-based sorbent at 20 °C; identical dependence was observed at other temperatures (40 and 60 °C). The value of the pseudo-second order rate constant decreases when increasing the initial dye concentration and the decrease of the sorbent amount when increasing the temperature.

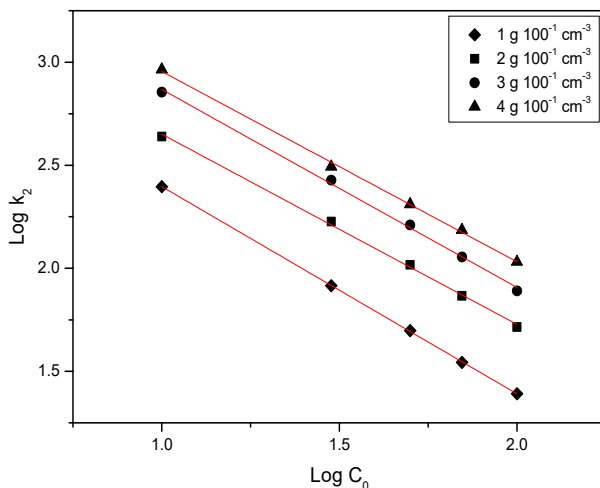


Figure 6. Dependence of the pseudo-second order constant rate on the initial dye concentration at a constant temperature (20 °C)

Based on the previous results and the presented dependencies, it is assumed that there is a complex dependence of the following form between the rate constant of the pseudo-second order and the amount of the cellulose-based sorbent, the initial dye concentration and the temperature:

$$k_2 = A_1 \cdot w^m \cdot C_0^n \exp\left(-\frac{E_a}{R \cdot T}\right) \quad (9)$$

Equation (9) is first transformed into a linear form:

$$\ln(k_2) = \ln(A_1) + m \cdot \ln(w) + n \cdot \ln(C_0) - \frac{E_a}{R} \cdot \frac{1}{T} \quad (10)$$

The multiple linear regression method (Table 5) was used to calculate the parameter values of the equation (10) m , n and E_a . Analysis of variance (ANOVA) showed that all factors and the model itself were statistically significant, with the probability of 95% (Table 5 and 6). Furthermore, the coefficient of determination and the adjusted coefficient of determination have the same values, close to 1 (0.997).

Based on the results of multiple linear regression, the following mathematical dependence was determined between the rate constant of the pseudo-second order and the amount of the cellulose-based sorbent, the initial dye concentration and the temperature:

$$\ln(k_2) = 8.32756 + 1.02005 \cdot \ln(w) - 0.95763 \cdot \ln(C_0) - 196.73 \cdot \frac{1}{T} \quad (11)$$

that is:

$$k_2 = 4136.3 \cdot w^{1.02} \cdot C_0^{-0.96} \exp\left(-\frac{196.73}{T}\right) \quad (12)$$

Therefore, the pseudo-second order rate constant is directly proportional to the amount of cellulose-based sorbent and inversely proportional to the initial dye concentration, whereas the effect of temperature is in accordance with *Arrhenius'* exponential law.

The value of activation energy (E_a) can easily be calculated from the equation (12). For the observed system it is 1.63 kJ·mol⁻¹. A low value of E_a means that the adsorption of dye on the sorbent is mostly of a physical nature. On the other hand, lower E_a may indicate the fact that the increase in the reaction rate is achieved according to: facilitated electron transfer, moving to a more favorable position in the system, larger cellulose-based sorbent–dye molecule, better mutual orientation, etc. [11].

Table 5. Results of applying the multiple linear regression method for calculating the parameters of mathematical expression of new kinetic model

Parameter	Value	Error	t- Value	Prob> t
Y- Intercept	8.32756	0.13645	61.02974	<0.0001
w	1.02005	0.01326	76.90882	<0.0001
C_0	-0.9576	0.00862	-111.06828	<0.0001
$1/T$	-196.73	41.2291	-4.77173	<0.0001
R-Square(COD)	Adj. R-Square	Root-MSE(SD)	-	-
0.997	0.997	0.05349	-	-

Table 6. ANOVA for the observed system cellulose-based sorbent–reactive dye

Item	Degrees of Freedom	Sum of Squares	Mean Square	F Statistic	Prob>F
Model	3	52.28	17.43	6091.3	<0.0001
Error	56	0.16	0.00286	-	-
Total	59	52.44	-	-	-

To check the previous modelling and analysis, thermodynamic parameters (changes in free energy, enthalpy and entropy) and activation energy (for maximum initial dye concentration, 100 mg·dm⁻³ and sorbent amount of 1 g) were calculated according to standard calculation formulas (equation 15).

Graph $\ln(k_2/T)$ versus $1/T$ gives a straight line with slope $-\Delta H/R$ and intercept $\ln\left(\frac{k_b}{h}\right) + \frac{\Delta S}{R}$ from which enthalpy and entropy changes were calculated, shown in Figure 7. Coefficient of determination is was 0.997, which is excellent functionality for accepting results.

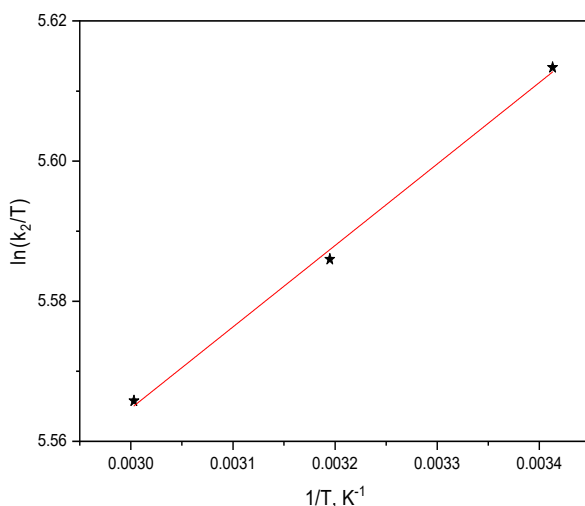


Figure 7. Dependence graph $\ln(k_2/T)$ of $1/T$ for calculating thermodynamic parameters

After the calculation (equation 15, 16), the following data were obtained: ΔS is $-0.15 \text{ kJ}\cdot\text{K}^{-1}\cdot\text{mol}^{-1}$, $\Delta H = -0.97 \text{ kJ}\cdot\text{mol}^{-1}$, while the change in free energy, ΔG , has values of 30.1, 32.2 and 34.4 $\text{kJ}\cdot\text{mol}^{-1}$, for 20, 40 and 60 °C, respectively.

As entropy is a state that can be viewed as a measure of the "bound" energy of a closed material system, negative changes in entropy change correspond to a decrease in the degree of freedom of adsorbed dyes, i.e., indicate that the disordered system on the particle-solution interface is reduced during the adsorption of dye on the sorbent [18].

Negative and relatively small values for enthalpy change indicate the exothermic nature of the adsorption interactions of applied dye and sorbent and a stable energy process. Variations in values for individual adsorption

conditions should be explained by the fact that the bonds between bulky adsorbate molecules and the sorbent surface are broken, since the adsorbed dye molecules are not firmly bound to the sorbent surface.

The small value of the required amount of heat ($-0.97 \text{ kJ}\cdot\text{mol}^{-1}$) characterizes mainly the phenomenon of physisorption. The enthalpy of physical sorption ranges up to $20 \text{ kJ}\cdot\text{mol}^{-1}$ while the change in enthalpy of chemisorption ranges from 40 to $400 \text{ kJ}\cdot\text{mol}^{-1}$ and mainly depends on the nature of the sorbent. Chemisorption is slower than physisorption and is irreversible. Physical sorption is usually a reversible and fast process (does not require activation energy), which takes place at low temperatures [19].

The change in free *Gibb's* energy increases continuously with increasing temperature and has a positive value, which means that the adsorption of dye to the sorbent is unspontaneous but feasible. The results are explained by the fact that the entropy of adsorption plays a leading role in this case, namely the driving force of the adsorption process is more dominant than the force of chemical bonding [20].

From the graphical relation, $\ln(k_2) : 1/T$, the value of factor A ($47.92 \text{ g}\cdot\text{mg}^{-1}\cdot\text{min}^{-1}$) and activation energy ($E_a = 1.62 \text{ kJ}\cdot\text{mol}^{-1}$) were calculated, shown in Figure 8. Determination coefficient for this dependence is 0.996 , so the results, statistically, are absolutely accepted.

According to the numerical value, E_a is very small, so it can be said that the adsorption reaction is very fast, which is confirmed by the very fast and high adsorption of the dye. It is known that if the calculated activation energy is less than $40 \text{ kJ}\cdot\text{mol}^{-1}$, the reaction rate is fast; if greater than $120 \text{ kJ}\cdot\text{mol}^{-1}$, the reaction rate is quite slow [20].

The value of activation energy gives an idea of the type of adsorption, which is mostly physical or chemical. It is known that the activation energy corresponds to the physical sorption mechanism in the range up to $40 \text{ kJ}\cdot\text{mol}^{-1}$, while the range from 40 to $800 \text{ kJ}\cdot\text{mol}^{-1}$ suggests the chemisorption mechanism [21].

If we compare the values of activation energy from the new kinetics model ($E_a = 1.63 \text{ kJ}\cdot\text{mol}^{-1}$, according to equation 12) and the calculated activation energy ($E_a = 1.62 \text{ kJ}\cdot\text{mol}^{-1}$, according to equation 17), absolute concordance of values is observed, which confirms the adequacy and applicability of the new model for adsorption rate.

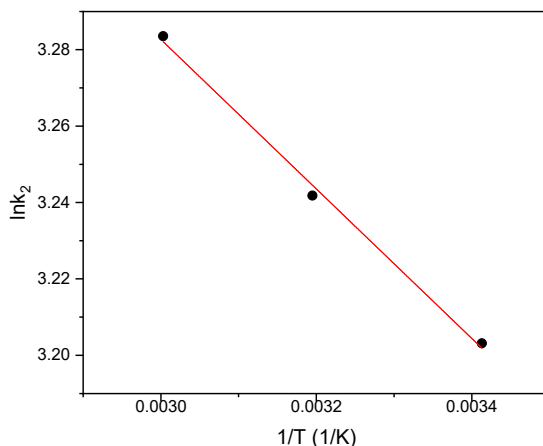


Figure 8. Dependence graph $\ln(k_2) : 1/T$ to calculate activation energy

CONCLUSION

In the research presented in this manuscript, the two most significant goals were achieved. A cheap sorbent was obtained from waste cotton textiles and a new mathematical model was formed that describes the adsorption kinetics in this case.

Furthermore, the applied unconventional and cheap sorbent from natural waste indicates high values of adsorption capacity, as well as high affinity for the reactive dye. The kinetics of adsorption of reactive dye followed the pseudo-second order model. Also, the new model of adsorption kinetics has been established, the pseudo-second order constant rate is almost directly proportional to the amount of the cellulose-based sorbent, inversely proportional to the initial concentration of the reactive dye, whereas the temperature effect is in accordance with the *Arrhenius'* exponential law.

Thermodynamic parameters, changes in free energy, enthalpy and entropy clarify and confirm the validity of the new kinetic model. The change in free energy has a positive value, which reflects the spontaneity but feasibility of the adsorption process. Negative and small value for enthalpy change reveals the exothermic nature of adsorption interactions and a stable energy process with the existence of physisorption. Negative values of entropy change indicate a decrease in the disordered system at the interface during dye adsorption on the sorbent. Very close values between the activation energy from the kinetic model and the calculated activation energy confirm the adequacy and applicability of the new kinetic model for the specific case of adsorption.

EXPERIMENTAL SECTION

The sorbent was obtained by chemical and physical modifications of cotton waste from textile plants, spinning mills and weaving mills (Jumko, Serbia). After the collection, the textile waste (short cotton fibers) was washed with Felosan NKB (CHT, Germany) in warm distilled water (60 °C). After drying, chemical modification was performed by impregnating textile waste with phosphoric acid solution (85%, Tehnohemija, Serbia); the size of the bath was 1:5, and it was kept in a desiccator for 48 h at room temperature with occasional manual stirring. After squeezing, physical modification followed, the samples were placed in stainless steel containers and annealed at 600 °C for 2 hours in the presence of air. After cooling, it was rinsed with distilled water and neutralized with a solution of baking soda until a neutral reaction. Finally, drying (100 °C) to dryness and manual grinding was performed. The sorbent based on cellulose in powder form obtained was used for research.

The adsorption test was performed in glass reactive vessels in which the cellulose-based sorbent was suspended in a reactive dye solution (adsorbate). The reaction vessels were placed on a circular motion shaker (the speed of the shaker rotation was 130 rpm) at temperatures of 20, 40 and 60 °C and they were kept for a certain period. The sorbent amount was constant, 1, 2, 3 and 4 g, whereas the amount of the solution constantly of 0.1 dm³, contained a reactive dye of the following concentration: 10, 30, 50, 70 and 100 mg·dm⁻³. The processing period, with continuous stirring, was 5, 10, 20, 30, 45 and 60 min. The pH of the aqueous dye solution was adjusted at 2-3. The time of 60 min was taken as the equilibrium time because afterwards (a check went up to 120 min) there was no significant change in the amount of the adsorbed dye on the sorbent.

Measurement of the solution adsorption was performed on a UV-VIS spectrophotometer (Cary 100 Conc UV-VIS, Varian) at 620 nm (maximum wavelength of the spectrum of the solution used).

SEM measurements were performed on a TESCAN MIRA3 microscope, using a secondary electron detector, and EDS detector was used for measuring characteristic X-rays of the main elements.

The chemical structure of the reactive dye used, Reactive Blue 2 (C₂₉H₁₇ClN₇Na₃O₁₁S₃, M=840.11 g·mol⁻¹) is shown in Figure 9.

It is well-known that reactive dyes are dyed substances having groups capable of rewarding covalent connections between carbon ions or dye molecules and oxygen, nitrogen or sulphur atoms from hydroxyl, amino or methanethiol groups of the corresponding substrate–textile fibers [13].

According to the structure from Figure 9, it can be noticed that it is an anthraquinone dye (anthraquinone or anthracene derivate) by a self-chlorotriazine ring via which this dye binds to a fiber (cellulose), via a chlorine atom.

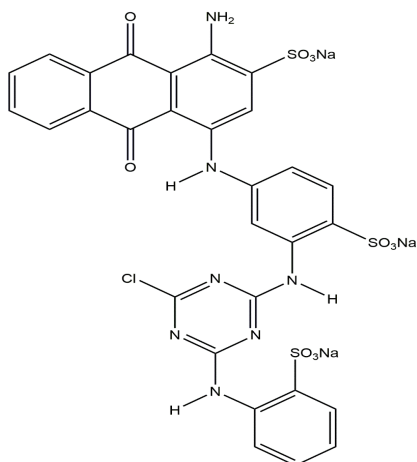


Figure 9. Structure of the applied reactive dye Reactive Blue 2

The adsorption capacity or amount of the adsorbed dye (adsorbate) per unit mass of sorbent in time t (q_t) or equilibrium balance (q_e) is determined [22] by the following expressions:

$$q_{t,e} = \frac{(C_0 - C_{t,e}) \cdot V}{w} \quad (13)$$

where: C_0 – is the initial adsorbate concentration ($\text{mg} \cdot \text{dm}^{-3}$), $C_{t,e}$ – equilibrium concentration of the adsorbate after time t and in equilibrium, respectively ($\text{mg} \cdot \text{dm}^{-3}$), w – sorbent mass (g) and V – volume of adsorption solution (dm^3).

Pseudo-second order model [14] describes the adsorption kinetics as follows:

$$\left(\frac{t}{q_t}\right) = \frac{1}{k_2 \cdot q_e^2} + \frac{1}{q_e} \cdot (t) \quad (14)$$

where: k_2 – is the constant rate of the second order adsorption ($\text{g} \cdot \text{mg}^{-1} \cdot \text{min}^{-1}$), q_e, q_t – the capacity of adsorption in equilibrium and after time t , respectively ($\text{mg} \cdot \text{g}^{-1}$).

The graph t/q_t towards t provides a straight line for all applied dye concentrations, whereby the applicability of the pseudo-second order equation is confirmed. The values k_2 and the equilibrium capacity of adsorption q_e were calculated from the segment and the slope of the dependence graph curve t/q_t to t , respectively.

Thermodynamic parameters for adsorption systems were calculated using the following equations [23]:

$$\ln\left(\frac{k_2}{T}\right) = \ln\left(\frac{k_b}{h}\right) + \frac{\Delta S}{R} - \frac{\Delta H}{R \cdot T} \quad (15)$$

$$\Delta G = \Delta H - T \cdot \Delta S \quad (16)$$

where: k_2 - second order adsorption rate constant ($\text{g} \cdot \text{mg}^{-1} \cdot \text{min}^{-1}$); T - temperature (K); k_b - Boltzmann constant ($1.38065 \cdot 10^{-23} \text{ J} \cdot \text{K}^{-1}$); h - Planck constant ($6.626 \cdot 10^{-34} \text{ J} \cdot \text{s}$); ΔS - entropy change ($\text{J} \cdot \text{K}^{-1} \cdot \text{mol}^{-1}$); R - universal gas constant ($8.314 \text{ J} \cdot \text{K}^{-1} \cdot \text{mol}^{-1}$); ΔH - enthalpy change ($\text{J} \cdot \text{mol}^{-1}$); ΔG - change of free Gibbs's energy ($\text{J} \cdot \text{mol}^{-1}$).

Activation energy is calculated according to the formula [20]:

$$\ln k_2 = \ln A - \frac{E_a}{R \cdot T} \quad (17)$$

where: E_a activation energy ($\text{J} \cdot \text{mol}^{-1}$); k_2 - second order adsorption rate constant ($\text{g} \cdot \text{mg}^{-1} \cdot \text{min}^{-1}$); A - frequency factor or frequency sorption factor ($\text{g} \cdot \text{mg}^{-1} \cdot \text{min}^{-1}$).

REFERENCES

1. S. Samsami; M. Mohamadi; M.H. Sarrafzadeh; E.R. Rene; F. Meysam; *Process Saf. Environ. Prot.*, **2020**, *143*, 138-163.
2. M. Stagnaro; S. Volzone; C. Huck; *Procedia Mater. Sci.*, **2015**, *8*, 586-591.
3. G. Ciobanu; S. Barna; M. Harja; *Arch. Environ. Prot.*, **2016**, *42*, 3-11.
4. S. Wong; N.A.N. Yac'cob; N. Ngadi; O. Hassan; I.M. Inuwa; *Chin. J. Chem. Eng.*, **2018**, *26*, 870-878.
5. G. Duran-Jimenez; L.A. Stevens; G.R. Hodgins; J. Uguna; J. Ryan; E.R. Binner; J.P. Robinson; *Chem. Eng. J.*, **2019**, *378*, 121774.
6. Ajmania; C. Patra; S. Subbiah; S. Narayanasamy; *J. Environ. Chem. Eng.*, **2020**, *8*, 103825.
7. J. Li; J. Cai; L. Zhong; H. Cheng; H. Wang; Q. Ma; *Appl. Clay Sci.*, **2019**, *167*, 9-22.
8. T. Shahnaz; M.M.S. Fazil; V.C. Padmanaban; S. Narayanasamy; *Int. J. Biol. Macromol.*, **2020**, *151*, 322-332.
9. A.K. Nayak; A. Pal; *J. Mol. Liq.*, **2019**, *276*, 67-77.
10. M. Daoud; O. Benturki; Z. Kecira; P. Girods; A. Donnot; *J. Mol. Liq.*, **2017**, *243*, 799-809.
11. S. Kittappa; F.M. Jais; M. Ramalingam; N.S. Mohd; S. Ibrahim; *J. Environ. Chem. Eng.*, **2020**, *8*, 104081.

12. C. Patra; R. Gupta; D. Bedadeep; S. Narayanasamy; *Environ. Pollut.*, **2020**, 266, 115102.
13. K. Blus; J. Paluszkiwicz; W. Czajkowski; *Fibres Text. East. Eur.*, **2005**, 13, 75-78.
14. A. Ajmani; T. Shahnaz; S. Subbiah; S. Narayanasamy; *Environ. Sci. Pollut. Res.*, **2019**, 26, 32137-32150.
15. G.D. Degermenci; N. Degermenci; V. Ayvaoglu; E. Durmaz; D. Cakir; E. Akan; *J. Cleaner Prod.*, **2019**, 225, 1220-1229.
16. M.C. Menkiti, C.O. Aniagor, C.M. Agu, V.I. Ugonabo, *Water Conserv. Sci. Eng.*, **2018**, 3, 33-46.
17. G.G. Sonai; S.M.A.G.U. de Souza; D. de Oliveira; A.A.U. de Souza; *Journal of Environmental Management*, **2016**, 168, 149-156.
18. A. Ozcan, E.M. Oncu, A.S. Ozcan, *Colloids and Surfaces A: Physicochem. Eng. Aspects*, **2006**, 277, 90-97.
19. S.P.D.M. Blanco, F.B. Scheufele, A.N. Modenes, F.R. Espinoza-Quinones, P. Marin, A.D. Kroumov, C.E. Borba, *Chem. Eng. J.*, **2017**, 307, 466-475.
20. F. Chen, C. Zhou, G. Li, F. Peng, *Arabian J. Chem.*, **2016**, 9, S1665-S1669.
21. V.J. Inglezakis, A.A. Zorpas, *Desalin. Water Treat.*, **2012**, 39, 149-157.
22. J. Kyziol-Komosinska; C. Rosik-Dulewska; M. Pajak; I. Krzyzewska; A. Dzieniszewska; *Pol. J. Chem. Technol.*, **2014**, 16, 33-40.
23. M. Dogan, Y. Zdemir, M. Alkan, *Dyes Pigm.*, **2007**, 75, 701-713.

A NOVEL SCHIFF BASES/MULTIWALLED CARBON NANOTUBE BASED ADSORBENTS TO REMOVE ^{210}Pb FROM WATER

NAZIFE ASLAN^{a*}, ORHAN ATAKOL^b, NILGÜN ŞEN^c

ABSTRACT. This work presents the development of new adsorbent materials to remove lead-210 (^{210}Pb) from water. Adsorbents were constructed from the carboxylated carbon nanotubes modified with N,N'bis(salicylidene)1,3-diaminopropane (LH2) Schiff Base and N,N'bis(salicylidene)1,3-diaminopropane-Cu(II) (CuL) complexes. Scanning electron microscopy (SEM) was used to characterize the morphological features of the adsorbents. The effects of pH, contact time, temperature, and Schiff base concentration on lead(II) absorption were investigated in order to optimize the experimental conditions. The adsorption capacity of the adsorbents was determined using atomic absorption spectrometry. Both adsorbents had high adsorption capabilities, with about 98.0% in the first 30 minutes of contact time. The adsorption processes were also in good agreement with the Langmuir isotherm and pseudo-second-order kinetic models. The adsorption of ^{210}Pb from the tap water sample confirmed the applicability of the proposed adsorbents, and the results were satisfactory.

Keywords: *Multiwalled carbon nanotube, ^{210}Pb removal, Schiff base, radioisotopes*

INTRODUCTION

As a natural result of developing technology, toxic metal pollution poses a threat to public health and natural life. Unlike organic pollutants, they are not biodegradable in the environment. Therefore, most of the toxic metals accumulate in biological organisms and cause serious diseases such as thyroid, neurological, autism, infertility and even death.

^a Ankara Hacı Bayram Veli University, Polatlı Science and Arts Faculty, Chemistry Department, Turkey

^b Ankara University, Science Faculty, Chemistry Department, Ankara, Turkey

^c Turkish National Police Academy, Institute of Forensic Sciences, Ankara, Turkey

* Corresponding author: nazife.aslan@hbv.edu.tr

Toxic metals from industrial and urban waste are the most common sources of contaminants in water and soil, and lead is one of the most dangerous. It must be carefully monitored for human health and environmental damage because it is both chemically hazardous and has a radioactive isotope [1,2]. Lead does not have a physiological role in the body. Its presence can lead to toxic effects in every organ system, regardless of age, gender, or exposure pathway. Of all the organs, the nervous system is most affected by lead toxicity, both in children and adults. The toxicity on children is, however, of a more significant impact than in adults. Prolonged exposure to lead is known to cause anemia with increased blood pressure [3-6].

The human body can discharge 1-2 mg of lead per day with regular functions. However, lead which is unable to be excreted from the body accumulates in the bones, liver, kidneys, and muscles, causing a variety of ailments such as hypertension, nausea, obesity, and behavioral disorders. It means that the $15 \mu\text{g.L}^{-1}$ lead level in water set by the United States Environmental Protection Agency (EPA) is not a public health threshold, and that decreasing below it does not guarantee the water is safe [7].

Several separation techniques such as ion exchange, chemical precipitation, reverse osmosis, evaporation, membrane filtration, solvent extraction, biological absorption, and adsorption treatment have been reported recently [8-18]. The adsorption process offers several advantages over the others regarding rapid response, high sensitivity, and ease of preparation. As a result of these factors, there is a growing interest in developing new adsorbents to remove harmful metals as well as natural and anthropogenic radioisotopes from environmental samples. [19-20].

Nanotechnology is one of the most important trends in material science right now. Nanoparticles are also being investigated for application in the production of high-performance adsorbents. Carbon nanotubes (CNTs) demonstrate an essential group of nanomaterials. They have unique physical and chemical properties such as large specific surface area, high reactivity, high adsorption and desorption capacity, and low-temperature modification ability. These characteristics have enhanced the usage of carbon nanotubes in environmental technologies [21,22]. However, the insolubility of new generation carbon nanotubes in a variety of solvents restricts their use. In their natural form, carbon nanotubes are chemically inert, but they can be chemically modified with a variety of organic compounds. Thus, they are easy to interact with adsorbates and have greater maximum adsorption capacity after modification [23,24].

Modification can be achieved in two ways: covalent and non-covalent. The electrical structure of CNT is not damaged as a result of its non-covalent modification, which is one of its key advantages. CNTs can be modified using

oxidants such as photo-oxidation, oxygen plasma, or gas phase. On the other hand, the discovery of ultrasonic treatment with nitric and/or sulfuric acid as an oxidation technique, on the other hand, is a major turning point in CNT chemistry. Covalent modification of CNT walls in a systematic and controlled manner is also crucial for many CNT applications and is vital.

Schiff bases (SB) are azomethine-containing compounds, which were first synthesized by Hugo Schiff in 1864. They are condensation products of ketones (or) aldehydes with primary amines. Schiff base ligands can form stable complexes with various metal ions. This property improves their suitability as a novel adsorbent material for the removal of a number of hazardous metals and radioisotopes.

This work aimed to prepare new adsorbent materials for the rapid, sensitive, and practical removal of ^{210}Pb radioisotope from water. For this purpose, multiwalled carbon nanotube (MWCNT) surfaces are carboxylated (F-MWCNT) by an appropriate oxidation procedure and the adsorption of Schiff bases to the surface is provided. The obtained Schiff base-multiwalled carbon nanotube (SB/F-MWCNT) was characterized by scanning electron microscopy (SEM) analysis. Measurements focused on several adsorption parameters such as adsorption capacity, adsorption time, the influence of the Schiff base concentrations, pH of the solution, and temperature. Firstly, the experimental parameters that can affect the adsorption performance investigated using a non-radioactive Pb(II) solution, and optimum working conditions were determined. The results showed that these new adsorbents have a high adsorption capacity towards Pb(II) ions from aqueous solutions and encouraged us to use these materials for the removal of ^{210}Pb radioisotopes in water samples. The adsorption mechanism of lead(II) ions onto SB/F-MWCNT was evaluated thermodynamics and kinetics. For this, Freundlich and Langmuir adsorption isotherm models and kinetic parameters were derived using adsorption's experimental results.

It is known that there are many studies published in the literature concerning the removal of toxic lead(II) ions by using several adsorbents. But only a few works of literature were found about the removal of ^{210}Pb in drinking water. We think that the results of the study will make valuable contributions to the literature in this respect, too.

RESULTS AND DISCUSSION

Surface characterization studies of treated MWCNTs using SEM

SEM was used to obtain morphological images of modified carbon nanotubes. Figures 1a, 1b, and 1c show F-MWCNTs images before and after modification with LH2 and CuL, respectively. In Figures 1a, 1b, and 1c, we

can see some yarns that look just like fibers. The SEM analysis indicates that products have a tubular surface morphology. The modified carbon nanotube's morphological structure is not uniform, and there are white spots in the presence of clots. The white patches and dots are not representative of carbon nanotubes. When the images were compared, it was seen that the carbon nanotubes had an apparent thickening in their diameters. The source of this increase is the Schiff base, which adsorbs to the surface.

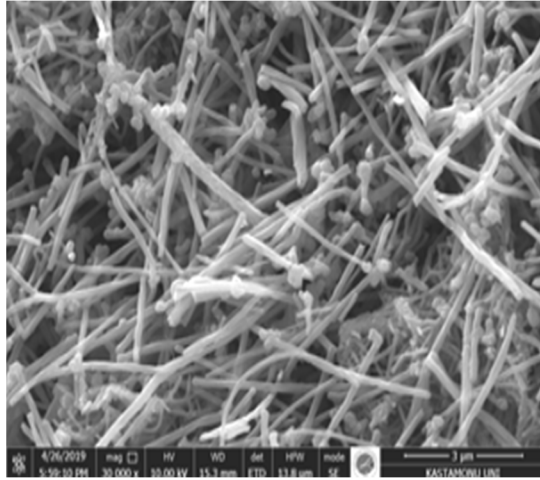


Figure 1a. SEM images of F-MWCNTs before the modification

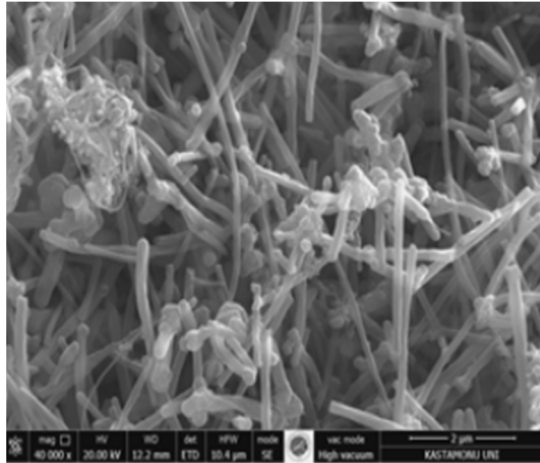


Figure 1b. SEM images of F-MWCNTs after the modification with LH2

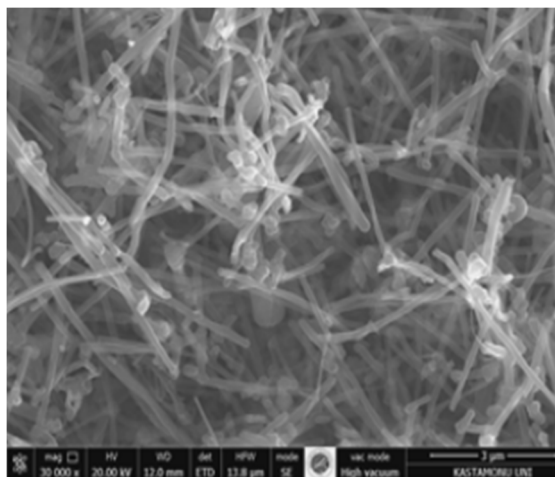


Figure 1c. SEM images of F-MWCNTs after modification with CuL

Effect of contact time

Contact time determination is one of the crucial parameters in the adsorption process. 2 g.L^{-1} adsorbent and 20 mg.L^{-1} lead(II) concentration are used to determine the equilibrium time in removing lead(II) ions with LH2/F-MWCNTs and CuL/F-MWCNTs at room temperature. As indicated in Figure 2, the contact time experiment was carried out for up to 120 minutes to see when the adsorption reached equilibrium. The adsorption of Pb(II) ions was rapid initially, but as contact time increased, it became slower until it reached equilibrium. The removal of lead (II) ions was particularly fast within the first 30 minutes of contact time because the adsorbents have many empty surface sites for adsorption. LH2/F-MWCNTs have a higher adsorption capacity than CuL/F-MWCNTs, as seen in the Figure 2.

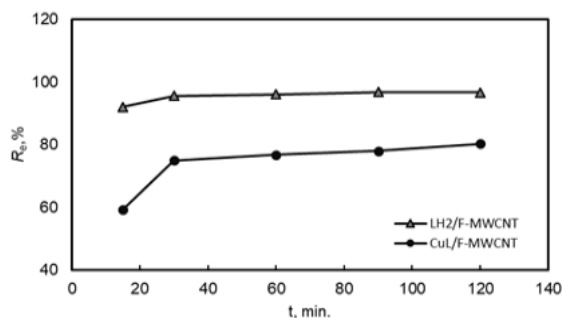


Figure 2. Effect of contact time on removal of Pb(II).

Effect of pH on adsorption

The pH value is significant parameter in the adsorption operations because adsorption capability is highly dependent on pH. When the pH of a solution changes, the adsorbent properties differ due to complex formation, hydrolysis, precipitation, and redox reactions in the solution.

An optimum pH was examined within a range of 2.0 – 7.0 in the 20 mg.L⁻¹ initial Pb(II) concentration. Figure 3 shows that Pb(II) adsorption increases with pH until it reaches 6.0 and then decreases. The concentration of H⁺ ions in the solution is high at low pH values, and lead ions exist in the form of Pb²⁺. Lead ions compete with protons to diffuse onto adsorbent surfaces in this case [17]. Because the adsorbent surface is positively charged at low pH, it repels Pb(II) ions. The concentration of hydrogen ions competing with the lead(II) ions decrease as the pH of the solution increases, but the number of lead(II) ions adsorbed rises. Many researches have claimed that different adsorbents remove metal ions in the same way. [25-26].

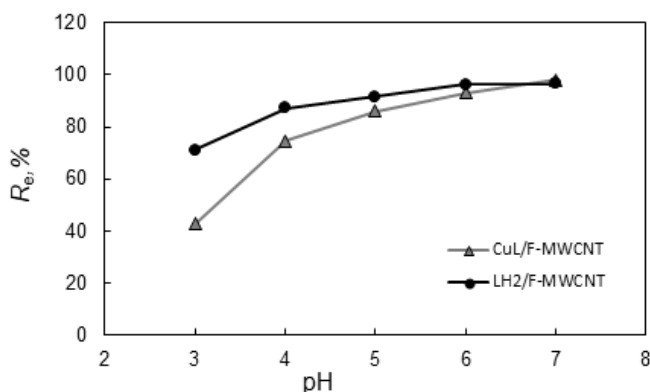


Figure 3. Effect of solution pH on the adsorption percentage of Pb²⁺ onto SB-F-MWCNT (M=2 g.L⁻¹; C₀=20 mg.L⁻¹, V=0.025 L, T=298 K, and adsorption period=30 min.).

Influence of initial Pb(II) concentration

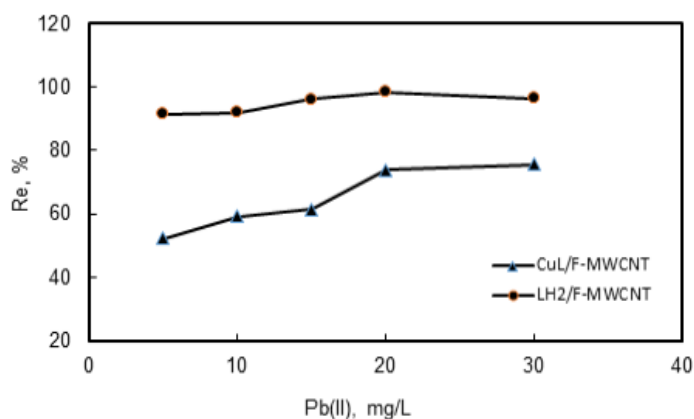
Optimization of the initial metal concentration is another crucial parameter to achieve the best adsorption conditions. At a constant SB/F-MWCNT concentration of 2 g.L⁻¹, the effect of the initial Pb(II) concentration on adsorption behavior was examined between 5.0 - 30.0 mg.L⁻¹. Table 1 presents the outcomes of the experiments. LH2/F-MWCNT and CuL/F-MWCNT had a maximum adsorption efficiency of 99.5% and 84.3%, respectively.

Table 1. The effect of initial Pb (II) concentration on the adsorption efficiency.

	R_e , %	R_e , %	q_e , mg.g ⁻¹	q_e , mg.g ⁻¹
C_o , mg.L ⁻¹	LH2/F-MWCNT	CuL/F-MWCNT	LH2/F-MWCNT	CuL/F-MWCNT
5	88.6	56.3	2.63	2.01
10	92.0	74.1	4.85	4.15
15	97.9	81.1	6.25	6.01
20	99.5	84.3	8.72	8.14
30	95.5	83.6	13.8	13.1

Since the adsorbent surface has a sufficient number of binding sites to which the metal can bind, the adsorption efficiency will initially increase as the metal concentration increases.

When the lead(II) concentration exceeds 20 mg.L⁻¹, however, the adsorption efficiency decreases, as seen in Figure 4. After 20 mg.L⁻¹, the adsorbent surface to which the metal will bind decreases due to the saturation of empty centers.

**Figure 4.** Effect of initial Pb(II) concentration on the adsorption efficiency.

Effect of Schiff base dosage

One of the most critical parameters determining the metal ions' adsorption rate from an aqueous solution is the adsorbent quantity. The effect of changing the Schiff base concentration (0.1% - 0.3% (w/v)) was investigated. When the amount of adsorbents was increased from 0.1% to 0.3%, the percentage of Pb(II) removed increased from 93.2 to 98.8% and

71.4 to 84.2% for LH2/F-MWCNT and CuL/F-MWCNT, respectively. By increasing the amount of adsorbent, the bonding groups available on the adsorbent surface increase and provide more adsorption sites for the Pb(II) ions. Thus, an increase in metal ion uptake occurs. However, there was no significant increase in the percentage removal for both adsorbents after the 0.2% (w/v) dosage. Thus, each Schiff base optimum concentration is considered to be 0.2% and used in further experiments.

The effect of temperature

For some adsorbents, temperature can have a significant impact on the adsorption process. Therefore, the effect of temperature on Pb(II) adsorption was investigated at 20°C, 30°C, and 40°C (Figure 5). As seen in the Figure 5, temperature has a minor effect on the adsorption capabilities of both adsorbents. The adsorption capacities of LH2/F-MWCNT and CuL/F-MWCNT decreased from 8.25 mg/g to 7.96 mg/g and from 8.09 mg/g to 7.58 mg/g, respectively, with the increase in temperature from 20 °C to 40 °C.

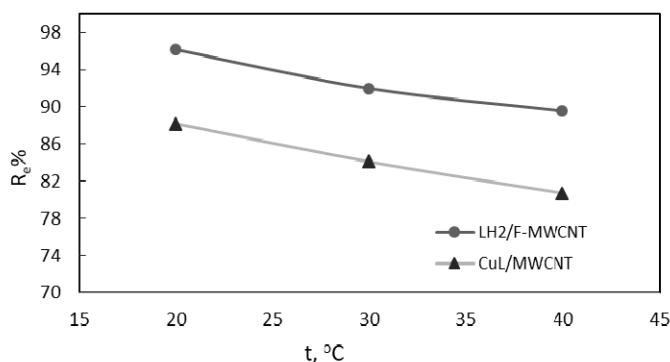


Figure 5. Temperature effects on the removal of Pb (II) ions onto (●) LH₂/F-MWCNTs and (Δ) CuL/F-MWCNTs.

Adsorption kinetics

To examine the kinetic parameters affecting the adsorption of lead(II) onto LH2/F-MWCNT and CuL/F-MWCNT, contact times were varied from 0 to 120 minutes. The relationships between t and t/q_t were plotted according to the experimental values (Figure 6). The data was then used to create pseudo-first and pseudo-second-order models. The intercepts and slopes of the linear plots were used to calculate the pseudo-first and pseudo-second-

order constants k_1 and k_2 , as well as the equilibrium capacity q_e . The q_e value calculated from the pseudo-first-order kinetic model is considerably lower than the experimental data. The q_e value of the pseudo-second-order kinetic model, on the other hand, is closer to the experimental q_e value (Figure 6, Table 2). The obtained R^2 values also indicate that the correlation for both adsorbents is extremely high. Based on these findings, we may conclude that the adsorption behavior of this system is consistent with the pseudo-second-order kinetic model.

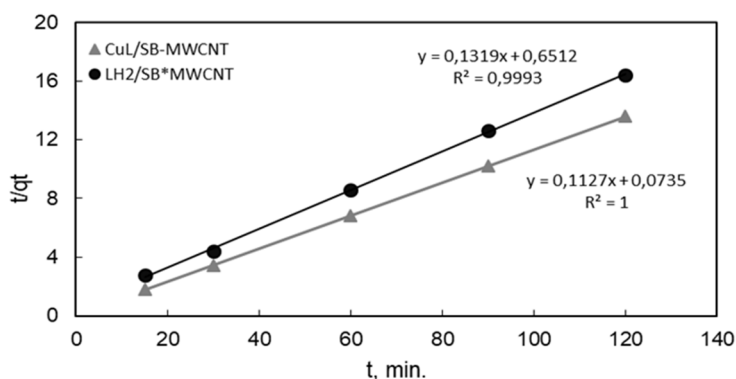


Figure 6. Pseudo-second-order kinetic of Pb(II) adsorption on SB/F-MWCNT ($M=2 \text{ g.L}^{-1}$, $C_0=20 \text{ mg.L}^{-1}$, $V=0.025 \text{ L}$, $T=298 \text{ K}$, and adsorption period=30 min.)

Table 2. Kinetic parameters of pseudo-second-order equations for Pb(II) adsorption onto SB/F-MWCNT at 20 mg.L^{-1}

Adsorbents	$q_{e\text{-exp.}}$ (mg.g^{-1})	$q_{e\text{-calc.}}$ (mg.g^{-1})	k_2 ($\text{g.mg}^{-1}.\text{min}^{-1}$)	R^2
LH2/F-MWCNT	8.713	8.873	0.1728	0.9993
CuL/F-MWCNT	7.066	7.582	0.0267	1.0000

Adsorption isotherms

At a constant temperature, the adsorption isotherm describes the relationship between concentration and the amount of substance adsorbed by the adsorbent. For the study of equilibrium data, developing an equation that can be used to optimize experimental circumstances is critical. In wastewater treatment applications, the Langmuir and Freundlich isotherm models have been widely used [27]. Plotting Langmuir and Freundlich isotherm curves explained the adsorption behavior of LH2/F-MWCNT and CuL/F-MWCNT against rising Pb(II) initial concentrations.

The equilibrium Pb (II) concentration was taken into account in isotherm experiments, and the isotherm constants were calculated using Equation 6-8. The linearized Langmuir and Freundlich isotherms were used to determine the adsorption capacities of LH2/F-MWCNT and CuL/F-MWCNT for lead (II) ions, as seen in Table 3.

Table 3. Langmuir and Freundlich isotherm parameters for Pb(II) adsorption onto SB/F-MWCNT

Adsorbents	Langmuir constants			Freundlich constants			
	q_m , mg.g ⁻¹	K_L , L.mg ⁻¹	R^2	1/n	n	K_f , (mg/g)(L/mg) ^{1/n}	R^2
LH2/F-MWCNT	7.95	31.44	0.992	0.476	2.10	8.31	0.787
CuL/F-MWCNT	4.35	0.358	0.949	0.408	2.45	0.683	0.875

The data in Table 3 shows that the R^2 values of the two isotherm models were reasonably suitable for describing the adsorption. However, the Langmuir equation provided a better fit than the Freundlich equation. The determination coefficients (R^2) show that the adsorption data for Pb(II) best fit the Langmuir isotherm for both adsorbents. LH2/F-MWCNT has a better adsorption capacity (q_m) than CuL/F-MWCNT.

For comparison, Table 4 summarizes the adsorption capabilities of adsorbents previously described in the literature. The highest adsorption capacity, q_m (mg.g⁻¹), determined in this study was in good conformity with those reported in the literature. However, differences in adsorbent properties like structure, surface area, porosity, and functional groups could explain the variations in adsorption capabilities.

Table 4. Comparison of the adsorption capacity of various adsorbents for Pb(II)

Adsorbents, q_m (mg.g ⁻¹)		Adsorption Conditions				
		pH	t (°C)	C_0 (mg.L ⁻¹)	Adsorbent Dosage (g.L ⁻¹)	Ref
Polypyrrole-based AC	50.0	5.5	23	100	5.0	[2]
Acidified CNTs	17.44	5.0	-	10	-	[12]
PPyO/MWCNT composite	26.32	6.0	25	10 - 100	1.0	[36]
Activated C	21.38	6.0	20 ± 2	10 - 100	0.2 - 2	[38]
SB/F-MWCNT	40.69	6.0	25	20	2.0	This work

Real sample application of the adsorbents Removal of ^{210}Pb radioisotope in spike tap water

The main purpose of this study was to develop new adsorbents for removing ^{210}Pb from water using multiwalled carbon nanotube modified with Schiff bases. The radioactive and non-radioactive isotopes of a metal ion have identical chemical characteristics. As a result, the best adsorption conditions were first identified using a non-radioactive lead(II) solution. After that, the real-sample applications of the developed adsorbents were made in tap water samples spiked with ^{210}Pb reference solution. To achieve this, a standard reference ^{210}Pb solution with about 25 Bq activity was added to a tap water sample containing 2 g.L^{-1} of adsorbent at pH 6.0.

Liquid Scintillation Spectrometry (LSS) was used to determine both the added and measured activity concentrations of ^{210}Pb , and the results are shown in Table 5.

Table 5. Removal of ^{210}Pb from tap water using LH2/F-MWCNT and CuL/F-MWCNT adsorbents ($V = 0.025 \text{ L}$, $t = 25^\circ \text{ C}$ and adsorption time = 30 min.).

Sample code	Adsorbent mass, (g)	Added activity, Bq	Measured activity, Bq	Adsorption efficiency, %
LH2/F-MWCNT	0.0505	27.89	0.09	99.7
CuL/F-MWCNT	0.0505	22.98	0.09	99.6

After only 30 minutes of adsorption, the proposed adsorbents can remove almost all of the ^{210}Pb isotopes. These results support the use of LH2/F-MWCNT and CuL/F-MWCNT to control the quality of drinking water in radiological emergencies.

CONCLUSIONS

Our research is divided into two parts: adsorption condition optimization and real sample applications. Batch experiments were performed with two new adsorbents developed using N,N'bis(salicylidene)1,3-diaminopropane Schiff Base and N,N'bis(salicylidene)1,3-diaminopropane-Cu(II) complexes modified with MWCNT-COOH. In terms of radiation protection, the outcomes of the study indicate that both adsorbents developed can successfully remove ^{210}Pb from drinking water in a short period of time with a high adsorption efficiency.

EXPERIMENTAL SECTION

Materials and methods

Reagents and solutions

All materials and chemicals were of analytical grade and used without further purification. The 18.2 mΩ deionized water needed throughout the study was obtained from pure water equipment Millipore, Milli-Q A-10 (Darmstadt, Germany). Hydrochloric (37%, Merck) acid and nitric acid solutions ($\geq 69\%$, Fluka), used for the pH adjustment, were prepared by diluting concentrated solutions. Multiwalled carbon nanotube (MWCNT; $D \times L = 110\text{--}170\text{ nm} \times 5\text{--}9\text{ }\mu\text{m}$) obtained from Sigma Aldrich (Milwaukee, WI, USA). In the modification of the adsorbents, Triton X-100 (Fluka) was used. The standard solution of $1000 \pm 2\text{ mg/L Pb(II)}$ was purchased from ORION (94-26-06). Again, this standard solution was diluted with ultrapure water to obtain the relevant initial concentrations of Pb(II) working solutions. HNO_3 or NaOH was used to change the initial pH of the solutions.

The ^{210}Pb standard solution was used, with a reference date of June 15, 2019, and an activity concentration of 7.467 kBq.g^{-1} (Eckert and Ziegler Isotope Products, catalog number 7210). , A working standard solution with 27.96 Bq.g^{-1} was prepared by diluting this reference solution in 1 M HNO_3 . A quench set with a tritium (^3H) activity concentration of 7.385 kBq/g was prepared using a certified reference solution from Eckert and Ziegler Isotope Products (reference date is August 1, 2009, and Source No: 7003). A High-capacity Ultima Gold cocktail was used as a scintillator.

Instrumentation and measurements

All atomic absorption measurements were carried out with a flame atomic absorption spectrophotometer with a deuterium lamp (BGC-D2) (FAAS) (PinAAcle 900T, PerkinElmer, Waltham, MA, USA) and an automatic data processor. An acetylene-air flame was used for the determination of lead by FAAS.

Scanning Electron Microscope images were obtained using SEM from Thermo Fischer FEI Quanta FEG 250. The pH of the solutions was measured using an Orion Model 720A pH/ion meter and a combined pH electrode.

The Wallac 1220 Quantulus ultra low-level liquid scintillation spectrometer was used to measure beta radiation of ^{210}Pb . The efficiency of the instrument was calculated with the CIEMAT/NIST tritium efficiency tracing method. [28,29]. For this purpose, a standard tritium solution with known activities was put into low diffusion polyethylene vials, and 0 to 200 μL nitromethane was added

as a quenching agent. The dependence of the ^3H counting efficiency on the quench parameter (SQP[E]) was measured experimentally. Combining the theoretical and experimental quench curves allowed for calculating the efficiency of ^{210}Pb using the C/N 2005 program (E. Gunther, PTB/Latest version August 2005). 20 mL Teflon coated low diffusion polyethylene vials (Perkin Elmer) were used for counting the samples. To obtain a homogeneous mixture, the sample vials were sealed and shaken. The counting window was set to channels 1–1024 in the C/N methods. The activity of non-adsorbed ^{210}Pb radioisotopes remaining in the solution was determined using EASY View Spectrum Analysis Software.

Functionalization of MWCNT

Raw-MWCNT (2.0 g) with a purity of >95% was dispersed in 50 mL of concentrated HNO_3 . Then the mixture was refluxed for 6 h at 140°C to produce oxidized carbon nanotubes MWCNT-COOH (F-MWCNT). The samples were filtered and washed with deionized water several times until neutral pH was reached, finally dried in a vacuum oven at 100°C for 24 h.

Preparation of the adsorbents (Schiff Base/F-MWCNT)

The modification of functionalized carbon nanotubes was made using Triton X-100 and two Schiff bases synthesized previously in our laboratory. These Schiff bases were called N,N'-bis(salicylidene)1,3- diaminopropane and N,N'-bis(salicylidene)1,3-diaminopropane-Cu (II), respectively (Figure 7a and Figure 7b).

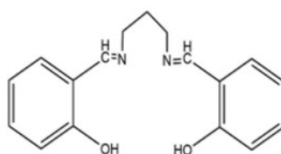


Figure 7a. N,N' bis(salicylidene) 1,3 diaminopropane.

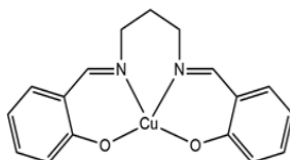


Figure 7b. N,N' bis (salicylidene) 1,3 diaminopropane-Cu (II)

The modification was made according to the following procedure. 50 mL of a 0.2 percent (w/v) methanol solution of each LH2, CuL, and 0.4 g of Triton X-100 were added to 200 mg of functionalized carbon nanotube. The mixture was first sonicated in an ultrasonic bath for 4 hours and then stirred on a magnetic stirrer for 12 hours. The Schiff bases adsorbed on functionalized multiwalled carbon nanotube (SB/F-MWCNT) was vacuum filtered and dried at room temperature. Two different adsorbent materials were prepared using Schiff bases bound to CNT surfaces at the end of this process. Triton X-100 helped the physical adsorption of Schiff bases onto the CNT surfaces and increased the dispersing ability of adsorbent materials.

Characterization of F-MWCNTs and SB/F-MWCNT

The surfaces of functionalized carbon nanotubes (F-MWCNTs) were examined with a Scanning Electron Microscope (Thermo Fischer FEI Quanta FEG 250 SEM) with 1.2 nm resolution before and after modification with CuL and LH2 Schiff bases.

Adsorption experiments

By diluting an accurately measured stock $\text{Pb}(\text{NO}_3)_2$ solution in deionized water, a working solution with a concentration of 100 mg/L was prepared. Different Pb(II) concentrations were obtained by diluting the working solution with deionized water. For all experiments, freshly produced solutions were used. The adsorption studies were carried out in a glass beaker at room temperature. To begin, 50.0 mg of adsorbent and 25 mL of known concentration of Pb (II) were taken into a glass beaker and mixed with a magnetic stirrer at a constant stirring speed of 150 rpm. Following adsorption, a 1.0 mL sample solution was taken from the exact part of the reaction mixture at predetermined intervals. FAAS was used to measure Pb(II) concentrations. According to the results, both of the novel adsorbents efficiently adsorbed the lead(II) ions from the water sample. The effect of parameters including pH, contact time, and adsorbent quantity on the adsorption behavior of the adsorbents was also examined. One parameter was changed and studied for each case, while the other parameters remained constant.

50.0 mg of SB/F-MWCNT was mixed with 25 mL of Pb(II) ion solution to evaluate the kinetic mechanism of the adsorption process. The initial lead(II) ion concentration was changed from 10 mg.L⁻¹ to 30 mg.L⁻¹. To adjust the pH of the solutions, 0.100 M HNO_3 and 0.100 M NaOH solutions were prepared. The difference between the initial and equilibrium Pb(II) concentrations of the solutions was used to calculate the amount of lead(II) ion adsorbed on the adsorbents during the given time intervals (0, 15, 30, 60, 90, and 120 minutes). At least three replicates were averaged for each measurement.

Theoretical calculations

Due to its simplicity, the adsorption of lead was studied by batch operation at room temperature. The Pb(II) ion concentration before and after adsorption was determined using flame atomic absorption spectrometry. The adsorbed amount of lead ions onto the LH2/F-MWCNT and CuL/F-MWCNT adsorbents was calculated according to the following Equations:

$$q_e = (C_0 - C_{eq}) \times \frac{V}{m} \quad (1)$$

$$R_e \% = \frac{(C_0 - C_{eq})}{C_0} \times 100 \quad (2)$$

where C_0 (mg/L) is the initial Pb(II) ion concentration, and C_{eq} (mg/L) is the concentration of Pb(II) after adsorption for particular time intervals. m denotes the adsorbent mass used in adsorption (g), and V denotes the volume of the solution (L).

The distribution coefficient, K_d (mL.g⁻¹), was calculated using Equation 3:

$$K_d = \frac{(C_0 - C_{eq})}{C_{eq}} \times \frac{V}{m} \quad (3)$$

Adsorption kinetics

Adsorption is a time-dependent process. Knowing the adsorption rate is essential in terms of both design and investigation of adsorbent usability. To do this, various equilibrium and kinetics analyses are used. The Langmuir and Freundlich isotherm models were used to analyse the results obtained for examining the adsorption equilibrium conditions. The adsorption kinetics of the SB/F-MWCNT adsorbent were investigated using pseudo-first-order [30] and pseudo-second-order [31] models. The Pseudo-first-order model, based on the adsorbent capacity, is given in Equation 4:

$$\log(q_e - q_t) = \log(q_e) - \frac{k_1 t}{2.303} \quad (4)$$

This kinetic model's applicability is possible if the plot of $\log(q_e)$ versus t gives a straight line. The q_e and k_1 values can be calculated from the slope of the line and the y-axis intercept. However, this model is not applicable for the total adsorption time in most cases; it is generally applicable for the first 20-30 minutes of the adsorption process.

The Pseudo second-order kinetic model is also a model based on the adsorbent capacity. The adsorption process considers the chemical adsorption mechanism. Unlike the first-order kinetic model, this model predicts behavior over the entire adsorption period [32,33]. The second-order kinetic model is represented by Equation 5:

$$\frac{t}{q_t} = \frac{1}{k_2 q_e^2} + \frac{t}{q_e} \quad (5)$$

Where, k_2 is the second-order adsorption constant (g/mg.min). The t/q_t values were plotted against the t to determine k_2 and q_e .

Adsorption isotherms

Adsorption is similar to an equilibrium reaction. When the solution comes into contact with a certain amount of adsorbent, the adsorbed material concentration decreases until it reaches equilibrium with those on the adsorbent surface. After the adsorption equivalence is established, the adsorbed substance's concentration in the solution phase remains constant. The amount of substance adsorbed by the adsorbent's unit mass is a function of temperature, concentration, pressure, or equilibrium pressure.

There are some mathematical models suggested for adsorption isotherms. Freundlich and Langmuir's isotherms are used more than other isotherms. In the Langmuir isotherm, assumptions are made that the adsorbed molecules on the surface are adsorbed as a single layer. The adsorption energy is the same all over the surface. There is no interaction between them the molecules attached to the surface [34]. The following Equation expresses the Langmuir isotherm;

$$\frac{1}{q_e} = \frac{1}{q_m} + \frac{1}{K_L q_m C_e} \quad (6)$$

where q_m (mg/g) is the maximum adsorption capacity of the adsorbent (constant) and K_L (L/mg) is the Langmuir adsorption constant. Langmuir isotherm can be determined by plotting $1/q_e$ versus $1/C_e$.

Freundlich's model applies to adsorption on heterogeneous surfaces. It describes an empirical relationship that explains the adsorption of solutes from a liquid to a solid surface and the exponential distribution of active fields and energies [35,36].

$$q_e = K_F C_e^{1/n} \quad (7)$$

The logarithmic form of Equation 7 becomes

$$\log q_e = \log K_F + \frac{1}{n} \log C_e \quad (8)$$

K_f is the Freundlich constant related to the multilayer adsorption capacity, and n is the heterogeneity factor. The n parameter determine the type of process. If $n = 1$, the process is linear; if $n > 1$, the process is chemical; if $n < 1$, the process is physical [37,38].

ACKNOWLEDGMENTS

The authors thank the Turkish Atomic Energy Authority, Sarayköy Nuclear Research, and Training Center, Liquid Scintillation Spectrometry Laboratory for the radioactivity measurements of the samples.

REFERENCES

1. B.M.W.P.K. Amarasinghe; R.A. Williams; *Chem. Eng. J.* **2007**, 32, 299-309
2. N.R. Axtell; S.P.K. Sternberg; K.C. Laussen; *Bioresour. Technol.* **2003**, 89, 41-48
3. A.L. Wani; A. Ara; J.A. Usmani; *Interdiscip. Toxicol.* **2015**, 8(2), 55-64
4. WHO/FAO/IAEA, Trace Elements in Human Nutrition and Health. Switzerland: Geneva, **1996**, 22-25.
5. A.D. Woolf, R. Goldman and D.C. Bellinger, *Pediatr. Clin. North. Am.* **2007**, 54, 271-294.
6. A. Anjum; P. Lokeswari; M. Kaur; M. Datta; *J. Anal. Sci. Methods Instrum.* **2011**, 1(2), 25-80.
7. EPA, United States Environmental Protection Agency, News Releases from Headquarters Water (OW). "EPA Proposes Updates to Lead and Copper Rule to Better Protect Children and At-Risk Communities", 10.10.2019.
8. A. Anjum; *Sustainable Heavy Metal Remediation*, **2017**, 2, 25-30.
9. C.K. Ahn; D. Park; S.H. Woo; J.M. Park; *J. Hazard. Mater.* **2009**, 164(2-3), 1130-1136.
10. G. Issabayeva; M.K. Aroua; N. Meriam; N. Sulaiman; *J. Hazard. Mater.* **2008**, 155(1-2), 109-113.
11. T.A. Kurniawan; Y.S. Chan Gilbert; W.H. Lo; S. Babel; *Chem. Eng. J.* **2006**, 118, 83-98.
12. D.W. O'Connell; C. Birkinshaw; T.F. O'Dwyer; *Bioresour. Technol.* **2008**, 99, 6709-6724.

13. I.A. Elmaksod; S.A. Kosa; H. Alzahrani; E. Hegazy, *Egypt. J. Chem.* **2019**, 62(11), 2119-2129.
14. A. Agrawal; K.K. Sahu; B.D. Pandey; *Colloids and Surfaces A: Physicochem. Eng. Aspects*, **2004**, 237, 133-140.
15. M. Ghaedi; E. Asadpour; A. Vafaie; *Spectrochim. Acta Part A: Molecular and Biomolecular Spect.* **2006**, 63(1), 182-188.
16. Y. Liang; X.H. Zhao; Q.M. Li; F.L. Cui; G.G. Liu; *Chinese J. Chem.* **2007**, 25(4), 521-526.
17. G. Issabayeva, M.K. Aroua and N.M.K. Sulaiman, *Bioresour. Technol.* **97**, 2350 (2006).
18. M.A. Olatunji; M.U. Khandaker; Y.M. Amin; H.N.M.E. Mahmud; *Plos One*, **2016**, 11(10), 1-14.
19. M.A. Olatunji; O.B. Uwatse; M.U. Khandaker; Y.M. Amin; G. Faruq; *Royal Swedish Academy of Sciences, Physica Scripta*, **2014**, 89(12), 125002-125008.
20. N.A. Kabbashi; M.A. Atieh; A. Al-Mamun; M.E.S. Mirghami; M.D.Z. Alam; N. Yahya, *J Environ. Sci.* **2009**, 21, 539-544.
21. S. A. Kosa; G. Al-Zhrani; M. A. Salam; *Chem. Eng J.* **2012**, 181-182, 159-164.
22. Q. Li; J. Yu; F. Zhou; X. Jiang; *Colloids Surf A: Physicochem. Eng. Aspects*, **2015**, 482, 306-314.
23. M. Abdel Salam; G. Al-Zhrani; S.A. Kosa; *Comptes Rendus Chimie.* **2012**, 15(1-3), 398-408.
24. V.K. Gupta; S. Agarwal; T.A. Saleh; *Water Research*, **2011**, 45(6), 2207-2212.
25. M. Mohapatra; S. Anand; *J. Hazard. Mater.* **2007**, 148(3), 553-559.
26. L. Mouni; D. Merabet; A. Bouzaza; L. Belkhiri; *Desalination*, **2011**, 276, 148-153.
27. M.R. Matsumoto; *Sep. Sci. Technol.* **1993**, 28(13-14), 2179-2186.
28. A.G. Malonda; E. Garcia-Toraño; J.M. Los Arcos, *Int. J Appl. Radiat. Isot.*, **1985**, 36, 157-157.
29. A.G. Malonda; E. Garcia-Toraño; *Int. J Appl. Radiat. Isot.* **1982**, 33, 249-253.
30. S. Lagegren; B. Svenska, *Vetenskapsakademiens Handlingar*, **1898**, 24, 1-39.
31. Y.S. Ho; G. McKay, *Process. Biochem.* **1999**, 34(5), 451-465.
32. J. Guo; Y. Song; X. Ji; L. Ji; L. Cai; Y. Wang; H. Zhang; W. Song, *Materials*, **2019**, 12(2), 241-258.
33. K. Mohanty; M. Jha; B. Meikap; M. Biswas, *Chem. Eng. Sci.* **2005**, 60(11), 3049-3059.
34. I. Langmuir; *J. Am. Chem. Soc.* **1918**, 40, 1361-1403.
35. H. Freundlich; *J. Phy. Chem.* **1906**, 57, 1100-1107.
36. L. Wang; J. Zhang; R. Zhao; Y. Li; C. Li; C. Zhang; *Bioresour. Technol.* **2010**, 101(15), 5808-5814.
37. A. Özer; H.B. Pirincci; *J. Hazard. Mater.* **2006**, 137(2), 849-855.
38. M.A. Hashem; *Int. J Phys. Sci.* **2007**, 2(7), 178-184.

STUDY CONCERNING PERFORMANCES OF TWO TYPES OF PREHYDROLYZED POLYMER IN COMPARISON WITH ALUMINUM SULPHATE AS A COAGULANT FOR WASTE WATER

DAN CRISTIAN DANIELESCU^a, ADRIAN EUGEN CIOABLĂ^{b*},
VASILE PODE^c

ABSTRACT. The main environmental problems of pulp and paper production are water consumption, pollutant fillings of effluents (biogenic and refractory organic compounds, suspended solids, colloids, toxic inorganic compounds). This industry is obliged to minimize its impacts on the aquatic environment and at the same time, due to huge water consumption, must adopt strategies for sustainable use of water resources, in the context of ensuring European requirements for integrated pollution prevention and control and implementation of the Framework Directive of water.

The original experimental research refers to the improvement of the efficiency of conventional physicochemical treatment of residual effluents from the pulp and paper industry by using new prehydrolysed coagulation-flocculating agents. This stage is preliminary to the advanced effluent treatment stage, for its recirculation in the technological process.

Correlating these structures with the efficiencies obtained in coagulation, it is noted that the low coagulant doses of PAC-1 and PAC-2 compared to SA, are due to the existence of more active polymeric species of Al_{13}^{7+} or Al_{30}^{18+} , with higher load and molecular weight than in the case of aluminium monomeric species formed in the use of aluminium sulphate.

There are high efficiencies for removing turbidity between 98-99% as well as organic loading of about 70% for the three coagulants studied (SA, PAC-1, PAC-2), but for the same efficiencies the doses of SA were double or even triple those required for PAC-1 and PAC-2.

Key words: *pollutants, water treatment, flocculation coagulation*

^a SC Vital SA, Sighetu Marmăției, Zimbrului, Str. No.94, zip RO-435500, Romania

^b Politehnica University of Timisoara, Faculty of Mechanical Engineering, 1 Mihai Viteazu blvd., RO-300222, Timisoara, Romania

^c Politehnica University of Timisoara, Faculty of Industrial Chemistry and Environmental Engineering, 6 Vasile Parvan blvd., RO-300223, Timisoara, Romania

* Corresponding author: adrian.cioabla@upt.ro

INTRODUCTION

The pulp and paper industry are large consumers of high-quality water and involve two stages of manufacture: that of pulp and paper so the resulting effluents have different pollutants. Paper industry consumes large amounts of water (about 250-300 m³/t of paper produced) and generates almost an equal amount of wastewater having biochemical oxygen demand (BOD), chemical oxygen demand (COD), turbidity and colour [1-3]. The pulp and paper industry are one of the industries that is obliged to reduce their impact on the aquatic environment and at the same time to develop and adopt sustainable strategies for the use of water resources; in the context of ensuring European requirements for integrated pollution prevention and control and implementation of the Framework Directive of water [3-7].

Although several treatment methods are in use in large mills, including physicochemical and biological, small mills suffer from the unavailability of proper treatment systems due to financial constraints [8-9].

Thus, one of the possibilities to improve the conventional treatment processes is to improve the efficiency of conventional physicochemical treatment (because this type of treatment is intended for several types of pollutants, such as: biogenic and refractory organic compounds, solid in suspension and colloids), by using new coagulation or flocculating agents; or by modifications made to the coagulation-flocculation process in order to increase the global purification efficiencies [1], [10-16]. Coagulation using alum, poly aluminium chloride (PAC-1) and (PAC-2) have been studied extensively [17-19]. Poly aluminium chloride has been used by many investigators in the treatment of oil-water emulsions, however, the use of PAC for the removal of soluble and colloidal organics from pulp and paper mill effluents has been scarcely studied [20-23].

PAC, which is an inorganic polymer, has been found to exhibit improved performance over other coagulants in terms of removal of turbidity, organic load, etc. PAC treatment requires smaller dosage leading to generation of smaller sludge volume than that obtained with other coagulants. The use of synthetic polymers poly aluminium chloride (PAC) for the removal of COD and turbidity from wastewater has been investigated by many research workers [24-25].

The primary goal of this study was to derive experimental data for the removal of COD and turbidity from the acid wastewaters, of the small agri-based pulp and paper mill by means of the coagulant (PAC), (SA). The specific objectives of this study were to examine the removal of COD and turbidity from wastewater of agri-based pulp and paper mills. The study also focused on the single stage wastewater treatment using PAC-1, PAC-2 and SA [14-15].

RESULTS AND DISCUSSION

Characterization of PAC-1 and PAC-2 coagulants

Basic aluminum polychloride is an acidic product in liquid form, commercial products (called PAC-1 and PAC-2, produced in Hungary), were used with the following characteristics:

Table 1. Physicochemical properties of basic aluminum polychloride PAC-1 and PAC-2

No.	Parameter	PAC-1	PAC-2
1.	Concentration, (g Al/L)	127.00	63.96
2.	pH (concentrate)	$3.8 \pm 0,3$	2.60
3.	Density, (kg/dm ³)	1.27 ± 0.02	1.30 ± 0.03
4.	Viscosity, (mPas)	<10	-
5.	Basic, (%)	83.0	65.0
6.	Al content, (%)	10.0	5.20
7.	Chloride composition, (%)	8.0	12.50
8.	Content Al_{13}^{7+}	80.94 %	5.19 %
9.	Content Al_{30}^{18+} , or other species	19.06	94.81 %

Basic aluminum polychloride (PAC) is a polymer that can be prepared "in situ", even before use or delivered in concentrated solution, and less often in powder form. The preparation "in situ" is done by neutralizing the aluminum chloride with a base. The commercial product, known in Europe as PAC, WAC, Saptoclar, is of two categories: with or without aluminum sulphate, having as chemical formulas $Al_n(OH)_m(SO_4)_kCl_{3n-m-2k}$ or $Al_n(OH)_mCl_{3n-m}$ [22-25]

Figure 1 shows the spectra obtained in the NMR analysis of basic aluminum polychlorides PAC-1 and PAC-2, for the structural characterization of coagulants prehydrolyzed by Al_{13}^{7+} and Al_{30}^{18+} species. [27]

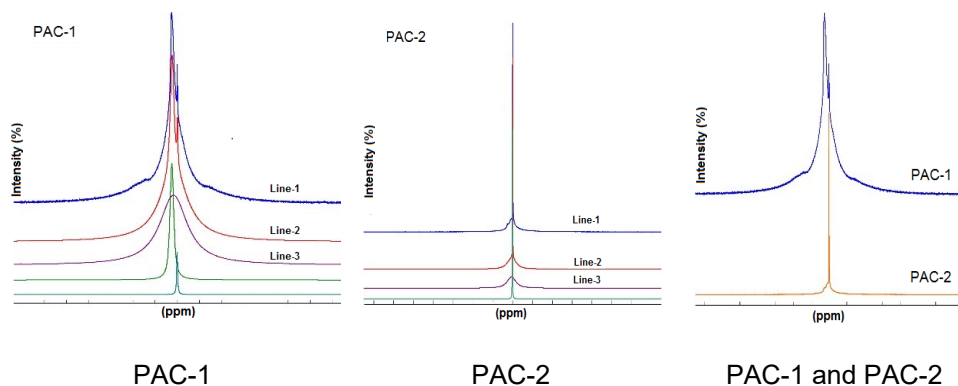


Figure 1. NMR spectra of basic aluminum polychloride PAC-1, PAC-2
The data obtained by NMR analysis of basic aluminum polychloride
are presented in table 4.

Table 2. The values obtained in the NMR analysis of the basic polychlorides
PAC-1 and PAC-2.

	PAC-1			PAC-2		
	Line-1	Line-2	Line-3	Line-1	Line-2	Line-3
Amplitude (u.a.)	14675.73	24525.92	9229,20	28609.23	0.00	522231.90
Position (ppm)	6.19	9.18	-0.40	1.73	0.00	-0.05
Width (ppm)	60.27	8.00	2.00	20.92	0.00	0.45
Intensity (%)	30.30	50.64	19.06	5.19	0.00	94.81

From the NMR spectrum it results that the majority species in PAC-1 is Al_{13}^{7+} in proportion of 80.94%, and in PAC-2 Al_{30}^{18+} in proportion of 94.81%.

Correlating these structures with the coagulation efficiencies, it is noted that the low coagulant doses of PAC-1 and PAC-2 compared to SA, are due to the existence of more active polymeric species (Al_{13}^{7+} sau Al_{30}^{18+}) of or with higher molecular weight and weight than in the case of species. monomeric aluminum formed in the use of aluminum sulfate. [27-29]

In figure 2 are presented the images for the resulting flocs from type 1 coagulation of synthesis water SET 1 for the three coagulants: A) SA, B) PAC-1, C) PAC-2.

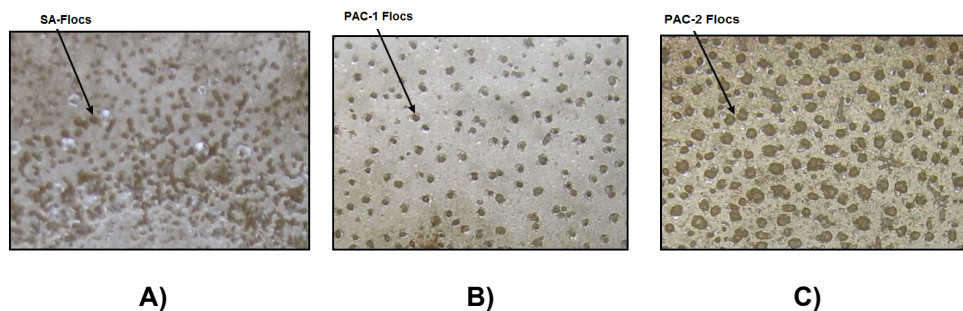


Figure 2. Behavior of aluminium base coagulants (SA, PAC-1, PAC-2 for type 1 water treatment

Prepolymerised forms of Al_{13}^{7+} și Al_{30}^{18+} from PAC-1 and PAC-2, are stable and present opportunities for adsorption on negative colloidal particles and neutralization of negative charges.

Coagulation experiments were performed at pH-7, which is the optimal pH for which it has a slightly higher neutralizing capacity than Al_{30} . Instead, Al_{30} can form more stable and larger flakes than Al_{13} [26-29].

Characterization of synthetic waters

Table 3 shows the characteristics of synthetic waters studied and prepared in the laboratory compared to the characteristics of real wastewater from the pulp and paper industry.

Table 3. Values of the characteristic parameters of synthetic waters shared with the characteristics of real wastewater from the pulp and paper industry.

No	Parameters	SET-1				SET-2				AR
		1	2	3	4	1	2	3	4	
1.	pH	4.12	4.12	4.08	4.11	4.14	4.14	4.26	4.16	6.73
2.	T°(NTU)	260	290	280	300	230	210	230	229	1180
3.	S.S. (mg/L)	400	400	400	400	250	250	250	250	3600
4	Salts content: NaCl (mg/L)	1000	250	1000	250	1000	250	1000	250	350
	Na ₂ SO ₄ (mg/L)	1000	250	250	1000	1000	250	250	1000	524
5.	CCO-Cr (mgO ₂ /L)	1000	1000	1000	1000	700	700	700	700	2285

Two types of synthetic waters characterized by organic loading of 1000 mg O₂/L and 700 mg O₂/L were studied, with solid suspensions of 400 mg/L and 250 mg/L. The waters were prepared to establish the optimal doses of coagulant SA, PAC-1, PAC-2, and for the database which represents a model for the application of the coagulation process in the case of real waters from the pulp and paper industry.

For SET-1 water the pH values were between 4.08 - 4.12, turbidity 260 - 300 (NTU); suspended matter 400 mg/L, organic load 1000 mg O₂/L CCO-Cr. The content of inorganic salts was between 250 - 1000 mg/L Na₂SO₄, and in the case of NaCl the values were in the range of 500 - 2000 mg/L.

In the case of SET-2 synthetic water, the content of suspended matter was lower, 250 mg/L. The values of the turbidity parameter ranged from 210 - 230 NTU. Also the organic matter load was lower than 700 mgO₂/L CCO-Cr, and the inorganic salt content was similar to the waters of SET-1.

Table 4. Characteristics of synthetic and real water samples obtained when applying the optimal doses of classic and prehydrolyzed coagulants based on aluminum.

No.	Coagulant	Water type	Coagulant dose (mg Al/L)	Treated waters					
				SET-1		SET-2		AR	
				T (NTU)	CCO-Cr mgO ₂ /L	T (NTU)	CCO-Cr mgO ₂ /L	T (NTU)	CCO-Cr mgO ₂ /L
1.	SA	1.	2.00	9.55	412.20	8.50	362.18	-	-
		2.	6.00	5.50	405.00	8.25	421.54	-	-
		3.	6.00	6.60	396.80	6.64	247.87	-	-
		4.	6.00	6.75	431.20	7.45	247.80	-	-
		AR	10.02	-	-	-	-	180.0	394.40
2.	PAC-1	1.	1.52	7.80	428.90	9.26	297.15	-	-
		2.	1.52	9.50	433.50	8.45	279.93	-	-
		3.	1.52	8.20	400.30	8.45	271.32	-	-
		4.	1.52	7.55	385.30	9.75	261.52	-	-
		AR	12.70	-	-	-	-	285.0	374.28
3.	PAC-2	1.	1.76	5.35	416.70	7.90	286.58	-	-
		2.	1.51	6.80	392.30	7.40	256.83	-	-
		3.	1.76	9.85	387.00	7.40	267.54	-	-
		4.	1.76	9.45	425.00	6.35	246.61	-	-
		AR	10.08	-	-	-	-	145.0	366.97

Figures 3 and 4 show the results of applying the Jar-Test method for each type of water using coagulation agents used: aluminum sulfate (SA); basic aluminum polychloride type 1 (PAC-1) and basic aluminum polychloride type 2 (PAC-2).

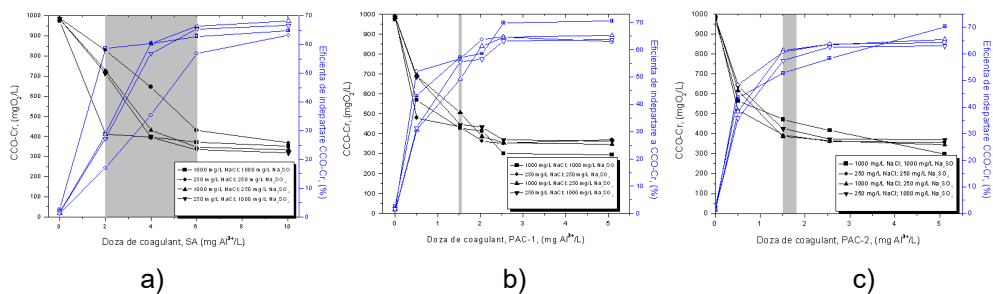


Figure 3. Variation of organic charge for SET-1 of synthetic water, when establishing the optimal coagulant doses (a - SA, b - PAC-1, c - PAC-2)

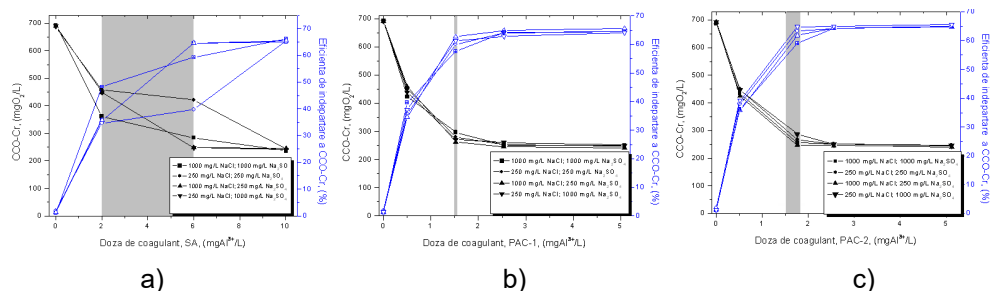


Figure 4. Variation of organic charge for SET-2 of synthetic waters, when establishing the optimal coagulant doses (a - SA, b - PAC-1, c - PAC-2)

Optimal coagulant doses were established for residual turbidity less than or equal to 10 NTU and organic load expressed by the CCO-Cr parameter less than or equal to 500 mg O₂/L according to NTPA 002.

According to the graphical representation of Figure 2, the optimal doses of SA coagulant used to remove organic matter and turbidity was 2.0 mg Al/L for type 1 water from SET-1 and SET-2 synthetic water. At this dose the turbidity was between 9.55 - 8.50 NTU and the organic load was in the range of 412.20 - 362.18 mg O₂/L.

For waters of type 2, 3, 4, from SET-1 and SET-2, respectively, the optimal dose of coagulant was 6 mg Al/ L when treated waters with turbidity between 5.50 - 8.25 NTU were obtained and the loading organic was in the range of 247.80 - 431.20 mg O₂/L (below the level allowed by NTPA 002).

When using the PAC-1 coagulant, figure 2b, the optimal doses of coagulant for the removal of organic matter and turbidity was 1.52 mg Al/L for all types of water from both SET-1 and SET-2. At this dose the turbidity was between 7.55 and 9.75 and the organic load was in the range of 433.50 - 261.52 mg O₂/L.

In the case of PAC-2 coagulant, figure 2c, for type 1, 3, 4, waters from SET-1 and SET-2, respectively, the optimal dose of coagulant was 1.76 mg Al/L, when water treated with turbidity was between 5.35 - 9.85 NTU, and the organic load was in the range of 246.61 - 425.00 mg O₂/L. Also in the case of type 2, SET-1 and SET-2 water, the optimal dose of coagulant was 1.51 mg Al/L. At this dose the turbidity was between 6.80 - 7.40 NTU and the organic load was in the range of 256.83 - 392.30 mg O₂/L.

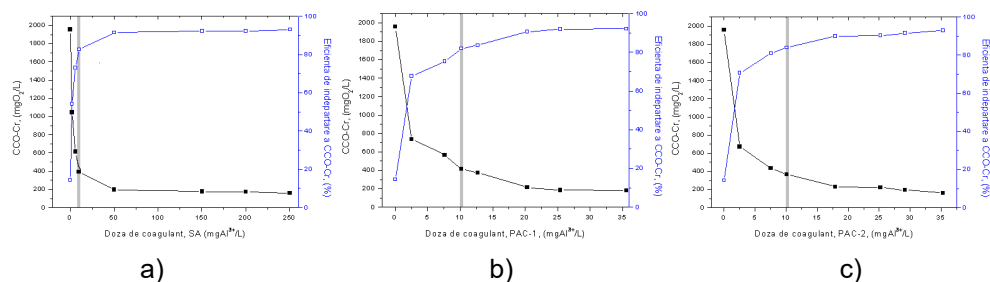


Figure 5. Variation of organic load for wastewater from the pulp and paper industry, in determining the optimal coagulant doses (a - SA, b - PAC-1, c - PAC-2)

According to the graphical representation, figure 5-a), the optimal dose of SA coagulant used for the removal of organic matter and turbidity was 10.02 mg Al/L for wastewater from the pulp and paper industry.

When using the basic aluminum polychloride coagulant PAC-1, figure 5-b), the optimal dose in removing organic load and turbidity was 10.16 mg Al/L. In the case of the basic aluminum polychloride coagulant, PAC-2, figure-5c), the optimal dose established in removing the turbidity and the organic load was 10.08 mg Al/L.

CONCLUSIONS

Wastewater from the pulp and paper processing industry is water with variable organic and inorganic loading.

The technological process of purification of these waters has the basic coagulation-flocculation operation.

In order to optimize the coagulation operation, a model was developed based on a database based on 8 types of synthetic waters prepared in the laboratory. The agent used in the technological process is a classic coagulating agent aluminum sulphate SA and two types of prehydrolyzed coagulants. PAC-1 with Al_{13}^{7+} species content of 80.94% and Al_{30}^{18+} or other species of 19.06%. PAC-2 prepolymerized agent with Al_{13}^{7+} species content of 5.19% and Al_{30}^{18+} species or other species of 94.81% requires lower doses by up to 25% compared to aluminum sulfate.

A successful and important method for improving the efficiency of inorganic coagulants is the partial hydrolysis of the respective salts with the formation of optimal polymeric species.

The efficiency of two prepolymerized coagulants (prehydrolyzed), based on aluminum called basic aluminum polychloride PAC-1 and PAC-2, was compared with the classical coagulant aluminum sulphate (SA).

In order to evaluate the performances attributed to the prepolymerized metal coagulants compared to the conventional ones, characterization analyzes of the materials and structure of the polymeric species contained in the two types of basic aluminum polychloride studied PAC-1 and PAC-2 were performed. From the NMR spectrum it results that the majority species in PAC-1 is Al_{13}^{7+} in proportion of 80.94%, and in PAC-2 Al_{30}^{18+} in proportion of 94.81%.

Correlating these structures with the coagulation efficiencies, it is noted that the low coagulant doses of PAC-1 and PAC-2 compared to SA, are due to the existence of more active polymeric species of or with higher molecular weight and weight than in the case of species. monomeric aluminum formed in the use of aluminum sulfate.

EXPERIMENTAL PART

Reagents used:

Aluminum sulphate (SA), • 18H₂O.

Commercially produced aluminum sulphate (SA) was used to prepare the coagulant solution. The solution prepared by the coagulant had a concentration of 309.00 g/L and a density of 1.277 g/L [14], [16-25].

Basic aluminum polychloride.

Two commercial products called PAC-1 and PAC-2, produced in Hungary, were used [30-32]. The concentrations of basic aluminum polychloride (PAC-1; PAC-2) used in experimental coagulation studies were 1:100 compared to the concentration of SA.

Sodium hydroxide (NaOH).

In the preparation of the sodium hydroxide solution used to correct the pH of the water, 98.0% pure NaOH of the CHEMAPOL type, produced in the Czech Republic, was used.

Bentonite, potassium acid phthalate, sodium chloride and sodium sulfate.

Used in the preparation of wastewater, similar to those in the pulp and paper industry.

Potassium acid phthalate, 99.5-100% purity, RENAL type, produced in Hungary.

The bentonite used was in powder form, from the Aghireş quarry, Cluj county, (Aghireş bentonite).

Anhydrous sodium sulphate of 99.0% purity of the MERCK type, produced in Germany.

Anhydrous sodium chloride (NaCl), 99.0-100% purity, MERCK type, produced in Germany.

METHODS

The "Jar-test" method was used to determine the optimum coagulation conditions. The doses of coagulation reagents were added in samples of 250 ml wastewater, which were fast stirred for 3 minutes, with a speed of 160-170 (rotations/minute), then slow stirred for 15 minutes with a speed of 40-45 (rotations/minute) and placed for sedimentation for 30 minutes. From the supernatant were taken samples of treated water to determine the following parameters: turbidity, organic load expressed by the chemical oxygen demand (COD-Cr). For the coagulation experiments an agitating device of type FC6S VELP (SCIENTIFICA) was used. To determine the turbidity a HACH 2100 turbidimeter was used. Water turbidity was expressed in NTU [22,23].

COD parameter was determined in accordance with SR ISO 6060-96, and suspended solids in accordance with STAS 6953-81 [33-35]

Chlorides (Cl^- mg/L) was determined in accordance with STAS 8663-70; and sulfates (SO_4 mg/L) in accordance with STAS 8601-70 [36-37]

The pH was determined using an electronic "INOLAB" pH meter with an electrode of the "SenTix41 Electrode" type [33]

NMR analysis of basic aluminum polychlorides (PAC-1; PAC-2) was performed with the "Bruker Spectrometer NMR 400 Avance" with a central field of 9.4 Tzla for the structural characterization of coagulants prehydrolyzed by Al13 and Al30 species.

Preparation of synthetic waters

Two sets of synthetic waters (SET-1, SET-2) were prepared, each comprising four types of water, different from each other by adding organic, inorganic and turbidity matter; experimental studies of the coagulation process were performed on synthetic waters having the characteristics presented in table 5. In the preparation of synthetic waters, the composition of "real" wastewater resulting from the manufacture of pulp and paper was taken into account.

Table 5. Domains of variation of the initial characteristic parameters of the synthetic wastewater, subjected to the coagulation process.

Parameter	CCO-Cr (mgO ₂ /L)	s.s. (mg/L)	Cl ⁻ (mg/L)	SO ₄ ²⁻ (mg/L)
Range of concentration variation	400-1000 (K acid phthalate); C ₈ H ₅ O ₄ K	150-400 (bentonite from Aghireş)	250-1000 (NaCl)	250-1000 (Na ₂ SO ₄)

The studied wastewater was taken from a pulp and paper processing plant.

Table 6. Values of characteristic parameters, wastewater from the pulp and paper industry subjected to the coagulation process.

Parameter	pH	CCO-Cr (mgO ₂ /L)	s.s. (mg/L)	Cl ⁻ (mg/L)	SO ₄ ²⁻ (mg/L)
Values for initial concentration	6.73	2285.00	3600	350	525

Table 6 shows the values of some characteristic parameters: organic charge expressed by CCO-Cr, solid suspensions, turbidity, chlorides and sulfates. Wastewater from the pulp and paper industry showed great variations in its composition. The composition of the water includes: very high organic load, high turbidity, a very large amount of suspended solids, the presence of dyes (a pink color), mineral substances (sodium sulfate, sodium chloride, etc.).

REFERENCES

- 1 O. Blăgoi, E.L. Pușcaș, *Metode Chimice - Tratarea Apelor de Suprafață*, Ed. Dosoftei, Iași, Romania, **1997**, 5-17;
- 2 A. Gherghel, C. Teodosiu, S.A De Gisi, review on wastewater sludge valorisation and its challenges in the context of circular economy. *J. Clean. Prod.*, **2019**, 228, 244–263;
- 3 C. Teodosiu, A.-F. Gilca, G. Barjoveanu; S. Fiore, A review on processes and environmental performances assessment. *J. Clean. Prod.* **2018**, 197, 1210–1221;
- 4 Available online:
https://ec.europa.eu/commission/presscorner/detail/en/ip_20_420
(accessed on October 20, **2021**);
- 5 Directive: <https://eur-lex.europa.eu/eli/dir/2008/105/oj> (accessed on October 21, **2021**);
- 6 Decision: <https://eur-lex.europa.eu/legal-content/EN/TXT/?uri=CELEX%3A32018D0840> (accessed on October 22, **2021**);
- 7 <https://www.epa.gov>;
- 8 V.E. Akpan, D.O. Omole, D.E. Bassey, Helyon Cel Press, **2020**, 6, 10, 52-46;
- 9 F.E. Titchou, H Zazou, H.A.J. El Gaayda, R.A. Akbour, M. Hamdani, *Groundw. Sustain. Dev.*, **2021**, 13;
- 10 J. Shi, W. Huang, H. Han, C. Xu, *Renew. Sust. Energ. Rev.*, **2021**, 143;
- 11 S.A.R. Khan, P. Ponce, Z. Yu, H. Golpîra, M. Mathew, **2022**, 286, Part 1;
- 12 B. Medina, D. Smith, U. Wehn, J.N.M. Brummer, *Environ Sci Policy*, **2022**, 128, 36-40;
- 13 S.H. Antwi, A. Rolston, S. Linnane, D. Getty, *Sc. of The Tot. Environ.*, **2022**,
- 14 H. Ye, L. Chen, Y.Z.T. How, P.C. Ayala, Q. Wang, Z. An, S. Guo, C. Chen, M.G.E. Din, *Chemosph.* **2021**, 264, Part 2, 128-531;
- 15 I.D. Gómez, M.Á.G. García, *Sci. Total Environ.*, **2021**, 764, 142-818;
- 16 S. Delgado, F. Díaz, D. Garcia, N. Otero, *Filtr. Sep.*, **2003**, 7, 42;
- 17 M. Ghazouani, H. Akrou, S. Jellali, L. Bousselmi, *Sci. Tot. Environ.*, **2019**, 647, 1651-1664;
- 18 W. Wang, H. Yang, X. Wang, J. Jiang, W. Zhu, *J. Environ. Sci.*, **2010**, 22, 1, 47-55;
- 19 M. Khayet, A.Y. Zahrim, N. Hilal, *Chem. Eng. Jou.*, **2011**, 167, 1, 77-83;
- 20 A.M. Domínguez, M.L. Rivera-Huerta, S. Pérez-Castrejón, S.E. Garrido-Hoyosl. E. Villegas-Mendoza, S.L. Gelover-Santiago P. Drogui, G. Buelna, *Sep. and Purif. Tech.*, **2018**, 200, 266-272;
- 21 B.Y. Gao; H.H. Hahn; E. Hoffmann; *Wat. Res.* **2002**, 36, 3573–3581;
- 22 B.Y. Gao; Q.Y. Yue; B.J. Wang; Y.B. Chu; *Colloids Surf, A Physicochem. Eng. Asp.* **2003**, 229, 1-3, 121-127;
- 23 B. Gao; Q. Yue; *Chemosph.*, **2005**, 61, 579–584;

- 24 Z. Chen, B. Fan, X. Peng, Z. Zhang, J. Fan, Z. Luan, *Chemosph.*, **2006**, 64, 912–918;
- 25 E. Cical; G. Burtica; G. Gasparik; M. Mecea; *Environment & Progress*, Eds. Cluj-Napoca, Romania, **2005**, 83-87;
- 26 D. Kaušpėdienė, R. Ragauskas, J. Vaičiūnienė, A. Selskienė, V. Jasulaitienė, R. Ramanauskas, *Experim. And Modell.*, **2021**, 7, 1, 59-93;
- 27 M. Xue, B. Gao, R. Li, *Jour. of Environ. Scien.*, **2018**, 74, 95-106;
- 28 L.F. Taulelle,, *Inorg. Chem. Commun.* **2003**, 6, 9, 1167-1170;
- 29 J. Fafard, V. Terskikh, C. Detellier, *Clay Miner.*, **2017**, 65, 3, 206–219;
- 30 E. Cical; G. Burtica; M. Mecea; *Environment & Progress*, Eds. Cluj-Napoca, **2007**, 9, 113-118;
- 31 E. Cical; G. Oprea; C. Mihali; L. Ardelean; G. Burtică; L. Lupa L; *Rev Chim*, **2008**, 59 9, 1030-1036;
- 32 D.J. Pernitsky; J.K. Edzwald; *J. Wat. Sup.: Res. and Technol. – AQUA*, **2006**, 55, 2, 121-141;
- 33 D.C. Hopkins; J.J. Ducoste; *J Coll. Interf. Sci*, **2003**, 264, 1, 184–194;
- 34 COD parameter was determined in accordance with SR ISO 6060-96;
- 35 Suspended solids in accordance with STAS 6953-81;
- 36 Chlorides (Cl^- mg/L) was determined in accordance with STAS 8663-70;
- 37 Sulfates (SO_4 mg/L) in accordance with STAS 8601-70.

NEWLY DEVELOPED STATISTICALLY INTENSIVE QSAR MODELS FOR BIOLOGICAL ACTIVITY OF ISATIN DERIVATIVES

RABAH ALI KHALIL^{a*}, SHAYMA'A HASHIM ABDULRAHMAN^a

ABSTRACT. The present study introduces a new approach for the quantitative structure-activity relationship (QSAR) issue, which can be called a statistically intensive or condensed QSAR model. This idea was successfully applied to the published data of 32 biologically active molecules derived from 4-(1-aryl-2-oxo-1,2-dihydro-indol-3-ylideneamino)-N-substituted benzene sulfonamides for mixed bacteria and specific bacteria like *B.subtilis*, *E.coli*, and *S.aureus*. The suggested four statistically intensive QSAR (SIQSAR) models possess only two descriptors with excellent statistical parameters, as their values of the square regression coefficient (r^2) and cross-validation (q^2) are lying within the range of 0.967–0.997 and 0.961–0.996, respectively. A zero-one correction term (ZO) reflects the effect of substituents, which was proposed as a second descriptor for two sets of biologically active compounds. In general, the results showed that the biological activity is depended majorly on the topographical properties, and predominated by the field-effect in contrast to an electronic one. The interesting feature of SIQSAR models is their closeness to mathematical methods such as simultaneous linear equation method by eliminating the common inaccuracy and unrealistic statistical treatments. The obtained SIQSAR models were employed for predicting new and efficient biologically active molecules derived from isatin.

Keywords: QSAR, computational chemistry, isatin derivatives, biological activity, DFT

INTRODUCTION

Quantitative structure-activity relationship (QSAR) studies can be considered as a powerful tool for scientists, particularly for significant assistance in reducing trial and error [1–6]. Moreover, utilizing QSAR to assess the biological

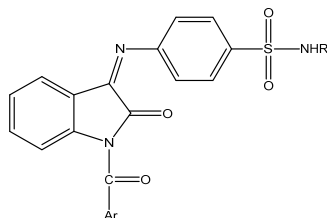
^a Department of Chemistry, College of Science, University of Mosul, Mosul, Iraq

* Corresponding author: rakhalil64@yahoo.com

activity, which is termed *in silico* might be considered as parallel to that of experimental *in vivo* and *in vitro*, giving considerable value to this method [2]. At the same time, the background of QSAR is statistical rather than an accurate mathematical method such as simultaneous linear equation method [7]; therefore, researchers who deal with statistical analysis for building up their requested models should consider it attentively. In other words, the statistical treatments always produce results regardless of the correctness and reliability of the provided or input data [8,9]. Furthermore, the outcome of statistical data may be meaningless or without physical meaning, as the statistical calculations are adjusted by researchers in order to give a good correlation coefficient and a lower standard deviation [8–16]. For this reason, the confidence of statistical results depends on the number of both descriptors and observations. Consequently, the decrease in the number of descriptors increases the reliability of the results, while, the decrease in the number of observations makes the results less reliable. Thus, selecting the right descriptors can be considered as a crucial for building up a suitable model.

In general, there are thousands of published articles related to biological activity, using QSAR [17–22]. Most of QSAR studies are dealing with antimicrobial and antifungal activity. No serious efforts have been found for adopting models with statistical significance by reducing the number of descriptors of the suggested model, including physical meaning. In other words, there is always gain combined with loss, as using a few descriptors leads to weak statistical parameters. For instance, the square of the correlation coefficient (r^2) or coefficient of determination cannot exceed 0.937 for two descriptors with 14 observations, and a low value of cross-validation (q^2) up to 0.889 has been found for the same model [23]. Furthermore, the developed model by the QSAR model for biological activity and drug design should be more accurate than that of toxicity.

In the present study, efforts have been made to obtain an intensive QSAR model from already published data for a set of 32 biologically active molecules derived from 4-(1-aryl-2-oxo-1,2-dihydro-indol-3-ylideneamino)-N-substituted benzene sulfonamides (Scheme 1) [24]. To the best of our knowledge, no QSAR models with high statistical and physical significance similar to the model presented here, have been found in the literature.



Scheme 1. The skeleton of isatin derivatives

RESULTS AND DISCUSSION

Table 1 exhibits the estimated properties of isatin derivatives, using HF and PM3 calculations. These descriptors, shown in Table 1, were selected with regard to the dependency between each other, and according to the correlation matrix that was built up for this purpose. The correlation matrix that is built up for filtered properties from the correlation issue is illustrated in Table 2. It is apparent from the data of this table that the properties belong to topography, have the best correlation or dependency with the biological activity of isatin derivatives. Therefore, the models were built up with respect to these parameters. Indeed, the aim of the present study was to solve the QSAR issue, by suggesting an intensive model that is nearly close to accurate mathematical methods with excellent regression parameters. Thus, the first descriptor was selected in accordance with the simple correlation between the biological activities and the adjusted parameters, as exhibited in Table 2. According to the values of correlation coefficient (r), a very good correlation has been observed for those belonging to the topographical properties such as molar refractivity (MR) and Balaban Index (J). However, an additional descriptor must be found in order to enhance the efficiency of the model by supporting physical and statistical significance. It should be noted that the presented training set contains 28 observations, which definitely need multiple descriptors for building up the required model. The aim of this study was to develop an intensive and reliable model that can be used with confidence. Therefore, a second descriptor was added to reinforce the model that already contains the first main topographical parameters, as shown in Table 2. For those of MICec and MICsa, the model of both consists of two descriptors, including cluster count (CCO) together with a molecular topological index (MTI), showing excellent statistical parameters, as demonstrated in Table 3. This phenomenon could indicate that both of these antimicrobial agents (MICec and MICsa) use the same antibacterial mechanism. While for other antimicrobial agents (MICab and MICbs), the first descriptor for both is the molar refractivity (MR), which also belongs to topography. The suggested second descriptor is called zero-one correction term (ZO) that is developed with respect to the chemical structure of the molecule of which depends merely on substituents. This new proposed descriptor boosts the model from a statistical point of view. Indeed, this adopted descriptor has a value of one or zero, which could support the physical impact of the model due to the blind issue of statistical treatments. The new descriptor, ZO depends on the chemical structure of the derivatives, through recognizing the structural effect, according to the residuals of predicted values from the simple regression with MR descriptor. Hence, a value equal to one will be taken only if there is a structural

effect in the substituent. In the presented model, only five observations with the structural effect were detected, where the correction term ZO was included, which takes the value of one in contrast to the value of zero as no correction for the rest of the derivatives. This indicates that only 15.6% of the molecules, including both sets of training and test, have two descriptors in the suggested model, in comparison to only one descriptor for others. However, the structural effect of the correction term includes the field-effect that produced from para chlorine of the aryl group, in addition to the presence of β,β -dinitrogen with respect to the imine group, as compounds 8, 9, 16, and 27, and also in the presence of acetyl groups, as compound 30. In other words, there is a notable field-effect that resulted from the presence of chlorine at the para position of the aryl group, as well as the presence of β,β -dinitrogen, and acetyl groups with regard to the imine group. Indeed, such a phenomenon supports the use of the correct statistical point in understanding the substituent effect on the biological activity of molecules. However, we cannot give a more in-depth explanation about the effects of substituents for the five compounds that required the correction factor.

Table 3 displays the obtained models for antibacterial activity as the MIC for the four types of antimicrobials. We know that the presence of a structural effect like ZO has a negative effect on antibacterial activity. Excellent statistical parameters for these models were found despite the very low number of descriptors that have been used for building up the current models. This clearly announces the achievement in developing the QSAR studies. The interesting values of cross-validation (q^2) as very close to unity, indicate the significant confidence of the developed models, which are very close to reality. It should be noted that the number of descriptors is less than that recommended by the Topliss-Costello rule, with values of r^2 and q^2 better than that recommended by this rule [1]. As mentioned above in the introductory section, the value of q^2 of previous studies cannot exceed 0.889, in contrast to the values of 0.979, 0.996, 0.965, and 0.961 for the current models, despite using lower descriptors and more observations [23]. Furthermore, the already published QSAR model for 28 observations of presented MICab contains one descriptor (molecular connectivity) with r^2 and q^2 equal to 0.702 and 0.639, respectively [24]. Such excellent values of QSAR statistical properties obtained in this study may be due to the considerable confidence that resulted from only two descriptor models of 28 observations. In general, the developed models suggest that field-effect plays a major role in the biological activity of the selected bacteria. This suggestion is raised from that the position of chlorine substituted at the benzene ring of the aryl group, giving a remarkable effect to the biological activity, and indicating the high efficiency of field-effect in contrast to an electronic one.

Table 1. The values of selected descriptors used in the regression analysis in addition to adopted zero-one correction term (all of these theoretical descriptors were estimated, using DFT method, except for those of ϵ_{HOMO} and ϵ_{LUMO} , which are calculated, using the PM3 method)

No.	CCO	MTI	MR	J	logP	PSA	ϵ_{HOMO}	ϵ_{LUMO}	zero-one
Training set									
1	35	29638	128.901	1816557	3.938	117.50	-0.35284	-0.04909	0
2	32	22508	116.888	1359822	2.762	112.98	-0.37258	-0.04478	0
3	36	32686	133.506	2083132	3.994	120.63	-0.37091	-0.04570	0
4	39	40047	142.160	3058009	4.469	139.09	-0.36196	-0.04659	0
5	37	35317	136.793	2414561	4.288	129.86	-0.34764	-0.04929	0
6	35	30276	130.153	1816973	4.092	108.27	-0.33533	-0.04799	0
7	36	31240	133.706	2080770	4.497	117.50	-0.36908	-0.05084	0
8	37	34402	138.311	2377200	4.552	120.63	-0.35199	-0.04802	1
9	40	41982	146.965	3455532	5.027	139.09	-0.35069	-0.05352	1
10	38	37102	141.598	2743970	4.847	129.86	-0.37963	-0.04950	0
11	36	30974	133.706	2054269	4.497	117.50	-0.36876	-0.05171	0
12	33	23616	121.693	1555851	3.321	112.98	-0.36556	-0.04888	0
13	36	31342	133.412	2054706	3.848	120.63	-0.37483	-0.05156	0
14	37	34124	138.311	2348338	4.552	120.63	-0.34627	-0.04443	0
15	35	28285	133.459	1784218	4.991	108.27	-0.34851	-0.04737	0
16	40	41682	146.965	3418784	5.027	139.09	-0.35319	-0.05184	1
17	38	36818	141.598	2712561	4.847	129.86	-0.37089	-0.05041	0
18	36	31644	134.958	2054706	4.65	108.27	-0.36676	-0.04836	0
19	34	26725	121.323	1585232	2.554	126.73	-0.37462	-0.05160	0
20	31	20085	109.310	1169971	1.378	122.21	-0.36489	-0.05191	0
21	34	27058	121.029	1585627	1.905	129.86	-0.36455	-0.05813	0
22	35	29579	125.929	1824777	2.609	129.86	-0.34498	-0.04451	0
23	33	24293	121.076	1366340	3.049	117.50	-0.36043	-0.04876	0
24	38	36464	134.583	2705554	3.084	148.32	-0.35137	-0.05120	0
25	36	32043	129.215	2124021	2.904	139.09	-0.37358	-0.05034	0
26	34	27329	122.575	1585627	2.708	117.50	-0.36543	-0.04631	0
27	36	31610	133.412	2081207	3.848	120.63	-0.37672	-0.05464	1
28	35	28541	133.459	1808479	4.991	108.27	-0.35835	-0.05049	0
Test set									
29	35	29989	128.607	1816973	3.289	120.63	-0.34537	-0.04565	0
30	33	23854	121.693	1579399	3.321	112.98	-0.36266	-0.05132	1
31	34	27032	128.654	1572317	4.433	108.27	-0.37091	-0.04791	0
32	36	31914	134.958	2081207	4.650	108.27	-0.26135	-0.12206	0

Table 2. The correlation matrix of biological activity of mixed antibacterial activity (MICab) specified bacteria like *B.subtilis* (MICbs), *E.coli* (MICec), and *S.aureus* (MICsa) with the selected descriptors

	MICab	MICbs	MICec	MICsa
ϵ_{HOMO}	0.168	0.152	0.152	0.150
ϵ_{LUMO}	-0.289	-0.319	-0.167	-0.146
logP	0.616	0.458	0.792	0.811
PSA	0.384	0.325	0.436	0.401
J	0.805	0.664	0.915	0.899
CCO	0.793	0.633	0.946	0.939
MTI	0.772	0.620	0.914	0.905
MR	0.794	0.623	0.964	0.967

Table 3. The suggested statistical intensive models for antimicrobial activity associated with statistical parameters

Eq. no	Model	r^2	q^2	S.E.
1	$MICab = 0.990 + 0.00318MR + 0.108 ZO$	0.985	0.979	0.007
2	$MICbs = 0.890 + 0.00318 MR + 0.308 ZO$	0.997	0.996	0.007
3	$MICec = 0.268 + 0.0508 CCO - 0.000015 MTI$	0.971	0.965	0.005
4	$MICsa = -0.034 + 0.0512 CCO - 0.000016 MTI$	0.967	0.961	0.006

Figures 1–4 show the linear relationship between estimated and observed antibacterial activity resulted from the application of the suggested models (Table 3) of both training and test sets for MICab, MICbs, MICec, and MICsa, respectively. The relationship of these figures exhibits excellent linearity as the coefficient of determination (r^2) is equal to 0.986, 0.997, 0.963, and 0.959 for MICab, MICbs, MICec, and MICsa, respectively. The residual standard error (SE) was calculated using the following equation:

$$SE = \sqrt{\frac{\sum(Y - Y_{est})^2}{n - 2}}$$

where Y is the observed MIC, Y_{est} is the estimated MIC and n is the number of observations. The values of SE for the training set of 28 observations are quite low, like 0.0073, 0.0073, 0.0053, and 0.0055 for MICab, MICbs, MICec, and MICsa, respectively. Indeed, these excellent values of SE demonstrate the success of the presented intensive models. In contrast, the values of SE get higher when the test set is included, as having values of 0.0211, 0.0075, 0.0781 and 0.0825 for MICab, MICbs, MICec, and MICsa, respectively, which is generally may be due to the issue of the correction term.

In general, the obtained results are quite significant from both prediction and statistical points, supporting the success of building up a SIQSAR model, as having only two descriptors with 32 observations of the presented types of antimicrobials.

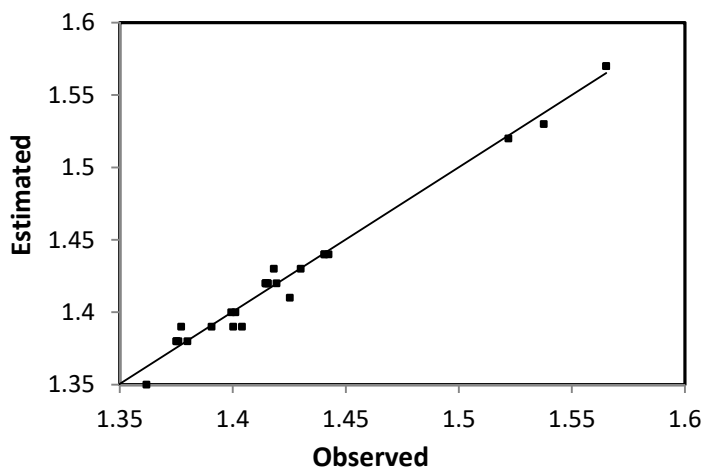


Figure 1. The plot of estimated MICab values versus observed MICab values according to the developed model 1, presented in Table 3.

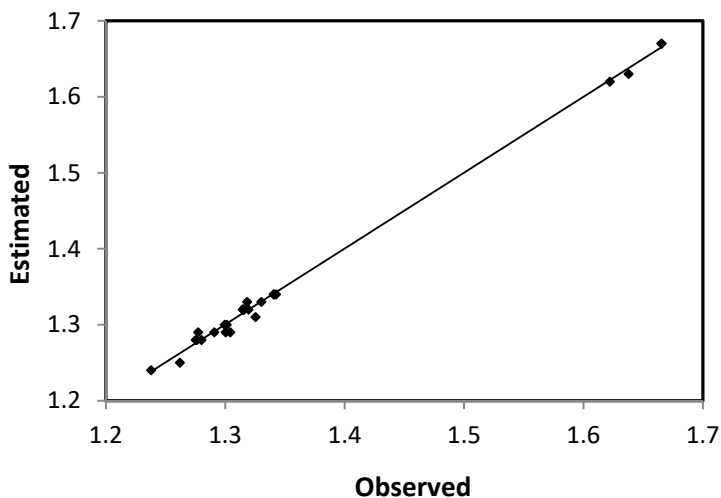


Figure 2. The plot of estimated MICbs values versus observed MICbs values according to the developed model 2, presented in Table 3.

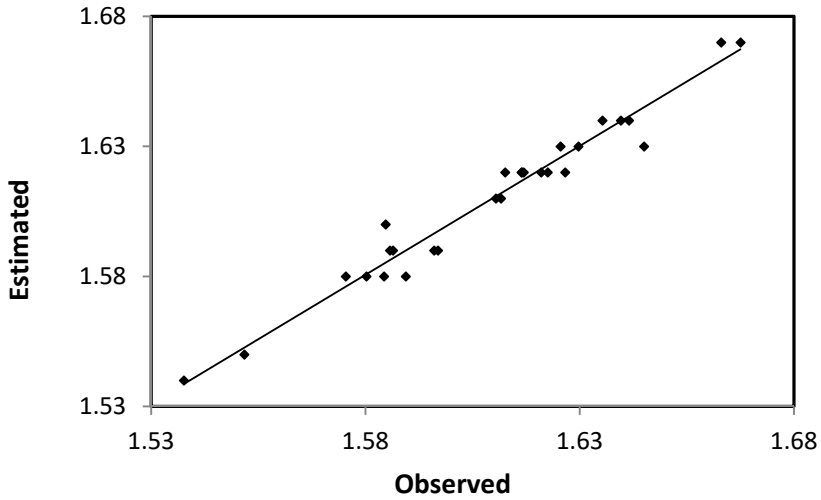


Figure 3. The plot of estimated MICec values versus observed MICec values according to the developed model 3, presented in Table 3.

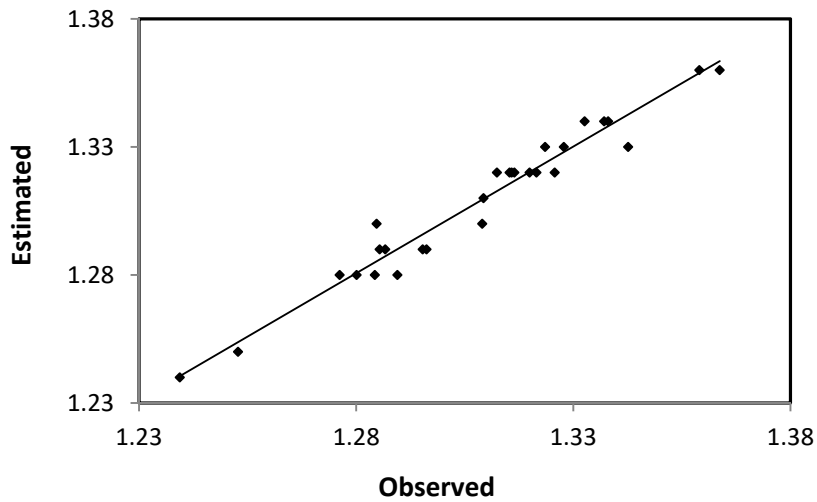
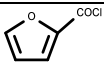
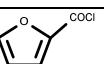
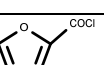
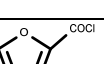
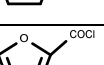


Figure 4. The plot of estimated MICsa values versus observed MICsa values according to the developed model 4, presented in Table 3.

The developed SIQSAR models were also used for predicting new biologically active compounds derived from isatin, as relatively having more efficient activity towards microbial agents. Such a study gives great advantages, particularly, in reducing the difficulty of trial and error. Table 4 shows the resulting predicted molecules in terms of the lowest MIC values together with their theoretically calculated properties. For MICec, no predicted molecule with the highest efficiency has been found, in contrast to that of compound number 29 (MICec = 1.29). For other types of antimicrobials, some new derivatives are suggested in Table 4. It should be noted that the selection of the predicted compounds is not limited to the smallest value of MIC, but considerations should also be given to the value of the partition coefficient of the compound between water and octanol (logP). The lower the value of logP is, the more favored is from a pharmaceutical point of view. For MICab, the minimum MIC value is equal to 1.29 (Table 5) with logP equal to 3.289, but the predicted molecule is close to this value with lower logP, such as compounds *a* and *c* (Table 4). While for MICbs, three predicted derivatives have MIC values equal to 1.211, 1.217, and 1.223, with comparable logP, in contrast to molecule number 20 with MIC value equal to 1.24. Also, for MICsa there are three predicted molecules, possessing MIC values equal to 1.162, 1.185, and 1.189 with lower logP, in comparison with molecule number 20, which has a MIC value equal to 1.24. Thus, it is apparent that the developed SIQSAR models can be considered as a powerful tool for the prediction of new efficient biologically active compounds.

Table 4. The predicted molecules with their calculated properties, acting as antimicrobials using the developed models, presented in Table 3.

	Aryl group	R group	MR	CCO	MTI	logP	MICab	MICbs	MICec	MICsa
a		H	100.929	28	14852	1.667	1.311	1.211	1.467	1.162
b		CH ₃	105.753	29	16619	1.506	1.326	1.226	1.491	1.185
c		OH	102.746	29	16153	1.468	1.317	1.217	1.499	1.192
d		NH ₂	104.803	29	16386	0.892	1.323	1.223	1.495	1.189
e		-COH	104.718	30	18084	1.264	1.323	1.223	1.521	1.213

CONCLUSIONS

It can be concluded that the present approach of SISQAR for developing QSAR can be considered as a powerful tool for multiple linear regression studies of activated compounds. This can be attributed to the increases in the number of descriptors that decrease the probability of obtaining reliable results. The interesting feature of SIQSAR models can be deduced from eliminating the common inaccuracy and unrealistic statistical treatments, but it is not an accurate method, in contrast to mathematics. The application of the current approach to four sets of biologically active molecules produces excellent statistical parameters, which have not already obtained even using models with more descriptors and fewer observations. The new suggested term of SIQSAR may be attributed to any developed QSAR model of at least 20 observations, and possess one or two descriptors with excellent statistical parameters. Furthermore, the statistical properties that could be obtained from SIQSAR models have more efficiency than that of the best models, according to the Topliss-Costello rule [1]. Finally, this development in solving the QSAR issue shows the potential use of QSAR for drug design and biological activity, which requires more accuracy, in comparison with other related issues such as toxicity and environmental protection.

EXPERIMENTAL SECTION

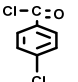
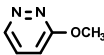
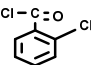
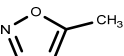
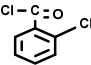
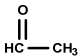
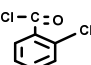
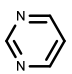
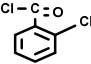
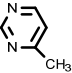
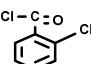
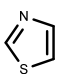
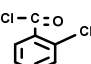
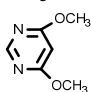
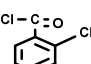
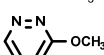
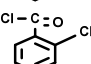
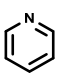
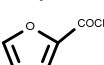
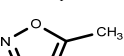
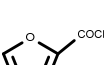
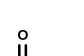
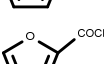
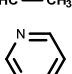
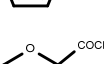
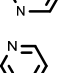
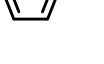
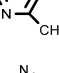
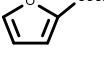
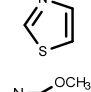
In the current investigation, the biological activity data showed the minimum inhibition concentration (MIC) for a set of thirty-two derivatives of isatin (Scheme 1), adopted from the study of Kumar *et al.* [24]. This set of molecules, as illustrated in Table 5, was subdivided into twenty-eight compounds as a training set, and the rest four were left as a test set. This included the biological activity for the mixed antibacterial activity (MICab) of which was performed against Gram-positive bacteria: *S. aureus*, *B. subtilis*, and the Gram-negative bacteria *E. coli* and some specified bacteria like *B. subtilis* (MICbs), *E. coli* (MICec), and *S. aureus* (MICsa).

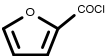
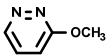
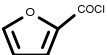
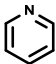
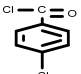
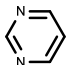
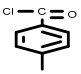
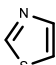
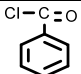
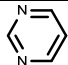
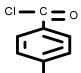
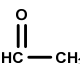
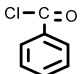
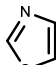
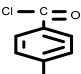
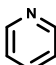
The chemical structures of istain derivatives and their models have been drawn, using two- dimensional Chemdraw ultra version 11.0. Each molecular structure has been transferred to undergo a systematic energy minimization, using Chem 3D-ChemBioOffice software version 16.0.0.82 (level: Ultra). In order to reach the global minima, the optimization was started from molecular mechanics calculations MM2, then MMFF94 methods were used to get a value of smaller than 0.1 kcal/mol of the root mean square (RMS) gradient [10,15]. The minimization process was continued, using

semi-empirical calculations, including Austin Model number 1 (AM1), followed by Parameterized Model number 3 (PM3) methods to reach a negative sign of heat of formation, and a positive sign of frequency. For density functional theory (DFT) calculations, the energy minimizations were continued, using DFT at B3LYP level with a 6-311G (d, p) basis set, until the minimum RMS gradient of 0.1 was reached [10]. The estimations of descriptors were carried out by Gaussian 03w software, using DFT, Hartree–Fock *ab initio* (HF), and PM3 methods (closed-shell MOs), depending on the type of selected descriptor. Statistical analysis for QSAR was performed, using Minitab software release 14.1.

Table 5. The structure of isatin derivatives with their antibacterial activity as minimum inhibitory concentration (MIC, I mol/mL), adopted from Kumar et al. [24].

No. of compound	Aryl Group	R. Groups	MICab	MICbs	MICec	MICsa
Training set						
1			1.39	1.29	1.59	1.29
2			1.35	1.25	1.55	1.25
3			1.40	1.30	1.60	1.30
4			1.44	1.34	1.64	1.34
5			1.41	1.31	1.61	1.31
6			1.39	1.29	1.59	1.29
7			1.42	1.32	1.62	1.32
8			1.53	1.63	1.63	1.33
9			1.57	1.67	1.67	1.36

No. of compound	Aryl Group	R. Groups	MICab	MICbs	MICec	MICsa
10			1.44	1.34	1.64	1.34
11			1.42	1.32	1.62	1.32
12			1.39	1.29	1.59	1.29
13			1.42	1.32	1.62	1.32
14			1.43	1.33	1.63	1.33
15			1.42	1.32	1.62	1.32
16			1.57	1.67	1.67	1.36
17			1.44	1.34	1.64	1.34
18			1.42	1.32	1.62	1.32
19			1.38	1.28	1.58	1.28
20			1.34	1.24	1.54	1.24
21			1.38	1.28	1.58	1.28
22			1.39	1.29	1.59	1.29
23			1.38	1.28	1.58	1.28
24			1.43	1.33	1.63	1.33

No. of compound	Aryl Group	R. Groups	MICab	MICbs	MICec	MICsa
25			1.40	1.30	1.61	1.30
26			1.38	1.28	1.58	1.28
27			1.52	1.62	1.62	1.32
28			1.42	1.32	1.62	1.32
Test set						
29			1.29	1.29	1.29	1.29
30			1.49	1.59	.59	1.29
31			1.39	1.29	1.59	1.29
32			1.42	1.32	1.32	1.62

ACKNOWLEDGMENTS

Thanks should go to the University of Mosul for supporting this research.

REFERENCES

1. J. Leszczynski, M.K. Shukla; *Practical Aspects of Computational Chemistry II: An Overview of the Last Two Decades and Current Trends*, Springer, Dordrecht, **2012**, pp. 1-361
2. E. Benfenati; *Theory guidance and applications on QSAR and REACH*, Istituto di Ricerche Farmacologiche "Mario Negri", Milan, Italy, **2012**, pp. 1-39
3. Y. Fukunishi, S. Yamasaki, I. Yasumatsu, K. Takeuchi, T. Kurosawa, H. Nakamura; *Mol. Inform.*, **2017**, 36 ,1-9

4. I. Hussain, K.K. Bania, N.K. Gour, R.C. Deka; *ChemSelect*, **2019**, 1, 4973-4978
5. Y. Cao, J. Romero, J.P. Olson, M. Degroote, P.D. Johnson, M. Kieferová, I.D. Kivlichan, T. Menke, B. Peropadre, N.P.D. Sawaya, S. Sim, L. Veis, A. Aspuru-Guzik; *Chem. Rev.*, **2019**, 119, 10856-10915
6. J.C.G. Martinez, E.G. Vega-Hissi, M.F. Andrada, M.R. Estrada; *Expert. Opin. Drug. Discov.*, **2014**, 10, 37-51
7. R.A. Khalil, A.A. Zarari; *Appl. Surf. Sci.*, **2014**, 318, 85-59
8. R.A. Khalil; *Colloid Surface A.*, **2006**, 286, 51-56
9. Y.A. Shahab, R.A. Khalil; *Spectrochim. Acta A.*, **2006**, 65, 265-270
10. R.A. Khalil, A.Y. Hamed; *Arab J. Phys. Chem.*, **2015**, 2, 56-63
11. R. Pingaew, P. Mandi, V. Prachayasittikul, S. Prachayasittikul, S. Ruchirawat, V. Prachayasittikul; *Eur. J. Med. Chem.*, **2018**, 143, 1604-1615
12. R.A. Khalil, A.A. Zarari; *J. Turk. Chem. Soc. A. (JOTCSA)*, **2015**, 2, 42-52
13. M.B. Larsson, M.M. Kumar, M. Tysklind, A. Linusson, P.L. Andersson; *SAR QSAR Environ. Res.*, **2013**, 24, 416-479
14. J. Liu, F. Li, Y. Wang, H. Zhang, J. Dong, P. Sun, Y. Li, Z. Li; *Chinese Chem. Lett.*, **2019**, 30, 668-671
15. R.A. Khalil; *A Simple Approach to Quantum Chemistry*. Nova Science Publoshers, Inc., New York, **2020**, pp. 119-127
16. S. Mor, P. Pahal, B. Narasimhan; *Eur J. Med. Chem.*, **2016**, 53, 176-189
17. D.F. Kawano, C.A. Taft, C.H.T.P. da Silva; *Curr. Phys. Chem.*, **2016**, 6, 105-114
18. O.M. Antypenko, S.I. Kovalenko, O.V. Karpenko, V.O. Nikitin, L.M. Antypenko; *Helv. Chim. Acta.*, **2016**, 99, 621-631
19. M. Majewsky, D. Wagner, M. Delay, S. Bräse, V. Yargeau, H. Horn; *Chem. Res. Toxicol.*; **2014**, 101, 1821-1828
20. J.T. Ristovski, N. Janković, V. Borčić, S. Jain, Z. Bugarčić, M. Mikov; *J. Pharmaceut. Biomed.*, **2018**, 155, 42-49
21. P. Kumar, B. Narasimhan, K. Ramasamy, V. Mani, R.K. Mishra, A. Abdul Majeed; *Curr. Top. Med. Chem.*, **2015**, 15, 1050-1064
22. M. Ghamali, S. Chtita, A. Aouidate, A. Ghaleb, M. Bouachrine, T. Lakhliifi; *J. Taibah. Univ. Sci.*, **2017**, 11, 422-433
23. D. Verma, P. Kumar, B. Narasimhan, K. Ramasamy, V. Mani, R.K. Mishra, A. Abdul Majeed; *Arab. J. Chem.*, **2019**, 12, 2882-2896
24. M. Kumar, K. Ramasamy, V. Mani, R.K. Mishra, A. Abdul Majeed, E. De Clercq, B. Narasimhan; *Arab. J. Chem.*, **2014**, 7, 396-408

ANTIOXIDANT RESPONSE OF TOMATO TO LATE BLIGHT (*PHYTOPHTHORA INFESTANS*) INFECTION DEPENDING ON SYMPTOMS INTENSITY

SLAĐANA MEDIĆ PAP^a, DARIO DANOJEVIĆ^a,
SVETLANA GLOGOVAC^a, MARIJANA PEIĆ TUKULJAC^b,
DALIBOR ŽIVANOV^a, DEJAN PRVULOVIĆ^{b*}

ABSTRACT. Late blight (LB) caused by the *Phytophthora infestans* is a devastating tomato disease, distributed worldwide. Tomato wild species could be a potential source of resistance, however, there are little data about their biochemical response to LB infection. Therefore the aim of the study was to evaluate total phenolic and total flavonoid content and antioxidative activity in the leaves of wild (*Solanum pimpinellifolium*) and cultivated genotype (Bizon) depending on disease severity. *S. pimpinellifolium* compared to Bizon was less susceptible and had five times lower disease severity index (11% and 55% respectively). Additionally, during the disease progression wild genotype showed a much slower decrease of total biochemical parameters compared to the cultivated one. Parameters such as total phenolic content (TP), DPPH (2,2-diphenyl-1-picrylhydrazyl) radical scavenging test and ABTS (2,2'-azinobis-(3-ethylbenzothiazoline-6-sulfonic acid)) radical scavenging activity in the symptomless leaves and the leaves infection 10-25% remained the same in *S. pimpinellifolium*. The susceptible genotype Bizon had about 40% of leaves with the disease severity 25-50%, and a rapid decrease of all biochemical parameters. A strong negative correlation was observed between late blight infection and biochemical parameters in Bizon, while in *S. pimpinellifolium* late blight infection negatively correlated only with TP, TF (total flavonoid content) and total antioxidant activity (TAA).

Keywords: biochemical response, late blight, *S. pimpinellifolium*

INTRODUCTION

Late blight (LB), caused by cosmopolitan pathogen *Phytophthora infestans*, is a destructive disease of tomato (*Solanum lycopersicum*) causing

^a Institute of Field and Vegetable Crops, National Institute of the Republic of Serbia, Maksima Gorkog 30, Novi Sad, Serbia

^b University of Novi Sad, Faculty of Agriculture, Trg Dositeja Obradovića 8, Novi Sad, Serbia

* Corresponding author: dejanp@polj.uns.ac.rs

severe losses. The yield losses due to tomato late blight can be significant, despite the progress in weather-based software for the disease forecast and the availability of chemical control agents [1]. Changes in *P. infestans* pathogenicity, the introduction of new pathogen isolates, and increased resistance of the pathogen to fungicides, made late blight control highly demanding [2]. All these concerns have made the selection and use of late blight-resistant tomato cultivars a more attractive approach [3]. Since this disease poses problems, especially to organic tomato growers, wide hybridization is considered as a method for introduction of late blight resistance from wild relatives into cultivated tomato [4].

The *Solanum* section *Lycopersicon* is an economically important group of organisms and consists of 14 species including the cultivated tomato *Solanum lycopersicum* and its closest wild relative *Solanum pimpinellifolium*-currant tomato [5,6]. Although *S. pimpinellifolium* is native to Ecuador and Peru [7], it has spread worldwide and due to small red sweet fruits commonly grown as heirloom tomato. Additionally, the tomato wild species bear a wealth of genetic variability for many agriculturally and biologically important characteristics. *S. pimpinellifolium* is regarded as an important source of genes that can confer favourable stress tolerance to cultivated tomato. *S. pimpinellifolium* offers a wealth of breeding potential for desirable traits such as tolerance to abiotic [4] and biotic stresses [8,9], horticultural traits [10] and fruit quality traits [11,12]. Furthermore, possibility of transfer of late-blight resistance from *S. pimpinellifolium* to the cultivated tomato via a traditional backcross breeding approach [13] and its high cross compatibility with the cultivated tomato makes this species very desirable for breeding purposes [14].

As stated by some authors [15,16], among numerous defense mechanisms involved in late-blight resistance, alteration of metabolic pathways may be one of the most important disease defense responses [17]. Plants and pathogens are developing a complex relationship during microbial colonization stages generally involving the activation of host immune responses and the intention of the pathogen to manipulate plant cell processes [18]. Additionally, pathogen infection leads to various stress responses, depending on the plant - pathogen combination, the most common is the production of ROS (reactive oxygen species) [19]. Changes in antioxidant status and accumulation of some antioxidant metabolites indicate a plant response against pathogen invasion [20], although the rapid accumulation of plant ROS at the pathogen attack site, a phenomenon called oxidative burst, is toxic to plant directly [21]. Aside from the enzymatic antioxidants such as superoxide dismutase, peroxidase and catalase, low mass compounds such as glutathione, ascorbic acid, α -tocopherol, carotenoids, and phenolic compounds are involved in the ROS-scavenging [22,23]. Recent findings revealed that some highly toxic ROS components, such as singlet oxygen and hydroxyl radicals, can be scavenged only by nonenzymatic antioxidants ROS [24].

ANTIOXIDANT RESPONSE OF TOMATO TO LATE BLIGHT (*PHYTOPHTHORA INFESTANS*)
INFECTION DEPENDING ON SYMPTOMS INTENSITY

The expression of phenolic compounds is promoted by biotic and abiotic stresses (e.g., herbivores, pathogens, unfavourable temperature and pH, saline and heavy metal stress, and UV radiation) [25]. Phenolic compounds as a secondary metabolites can participate directly in plant defence as regulatory signals of the response to pathogen attack through their direct toxic effects on the pathogen, as a component in lignin formation and cell wall strengthening, and reductant of cell-wall ROS [26]. Specific phenolic compounds in different plant-pathogen interactions could also be possibly integrated with an automatic plant stress resistance screening programs [27]. Flavonoids, a group of phenolic compounds, have antimicrobial properties based on their abilities to act as antioxidants, inhibit certain enzymes, disrupt cell membranes, prevent viral binding and penetration into cells, and trigger a host cell self-defence mechanisms [28]. Antioxidative activity of plant extract is the capability of the plant to scavenge free radicals to avoid their harmful effect [29]. Therefore the aim of this study was to evaluate the reaction of wild and cultivated tomato genotypes to late blight (caused by invading *P. infestans*) infection through the development of the disease symptoms on the leaves as well as through the phenolic and flavonoid content and antioxidative activity.

RESULTS AND DISCUSSION

Evaluation of the late blight infection on tomato leaves indicated over 60% of *S. pimpinellifolium* leaves were without symptoms. In addition to 60% symptomless leaves, there were 23.3% of leaves with infection rate up to 5%. On the contrary, Bizon had almost 40% of leaves with infection rate 25-50% and nearly five times higher disease severity index (DSI) (Table 1). Bonferroni test showed a significant difference between the susceptibility of these genotypes.

Table 1. Incidence of late blight infection on leaves of two tested genotypes

Genotype		S.pimpinellifolium		Bizon	
leaf disease rate	leaf area infected	leaves per category			
	(%)	(no)	(%)	(no)	(%)
0	0	19	63.33	2	6.67
1	< 5	7	23.33	4	13.3
2	5-10	2	6.67	7	23.33
3	10-25	2	6.67	6	20
4	25-50	0	0	11	36.67
DSI (%)		11.3		53.3**	

** – significant at 1% level

The linkage between the level of infection and antioxidant activity is shown in the Table 2. Genotype (G), late blight infection (LB) and the interaction of these two factors had a strong influence on biochemical parameters in the leaves (Table 2).

Table 2. F values for biochemical parameters in tomato leaves

	d.f	TP	TF	DPPH	ABTS	FRAP	NBT test	TRC	TAA
(G)	1	526.13**	460.75**	31.13**	94.13**	1764.4**	126.55**	298.09**	32.30**
(LB)	3	225.74**	862.61**	40.67**	41.39**	790.2**	84.80**	68.45**	96.83**
G × LB	3	85.58**	161.87**	24.07**	23.59**	516.2**	250.08**	95.02**	2.81 ns

d.f. – degree of freedom, ** – significant at 1% level; n = 3 QE – quercetin; DW - dry weight;

Furthermore, detailed analysis of TP, TF and antioxidant activity tests provide an insight into the physiological response and revealed differences of both tested genotypes reaction to late blight infection. Changes in biochemical parameters depending on the leaf area covered by late blight is shown in Figure 1. Two tomato cultivars with different levels of resistance to late blight express differences in the biochemical response to the disease.

Generally, initial symptoms of late blight are followed by the increase of antioxidant activity measured by DPPH, ABTS, FRAP, TRC and TAA test in susceptible genotype (Bizon). However, when the leaf area was covered by late blight symptoms more than 5%, all the observed parameters, excluding TRC, decreased rapidly in this genotype, for example flavonoids declined several times. Along with the disease progress, when the symptoms have affected more than 10% of leaf surface, biochemical parameters remained on the same level, except the ABTS which decrease more. Conversely, in *S. pimpinellifolium*, in the case of leaf infection up to 5%, only an increase of TP and DPPH values was obtained, while there was no significant difference in other parameters compared to symptomless leaves. Furthermore, with disease progression, 5-10% of leaf area covered, six out of eight biochemical parameters (TP, DPPH, ABTS, FRAP, NBT and TAA) in *S. pimpinellifolium* were on the level of values measured in leaves without visible symptoms. When the late blight symptoms reached 10-25% of leaves area FRAP, NBT and TRC had the highest values (even higher than in symptomless leaves) in *S. pimpinellifolium*. On the contrary, in genotype Bizon in the same disease rank, FRAP and NBT obtained the lowest values, while TRC remained at the same level as a symptomless leaves.

Various methods have been published about the determination of antioxidant activity in different biological systems. Antioxidant activity of selected natural assays as a complex process, must be measured by more than one mode of action [30].

Phenolic compounds belong to the primary defence line in the host-pathogen reaction of tomato and *P. infestans* by inhibiting pathogen penetration [31]. This indicates that at the beginning of the infection plants defend themselves by increasing the antioxidative activity measured by selected assays. Moreover, in our research during the disease development the content of TP and TF in the leaves of tolerant genotype *S. pimpinellifolium* remained at higher concentration values than in Bizon (Figure 1A and B). The similar findings were obtained by Komy et al. [32] who found a significant increase in phenolic compounds in potatoes after infection by *Phytophthora infestans*, with phenolic concentration significantly higher in the resistant plants. These results are in agreement with the earlier reports of Henriquez et al. [33], who suggested the relationship between the accumulation of flavonoids and terpenoids and the late blight level. Also the accumulation of total phenolics correlated with increased potato defence responses to *A. solani* [34]. On the other hand, the high content of TP and TF in tomato leaves is genotype dependent and does not mean the resistance to late blight automatically [35,36].

The delicate balance between ROS generation and ROS scavenging is disturbed by the different types of stress factors among them pathogens infection [37]. The flexible antioxidant system is able to control the optimum ROS levels [38]. In our study, the majority of the antioxidative activity parameters in *S. pimpinellifolium* maintained higher stability than in Bizon, which could influence the disease development. On the contrary, the disease progress (Scheme 1) was much slower in wild genotype. This is in accordance with the results obtained by Liljeroth et al. [39], once the late blight infection had been established, the lesions expanded more rapidly in susceptible than in partially resistant cultivar.

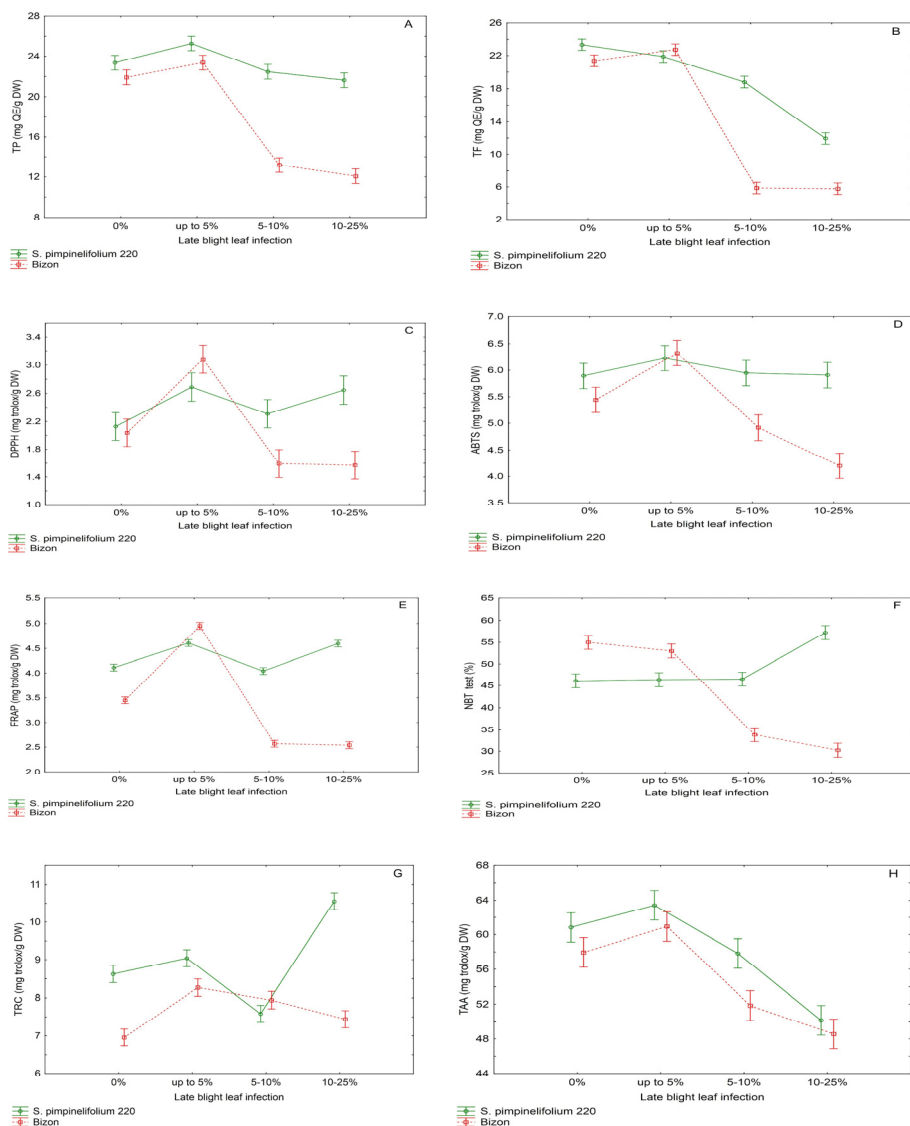
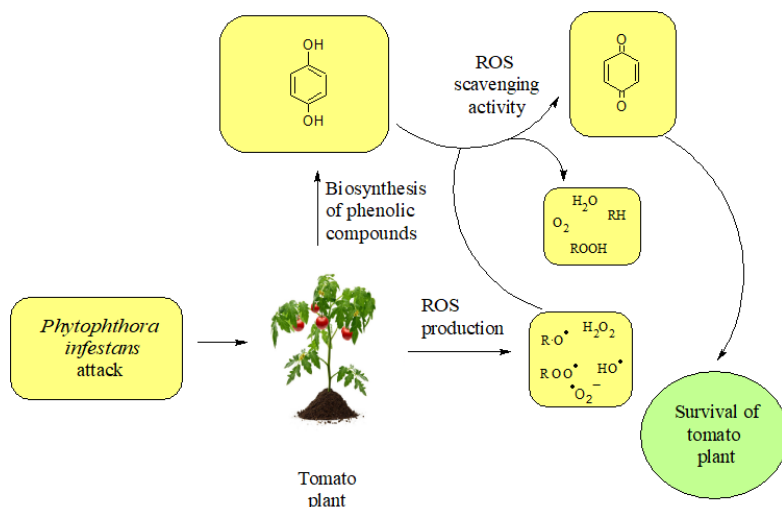


Figure 1. A) Total polyphenol content (TP) in tomato leaves B) Total flavonoid content (TF) in tomato leaves; Antioxidant activity in tomato leaves measured by C) Radical Cation Scavenging Activity (DPPH test); D) Radical Cation Scavenging Activity (ABTS), E) Ferric-reducing antioxidant power (FRAP); F) Nitroblue tetrazolium test (NBT test); G) Total Reduction Capacity (TRC); H) Total Antioxidant Activity (TAA) Means of three independent experiments with three replications; Bars represent standard errors.

ANTIOXIDANT RESPONSE OF TOMATO TO LATE BLIGHT (*PHYTOPHTHORA INFESTANS*)
INFECTION DEPENDING ON SYMPTOMS INTENSITY



Scheme 1. Defence mechanism of tomato plant against *P. infestans* attack

Correlation coefficients revealed that almost all parameters (excluded TRC) in Bizon were significantly influenced by leaf infection (Table 3). This negative correlation is in accordance with the strong decrease of these parameters during the disease development, especially comparing the leaves with up to 5% and 5-10%. Despite the fact that TP content in tolerant genotype *S. pimpinellifolium*, increased with the initial symptoms and then remained on the level in symptomless leaves, negative correlation between TP and the leaf disease incidence was achieved. Additionally, strong positive correlation of TP and TAA in both genotypes was obtained. These results are in the accordance with Cai et al. [40] who stated that the higher total phenolic content of the plant resulted in higher total antioxidant capacity.

Surely, that TP and TF have some role in the scavenging of the free radicals and increasing TAA in the initial stage of infection, but such results, indicated that some other non-enzymatic factors are also involved in the tomato defence against late blight. This statement could be confirmed by the fact that there was no significant correlation between TP and certain antioxidative tests (DPPH, FRAP and TRC) in tolerant genotype.

Table 3. Correlation coefficients in tomato leaves

Variable	G	TP	TF	DPPH	ABTS	FRAP	NBT	TRC	TAA
leaf infection	<i>S.p.</i>	-0.60*	-0.93**	0.43 ns	-0.19 ns	0.26 ns	0,67*	0,39 ns	-0.77**
	<i>Bizon</i>	-0,88**	-0,83**	-0,84**	-0,88**	-0,86**	-0,99**	-0,39 ns	-0,89**
TP	<i>S.p.</i>		0,54 ns	0,28 ns	0,77**	0,28 ns	-0,58*	-0,15 ns	0,79**
	<i>Bizon</i>		0,94**	0,94**	0,98**	0,97**	0,88**	0,67**	0,95**
TF	<i>S.p.</i>				-0,36 ns	0,15	-0,30 ns	-0,68*	-0,30 ns
	<i>Bizon</i>				0,95**	0,92**	0,96**	0,80**	0,62*

** – significant at 1% level; * – significant at 5% level; ns non-significant

CONCLUSIONS

S. pimpinellifolium showed less susceptibility to the late blight infection compared to Bizon. Genotype (G), late blight infection (LB) and their interaction had a strong influence on biochemical parameters in the leaves. During the progression of late blight symptoms TP, TF and antioxidant activity measured by several assays (except TAA) in susceptible genotype Bizon, decreased rapidly. On the other side in wild genotype that decline was much lower. The results obtained in this experiment indicated that, beside TP and TF, some other secondary metabolites with antioxidant capacity are also involved in the tomato defence system against late blight infection.

EXPERIMENTAL SECTION

The field trial was conducted in 2014 at the experimental field of the Institute of Field and Vegetable Crops (IFVCNS) at Rimski Šančevi, Serbia. Two genotypes from the IFVCNS collection were included in the trial. Bizon a susceptible one, the accession originated from Bulgaria, is an early heirloom variety with determinate growth type and *S. pimpinellifolium* accession as a tolerant one. According to our previous research [41] these two genotypes showed significant difference in susceptibility to late blight.

Sowing for seedlings production in a glass house was done on 3rd of April and the plants were transplanted on 27th of May into the open field. The trial was set up in completely randomized block design with three replications

and ten plants in each. The between-row spacing was 140 cm, and within-row spacing was 50 cm. There was no fungicide application and *Phytophthora infestans* natural infection was evaluated.

The evaluation of the early blight symptoms on leaves was performed on 4th of August. Ten fully developed leaves per replication were taken from the top of each plant and assessed to the intensity of the late blight infection. Evaluation of the disease intensity on leaves was done according to the EPPO modified scale: 0 - without infection, 1 - less than 5% of leaf affected, 2 - spots covering 5-10%, 3 - spots covering 10-25%, 4 - spots covering 25-50%, 5 - spots covering more than 50% of the leaf.

The severity of the late blight in each leaf was determined using the disease severity index (DSI), calculated according to [42].

$$DSI (\%) = \frac{\sum (n \times v) \times 100}{N \times V}$$

(n = number of leaves per each category; v= value of each category; N= total number of observations; V= maximum value of the category)

Immediately after disease evaluation, leaves were frozen at -80°C for further biochemical analysis.

Weather conditions were mostly changeable with temperature fluctuations and higher amounts of precipitation in all months except June. The plants were transplanted in the end of May due to heavy rains. In July, August and September the raining was almost daily with occasional heavy rains which was favourable for the late blight development.

Analysis of biochemical parameters were performed after the disease assessment in the Laboratory for Biochemistry, Faculty of Agriculture, Novi Sad, Serbia during 2015. Analysis were done per each genotype and per each category of disease intensity in three replications. Plant material (200 mg) was extracted with 70% aqueous acetone solution (50 mL) by sonication for 20 minutes in an ultrasonic bath at ambient temperature. The extracts were rapidly vacuum-filtered through a sintered glass funnel and kept refrigerated until assayed.

The total phenolic (TP) content was determined in the acetone extracts using a Folin-Ciocalteu colorimetric method [43]. Plant extracts (200 µL) were mixed with 100 µL of saturated sodium carbonate solution and 3 mL of Folin-Ciocalteu reagent diluted with distilled water. The absorbance of the reaction mixture was measured after incubation at ambient temperature for 30 min at

720 nm. Quercetin was used as a standard (covering the concentration range between 0.1 and 1.0 mg/mL). The results were expressed in milligrams of quercetin equivalents per 1 g of leaf dry weight (mg QE/g DW).

The total flavonoid (TP) content was determined spectrophotometrically [44]. Briefly, 0.5 mL of leaf extracts was mixed with 3 mL of 2% AlCl_3 solution. Absorptions were measured spectrophotometrically at 415 nm after 1 h. The amount of flavonoids was calculated as a quercetin equivalent (QE) from the calibration curve of quercetin standard solutions.

Measurement of antioxidative activity. Scavenging of free radicals was tested in a DPPH (2,2-diphenyl-1-picrylhydrazyl) acetone solution [45]. The scavenging efficiency of the substance added is indicated by the degree of discoloration of the solution. Ferric-reducing antioxidant power (FRAP) assay was carried out according to the procedure described by [46]. The results were expressed as mg Trolox equivalents per gram of leaf dry weight (mg TE/g). The ABTS (2,2'-azinobis-(3-ethylbenzothiazoline-6-sulfonic acid)) assay was based on a method developed by [47]. A methanolic solution of known Trolox concentrations was used for calibration and the results were expressed as mg Trolox equivalents per g of dry leaf weight (mg TE/g). The total antioxidant activity (TAA) of leaf extracts was evaluated by phosphomolybdenum method as reported by [48]. The standard curve for total antioxidant activity was plotted using Trolox solution. A reducing power assay (total reduction capacity-TRC) was performed by the method of [44]. Trolox was used as a standard. The superoxide free radical scavenging activity was carried out by NBT (nitroblue tetrazolium) test [48]. The per cent inhibition of superoxide anion generated was calculated using the formula: scavenging activity (%) = $(1 - \text{absorbance of sample} / \text{absorbance of control}) \times 100$.

Statistical analysis. Obtained data were analysed using software *STATISTICA*, ver. 13.2 (Dell, Inc., USA). Values for DSI and biochemical parameters were tested by analysis of variance followed by a comparison of means by Bonferroni test ($p < 0.01$). Correlation coefficients were calculated according to Spearman.

ACKNOWLEDGMENTS

This research was supported by the Ministry of Education, Science and Technological Development of the Republic of Serbia, grants number: 451-03-68/2022-14/ 200032 and 451-03-68/2022-14/ 200117

REFERENCES

1. M. Kim; M. Mutschler; *J. Am. Soc. Hortic. Sci.*, **2006**, *131*, 637–645.
2. U. Gisi; F. Walder; Z. Resheat-Eini; D. Edel; H. Sierotzki; *J. Phytopathology.*, **2011**, *159*, 223–232.
3. M. Foolad; H. Merk; H. Ashrafi; *Crit. Rev. Plant Sci.*, **2008**, *27*, 75–107.
4. C. Zhang; L. Liu; X. Wang; J. Vossen; G. Li; T. Li; Z. Zheng; J. Gao; Y. Guo; R. G. Visser; J. Li; Y. Bai; Y. Du; *Theor. Appl. Genet.*, **2014**, *127*, 1353–1364.
5. S. Aflitos; E. Schijlen; H. De Jong; D. De Ridder; S. Smit; et al.; *Plant J.*, **2014**, *80*, 136–148.
6. R. Razali; S. Bougouffa; M. Morton; D. Lightfoot; I. Alam, M. Essack, S. Arold; A. Kamau; S. Schmöckel; Y. Pailles; M. Shahid; C. Michell; S. Al-Babili; Y. Ho; M. Tester; V. Bajic; S. Negrão; *Front. Plant Sci.*, **2018**, *9*, 1402. <https://doi.org/10.3389/fpls.2018.01402>
7. I.E. Peralta; D.M. Spooner; S. Knapp; *Taxonomy of wild tomatoes and their relatives (Solanum sect. Lycopersicoides, sect. Juglandifolia, sect. Lycopersicon; Solanaceae)*, *Systematic Botany Monographs*, Amer. Society of Plant Taxonomists, Michigan, USA, **2008**, pp. 1–186.
8. P. Thapa; M. Miyao; M. Davis; G. Coaker; *Theor. Appl. Genet.*, **2015**, *128*, 681–692.
9. J. Ni; S. Bai; L. Gao; M. Qian; L. Zhong; Y. Teng; *PLoS One*, **2017**, *12*, e0171523. <https://doi.org/10.1371/journal.pone.0171523>
10. L. Azzi; C. Deluche; F. Gévaudant; N. Frangne; F. Delmas; M. Hernould et al.; *J. Exp. Bot.*, **2015**, *66*, 1075–1086.
11. M.P. Kinkade; M.R. Foolad; *Theor. Appl. Genet.*, **2013**, *126*, 2163–2175.
12. Capel, C.; F.J. Yuste-Lisbona; G. Lopez-Casado; T. Angosto; J. Cuartero; R. Lozano; J. Capel; *Theor. Appl. Genet.*, **2017**, *130*, 213–222.
13. T. Sullenberger; M. Jia; S. Gao; M. Foolad; *Plant Breed.*, **2018**, *137*, 89–96.
14. M. Foolad; M. Sullenberger; E. Ohlson; B. Gugino; *Plant Breed.*, **2014**, *133*, 401–411.
15. P. Bhaskar; J. Raasch; L. Kramer; P. Neumann; S. Wielgus; S. Austin-Phillips; J. Jiang; *BMC Plant Biol.*, **2008**, *8*, 8.
16. Y. Chen; D. Halterman; *Phytopathology* **2011**, *101*, 263–270.
17. M. Nowicki; E. Kozik; M. Foolad; Late blight of tomato. In *Translational genomics for crop breeding*, R. Varshney; R. Tuberosa Eds.; John Wiley & Sons, New York, SAD, Chapter 13, **2013**, pp. 241–265.
18. H. Rovenich; J. Boshoven; B. Thomma; *Curr. Opin. Plant Biol.*, **2014**, *20*, 96–103.
19. C. Liu; X., Williams; J. Nemacheck; H. Wang; S. Subramanyam; C. Zheng; M. Chen; *Plant Physiol.*, **2010**, *152*, 985–999.
20. D. Radwan; K. Fayez; S. Mahmoud; L. Guoquan; *Acta Physiol. Plant*, **2010**, *32*, 891–904.
21. C. Lamb; R.A. Dixon; *Annu. Rev. Plant Physiol. Plant Mol. Biol.*, **1997**, *48*, 251–275.

22. P. Ahmad; C.A. Jaleel; M.A. Salem; G. Nabi; S. Sharma; *Crit. Rev. Biotechnol.*, **2010**, 30, 161-175.
23. A. Waśkiewicz; M. Beszterda; P. Goliński; Nonenzymatic Antioxidants In Plants in *Oxidative Damage to Plants*, 1st ed.; A. Parvaiz Eds.; Academic Press, University of Kashmir, Kashmir, India, **2014**, Chapter 7, pp. 201-234.
24. J. Bose; A. Rodrigo-Moreno; S. Shabala; *J. Exp. Bot.*, **2014**, 65, 1241-1257.
25. N. Santos-Sánchez; R. Salas-Coronado; B. Hernández-Carlos; C. Villanueva-Cañongo, Shikimic Acid Pathway in Biosynthesis of Phenolic Compounds in *Plant Physiological Aspects of Phenolic Compounds*; Soto-Hernández M. Eds.; IntechOpen, London, UK, **2019**, DOI: 10.5772/intechopen.83815
26. J. Obrien; A. Daudi; V. Butt; P. Bolwell; *Planta*, **2012**, 236, 765-779.
27. L. Chaerle; D. Hagenbeek; E. De Bruyne; D. Van der Straeten; *Plant Cell Tissue Organ Cult.*, **2007**, 91, 97-106.
28. M. Friedman; *Mol. Nutr. Food. Res.*, **2007**, 51, 116-134.
29. J. Mierziak; K. Kostyn; A. Kulma; *Molecules*, **2014**, 19, 16240-16265.
30. E. Shalaby; S. Shanab; *Afr. J. Pharmacy Pharmacol.* **2013**, 7, 528-539.
31. M. Nowicki; M. Foolad; M. Nowakowska; E. Kozik; *Plant Dis.*, **2012**, 96, 4-17.
32. M.H. Komy; A.A. Saleh; Y.E. Ibrahim; Y.Y. Molan; *Trop. Plant Pathol.*, **2020**, 45, 44-55.
33. M. Henriquez; L. Adam; F. Daayf; *Plant Physiol. Biochem.*, **2012**, 57, 8-14.
34. H. Shahbazi; H. Aminian; N. Sahebani; D. Halterman; *Phytopathology* **2010**, 100, 454-459.
35. S.R. Bhandari; M.C. Cho; J.G. Lee; *Hortic. Environ. Biotechnol.*, **2016**, 57, 440-452.
36. S. MediĆ-Pap; D. Danojević; D. Prvulović; S. Tančić-Živanov; J. Červenski; *J. Serbian Chem. Soc.*, **2020**, 85, 623-635.
37. K. Das; A. Roychoudhury; *Frontiers in Environmental Science* **2014**, <https://doi.org/10.3389/fenvs.2014.00053>.
38. E. Vranova; D. Inze; F. Van Breusegem; *J. Exp. Bot.*, **2002**, 53, 1227-1236.
39. E. Liljeroth; T. Bengtsson; L. Wiik; E. Andreasson; *Eur. J. Plant Pathol.*, **2010**, 127, 171-183.
40. Y. Cai; Q. Luo; M. Sun; H. Corke; *Life Sci.*, **2004**, 74, 2157-2184.
41. S. MediĆ Pap; D. Danojević; A. Takač; S. Maširević; J. Červenski; V. Popović; *Field Veg. Crop Res.*, **2017**, 54, 87-92.
42. K.S. Chiang; H.I. Liu; C.H. Bock; *Ann. Appl. Biol.*, **2017**, 171, 139-154.
43. V. Nagavani, T. Raghava Rao; *Adv. Biol. Res.*, **2010**, 4, 159-168.
44. A. Saha; R. Rahman; M. Shahriar; S. Saha; N. Al Azad; S. Das; *J. Pharmacogn. Phytochem*, **2013**, 2, 181-188.
45. H.Y. Lai; Y.Y. Lim; *Int. J. Environ. Sustain.*, **2011**, 2, 442-447.
46. P. Valentao; E. Fernandes; F. Carvalho; P. Andrade; R. Seabra; M. Bastos; *J. Agric. Food Chem.*, **2002**, 50, 4989-4993.
47. N. Miller; M. Rice-Evans; M. Davies; V. Gopinathan; A. Milner; *Clin. Sci.*, **1993**, 84, 407-412.
48. M. Kalaskar; S. Surana; *J. Chil. Chem. Soc.*, **2014**, 59, 2299-2302.

LACTOFERRIN MODULATES INCREASED LIVER DNA DAMAGE BY REDUCING SERUM CYTOKINE, HEPCIDIN AND IRON LEVELS IN LIPOPOLYSACCHARIDE-INDUCED ENDOTOXEMIA IN RATS

KEZBAN YILDIZ DALGINLI^a, CANAN GULMEZ^{b,*},
EMINE ATAKISI^c, ONUR ATAKISI^d

ABSTRACT. Endotoxemia, known as the presence of Gram (-) bacterial endotoxin in the circulation, is associated with high mortality. Here, it was aimed to investigate the effects of lactoferrin on inflammation and iron homeostasis and cytokine production in lipopolysaccharide (LPS)-induced experimental endotoxemia in rats. Tumor necrosis factor (TNF- α) and interferon gamma (IFN- γ) levels, which are important cytokines, and iron and hepcidin levels, which play a role in iron homeostasis, DNA damage marker 8-hydroxy-2'-deoxyguanosine levels were evaluated in endotoxemia model. Enzyme-linked Immunosorbent Assay (ELISA) method is a technique based on antigen-antibody complex and using enzymes as marking. Serum TNF- α , IFN- γ and hepcidin levels and the liver 8-OHdG levels were measured by ELISA methods, serum iron levels were determined using iron assay kit. The results indicated that increased serum TNF, hepcidin and iron levels decreased at 1st, 3rd and 6th hours after LPS injection with lactoferrin supplementation, and increased IFN- γ level at 3rd and 6th hours returned to normal range. 8-OHdG increased immediately after LPS injection and this damage returned to normal within 6 hours by lactoferrin. The findings of the study revealed that lactoferrin might be beneficial in the prognosis and treatment of endotoxemia.

Keywords: *lactoferrin, endotoxin, cytokine, 8-hydroxy-2'-deoxyguanosine, iron transport*

^a Department of Chemistry and Chemical Processing Technologies, Kars Vocational School Kafkas University, 36000, Kars, Turkey

^b Department of Pharmacy Services, Tuzluca Vocational High School, Igdir University, 76000, Igdir, Turkey

^c Department of Biochemistry, Faculty of Veterinary Medicine, Kafkas University, 36000, Kars-Turkey

^d Department of Chemistry, Faculty Science and Letter, Kafkas University, Kars, 36000, Turkey

*Corresponding author: canan_glm@hotmail.com, canan.gulmez@igdir.edu.tr

INTRODUCTION

Lipopolysaccharide (LPS), also known as endotoxin, is the component of gram (-) bacterial cell wall. LPS is the best-defined antigen in immunology, being major factor in formation of endotoxemia and septic shock. In experimental studies, LPS has a wide array of uses from modeling local inflammations to modeling septic shock but being dependent on the dose, frequency and way of administration and exposure time. Bacteria, viruses, fungi and parasites can cause septic shock and result in a mortality rate of around 20-80%. The presence of bacteria in the systemic circulation, the bacteremia, the systemic state of the infection is called sepsis whilst the presence of Gram (-) bacterial endotoxin in the circulation is called endotoxemia [1,2].

Lactoferrin is naturally present in colostrum and breast milk and is produced from milk proteins. It is a multifunctional protein that prevents the growth and reproduction of various infectious agents including gram-positive and negative bacteria, viruses, protozoa, or fungi. Lactoferrin is a single-chain glycoprotein of the transferrin gene family that binds iron at 80-kDa. Lactoferrin plays a role in many physiological processes such as regulation of iron metabolism, defense against a wide range of microbial infections, anti-inflammatory activity, regulation of cell growth and differentiation, and cancer prevention and anti-metastasis [3].

In any case of infection, cytokine release develops as a normal immune response. When LPS passes into the circulation, an inflammatory response is triggered by defense cells. Lactoferrin shows a prophylactic effect by reducing the release of interleukin-1, interleukin-6, tumor necrosis factor- α (TNF- α) and interferon gamma (IFN- γ) from monocytes in *in-vitro* and *in-vivo* conditions [3-6]. One of the most important antimicrobial functions of lactoferrin is to bind free iron to prevent infections. Iron is an important catalyst in the formation of reactive oxygen species. It shows important functional properties due to its characteristics such as high iron binding ability even at very low pH, resistance to proteolysis, net positive charge, and presence in many tissues. For this reason, it has been reported that lactoferrin reduces the harmful effects of reactive oxygen species produced by leukocytes in the inflammation region [7,8]. The hepcidin plays a central role in the regulation of systemic iron homeostasis by coordinating iron absorption, mobilization, and storage to meet the iron requirements of erythropoiesis and other iron-dependent processes [9]. It has also been reported that hepcidin, an acute phase 2 protein, has a positive correlation with inflammation indicators [10]. Lactoferrin has a great potential due to its roles in carrying iron and exhibiting antimicrobial, immune-modulatory, anti-inflammatory, and antineoplastic activities. Despite many new available drugs,

antibiotics and treatment protocols for immunomodulation, septic shock is still an important health problem with a 30-90% mortality rate [11]. Revealing the safe uses of LF for clinic and veterinary purposes with respect to the potent protective effects of LF against endotoxemia is important. Herewith the target, in our previous study, we aimed to determine the effect of lactoferrin on adenosine deaminase, nitric oxide and liver enzyme levels in endotoxemic rats. The results showed that LPS increased adenosine deaminase activity synthesis and NO release and LF acted as an anti-inflammatory and immunosuppressor in stimulating immune response [12]. In this study, we investigated the effect of lactoferrin on some important biochemical parameters such as serum TNF- α , IFN γ , hepcidin, iron and liver 8-OHdG levels at different hours (1, 3 and 6 h) following LPS administration.

RESULTS AND DISCUSSION

The experimental model can be designed according to the differences in the dose and frequencies of lipopolysaccharide administration in rat [5,12,13]. In this study, after lactoferrin supplementation (20 mg/kg/day) for 1 week, rats were given LPS (20 μ g/kg) at 3 different hours (1, 3 and 6 h post-injections of LPS) and blood was collected at the 1st, 3rd and 6th hours. Herewith the blood samples, the changes in serum TNF- α , IFN- γ , hepcidin, iron and liver 8-OHdG levels in an experimental endotoxemia model in Swiss Sprague rats were recorded after LF supplementation.

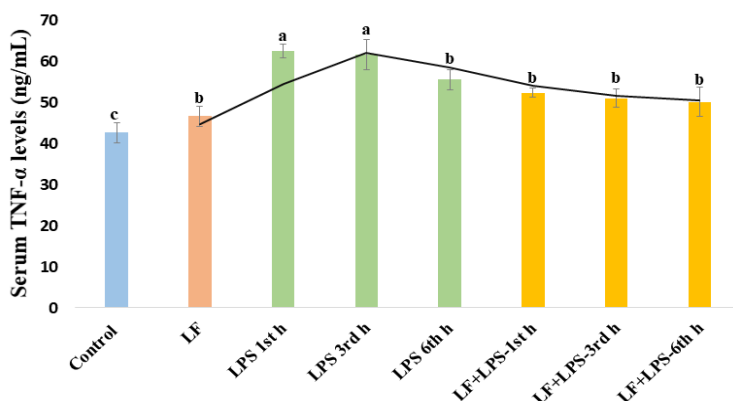


Figure 1. The effect of lactoferrin on serum TNF- α levels in LPS-induced endotoxemia model. The difference among the groups in different columns (a,b,c) was statistically significant ($P < 0.05$ for the 1st, 3rd and 6th hours).

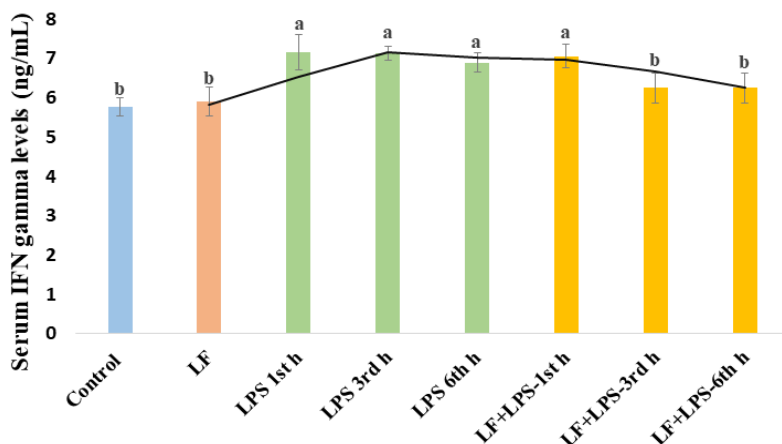


Figure 2. The effect of lactoferrin on serum IFN- γ levels in LPS-induced endotoxemia model. The difference among the groups in different columns (a,b) was statistically significant ($P < 0.05$ for the 1st, 3rd and 6th hours).

The findings of the study revealed that at serum TNF- α levels were higher in the LPS group compared to other groups ($P < 0.05$) (Figure 1). When the TNF- α levels in the groups were analyzed according to hours, no statistical difference was observed between the 1st, 3rd and 6th hours of the LF+LPS group. The IFN- γ levels were higher in the LPS group at the 1st, 3rd and 6th hours in comparison to the other groups ($P < 0.05$) (Figure 2). At 3rd and 6th hours IFN- γ levels in the LF + LPS group were lower than the LPS group and no statistical difference was observed between the control, LF and LF + LPS groups at the same hours.

The proinflammatory cytokines are endogenous polypeptides generated by immune system cells and mediate many kinds of immune response. The serum cytokine levels increase after injection of gram-negative bacteria, which is a component of the cell wall [14, 15]. In a previous study, it was reported that endotoxin remained in the blood for 6 hours and its level was higher than 1584.9 EU/mL in LPS-induced endotoxemia model in mice [16]. Hasegawa-Ishii et al. found that in sepsis-associated encephalopathy mouse model, LPS exposure (30 mg/kg, i.p.) responded to the production of multiple cytokines in the acute phase (4-24 hours) after LPS injection in all brain regions [17]. In endotoxemia, proinflammatory cytokines (TNF- α , IFN- γ), which are associated with the severity of the disease, are secreted and anti-inflammatory cytokines are secreted in response to the continuation of the infection [18-20]. TNF- α and IFN- γ is generally considered to be the critical

mediator for septic shock-related lethality induced by LPS [5, 21]. In this study, the serum TNF- α and IFN- γ levels after LPS injection was increased at all hours ($P < 0.05$). Lactoferrin administration significantly normalized TNF- α levels at the 1st, 3rd and 6th hours. It has been found that TNF- α , whose synthesis is stimulated by LPS, causes longer circulation (from 3 hours to 6 hours) in endotoxemia model. LF may play a protective role in endotoxemia by affecting the transcriptional levels of proinflammatory cytokines by affecting various signal pathways that control cytokine production involved in the immune response. Moreover, the inhibition effect of LF can be explained by the disruption of the membrane structure as a result of binding iron in the gram-negative bacterial membrane and thus showing prophylactic properties against septic shock [6,19,20].

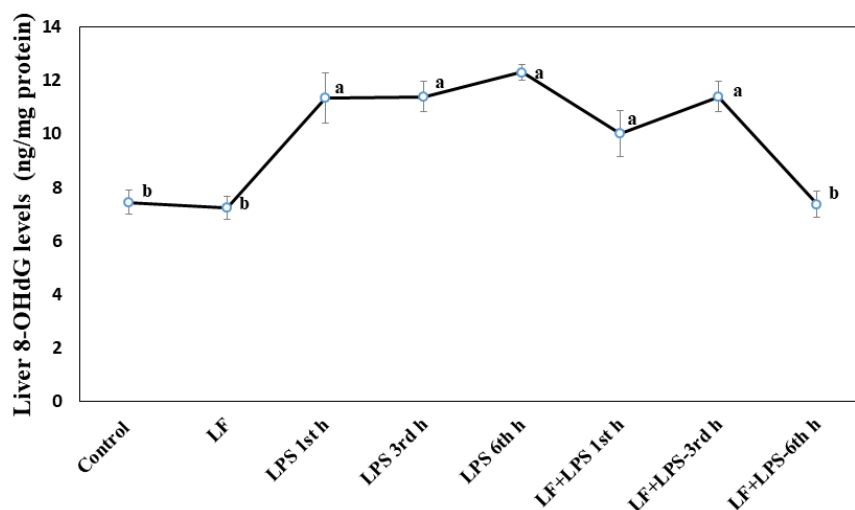


Figure 3. The effect of lactoferrin on liver 8-OH-2-Deoxyguanosine levels in LPS-induced endotoxemia model. The difference among the groups in different columns (a,b) was statistically significant ($P < 0.05$ for the 1st hour, $P < 0.001$ for the 3rd hour).

At the 1st and 3rd hours, the liver 8-OHdG levels were higher in the LPS and LF + LPS group than the other groups ($P < 0.05$ for the 1st hour, $P < 0.001$ for the 3rd hour) (Figure 3). At the 6th hour, liver 8-OHdG levels were significantly higher in the LPS group than in the other groups. While there was no difference between the 1st and 3rd hours, there was a difference between the 1st and the 6th and the 3rd and 6th hours ($P < 0.05$).

The 8-OHdG has been used commonly in many studies as a biomarker for the measurement of endogenous oxidative DNA damage and as a risk factor for many diseases. After LPS treatment, the liver is more susceptible to oxidative damage than other organs and causes mutagenic lesions such as 8-OHdG with DNA breakage [22]. In our previous study, LPS significantly was increased liver enzymes aspartate aminotransferase and gamma glutamyltranspeptidase activities, which are the precursors of disease risk. Also, liver NO level significantly with LPS injection. LF attenuated increased NO and liver enzyme levels during inflammation [12]. Liver 8-OHdG level reduced by LF supplementation was positively correlated with liver enzymes and NO level. In the LPS-induced murine neuroinflammation model, a significant increase in both peripheral and brain IL-1 β , TNF- α levels were shown to be accompanied by an increase in 8-OHdG levels [23]. In another study, it was stated that urothelium 8-OHdG expression increased in the LPS-induced cystitis model [24]. In this study, the liver 8-OHdG levels at the 6th hour were higher in the LPS group than in the other groups ($P < 0.001$). Lactoferrin supplementation did not reduce DNA damage in a short time, but normalized it by reducing DNA damage to the 6th hour in experimental endotoxemia model. Ogasawara et al. [25] showed that LF acts not only as a transient metal chelator, but also as a sacrificial scavenger for reactive oxygen species (ROS), and that it protects through direct interaction with hydrogen radicals. In another study, LF regulated the endotoxemic effect of LPS by reducing DNA damage especially after the 3rd hour. Some of the inflammation cascade mediators such as TNF- α , IFN γ , interleukins 1 and 6 and nuclear factor kappa B related to the action mechanism of 8-OHdG have been proposed [26].

The iron levels were higher in the LPS group at the 1st, 3rd and 6th hours compared to the other groups ($P < 0.05$) (Figure 4). At all hours, iron levels in the LF + LPS group were lower than the LPS group, and higher than the control and LF ($P < 0.05$). There was a difference between the 1st hour and the 6th hour in the LF + LPS group ($P < 0.05$). The hepcidin hormone levels were higher in the LPS group at the 1st, 3rd and 6th hours compared to the other groups ($P < 0.001$) (Figure 5). At all hours, hepcidin levels in the LF + LPS group were lower than the LPS group, and higher than the control ($P < 0.001$). Hepcidin levels increased at 1st hour compared to 6th hours in the both LPS and LF+LPS groups ($P < 0.05$). The hepcidin levels of LPS group were lower at 6th hours than both 1st and 3rd hours.

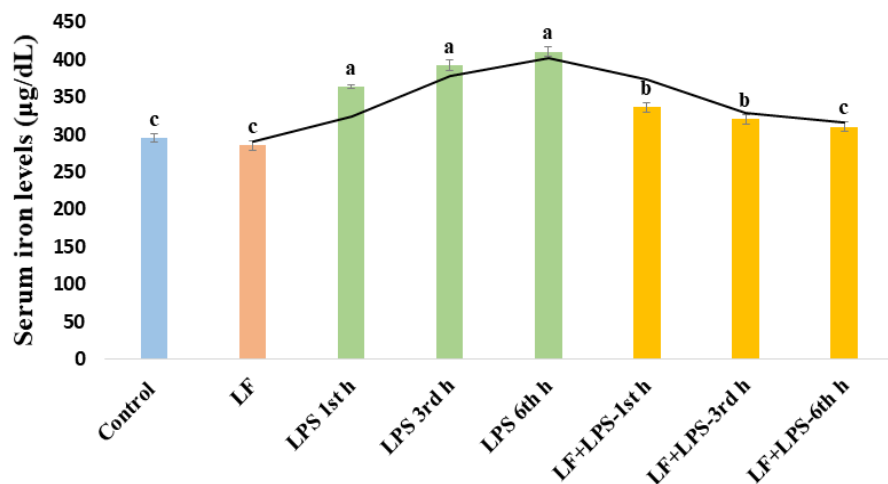


Figure 4. The effect of lactoferrin on serum iron levels in LPS-induced endotoxemia model. Serum iron levels were determined spectrophotometrically by drawing a standard curve at 100-1000 µg/dL Fe^{2+} concentrations at 590nm. The difference among the groups in different columns (a,b,c) was statistically significant ($P < 0.05$ for the 1st, 3rd and 6th hours).

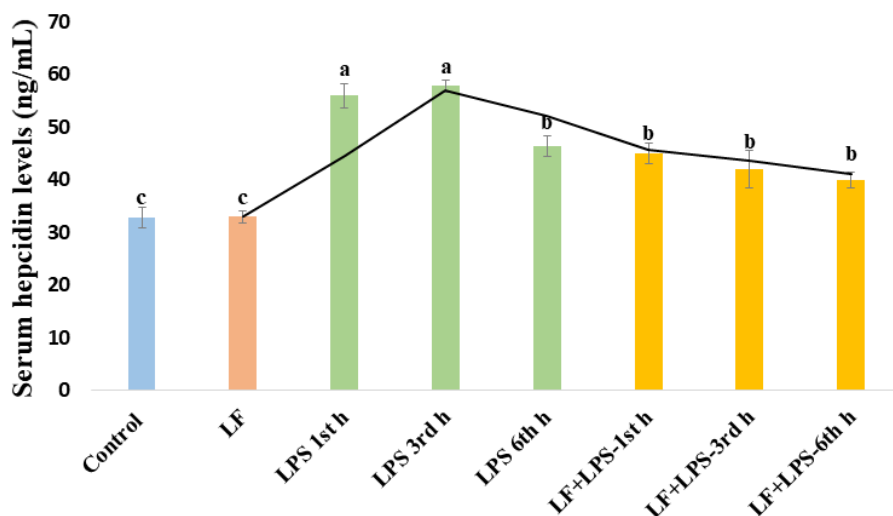


Figure 5. The effect of lactoferrin on serum hepcidin levels in LPS-induced endotoxemia model. The difference among the groups in different columns (a,b,c) was statistically significant ($P < 0.05$ for the 1st, 3rd and 6th hours).

The iron is necessary for pivotal metabolic processes including energy production, synthesis, repair and transcription of DNA, oxygen transport/storage and drug detoxification. The free available not bound- Fe^{3+} causes the ROS production through the Fenton and Haber-Weiss reactions, ROS causes oxidative stress and acute and chronic inflammation processes associated with various diseases. The high hepcidin levels, hindering iron export by ferroportin (Fpn) causes intracellular iron overload and the increased hepcidin level correlates with an increase in ferritin level in chronic inflammatory process [27]. It has been reported that serum hepcidin levels increase significantly after 4th and 8th hours compared to start values in acute kidney injury [28]. In LPS-induced inflammatory model mice, LPS has been reported to reduce the iron level and increase hepcidin, TNF- α and hepcidin signal pathway molecule STAT3 expressions [29]. Hepcidin is expressed to negatively regulate iron in circulation by inhibiting iron absorption from the duodenum. Therefore, hepcidin expression increases significantly during infection. This leads to a significant reduction in serum iron, thus bacteria are deprived of iron and reduce their growth rate [30]. Iron binding capacity of lactoferrin (bi) carbonate ion (CO_3^{2-}) depends on its existence and thus balances its positive charge. It shows this effect by interacting with the N-terminal lipid A portion and thus causing the lipopolysaccharide to separate, destabilize the outer membrane and increase its permeability [31].

Intracellular iron retention can be an inducer of infection, so the cell has to maintain the anti-inflammatory state in order to balance the iron level between tissues and blood. Previous studies found that the cyclic peptides formed by a bridge of disulfide bond tend to change structures and antimicrobial activity of some peptides. Despite the limited information evaluating the changes in the molecular structure of LF, there are studies regarding the effect of disulfide bonds on its antibacterial and anti-inflammatory activities [32,33].

CONCLUSIONS

The study emphasizes that lactoferrin is vital in the reduction of TNF- α and IFN- γ cytokines production and the complex relationship between iron and inflammation homeostasis during the endotoxemia process. It was observed that 8-OHdG levels increased immediately after LPS injection and this level returned to normal within 6 hours by lactoferrin. In addition to serum cytokines, changes in iron, hepcidin and 8-OHdG levels are important in the treatment and prognosis of endotoxemia. It has been concluded that increased serum cytokine, hepcidin, iron levels during endotoxemia contribute to 8-OHdG increase in the liver. It is worthy to note herein that lactoferrin might be beneficial in the prognosis and treatment of endotoxemia because it significantly reduces this damage.

EXPERIMENTAL SECTION

Animals

Swiss Sprague female rats, aged 6 months and weighing 280-310 g were used in this study. Before starting the study, a consent was obtained from Kafkas University, Animal Experiments Local Ethics Committee (Decision no: KAÜ-HADYEK: 2015/018). Animals were kept at constant conditions as follows: temperature (23 ± 2 °C), humidity (50 ± 10 %), and light (12 h light/dark cycles). All animals were allowed to access free standard chow and *ad libitum* freshwater. Same conditions were applied to all groups during the experiment.

Experimental design

A total of 80 Swiss Sprague rats were divided equally into 4 groups: Group I (control, n=10), Group II (20 mg/kg/day LF for 7 days (n=10)), Group III (20 µg/kg LPS single dose, n=30)) and Group IV (20 mg/kg/day LF for 7 days + the end of 7 days 20 µg/kg LPS single dose (n = 30)). In order to determine the effects of LPS administration at 3 different hours (1, 3 and 6 h post-injections of LPS), 30 rats were preferred in Groups III and IV. Lipopolysaccharides from *Escherichia coli* 0111:B4 (Sigma-Aldrich: L4391) were used as the LPS source. All injections were done as intraperitoneal injection. Blood samples and liver tissues were taken under anesthesia from the groups at 1, 3 and 6 h post-injections of LPS. Serum samples were obtained by centrifuging the blood samples for 15 minutes at 3000 rpm. All the samples were stored at -45°C until analyses. Serum samples taken were used to measure TNF-α and IFN-γ cytokines, hepcidin and iron levels. The liver samples were used to measure 8-OHdG levels.

Biochemical Analysis

Serum TNF-α, IFN-γ and hepcidin levels and the liver 8-OHdG levels were determined by commercial enzyme-linked immunosorbent assay (ELISA) kits (Sunred Biological Technology Co. Ltd., Shanghai, CHINA). Serum iron levels were measured using commercial kit (BioAssay Systems, Hayward, USA). All spectrophotometric analyzes were performed on the microplate reader (Bio-Tek Eon, USA).

Statistical Analysis

The statistical significance was evaluated using the SPSS 20.0 software package (SPSS ver. 20.0 for windows professional edition). Mean and standard error were used in data analyses. Kruskal-Wallis H analysis was conducted to determine the differences between the groups. Mann Whitney U-test was determined as the source of significant differences among groups. Level of significance was accepted as $P < 0.05$.

AUTHOR CONTRIBUTION

C.G. and K.Y.D performed experiments. All authors wrote the manuscript. O.A and E.A. conceived the original idea, designed and supervised the project.

ACKNOWLEDGMENTS

This work was supported by Kafkas University Scientific Research Projects Coordinator (Grand number: 2017-FM-79), Turkey.

CONFLICT OF INTEREST

All authors declare that there is no potential conflict of interest.

REFERENCES

1. M. Asperti; A. Denardo; M. Gryzik; A. Castagna; D. Girelli; A. Naggi; P. Arosio; M. Poli; *Biochem. Pharmacol.* **2020**, *175*, 113867.
2. F. Beheshti; M. Hosseini; M.T. Sarvtin; A. Kamali; A. Anaeigoudari; *Drug Chem. Toxicol.* **2019**, *29*, 1-7.
3. K. Buttenschoen; P. Radermacher; H. Bracht; *Langenbeck's Arch. Surg.* **2010**, *395*(6), 597-605.
4. A.Cutone; L. Rosa; M.S. Lepanto; F. Berlutti; M.C.B. di Patti; G. Musci; P. Valenti; *Front Immunol.* **2017**, *8*, 705.
5. H. Dong; X. Tang; Z. Zhang; C. Dong; *Biochim. Biophys. Acta Mol. Cell Biol. Lipids* **2017**, *1862*(11), 1461-1467.
6. M.F. Doursout, H., Horton; L. Hoang; S. Hwang; S. Boyd; J.K. Actor; M.L. Kruzel; *Int. Immunopharmacol.* **2013**, *15*(2), 227-231.
7. E. Ellass-Rochard; D. Legrand; V. Salmon; A. Roseanu; M. Trif; P.S. Tobias; J. Mazurier; G. Spik, et al.; *Infect. Immun.* **1998**, *66*(2), 486-491.
8. A.S. Farid; M.A.E. Shemy; E. Nafie; A.M. Hegazy; E.Y. Abdelhiee; *Drug Chem. Toxicol.* **2019**, *2*, 1-8.
9. C. Garré; G. Bianchi-Scarra; M. Sirito; M. Musso; R. Ravazzolo; *J. Cell Physiol.* **1992**, *153*(3), 477-482.
10. K. Suega; G.R Widian; *Hematol. Transfus. Cell. Ther.* **2019**, *41*, 342-348.
11. S. Hasegawa-Ishii; M. Inaba; A. Shimada; *Neurotoxicol.* **2020**, *76*, 67-74.

12. C. Gulmez; K.Y. Dalginli; E. Atakisi; O. Atakisi; *Kafkas Univ. Vet. Fak. Derg.* **2020**, *26* (6), 801-806,
13. L. Häversen; B.G. Ohlsson; M. Hahn-Zoric; L.A. Hanson, I. Mattsby-Baltzer; *Cell Immunol.* **2002**, *220*(2), 83-95.
14. X. Hou; G. Xu; Z. Wang; X. Zhan; H. Li; R. Li et al; *Int. Immunopharmacol.* **2020**, *81*, 1062-71.
15. C. Huang; O. Tsz-Wa Ng; J. Man-Tak Chu; M.G. Irwin; X. Hu; S. Zhu et al.; *Neurosci. Lett.* **2019**, *707*, 134309.
16. P. Huang; J. Wang; X. Lin; F.F. Yang; J.H. Tan; *Eur. Rev. Med. Pharmacol. Sci.* **2017**, *21*(15), 3469-75.
17. E. Kemna; P. Pickkers; E. Nemeth; H. van der Hoeven; D. Swinkels; *Blood* **2005**, *106*(5), 1864-1866.
18. T. Ilgun; K.Y. Dalginli; C. Gulmez; O. Atakisi; *Turk J. Biol.* **2016**, *40*(6), 1272-1277.
19. E. Keskin; E. Oztekin; R. Col; A. Sivrikaya; K. Uney; E. Yazar; *Acta Vet. Brno.* **2005**, *74*, 17-21.
20. H.J. Kim; H.I. Joe; Z. Zhang; S.W. Leed; K.Y. Leee; Y.B. Kook et al.; *Mol. Immunol.* **2020**, *119*, 123–131.
21. S.Y. Lee; L.W. Hsin; M.J. Su; C.C.C. Chien; H.C. Ku; *Pharmacol. Rep.* **2019**, *71*, 1281–1288.
22. W. Li; S. Yang; S.O. Kim; G. Reid; J.R.G. Challis, A.D. Bocking; *supernatant. Reprod. Sci.* **2014**, *21*(7), 939-947.
23. J. Malyszko, H. Bachorzewska-Gajewska; J.S. Malyszko; E. Koc-Zorawska; J. Matuszkiewicz-Rowinska; S. Dobrzycki; *Adv. Med. Sci.* **2019**, *64*(2), 211–215.
24. E. Nemeth, E.V. Valore; M. Territo; A. Lichtenstein; T. Ganz; *Blood.* **2003**, *101*(7), 2461-2463.
25. Y. Ogasawara; M. Imase; H. Oda; H. Wakabayashi; K. Ishii; *Int. J. Mol. Sci.* **2014**, *15*(1), 1003-1013.
26. C.Y. Ock; E.H. Kim; D.J. Choi; H.J. Lee; B.K. Hahm; M.H. Chung; *World J. Gastroenterol.* **2012**, *18*(4), 302-308.
27. D. Vyoral; J. Petrak; *Pharmacol. Res.* **2017**, *115*, 242-254.
28. L. Podmoliková; M.F. Mukanyangezi; A.J. Dahlqvist; A.T. Naluaid; L. Ny; D. Giglioae; *Int. Immunopharmacol.* **2020**, *83*, 106334.
29. S.M. Opal; *Int. J. Med. Microbiol.* **2007**, *297*(5), 365-377.
30. D. Vyoral; J. Petrak; *Pharmacol. Res.* **2017**, *115*, 242-254.
31. K. Brandenburg; G. Jurgens; M. Muller; S. Fukuoka; M.H. Koch; *Biol. Chem.* **2001**, *382*, 1215-1225.
32. T.J. Ochoa; M. Noguera-Obenza; T.G. Cleary; *Adv. Exp. Med. Biol.* **2004**, *554*, 463-466.
33. V. Krishnakumari; A. Sharadadevi; N. Sitaram; R. Nagaraj; *J. Pept Res.* **1999**, *54*(6), 528-35.

TESTING OF NEW EXPERIMENTAL GIOMERS: WATER SORPTION, CONVERSION DEGREE, RADIOCAPACITY, MICROSTRUCTURE AND BIOLOGICAL BEHAVIOR

SANDA-ILEANA CIMPEAN^a, IOANA AMBROSIE^a,
MADALINA MOLDOVAN^{b*}, ADA DELEAN^a, DOINA PRODAN^c,
CRISTINA PREJMEREAN^c, MARIOARA MOLDOVAN^c,
MARIA TOMOAIA-COTISEL^{d,e}, LOREDANA COLCERIU-BURTEA^a

ABSTRACT. Two experimental giomers (G1 and G2) were obtained and then evaluated for water sorption- by weighing the specimens before and after water immersion, for conversion degree (DC)- by Fourier Transform Infrared Spectrometry, for radiopacity- by using the intraoral sensor system Ez Sensor 1.5 Vatech E-Woo (Korea), in relation to their microstructural characteristics assessed by Scanning Electron Microscopy (SEM). They were compared to a commercial giomer: Beautifil II. Both experimental and commercial giomers were also tested by subcutaneous and intramuscular implantation tests, to establish and compare their biological behavior. Intensity of the inflammatory reaction, tissue repair status and the presence of the capsule were the main criteria assessed. After 7 days, the mean values of DC were: 65.8% (Beautifil II), 62.2% (G2) and 60.5 (G1). DC increased after the initial polymerization. Giomers showed mean values of water sorption, below 40 µg/mm³. A certain swelling of the polymer matrix without dislocations of particles could be seen on SEM images. The mean values of radiopacity were between 2.15-2.99 [mmAl]. Giomers were slight to moderate irritants for soft tissues, with no significant difference between the samples. Promising results make G1 and G2 possible alternative to Beautifil II, that can be further improved.

Keywords: giomer, conversion, water sorption, radiopacity, SEM, biocompatibility

^a Iuliu Hatieganu University of Medicine and Pharmacy, Faculty of Dental Medicine, Department of Conservative Odontology, 33 Motilor str., RO-400001 Cluj-Napoca, Romania

^b Iuliu Hatieganu University of Medicine and Pharmacy, Faculty of Dental Medicine, Department of Oral and Cranio-Maxilo-Facial Surgery, 33 Motilor str., RO-400001, Cluj-Napoca, Romania

^c Babes-Bolyai University, Raluca Ripan Institute of Research in Chemistry, 30 Fantanele str., RO-400294, Cluj-Napoca, Romania

^d Babes-Bolyai University, Faculty of Chemistry and Chemical Engineering, 11 Arany Janos str., RO-400028, Cluj-Napoca, Romania

^e Academy of Romanian Scientists, 54 Splaiul Independentei, 050094 Bucharest, Romania

* Corresponding author: madilazar@yahoo.com

INTRODUCTION

Giomers represent a new class of direct restoration materials, with fluoride controlled release, offering both protection against caries, but also, superior aesthetic properties, high radiopacity, and easy handling. These are hybrid materials that combine the characteristics of composite resins with those of glass ionomers. The main characteristic of giomers consists in the pre-reacted glass ionomer from their composition, previously obtained after a chemical reaction between a fluoro-aluminosilicate glass and a polyacrylic acid [1], [2]. Giomers are available on the dental materials market in different shapes, with different consistencies, depending on their area of applicability (for reconstruction of tooth anatomy, for marginal ridges, cavity liners, and small restorations, etc.) [3-7].

The degree of conversion (DC) is mostly influenced by the structure and relative ratio of each monomers of polymer matrix. DC is also influenced by the filling component of the material. Fillers based on Ba or Zr can improve radiopacity, but at the same time they can decrease the degree of conversion due to the fact that light can no longer penetrate so deep into the material. The proportions and type of components of the initiation system, but also the light source used, the time and the distance of polymerization are just some factors that can influence the DC of composite resins, respectively of the giomers. As the data in the literature show, the conversion is never complete, with a reported DC of 50% to 75% for the conventional composites and respectively of 50% to 81% for the bulk-fill composite materials [8].

Sorption can lead to the swelling of the polymeric matrix and to release of unreacted monomers or filler ions, but it may also affect the optical properties, so the longevity of restorations materials may be reduced. Therefore, although the fluoride-releasing property by the giomers is supported by the ability of water diffusion, a large amount of water can lead to plasticization of the polymer network negatively influencing the properties of the material [5], [9].

Radiopacity is one of the essential properties of all restorative materials including giomers. Adequate radiopacity of the material allows the clinician to differentiate secondary caries formation from restoration and surrounding tooth structure, to evaluate and detect voids, overhangs and open margins. In addition, studies conclude that, for optimum contrast, a restorative material with a radiopacity slightly greater than or equal to that of enamel is ideal for the detection of secondary caries on radiographs [10], [11].

The aim of this study was to evaluate and compare water sorption, conversion degree and radiopacity of two experimental giomers (G1 and G2) in relation to their microstructural characteristics, compared to the commercial giomer: Beautifil II (Shofu, Japan).

RESULTS AND DISCUSSION

1. Degree of conversion (DC)

The degree of conversion (DC) represents a fundamental parameter governing mechanical properties and biocompatibility of giomer materials, also influencing the water sorption.

After polymerization, a crosslinked three-dimensional polymer network which contains a significant amount (percent) of unreacted methacrylate groups (residual double bonds, RDB) is formed. Most of the RDB are pendant methacrylate groups attached to the polymer network and a small proportion of them (ca. 10%) represents the free residual monomer [12]. The frequently used technique for DC determination is FTIR. DC is determined by the proportion between remaining aliphatic C=C double bonds' concentration in the cured giomers reported to the total number of C=C bonds in the uncured giomers [13].

As shown in Figure 1, the conversion degree increases between the first and seventh day after the initial polymerization. This increase in conversion is more pronounced in the case of G1 (8.3%), G2 (7.8%), compared to Beautifil II (4.5%).

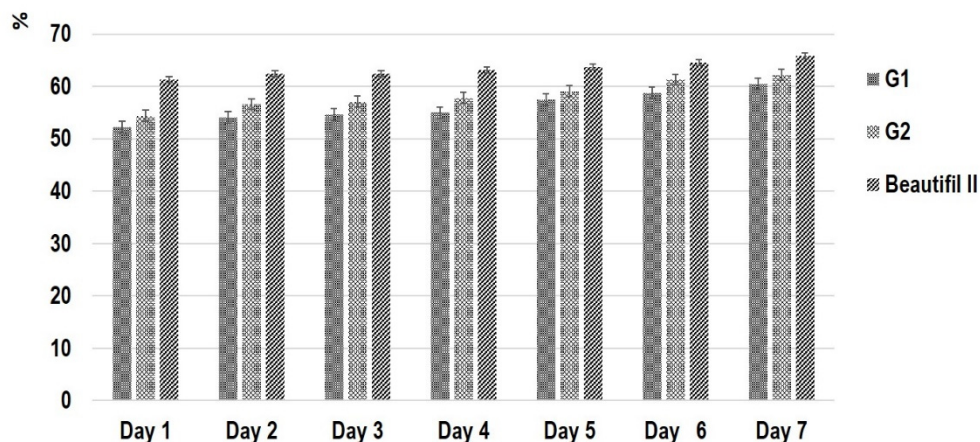


Figure 1. Degree of conversion of investigated giomers

For all the tested giomers (Figure 1), a daily increase of DC was found until the end of the investigation period, except on the 3rd day when the same value of DC was recorded as in the previous day, for the Beautifil II giomer.

The highest degree of conversion was recorded in case of Beautifil II, of 61.3% after the first day post polymerization and 65.8% after the 7th day post polymerization. After the first day, for the experimental giomer G2 a DC of 54.4% was registered and for G1 a DC of 52.2%. After 7 days from the polymerization a DC of 62.2% was registered for G2 respectively 60.5% for G1. It can be seen that the polymerization continued during the 7 days with a more significant increase from the first to the 7th day after polymerization for the experimental giomers.

2. Water sorption

The water sorption phenomena are mainly influenced by the structure of the polymer network, the nature of the inorganic fillers and the quality of the polymer/ filler interface. Small water molecules, associated by hydrogen bonds, can interact with the polar groups of the polymer, water sorption being influenced by the position of these groups in the three-dimensional polymer network. In case of giomers, the diffusion of water or aqueous solutions like saliva is a requirement in order to achieve the performance of continuous release of fluoride ions. The release of fluoride ions is conditioned by the ability of the material to allow the diffusion of water in its structure [14], [15].

The current study compared the water sorption behavior of a commercial giomer material with two different experimental giomers of varying composition. This was done over a period of 1 week. Mean values of water sorption/day for each giomers are presented in Figure 2.

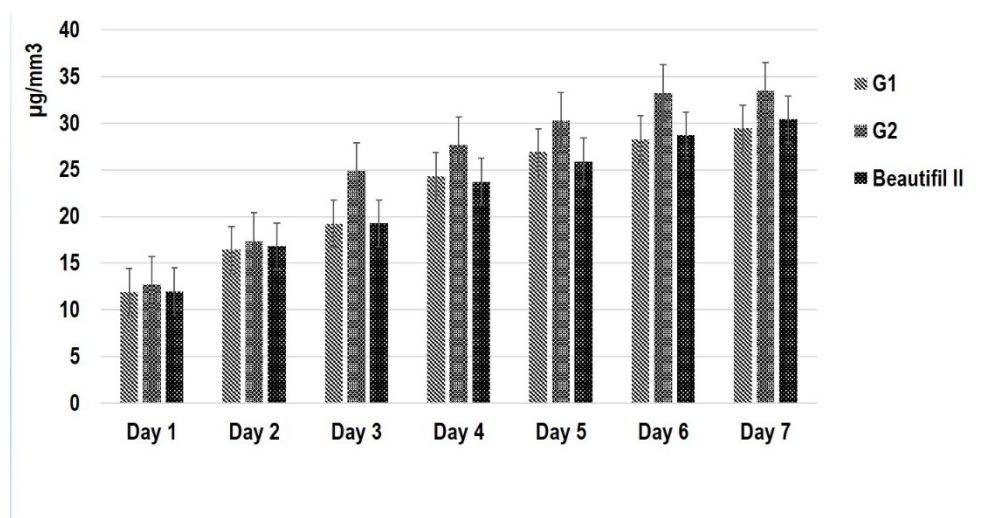


Figure 2. Water sorption of the investigated giomers

As it can be seen from Figure 2, for all tested giomers the water sorption increases all throughout the investigation period. After the first day, the lowest average value ($11.89\mu\text{g}/\text{mm}^3$) was recorded for the experimental giomer G1, similar to that of the Beautifil II giomer ($11.99\mu\text{g}/\text{mm}^3$). Also at the end of the investigation period, the lowest value of water sorption was recorded for G1 giomer, ($29.44\mu\text{g}/\text{mm}^3$), slightly lower than the average value recorded for Beautifil II ($30.4\mu\text{g}/\text{mm}^3$). The average value recorded, after day 7, for the experimental giomer G2 was $33.5\mu\text{g}/\text{mm}^3$. However, it was found that the water sorption for G2 giomer was the highest ($24.91\mu\text{g}/\text{mm}^3$) on the 3rd day, more by $7.53\mu\text{g}/\text{mm}^3$ than on day 2 and on day 7 it absorbed only $0.27\mu\text{g}/\text{mm}^3$ more than on the 6th day. Beautifil II absorbed on the 7th day with $1.74\mu\text{g}/\text{mm}^3$ more water than on the 6th day and G1 with $1.144\mu\text{g}/\text{mm}^3$ more water than on the 6th day. All this information leads us to the assumption that although the experimental G2 giomer recorded the highest values of water sorption, towards the end of the investigation period, sorption increased much slower compared to the other two giomers, with a alleged tendency to decrease in the following days if the study would have continued.

Thus, after 1 week, all the tested materials showed acceptable water sorption, below $40\mu\text{g}/\text{mm}^3$ (the maximum water sorption stated by the ISO 4049) [16].

Therefore, the difference in the water sorption value of the materials was due to the composition of each material. This was in agreement with several studies in terms of the maximum amount of water sorption gained within the first week [17], [18].

The water sorption values for G1, G2, Beautifil they are quite close. This behavior suggests that water sorption is influenced in this case by the nature of the polymer matrix in the giomers, and much less by the nature of the hybrid filling.

McCabe and Rusby 2004 reported that the nature and hydrophilicity of the resin matrix is a major parameter which may regulate rate and extent of water diffusion. The investigated materials contain bisphenol-A-glycol dimethacrylate (Bis-GMA) and triethylene glycol dimethacrylate (TEGDMA) oligomers in their matrices. These types of polymers are known of their high hydrophilic nature that might be attributed to strong hydrogen bonds formed between their hydroxyl groups and water molecules. This explains their increasing tendency for water sorption. Compared to other oligomers, TEGDMA is more heterogeneous in composition and has higher flexibility. The more heterogeneous the network, the larger are the micropores created between polymer clusters and the larger is the quantity of absorbed water. Being flexible, TEGDMA chains become more liable to swell and accommodate higher amounts of water. This explains the ability of materials to absorb water.

The resin matrix composition may not be the only factor that affects the amount of absorbed water. Giomers in presence of surface pre-reacted glass polyacid zones have the capability to generate an osmotic pressure that potentially increases water sorption [19], [20].

The difference in the composition of G1 and G2 materials is the type of pre-reacted glass. In the case of G2 material, the polyalkenoic acid that enters in the composition of the pre-reacted glass was grafted with methacrylic groups. By grafting, the degree of crosslinking increased and so did the degree of conversion. Also, the fact that meshes formed in the polymer network due to crosslinking, led to the predisposition of the G2 material to a higher release of fluorine, respectively to a higher water absorption, due to the diffusion phenomenon.

1. Scanning Electron Microscopy (SEM)

For this evaluation a scanning electron microscope (Quanta 3D FEG) was used. As an example, in Figure 3 SEM images of the G2 giomer are shown: the initial state and the appearance after 7 days of storage in water. A relative degree of swelling of the polymer matrix can be observed without dislocations of particles from the polymer matrix (Figure 3).

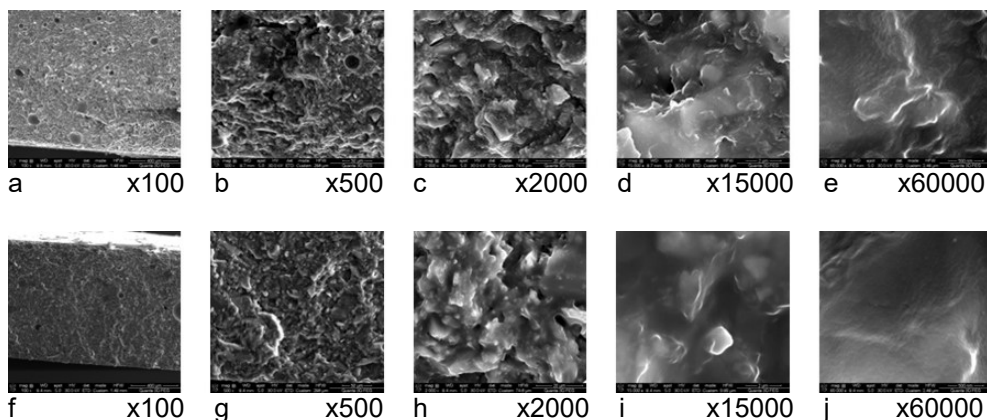


Figure 3. SEM images of the G2 experimental giomer (initial state a-e; after 7 days of storage in water f-j) at magnifications of: x100, x 500, x2000, x 15000, x60000

2. Radiopacity

Restorative materials should ideally be radiopaque to enable visualization and assessment by radiograph, and all newly developed materials should, therefore, be investigated in this order.

According to the International Standards Organization for Standardization (ISO 4049) [21], the radiopacity of such materials should be equal to or greater than the same thickness of aluminum. The radiopacity values in the case of experimental giomers G1 and G2 were lower than the value obtained for Beautifil II (Table.1, Figure 4.), but higher than the limit imposed by ISO 4049 (1mm Al) [21]. The dentin and enamel reference radiopacity values used in the present study were 1.09 ± 0.0 and $1,84 \pm 0.0$ mm Al, respectively. The results show that the radiopacity values of all the tested materials were greater than those of enamel and dentin, which means that none of the tested materials could be misinterpreted as dentinal caries on the radiographie.

Table 1. Radiopacity mean values of the investigated giomers

Sample	Beautifil II	G1	G2
Radiopacity [mmAl]	2.99	2.15	2.21

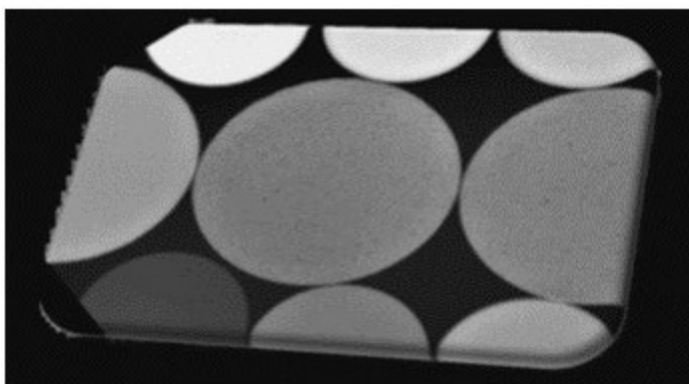


Figure 4. Radiopacity of giomers (In the middle line from left to right: Beautifil II, G1, G2 giomer. Third and first lines: The aluminum step wedges (thickness increasing by 1mm for each step to a maximum of 6 mm))

3. Implantation tests

Subcutaneous and intramuscular inoculation were well tolerated by all subjects. After the implantation, no changes in general status and behavior were noticed. Healing of the skin wound at the implant site occurred without any complications. Implants were well tolerated with a very short convalescence time, clinically insignificant, without rejection signs. Macroscopically, there was no difference between the groups. Neither necrosis, nor hemorrhage or granulative tissue were noticed around the implants.

Concerning the *subcutaneous implantation*, when the skin was removed, the implant's body appeared attached to the connective tissue and was wrapped in a transparent capsule. The body of the implant was well fixed in a cavity formed by connective tissue proliferation.

From microscopic point of view, the tissues surrounding the implants showed mild to moderate, chronic, inflammatory reaction. In case of G1 the repair process was in an early stage and a thin, fragile, capsule could be identified in contact with the implant (Figure 5). In case of the G2 and Beautifill, the inflammatory reaction was milder, and the surrounding tissue exhibited a moderate repair process.

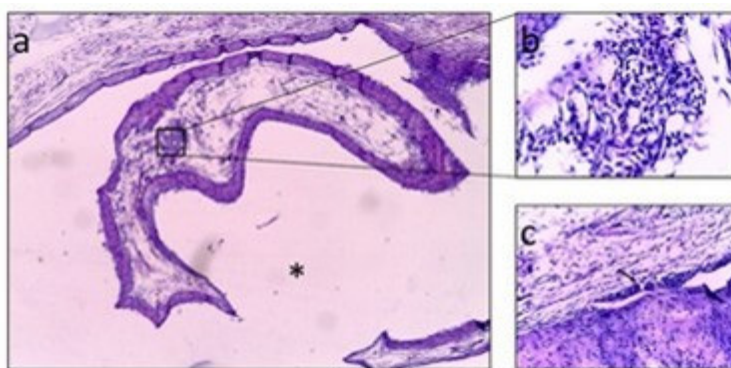


Figure 5. Subcutaneous implant with G1 giomer

* The place where the implant was a) 4x Magnification – overview -fibroconjunctive capsule in the vicinity of the implant; b) 40x Magnification – lympho- plasmocitary inflammatory infiltrate c) 20x Magnification – giant multinuclear cell

In case of *intramuscular implantation*, specimen analysis revealed moderate fibrosis and slight to moderate inflammatory reaction. Regenerating muscle cells could be seen in the tissue next to the implants, demonstrating the tendency of the muscle to restore to the normal structure.

In case of G1, the tissue around the implant showed foci of inflammatory cells (lymphocytes, PMN and plasma cells) along with few new blood vessels. The inflammatory reaction was milder in case of G2 was and characterized by the presence of lymphocytes, plasmocytes but also a minimal amount of adipose tissue associated with fibrosis. For Beautifil II fewer lymphocytes, plasmocytes, macrophages and PMNs were observed in the dense fibrous capsule and around the blood vessels (Figure 6).

TESTING OF NEW EXPERIMENTAL GIOMERS: WATER SORPTION, CONVERSION DEGREE,
RADIOPACITY, MICROSTRUCTURE AND BIOLOGICAL BEHAVIOR

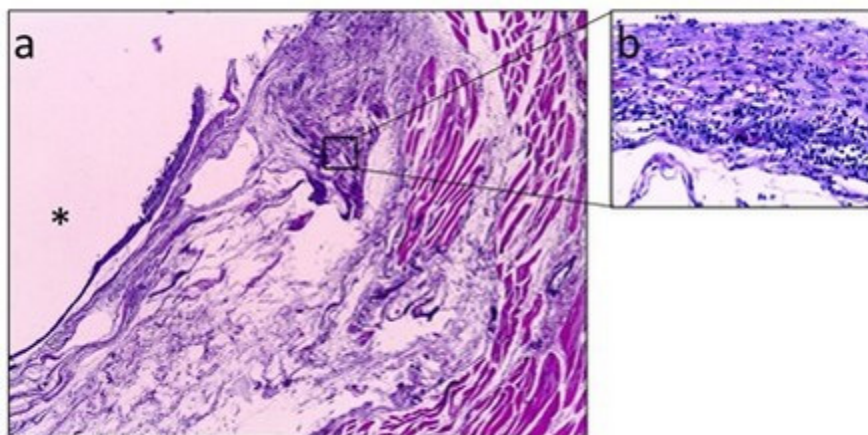


Figure 6. Intramuscular implant with giomer G2

* - the place where the implant was a) 4x Magnification – overview -fibroconjunctive capsule organization around the implant with connective tissue; b) 40x Magnification-inflammatory infiltrate Lympho- plasmocitary (the most representative part)

After evaluating each criterion of inflammation (presence of inflammatory cells, necrosis, neovascularization, fibrosis and adipose infiltration) according to ISO standards and calculating the final score, all tested materials were ranked as slight to moderate irritants for the soft tissues, with G2 and Beautifil II having almost the same scores regarding the biological behaviour. No statistically significant differences were found between the 3 groups regarding the inflammatory response of the subcutaneous or muscular tissue exposed to the experimental materials by implantation tests (Table 2 and Table 3).

Table 2. Scores of inflammation and materials ranking after subcutaneous implantation

Parameter	G1 subcutaneous Mean± SD	G2 subcutaneous Mean± SD	Beautifil II subcutaneous Mean± SD
PMN	0.67 +/-0.58	1+/-0.58	1+/-0.57
Lymphocytes	2.33+/-0.58	2+/-1	2/-1
Plasmocytes	1+/-0	1+/-0	1+/-0
Macrophages	0	0	0
Giant cells	0.67+/-0.58	0	0
Necrosis	0	0	0
SUB-TOTAL(x2)	9.33+/- 1.15	6.66+/-2.30	7.33+/-1.54
Neovascularization	1.33+/-0.58	1.33+/-0.58	1.33+/-0.58
Fibrosis	1+/-0	1+/-0	1+/-0
Adipose infiltration	0	0	0
SUB-TOTAL	2.33+/-0.57	2+/-0	2.33+/-0.57
TOTAL	11.6+/-1.52	9 +/- 1.73	9.6+/-0.57

Table 3. Scores of inflammation and materials ranking after intramuscular implantation

Parameter	G1 im Mean\pm SD	G2 im Mean\pm SD	Beautifil II im Mean\pm SD
PMN	1+/-0	0.33+/-0.58	0.33+/-0.58
Lymphocytes	1.67+/-0.58	1.67+/-0.58	1.33+/-0.58
Plasmocytes	1+/-0	1+/-0	0.67+/-0.58
Macrophages	0	0	0.33+/-0.58
Giant cells	0	0	0
Necrosis	0	0	0
SUB-TOTAL(x2)	7.33+/-1.15	6+/-2	5.33+/-2.30
Neovascularization	1.33+/-0.58	1+/-0	1.33+/-0.58
Fibrosis	1+/-0	1+/-0	1+/-0
Adipose infiltration	0	0.33+/-0.58	0
SUB-TOTAL	2.33+/-0.57	2.66+/-1.15	2.33+/-0.57
TOTAL	9.6+/-4.35	8.3+/-1.52	7.6+/-2.86

The favorable biological behavior induced by the giomers is due to their chemical and physical properties.

One of the most critical aspects of using polymer based composites for medical purposes is the release of residual monomer, which can induce cytotoxic, inflammatory, allergic and even mutagenic reactions [22]. The optimal conversion degree observed for the experimental giomers correlates with a lesser quantity of residual monomer release. Also, the quantity of residual monomer released by the giomers is influenced by the hydrophilic/hydrophobic character as well as by the amount, size and flexibility of the each monomer's specific molecules. Bis-GMA oligomers have large, rigid molecules and stronger hydrophobic character compared to the other monomers. This leads to a significantly smaller quantity of extracted Bis-GMA monomer in a hydrophilic medium [23], [24].

The biological response to the implanted materials depends not only on the chemical properties of the materials but also on the response to the trauma of surgery. Proper surgical technique, adequate preparation of the samples ensures valid results for the implantation test [25, 26].

CONCLUSIONS

Seven days after polymerization, a more pronounced increase in DC was found in G1 (8.3%) and G2 (7.8%), compared to Beautifil II (4.5%), which means that the polymerization was efficient and exhibited an ascending course. At the end of the investigation period, the decreasing order of water sorption for the studied giomers was: G2>Beautifil II> G1. Still, the process of water sorption reached a stable level in case of G2, while for G1 and Beutifil II an ascending trend was noted, with the probability of increase in the following days, in case the study would have continued. Comparing the SEM images before and after 7 days of storage in water, a swelling of the polymer matrix was observed, but without detachment of any portions of the material. The highest radiopacity was recorded in the case of the commercial giomer Beautifil II, but also all the tested giomers have values of radiopacity over those of enamel and dentin. All the tested materials were slight to moderate irritants for living tissues, with G2 and Beautifil II inducing almost the same reactions.

Since the difference in the composition of the experimental giomers is given only by the pre-reacted glass used, the small differences between the results obtained from the tests performed are given by the two polyalkenoic acids used in the syntesis of the pre-reacted glasses.

Promising results make G1 and G2 a possible alternative to Beautifil II, that can be further improved.

EXPERIMENTAL SECTION

Materials

2,2-bis[4-(2-hydroxy-3-methacryloxypropoxy)phenyl]propane (Bis-GMA), triethylene glycol dimethacrylate (TEGDMA) camphorquinone (CQ), dimethylaminoethyl-methacrylate (DMAEM), butylated hydroxy toluene (BHT), were purchased from Sigma Aldrich Chemical Co. (Taufkirchen, Germany) and used without additional purification.

Beautifil II giomer - shade A30- was purchased from Shofu, Japan, Bach no. 051215 (PN1420 2015-04).

Preparation of experimental giomer pastes

The experimental light-curing giomers were prepared as monopastes by mixing the resin matrices with the hybrid fillers.

The experimental resins were formulated using monomer mixtures of 2,2-bis[4-(2-hydroxy-3-methacryloxypropoxy)phenyl]propane (Bis-GMA) as

base monomer and triethylene glycol dimethacrylate (TEGDMA)) as diluting monomer. The ratio between the base monomer and diluting monomer was 70/30. In the composition of the resins, besides the methacrylic oligomers and monomers, a photosensitizer, camphorquinone (CQ) in an amount of 0.5% (by weight), and an accelerator dimethylaminoethyl-methacrylate (DMAEM), in an amount of 1% (by weight), were added. Butylated hydroxy toluene (BHT) was added in a quantity of 650 ppm related to the monomers mixture.

For the obtaining of hybrid fillers, the pre-reacted glass ionomer fillers (PRG1 and PRG2 respectively), fluorohydroxyapatite (FHAP), the silanized radiopaque glass powder and the silanized quartz particles (surface area 6.25 m²/g, particle sizes between 10-40 µm) were mixed and then sifted together.

The method of obtaining and characterization of the barium fluoro-alumino-boro-silicate glass (radiopaque glass) having the composition SiO₂ (25%), B₂O₃ (11%), Al₂O₃ (14%), BaF₂ (50%) was described in a previous study [27].

The experimental pre-reacted glass ionomer fillers (PRG1 and PRG2) were obtained following literature procedures [7]. PRG1 was prepared by hand-mixing the 50% aqueous solution of a polyalkenoic acid P(AA-co-IA-co-Leu), synthesized from N-acryloyl-L-leucine (Leu), acrylic acid (AA) and itaconic acid (IA) (molar ratio of 0.5:4:1) with the superficially active glass powder having the oxidic composition SiO₂ (49%), Al₂O₃ (22%), CaF₂ (29%) in a weight ratio of 1/2.4. PRG2 was obtained in a similar manner to PRG1, with the exception of using a polyalkenoic acid grafted with methacrylic groups P(AA-co-IA-co-LeuM) instead of P(AA-co-IA-co-Leu) [28], [29].

The method of obtaining and the characterization of FHAP was shown elsewhere [30].

Silanation of quartz and of BaF₂-based glass was carried out with 3-methacryloyloxypropyl-1-trimethoxy-silane (A-174 silane).

The composition of the experimental giomer pastes is presented in Table 4:

Table 4. The composition of the experimental giomer pastes

No.	Resin %		Hibrid fillers %				
	Bis-GMA	TEGDMA	PRG1	PRG2	FHAP	BaF ₂ glass	Quartz
G1	14	6	16	-	8	40	16
G2	14	6	-	16	8	40	16
Beautifil II*	1-10	1-5	Aluminofluoro-borosilicate glass 60-70 % (w) Al ₂ O ₃ 1-5 % (w)				

*Beautifil II giomer (A30) - Shofu, Kyoto, Japan.

Methods for characterizing the investigated material

1. Degree of conversion (DC)

The conversion of the resin in giomers was assessed by determination of the residual double bonds (RDB) using the infrared spectroscopy method. The baseline method for determining the peak absorbance was used. The amount of the RDB was determined as percentage of the amount of the originally methacrylic groups present in the monomer mixtures.

The decrease of the absorbance intensity of the methacrylate group $C = C$ absorbance (A_{meth}) from $1635 - 1640\text{ cm}^{-1}$ was monitored. The absorption band of the phenyl group (A_{arom}) from $1605 - 1610\text{ cm}^{-1}$ was used as internal standard.

The residual double bonds were calculated using the formula (1):

$$RDB\% = (A_{meth} / A_{arom})_F / (A_{meth} / A_{arom})_I \times 100 \quad (1)$$

where F means the final state (after curing) and I means the initial state of the material (before curing).

The degree of conversion (DC) was calculated using the relation:

$$DC\% = 100\% - RDB\% \quad (2)$$

ATR-FTIR spectra of giomers (pastes and solids) were recorded on FTIR spectrophotometer (Jasco FTIR-610) equipped with an ATR (attenuated total reflectance) attachment with a horizontal ZnSe crystal (Jasco PRO400S). The resolution of the spectra was 4 cm^{-1} . and scans were repeated 100 times. The appropriate amount of the samples were placed on the ZnSe crystal. and then the FTIR spectrum was measured.

2. Water sorption

Preparation of the Samples

A total of 30 disc shaped samples were prepared (10 from each giomer). Specimens were placed in cylindrical molds (16mm diameter X 1.0mm thickness) and the material packed was slightly overfilled into a brass ring mold set on a piece of transparent polyester film on a glass microscopic slide. It was then covered with another piece of polyester film while being pressed by another glass slide. The specimens were then light cured for 20 seconds by an LED dental light-curing lamp (Guilin Woodpecker Medical Instruments Co., Guangxi, China) with an irradiance of 950 mw/cm^2 of five points on the disc surface. After removing the glass and the celluloid band, the samples were light cured again for 20 sec and polymerisation of the giomers was achieved. Soflex discs (3M ESPE, St. Paul, MN, USA) were used to finish the specimens and to obtain uniform thickness.

Water sorption values were determined according to ISO 4949:2009 at 1, 2, 3, 4, 5, 6, 7 days of storage in water. The values for water sorption (Wsp), for each of the specimens were calculated using the formula (3):

$$Wsp = \frac{M1 - M2}{V} \quad (3)$$

M1 - the specimen mass after water immersion at a moment in time [μg]

M2 - the final mass of dried specimen [μg],

V - volume of the specimen [mm^3].

3. Scanning Electron Microscopy (SEM)

The surfaces structure of the giomer materials, before and after storage in distilled water/ after a 7-day period, was recorded on a scanning electron microscope (Quanta 3D FEG).

4. Radiopacity

Disc samples of giomers measuring 15 mm in diameter and 1 mm in thickness were made in teflon molds by exposing to a visible radiation generated by LED.E dental lamp for 20 seconds of five points on the disc surface. The giomers samples and the aluminum step wedges (thickness increasing by 1mm for each step to a maximum of 10 mm) were placed on an „Intraoral sensor” in vitro. The images were taken using the intraoral sensor system Ezsensor 1.5 Vatech E-Woo (Korea) and a dental X-ray machine HELIODENT DS Sirona (Germany) at 70 kV, 7 mA, 0.04 sec with a target-sensor distance at 30 cm. The mean gray values of each aluminum stepwedge and selected materials were measured by outlining a region of interest using images software. The regions were selected by avoiding areas containing air bubbles inside the material and the average gray value were recorded for every sample. For each radiograph images the calibration curve generated by the grey scale values as a function of the aluminum thickness was calculated. The radiopacity values of the samples were expressed in terms of the equivalent thickness of aluminum per 1 mm unit thickness of material [31].

5. Implantation tests

Sample preparation

Cylindrical samples (3 mm high/ 2 mm diameter) of the three giomers (A1, B1 and Beautifill) were prepared for subcutaneous and intramuscular implantation. Each sample was and carefully prepared to avoid any sharp edges. Before implantation, all instruments and samples used were sterilized

using plasma (Sterrad, J&J, Irvine, CA, USA). The animal study was carried out following the guidelines of the Ethics Committee of "Iuliu Hatieganu" University of Medicine and Pharmacy, Cluj-Napoca.

Subcutaneous implantation test

18 male Wistar Rats, weighing about 250g each, were randomly divided into 3 groups of 6 animals, according to the giomer tested. Before surgery, the rats were anesthetized via intraperitoneal ketamine HCL (50 mg/kg) and xylazine (7 mg/kg) injection. When animals became unresponsive, a 30 mm × 30 mm area on the dorsal area was shaved and disinfected with povidone-iodine. Sterilized samples of FRC were placed subcutaneously using a microchip syringe, complying with the asepsis and antisepsis regulations. After placing the samples, the wound area was disinfected with povidone-iodine. No suture was needed [32].

Intramuscular implantation test

Another 18 male Wistar Rats, weighing about 250g each, were randomly divided into 3 groups of 6 animals, according to the giomer tested. Before surgery, the rats were anesthetized via intraperitoneal ketamine HCL (50 mg/kg) and xylazine (7 mg/kg) injection. When animals became unresponsive, a 35 mm × 35 mm area on the hind leg was shaved and disinfected with povidone-iodine. The skin was sharply incised and the subjacent gluteal muscle exposed. Sterilized samples of giomers were placed intramuscularly using blunt longitudinal dissection of the muscle. After placing the samples, the wound area was disinfected with povidone-iodine. Suture was performed using resorbable material for the muscle and unresorbable for the skin.

After placing the samples, animals were housed in polysulfone type III-H open-top cages (Tecniplast, Buguggiate, Italy) and had access to filtered tap water in bottles and pelleted feed (Cantacuzino Institute, Bucharest, Romania) ad libitum. The bedding was a standard wood chips aseptic bedding (Lignocel®; J. Rettenmaier & Söhne GmbH + Co. KG, Rosenberg, Germany). The rats were kept in the Laboratory Animal Facility of the "Iuliu Hatieganu" University of Medicine and Pharmacy, Cluj-Napoca, Romania, at a standard room temperature of 22°C±2°C and a relative humidity of 55%±10%, in a 12:12-hour light: dark cycle (lights on, 7 am to 7 pm), at a light intensity of 300 lx at 1 m above the floor. All experimental protocols were approved by the Ethics Committee of "Iuliu Hatieganu" University of Medicine and Pharmacy and were conducted in accordance with the EU Directive 63/2010 (203/20.04.2015). For environmental enrichment, autoclaved braided cotton dental rolls were used (Celluron®, Hartmann, Heidenhelm, Germany). All

animal-handling procedures were performed according to the European and Romanian guidelines.

During the experiment period, assessments were made regarding the local changes, which occurred at the implant site and their impact upon the general status of the animals. All 30 animals were sacrificed 30 days after implantation, following the guidelines of the Ethics Committee. The skin overlaying the implants was shaved and the tissues surrounding the implants were dissected. Tissues surrounding the implants were macroscopically assessed. Implants were sharply removed together with the adjacent tissues. Tissue samples from the areas that contained the implants were fixed in 10% formalin for 5 days. Implants were gently removed before the tissue samples were embedded in paraffin. Histological sections were cut at 4 μm , mounted on slides and stained with hematoxylin-eosin [33], [34].

The most representative histological sections were evaluated. The number and type of inflammatory cells found (polymorphonuclear cells, lymphocytes, plasma cells, macrophages and giant cells), the presence of new blood vessels, edema, necrosis and the presence of a fibrous capsule (indicating a repair process) were microscopically assessed. Each criterion was evaluated according to ISO standards and irritant ranking of the materials assessed accordingly [35].

The inflammation at the implant site was quantified assessing scores:

0. Absent: no sign of inflammation
1. Mild: 1-5 inflammatory cells of each type/ high powered field (hpf)[$\times 400$]/ minimal capillary proliferation (1-3 buds)/ no edema/ early developed capsule
2. Moderate: 5-10 inflammatory cells of each type/hpf[$\times 400$]/ groups of 4-7 capillaries with supporting fibroblastic structures/ mild edema/ partially formed capsule
3. Severe: heavy or packed inflammatory infiltrate >20 cells/hpf[$\times 400$]/ broad band of capillaries with supporting structures/ severe edema/ completely formed capsule.

The scores given for each criterion were summed up and the results classified each material tested as being:

- Non-irritant (0 up to 2.9)
- Slight irritant (3 to 8.9)
- Moderate irritant (9 to 15)
- Severe irritant (over 15)

The data were statistically analyzed by one-way analysis of variance (ANOVA), with Tukey's test with the level of significance set at 0.05 in order to determine the significant differences between the mean values of the tested materials.

REFERENCES

1. S. Kimyai; M. Bahari; F. Naser-Alavi; S. Behboodi; *J. Clin. Exp. Dent.*, **2017**, 9(2), e249-253.
2. M.E. Rusnac; C. Gasparik; A.G. Delean; A.I. Aghiorghiesei; D. Dudea; *Med. Pharm. Rep.*, **2021**, 94, 99–105.
3. M.E. Rusnac; D. Prodan; S. Cuc; I. Petean; C. Prejmerean; C. Gasparik; M. Moldovan; *Mater.*, **2021**, 14(9), 2399.
4. U.M. Abdel-Karim; M. El-Eraky; W.M. Etman; *Tanta Dent. J.*, **2014**, 11, 213–222.
5. N.Gonulol; S.Ozer; E. Sen Tunc; *J. Esthet. Restor. Dent.*, **2015**, 27(5), 300-306.
6. D.A. Saba; F.K. Abdel Gawad; M.A. Abd Ellatif; *Egypt. Dent. J.* **2017**, 63, 205–214.
7. L. Colceriu-Burtea; C. Prejmerean; D. Prodan; I. Baldea; M. Vlassa; M. Filip; I. Ambrosie; **2019**, *Mater.*, 12(23), 4021.
8. Z. Tarle; M. Par; Degree of Conversion. In *Dental Composite Materials for Direct Restorations*, V. Miletic Eds.; Springer International Publishing AG, Cham, Switzerland, **2017**, Chapter 5, pp. 63-85.
9. P. Panpisut; A. Toneluck; *Dent. Mater. J.*, **2020**, 39(4), 608-615.
10. T. Hitij; A. Fidler; *Clin. Oral. Investig.*, **2013**, 17, 1167-77.
11. T. Yildirim; M.K. Ayar; M.S. Akdag; C. Yesilyurt; *Niger. J. Clin. Pract.*, **2017**, 20, 200-204.
12. J.L. Ferracane; *Dent. Mater.*, **2006**, 22.3, 211-222.
13. P. Yu; A.U.J.Yap; X.Y. Wang; *Oper. Dent.*, **2017**, 42(1), 82-89.
14. M.E. Rusnac; D. Prodan; M. Moldovan; S. Cuc; M. Filip; C. Prejmerean; D. Dudea; *Appl. Sci.*, **2021**, 11, 8921.
15. Noor Saira Wajid Najma Hajira; N Meena; *Int. J. Dent. Oral Health*, **2015**, 2(4): doi <http://dx.doi.org/10.16966/2378-7090.166>.
16. ISO 4049 Dentistry — Polymer-based restorative materials. International Organisation for standardization, pp 18-21.
17. S.A. Kareem; R.H. Jehad; *J. Bagh. Coll. Dent.*, **2012**, 24(3), 25-28.
18. H. Cui; G.S.P. Cheung; Lee-hoi Kei; S. Wei; *J. Adhes. Dent.*, **2002**, 4(1), 61-71.
19. F.L.E. Florez; H. Kraemer; R.D.Hiers; C.M.Sacramento; A.J.Rondinone; K. Gonzales Silvério; S.S. Khajotia; *Sci. Rep.*, **2020**, 10(1) doi:10.1038/s41598-020-70487-z.
20. M.A. Zankulia; H. Devlin; Silikasa N; *Dent. Mater.*, **2014**, 30, e324–e329.

21. ISO 4049 Dentistry — Polymer-based restorative materials. International Organisation for standardization, pp 4.
22. S.K. Gupta; P. Saxena; V.A. Pant; A.B. Pant, *Toxicol. Int.*, **2012**, 19(3), 225.
23. M. Moldovan; I.R. Balazs; A. Soanca; A. Roman; C. Sarosi; D. Prodan; M. Vlassa; I. Cojocaru; V. Saceleanu; I. Cristescu; *Mater.*, **2019**, 12 (13), 2109.
24. M.A. Moldovan; A.B. Bosca; R.C. Roman; H. Rotar; C. Prejmerean; D. Prodan; P. Bere; C. Cosma; D. Festila; M.C. Ghergie; *Mater. Plast.*, **2020**, 57, 131-139.
25. B. Swetha; S. Mathew; B.V. Sreenivasa; N. Shruthi; S.H. Bhandi; *Int. Dent. Med. J. Adv. Res.*, **2015**, 1, 1-6.
26. S. Tamilselvam; M.J. Divyanand; P. Neelakantan; *J. Clin. Pediatr. Dent.*, **2013**, 37(4), 403-406.
27. C. Prejmerean; D. Prodan; M. Vlassa; M. Streza; T. Buruiana; L. Colceriu; V. Prejmerean; S. Cuc; M. Moldovan; *Meas. Sci. Technol.*, **2016**, 27, 124008, doi:10.1088/0957-0233/27/12/124008.
28. T. Buruiana; M. Nechifor; V. Melinte; V. Podasca; E.C. Buruiana; *J. Biomater. Sci. Polym.*, **2014**, 25(8), 749-65. doi: 10.1080/09205063.2014.905029.
29. I. Hodisan; C. Prejmerean; I. Petean; D. Prodan; T. Buruiana; L. Colceriu; L. Barbu-Tudoran; M. Tomoaia-Cotisel; *Stud. Univ. Babes-Bolyai, Chem.*, **2017**, 62 (4), 143-154.
30. C. Prejmerean; M. Moldovan; C. Petrea; D. Prodan; L. Silaghi-Dumitrescu; V. Eugeniu; G. Furtos; S. Boboia; R. Silaghi-Dumitrescu; *Mater. Plast.*, **2011**, 48(4), 279-284.
31. V. Prejmerean; L. Silaghi-Dumitrescu; D. Prodan; C. Prejmerean; M. Moldovan; *Key Eng. Mater.*, **2014**, 587, 121-127.
32. N. Simsek; L. Akinci; O. Gecor; H. Alan; F. Ahmetoglu; E. Taslidere; *Eur. J. Dent.*, **2015**, 9(1), 31-35.
33. M.A. Lazar; H. Rotaru; I. Bâldea; A.B. Bosca, C.P. Berce; C. Prejmerean; D. Prodan; R.S. Câmpian; *J. Craniofac. Surg.*, **2016**, 27(7), 1694-1699.
34. M.A. Lazar; M. Filip; M.C. Vlassa, L.A. Sorcoi, R.S. Câmpian, C. Prejmerean; *Rev. Rom. Mater.*, **2016**, 46(2), 142-151
35. ISO 10993-6:2007, Biological evaluation of medical devices- Part 6: Tests for local effects after implantation.

ANTIMICROBIAL ACTIVITY AND THE QUANTITATIVE ANALYSES OF PHENOLIC COMPOUNDS AND HEAVY METALS OF RED MULBERRY EXTRACTS (*MORUS RUBRA* L.) FROM SERBIA

DANICA DIMITRIJEVIĆ^a, DANIJELA KOSTIĆ^b, DUŠAN PAUNOVIĆ^a,
MILAN MITIĆ^b, JOVANA KRSTIĆ^a, IVANA RAŠIĆ MIŠIĆ^b,
BILJANA ARSIĆ^{b,*}

ABSTRACT. All investigated extracts of red mulberry (*Morus rubra* L.) contain a high content of total phenols. The highest content of total phenols was shown by red mulberry in the ethanolic extract (50%). Certain extracts of the fruit of red mulberry (aqueous, ethanolic 50%, acetonic 50% and acetonic) contain very small quantities of anthocyanins. Four phenolic acids were identified in the extracts of red mulberry: chlorogenic, neochlorogenic, cryptochlorogenic acid and caffeic acid, and four flavonoids using HPLC analysis: quercetin-3-O-rutinoside, quercetin-3-O-glucoside, quercetin-3-O-rhamnoside, and kaempferol-3-O-rutinoside. Cyanidin-3-O-glucoside was identified in the methanolic extract of red mulberry. The content of heavy metals (Fe, Cu, Mn, Cd, Ni, Zn and Pb) was determined using atomic absorption spectroscopy in fruits and the extracts of red mulberry. Mulberry fruit has been shown the highest content of Fe and low content of toxic metals. The content of metals is the highest in the majority of cases in the extracts of acetone and acetone 50%. The methanolic extract of red mulberry shows the antimicrobial properties against all investigated bacteria except *Staphylococcus aureus*. Obtained results show that fresh fruits of red mulberry and its extracts can be used in nutrition and the preparation of pharmaceutical formulations.

Keywords: *Morus rubra* L., heavy metals, antimicrobial activity.

^a University "Union-Nikola Tesla", Faculty of Applied Sciences, Cara Dušana 62-64, 11158, Belgrade, Republic of Serbia

^b University of Niš, Faculty of Sciences and Mathematics, Department of Chemistry, Višegradska 33, 18106, Niš, Republic of Serbia

*Corresponding author: biljana.arsic@pmf.edu.rs

INTRODUCTION

Morus, a genus of flowering plants in the family Moraceae, comprises 10–16 species of deciduous trees commonly known as mulberries. The most popular species of genus *Morus* are *Morus alba* L. (white mulberry), *Morus rubra* L. (red mulberry), and *Morus nigra* L. (black mulberry). Mulberry is found from temperate to subtropical regions of the Northern hemisphere to the Southern hemisphere's tropics. They can grow in a wide range of climatic, topographical, and soil conditions.

Mulberry fruit may be colored white, red, or black when ripe. Deep-colored fruits are good sources of phenolics [1-5]. Mulberry fruit has been used as a folk remedy to treat oral and dental diseases, diabetes, hypertension, arthritis, and anemia [6]. The primary use of mulberry globally is as feed for the silkworm, but depending on the location, it is also appreciated for its fruit (consumed fresh, in juice, or as preservatives), as a delicious vegetable (young leaves and stems), for its medicinal properties in infusions (mulberry leaf tea), for landscaping and as animal feed [7]. Mulberry fruit can be used for making jams, jelly, pulp, fruit drinks, fruit sauces, and cakes. Many desserts are made from Persian mulberries, sauces, piemaking, cakes and jelly, and fruit teas [8-10].

Until now, methanolic extracts of red mulberry were investigated from the territory of Turkey, and total phenols were determined (1035 mg GAE/100 g) and total flavonoids (219 mg CE/100 g) [11].

The content of total phenols (215 mgGAE/100 g) and anthocyanins (10.9 mg cyanidin-3-O-glucoside/100 g) was determined in the ethanolic solution, and the antioxidant activity of this solution was found (442 mg expressed as mg Trolox Eq/100 g) [12].

It was also investigated the aqueous acetonic extract, and it was determined the content of total phenols (160.3 mg GAE/100 g), and anthocyanins (9.88 mg cyanidin-3-O-glucoside/100 g) [9].

Based on the available literature, we noticed that incomplete data are present on the analyses of various extracts, so we decided to perform a systematic analysis of aqueous, methanolic, ethanolic, acetonic, aqueous-ethanolic, aqueous-methanolic, and aqueous-acetonic extracts of red mulberry regarding the content of total phenols, flavonoids, anthocyanins, and antioxidant activity. Also, we aimed to have a microbiological analysis of obtained extracts.

With the aim of safe use of fruits of red mulberry and its extracts, it was necessary to analyze the content of metals with special attention to toxic metals.

RESULTS AND DISCUSSION

The results of the determination of total phenolic compounds, flavonoids, anthocyanins, and antioxidant activity (RSC-Radical Scavenger Capacity) in different extracts of red mulberry fruit are presented in Table 1.

Table 1. Content of total phenols, flavonoids, and anthocyanins, and antioxidant activity of red mulberry fruit extracts (*Morus rubra* L.).

Solvent	Total phenols (mgGAE/100 g)	Flavonoids (mgCE/100 g)	Monomeric anthocyanins (mgCy-3-O- Glu/100 g)	DPPH (mgTE/100 g)	RSC (%)
Water	210.4±0.5	192±2	2.6±0.2	118±1	54.11±0.09
Ethanol 50%	320.8±0.8	99.83±0.09	5.3±0.1	183±1	78.4±0.7
Ethanol	109.8±0.4	112.43±0.06	-	175±3	79.6±0.4
Methanol 50%	56.40±0.05	38.4±1.5	-	43.7±0.4	85.6±2.4
Methanol	90.3±0.2	143±2	-	55.4±0.6	87.56±0.03
Acetone 50%	85.9±0.7	49.8±0.1	1.7±0.3	60.00±0.00	89.4±0.4
Acetone	71.4±2.4	45.0±0.7	5.3±0.6	62.2±0.1	86.80±0.09

The content of the total phenols of *Morus rubra* L. was found to be 56.40 to 320.8 mg GAE/100 g for the methanol-water (50/50 v/v%) and ethanol-water (50/50 v/v%) extract, respectively.

Total flavonoid contents in *Morus rubra* L. were ranging from 38.4 mg CE/100 g (methanol-water (50/50 v/v%)) to 192 mg CE/100 g fresh fruit (water extract). The extracts of *Morus rubra* L. showed anthocyanins content in water, ethanol-water (50/50 v/v%), acetone-water (50/50 v/v%) and acetone extracts (2.6 mg, 5.3 mg, 1.7 mg and 5.3 mg of cyanidin-3-O-glucoside/100 g, respectively).

Comparing the results on the content of total phenols in the fruit of red mulberry from Southeast Serbia with the results published by authors from other countries, we concluded that our results are lower than theirs. Methanol extract of red mulberry fruit from Turkey contains 1035 mg GAE/100 g [12], while ethanol extract contains 169 mgGAE/100 g [11]. Acetone extract 50% showed slightly higher values of phenol content compared to our results (160 mg GAE/100 g) [9]. The differences in the content of total phenols are most likely due to the different methods of extraction, the climatic area in which the tree grows, and the type of soil on which the wood is grown.

Ethanol 50% and acetone extracts have equal amounts of anthocyanins (5.3 mg cyanidin-3-O-glucoside/100 g). The aqueous extract contains 2.6 mg while acetone 50% extract contains 1.7 mg of cyanidin-3-O-glucoside per 100 g of fresh fruit. Acetone 50% red mulberry fruit extract from Turkey contains 9.88 mg cyanidin-3-O-glucoside/100 g [9]. Unlike the ethanol extract from this paper which did not show anthocyanin content, the ethanol extract of red mulberry fruit from Turkey contains 10.9 mg of cyanidin-3-O-glucoside/100 g [11].

Antioxidant activity, using the DPPH method, is relatively high and ranges from 54.11% in the aqueous extract to 89.4% in acetone 50% in red mulberry fruit extract. Ethanol extract of red mulberry from Turkey, in addition to the content of total phenols, showed higher antioxidant activity compared to our results (442 mgTE/100 g) [11].

Tables 2 and 3 show phenolic acids and flavonoids identified in methanolic and acetone extract of the red mulberry fruit.

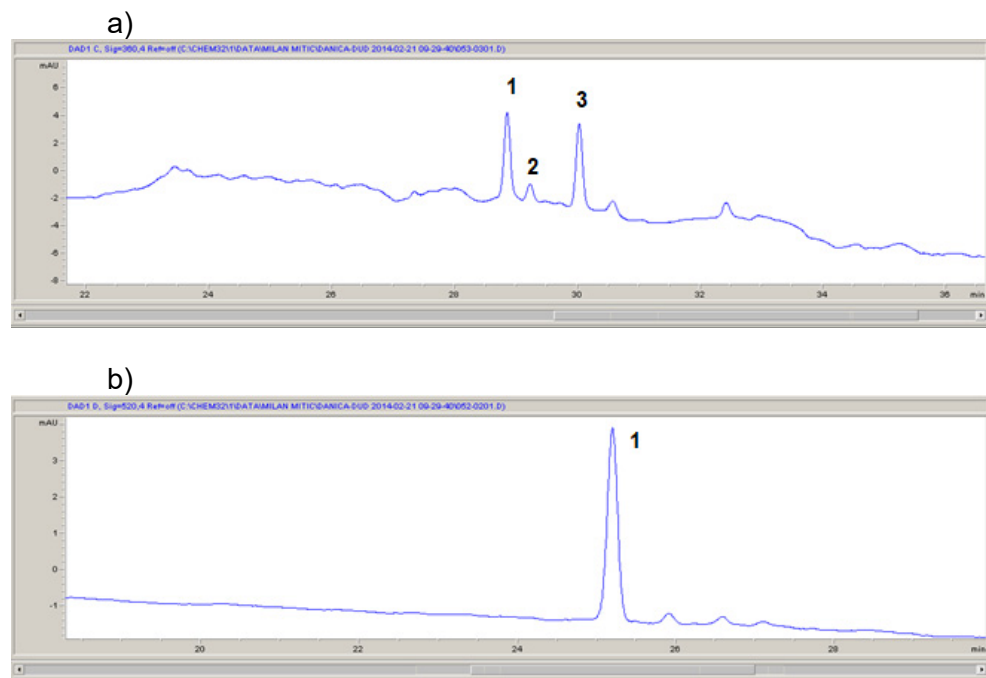


Figure 1. HPLC analysis of methanol extract of red mulberry fruit (*Morus rubra* L.) at a) 360 nm: quercetin-3-O-rutinoside (1), quercetin-3-O-glucoside (2), kaempferol-3-O-rhamnoside (3); b) 520 nm: cyanidin-3-O-glucoside (1).

Table 2. The identified phenolic acids content in red mulberry fruit extracts (mg/kg).

Phenolic acids (320 nm, mg/kg)	Red mulberry	
	Methanol	Acetone
Chlorogenic acid	9.22	-
Caffeic acid	3.87	-
Neochlorogenic acid	6.76	15.18
Cryptochlorogenic acid	-	8.57

HPLC analysis showed that the methanol extract contained the highest amount of chlorogenic acid and the lowest amount of caffeic acid. Cryptochlorogenic acid is not present in the methanolic extract of the red mulberry fruit. Acetone extract of red mulberry fruit contains two acids: neochlorogenic and cryptochlorogenic.

Table 3. Content of the flavonoids identified in red mulberry fruit extracts (mg/kg).

Anthocyanins (520 nm, mg/kg)	Red mulberry	
	Methanol	Acetone
Quercetin-3-O-rutinoside	12.59	13.94
Quercetin-3-O-glucoside	6.10	5.78
Quercetin-3-O-rhamnoside	-	22.85
Kaempferol-3-O-rutinoside	18.52	-

Methanol extract of red mulberry fruit contains the following flavonoids (Figure 1a): quercetin-3-O-rutinoside, quercetin-3-O-glucoside, and kaempferol-3-O-rutinoside. Of these three flavonoids, kaempferol-3-O-rutinoside was the most abundant, and quercetin-3-O-glucoside was the least abundant. Acetone extract does not only contain kaempferol-3-O-rutinoside. Among the flavonoids in the acetone extract, quercetin-3-O-rhamnoside was the most abundant, and the quercetin-3-O-glucoside was the least abundant.

HPLC analysis of red mulberry fruit extracts for anthocyanin content revealed that the methanol extract contained cyanidin-3-O-glucoside (Figure 1b) (6.10 mg/kg).

Thabti et al. [13] isolated neochlorogenic, cryptochlorogenic, and caffeic acids from the red mulberry fruit. They also identified flavonoids: quercetin-3-O-rutinoside, quercetin-3-O-glucoside, and kaempferol-7-O-glucoside, which largely agrees with our results. Several authors have identified cyanidin-3-O-glucoside in red mulberry fruit extracts.

The content of heavy metals such as iron, zinc, copper, manganese, nickel, lead, and cadmium in fruit and extracts of red mulberry fruit is shown in Table 4.

Table 4. Content of heavy metals in fruit and extracts of the red mulberry fruit.

Red mulberry							
System	Fe (mg/100 g)	Cu (mg/100 g)	Mn (mg/100 g)	Cd (µg/100 g)	Ni (mg/100 g)	Zn (mg/100 g)	Pb (mg/100 g)
Fruit	57±6	1.5±0.2	2.0±0.2	1.8±0.2	0.37±0.03	5.04±0.08	0.20±0.02
Water extract	1.0±0.2	0.01±0.00	0.09±0.01	-	0.05±0.01	0.43±0.03	-
Ethanol 50% extract	0.70±0.01	0.02±0.00	0.15±0.01	-	0.04±0.00	0.43±0.03	-
Ethanol extract	0.32±0.04	0.01±0.00	0.18±0.01	-	0.02±0.00	0.57±0.02	-
Acetone 50% extract	5.8±0.2	0.05±0.01	0.39±0.02	0.29±0.04	0.06±0.01	0.55±0.03	-
Acetone extract	5.7±0.4	0.28±0.01	0.59±0.07	0.27±0.06	0.05±0.01	1.04±0.02	-
Methanol 50% extract	0.31±0.04	0.09±0.01	0.09±0.01	-	0.04±0.00	0.08±0.01	-
Methanol extract	0.32±0.08	0.11±0.01	0.25±0.03	-	0.02±0.00	0.12±0.01	-

Red mulberry fruit contains the highest amount of iron (57 mg/100 g) and the lowest amount of cadmium (1.8 µg/100 g). The content of heavy metals in the fruit of red mulberry decreases in the following order: iron> zinc> manganese> copper> nickel> lead> cadmium (Table 4).

Ercisli et al. [11] published a significantly lower iron content in red mulberry fruit (5.00 mg/100 g). The manganese content was 5.00 mg/100 g which is higher than our results (2 mg/100 g). The amount of zinc confirmed in red mulberry fruit was 3.00 mg/100 g [11] which is slightly less than our results. Authors from Turkey have published lower iron, zinc, and copper values in red mulberry fruit (4.5, 3.2 and 0.4 mg/100 g, respectively) [12]. The amount of manganese was slightly higher than our values (4.00 mg/100 g).

The amount of iron in the extracts ranges from 0.31 to 5.8 mg/100 g in 50% methanol and 50% acetone extract, respectively. Aqueous and ethanolic extracts of red mulberry fruit contain the least amount of copper

(0.01 mg/100 g), while acetone extract contains 0.28 mg/100 g. The manganese content ranges from 0.09 mg/100 g in methanol 50% and aqueous extract to 0.59 mg/100 g in acetone extract. The presence of cadmium was detected only in acetone and acetone 50% extract (0.27 and 0.29 µg/100 g, respectively). The amount of nickel in red mulberry fruit extracts ranges from 0.02 in methanol and ethanol extract to 0.06 mg/100 g in acetone 50% extract. Methanol 50% extract contained the lowest amount of zinc (0.08 mg/100 g), while acetone extract showed the highest amount of zinc (1.04 mg /100 g). Lead content was not detected in any extract except the fruit (0.20 mg/100 g).

The microbiological tests show that methanol 50% mulberry extract shows antibacterial effect only on the bacterium *S. typhimurium*. Methanol extract of red mulberry shows the antibacterial effect on all tested bacteria except *Staphylococcus aureus*. At given concentrations, aqueous extracts of red mulberry fruit did not show antimicrobial activity.

In Table 5, the antimicrobial activity of red mulberry fruit extracts was given.

Table 5. Antimicrobial activity of red mulberry fruit extracts (*Morus rubra* L.).

Test microorganisms	Water		Methanol		Methanol 50%		DMSO	Tetracycline
	20 µl	50 µl	20 µl	50 µl	20 µl	50 µl	50 µl	30 µg
<i>Salmonella typhimurium</i> NCTC 6017	-	-	-	16 mm	16 mm	-	-	28 mm
<i>Pseudomonas aeruginosa</i> ATCC 9027	-	-	12 mm	16 mm	-	-	-	19 mm
<i>Bacillus subtilis</i> ATCC 6633	-	-	-	17 mm	-	-	-	36 mm
<i>Staphylococcus aureus</i> ATCC 6538	-	-	-	-	-	-	-	34 mm
<i>Escherichia coli</i> ATCC 8739	-	-	12 mm	16 mm	-	-	-	30 mm

CONCLUSIONS

In this paper, quantitative determination of phenolic compounds was performed in different fruit extracts of red mulberry (*Morus rubra* L.) from the Southeast region of Serbia, as well as the determination of the antioxidant

activity of tested extracts using the spectrophotometric methods. The content of heavy metals in the fruit and extracts was determined by the AAS method. Also, the antimicrobial activity of the tested extracts was determined. The results indicate red mulberry's fresh fruits and extracts are rich in phenolic compounds and have high antioxidant activity. Also, the tested samples did not show the presence of toxic metals, exhibit antibacterial activity, and can be used in the diet and the preparation of pharmaceutical formulations.

EXPERIMENTAL SECTION

Preparation of the fresh fruit extracts

Plant material was collected in Southeast Serbia in early July 2011. Voucher specimens (*Morus rubra* L. No 2-1753, Bela Palanka, UTM 34TDR2 01, determined by Mirjana Milenkovic, Faculty of Biology, University of Belgrade, Belgrade, Serbia) were deposited at the Herbarium of the Department of Biology and Ecology (BUNS Herbarium), Faculty of Natural Sciences, University of Novi Sad, Novi Sad, Serbia. Fresh fruit maturity was estimated based on the color [14]. Samples were stored in plastic bags and kept frozen until extraction. The frozen fresh fruit material was homogenized using a blender. Black, red, and white mulberry fresh fruits (10 g) were extracted with water, methanol-water (50/50, v/v%), methanol, ethanol-water (50/50, v/v%), and ethanol. All solvents were acidified with 1 ml conc. HCl. The extraction was performed with 100 ml of solvents using the ultrasonic bath for 30 minutes. The suspension was gravity-filtered through a Buchner funnel and Whatman No. 1 filter paper. Extracts were stored in the fridge at 5°C until their analyses.

Chemicals and apparatus

1,1-Diphenyl-2-picrylhydrazyl (DPPH), catechin, and AlCl_3 were purchased from Sigma Chemical Co. (St. Louis, MO, USA). The 6-hydroxy-2,5,7,8-tetramethylchroman-2-carboxylic acid (Trolox) was purchased from Acros Organics (New Jersey, USA). Folin-Ciocalteu's phenol reagent and sodium carbonate were purchased from Merck Chemical Suppliers (Darmstadt, Germany). Potassium chloride buffer (pH 1.0) and sodium acetate buffer (pH 4.5) were purchased from the same producer. The other used chemicals, including solvents, were of analytical grade. An Agilent 8453 UV/Vis spectrophotometer was used for absorbance measurements and spectra recording, using optical or quartz cuvettes of 1 cm optical path. The pH measurements were made with Hanna Instruments pH-meter equipped with a glass electrode.

Determination of the total phenolic compounds

Total phenol contents of the extracts were determined by the modified Folin-Ciocalteu method [15]. An aliquot of the extracts (1 ml) was mixed with 0.5 ml Folin-Ciocalteu reagent and 2 ml of sodium carbonate (20%). Absorbance was measured after 10 min incubation at room temperature at 760 nm. Total phenolic content was expressed as mg/100 g gallic acid equivalent (GAE). The result of each assay was obtained from three parallel determinations.

Determination of the total flavonoid content

Total flavonoid content was determined using a spectrophotometric method based on the formation of the flavonoid complex with aluminum [16]. Red mulberry extract (1 ml) was mixed with 3 ml deionized water and 0.3 ml NaNO_2 . After standing at room temperature for 5 minutes, 3 ml AlCl_3 was added to the solution, followed by the addition of 2 ml of NaOH after another 5 minutes of standing. The solution was then filled up with deionized water in a 10 ml flask. The absorbance of the prepared solution was measured at 510 nm. Total flavonoid content was calculated as catechin (mgCE/100 g) using the equation based on the calibration curve.

Determination of the total monomeric anthocyanins

The total monomeric anthocyanin content in the plant extracts was determined using the previously described pH-differential method [17]. Anthocyanins demonstrate a maximum absorbance at 520 nm at pH 1.0. The colored oxonium form of anthocyanin predominates at pH 1.0, and the colorless hemiketal form at pH 4.5. The pH-differential method is based on the reaction of the formation of oxonium forms. This allowed accurate and rapid measurement of total monomeric anthocyanins. Total monomeric anthocyanin pigment is expressed as mg of cyanidin-3-O-glucoside, using molar absorptivity (ϵ) of 26900 and a molecular weight of 449.2. For this method, 1 ml of the red mulberry extract, prepared by the previously described procedure, was poured into two separate 10 ml volumetric flasks. Then, one was filled up to the line with a solution of potassium chloride (KCl) (pH=1), and the second with sodium acetate (CH_3COONa) (pH=4.5). The two diluted solutions were left to stand for 15 minutes at room temperature in the dark.

Finally, the absorbance of both samples was measured at λ_{max} 520 nm and 700 nm. Absorbances (A) of the investigated extracts were calculated by Eq 1:

$$A = (A_{\lambda_{\text{vis-max}}-A_{700}})_{\text{pH}1.0} - (A_{\lambda_{\text{vis-max}}-A_{700}})_{\text{pH}4.5} \quad (1)$$

Content of the monomeric anthocyanin pigment (MAP) was calculated by Eq 2:

$$\text{MAP}(\text{mg l}^{-1}) = (A \cdot \text{MW} \cdot \text{DF} \cdot 1000) / (\epsilon \cdot l) \quad (2)$$

where A is absorbance calculated by equation 1, ϵ is the molar absorptivity ($26900 \text{ dm}^3 \text{ mol}^{-1} \text{ cm}^{-1}$), MW is the molecular weight (449.2 g mol^{-1}), and DF is the dilution factor, l is the path length (1 cm). The result, taken as the monomeric anthocyanin pigment (MAP), was expressed as mg of cyanidin-3-O-glucoside dm^{-3} .

Free radical scavenging activity

The free radical scavenging activity of the plant extracts was analyzed by using the 2,2-diphenyl-1-picrylhydrazyl (DPPH) assay [18-22]. The antioxidant assay is based on the measurement of the loss of color of DPPH solution by the change of absorbance at 517 nm caused by the reaction of DPPH with the tested sample. The reaction was monitored using a UV-VIS spectrophotometer. Plant extracts (1 ml), 5 ml of freshly prepared DPPH in methanol, and 4 ml of water were put into a cuvette at room temperature. After 30 minutes of incubation at room temperature, the absorbance was read against a blank at 517 nm. All measurements were performed in triplicate at a final concentration. The ability of extracts to inhibit DPPH in percents (RSC %) was calculated from the decrease of absorbance according to the relationship (Eq 3):

$$\text{RSC (\%)} = (1 - A_{\text{sample}}/A_{\text{blank}}) \cdot 100 \quad (3)$$

where A_{blank} is the absorbance of the control ($1 \cdot 10^{-4} \text{ mol dm}^{-3}$ DPPH methanol solution), and A_{sample} is the absorbance of the test sample. The results were expressed as milligrams of Trolox equivalents (TE) per 100 g of fresh sample (mgTE/100 g).

HPLC method

High-Performance Liquid Chromatography (HPLC) with UV/Vis and a high-resolution fluorescence detector was applied to determine and quantify the phenolic compounds in the prepared samples. The HPLC method was developed, with the following parameters showing the best results. Chromatographic separation was performed on an Eclipse XDB-C18 column (4.6 mm x 150 mm) using a solvent system:

A - ($\text{H}_2\text{O} + 5\% \text{HCOOH}$) and B - ($80\% \text{ACN} + 5\% \text{HCOOH} + \text{H}_2\text{O}$).

Separation of components was performed using the following linear gradient: 0-28 min, 0.0% B; 28-35 min, 25% B; 35-40 min, 50% B; 40-45 min, 80% B, and finally 0% B again for the last 10 min. The mobile phase flow

was 0.8 cm³/min. The sample solution (5 µl) was injected automatically using autosamplers. The column was thermostatically controlled at 30 ° C.

The phenolic components present in the samples were identified by comparing their retention times and spectra with the retention time and spectrum of standards for each component. The following standards were used: malvidin-3-O-glucoside, cyanidin-3-O-glucoside, chlorogenic acids, *p*-coumaric, caffeic and ferulic acids, catechin, epicatechin, quercetin, and kaempferol. The quantitative determination of the components was performed by the external standard method.

For each individual standard, a stock solution of a mass concentration standard of 1.0 mg/cm³ was prepared by dissolving in 10% methanol solution. A calibration curve for each standard was constructed based on the obtained surfaces, depending on the mass concentration of the standard. From the obtained linear dependence equation, mass concentrations of the components in the samples were calculated. For components in samples for which no standard was available, quantification was performed based on a calibration curve by the structure of the corresponding standard. All analyses were performed in triplicate.

Determination of the content of heavy metals

The standard procedure described by the Association of Official Analytical Chemists (AOAC) was followed for the preparation of the samples for the analysis of heavy metals [23]. Accurately weighed (2 g) sample was transferred into a silica crucible and kept in a muffle furnace for ashing at 450°C for 3 h and then 5 ml of 6 M hydrochloric acid was added to the crucible. Care was taken to ensure that all the ash came into contact with acid. Further, the crucible containing acid solution was kept on a hot plate and digested to obtain a clean solution. The final residue was dissolved in 0.1 M nitric acid solution and made up to 50 ml. Working standard solutions were prepared by diluting the stock solution with 0.1 M nitric acid to check the linearity. Red mulberry fresh fruits (10 g) were extracted with water, ethanol-water (50/50, v/v%), ethanol, acetone-water (50/50, v/v%), acetone, methanol-water (50/50, v/v%), and methanol. All solvents were acidified with 1 ml concentrated HCl. The extraction was performed with 100 ml of solvents using the ultrasonic bath for 30 minutes. The suspension was gravity filtered through a Buchner funnel and Whatman No. 1 filter paper. Extracts were stored in the fridge until their analyses.

Determination of antimicrobial activity

In vitro antimicrobial activity of the extracts was tested on a panel of laboratory control strains belonging to the American Type Culture Collection Maryland, USA (except one, which belongs to the National Collection Type

Cultures). Antibacterial activity was assessed against two Gram-positive and three Gram-negative bacteria. The Gram-positive bacteria used were *Bacillus subtilis* ATCC 6633 and *Staphylococcus aureus* ATCC 6538. The Gram-negative bacteria used in the experiment were *Escherichia coli* ATCC 8739, *Pseudomonas aeruginosa* ATCC 9027 and *Salmonella typhimurium* NCTC 6017. The disk diffusion method was used.

Inoculated bacterial strains were prepared from overnight broth culture, and suspensions were adjusted to a turbidity standard of 0.5 McFarland. 100 µl of a suspension containing 1.0×10^8 CFU/cm³ of spore bacteria was seeded on Mueller-Hinton agar (MHA, Torlak) and Sabouraud dextrose agar (SDA, Torlak), respectively, in sterilized Petri dishes (90 mm in diameter). Discs (diameter 9 mm, Macherey-Nagel, Düren) (Germany) were impregnated with 20 µl and 50 µl of extracts (conc. 30 mg/ml) and placed on inoculated agar. Negative control samples were prepared using the same solvent (ethanol).

Tetracycline (30 µg, Torlak) was used as a positive reference standard for determining the susceptibility of strains of each tested microorganism species. Inoculated plates were stored at 4 °C for 2 h and incubated at 37 °C (24 h) for bacterial strains. Antimicrobial activity was assessed by measuring the zone of inhibition for the tested microorganisms. Each trial of this experiment was repeated three times.

ACKNOWLEDGMENTS

Danijela Kostić, Milan Mitić, Ivana Rašić Mišić and Biljana Arsić want to thank for the financial support for this work to the Ministry of Education, Science and Technological Development of the Republic of Serbia (contract number 451-03-9/2021-14/200124).

REFERENCES

1. L.-K. Liu; F.-P. Chou; Y.-C. Chen; C.-C. Chyau; H.-H. Ho; C.-J. Wang; *J. Agric. Food Chem.*, **2009**, 57, 7605-7611.
2. A. Trappey II; H. A. Bawadi; R. R. Bansode; J. N. Losso; *Food Chem.*, **2005**, 91(4), 665-671.
3. S. Ercisli; E. Orhan; *Sci. Hortic.*, **2008**, 116, 41-46.
4. E. Cieslik; A. Greda; W. Adamus; *Food Chem.*, **2006**, 94(1), 135-142.
5. M.R. Perez-Gregorio; J. Regueiro; E. Alonso-Gonzalez; L.M. Pastrana-Castro; J. Simal-Gandara; *Food Sci. Technol.*, **2011**, 44, 1793-1801.
6. A. Sass-Kiss; J. Kiss; P. Milotay; M.M. Kerek; M. Toth-Markus; *Food Res. Int.*, **2005**, 38, 1023-1029.

7. Q. Du; J. Zheng; Y. Xu; *J. Food Compost. Anal.*, **2008**, 21, 390–395.
8. J.-Y. Lin; C.-Y. Tang; *Food Chem.*, **2007**, 101, 140-147.
9. M. Ozgen; S. Serce; C. Kaya; *Sci. Hortic.*, **2009**, 119, 275-279.
10. A.M. Pawlowska; W. Oleszek; A. Braca, *J. Agric. Food Chem.*, **2008**, 56, 3377–3380.
11. S. Ercisli; M. Tosun; B. Duralija; S. Voća; M. Sengul; M. Turan; *Food Technol. Biotechnol.*, **2010**, 48, 102–106.
12. S. Ercisli; E. Orhan; *Food Chem.*, **2007**, 103, 1380-1384.
13. I. Thabti; W. Elfalleh; H. Hannachi; A. Ferchichi; M. Da Graca Campos; *J. Funct. Foods*, **2012**, 4, 367–374.
14. M. Mora; M. Oyarce; C. Fredes; Fruit Maturity Estimation based on Color Scales,
http://sedici.unlp.edu.ar/bitstream/handle/10915/42329/Documento_completo.pdf?sequence=1, accessed on 25 February 2022
15. V.L. Singleton; J.A. Rossi; *Am. J. Enol. Vitic.*, **1965**, 16, 144-158.
16. A.A.L. Ordóñez; J.D. Gómez; M.A. Vattuone; M.I. Isla; *Food Chem.*, **2006**, 97, 452-458.
17. M.M. Guisti; R.E. Wrolstad; Characterization and measurement of anthocyanins by UV visible spectroscopy, In *Current protocols in food analytical chemistry*, New York: John Wiley & Sons, Inc., 591, **2001**.
18. C. Sanchez-Moreno; J.A. Larrauri; F. Saura-Calixto; *J. Sci. Food Agric.*, **1999**, 79, 1301-1304.
19. B. Fuhrman; N. Volkova; A. Suraski; M. Aviram, *J. Agric. Food Chem.*, **2001**, 49, 3164-3168.
20. D. Villano; M.S. Fernandez-Pachon; A.M. Troncoso; M.C. Garcia-Parrilla; *Food Chem.*, **2006**, 95, 394-404.
21. J. Lachman; M. Šulc; M. Schilla; *Food Chem.*, **2007**, 103, 802-807.
22. A. Turkoglu; M.E. Duru; N. Mercan; I. Kivrak; K. Gezer, *Food Chem.*, **2007**, 101, 267-273.
23. Association of Official Analytical Chemists International; Use of Statistics to Develop and Evaluate Analytical Method, Official Methods of Analysis, **2000**, p. 2000.

PREPARATION, PHYSICO-CHEMICAL CHARACTERIZATION AND ANTIBACTERIAL PROPERTIES OF CHITOSAN AND CHITOSAN–NISIN MEMBRANES

MARIANA ADINA MATICA^a, FINN LILLELUND AACHMANN^b,
ANNE TØNDERVIK^c, HÅVARD SLETTA^c, VASILE OSTAFE^{a*}

ABSTRACT. Different types of chitosan were used to prepare membranes with enhanced antibacterial properties, via the solvent casting method. Nisin, an antimicrobial peptide, already use in food preservation, was incorporated in chitosan membranes to enhance the bactericidal effect, to obtain a starting material intended for use as wound dressings. The physico-chemical properties of the membranes were monitored and the results showed a good swelling capacity and water vapor transmission rate of the membranes. Optical characterization data showed that chitosan-based membranes could provide ultraviolet light protection while *in vitro* biodegradability assay demonstrated good stability of the films under enzymatic degradation. Nisin improved significantly the antibacterial effect of the membranes, while the nisin-chitosan membrane-forming solutions had a bactericidal effect against both Gram-positive and Gram-negative bacteria.

Keywords: *chitosan, membrane, nisin, antimicrobial peptide, biodegradable polymer*

INTRODUCTION

The new approach in developing antibacterial materials for wound treatment implies the use of bioactive molecules, with innate properties that are safe to the human body as well as safe to the environment. Chitosan is

^a West University of Timișoara, Advanced Environmental Research Laboratories, 4 Oituz str., RO-300086, Timișoara, Romania

^b Norwegian Biopolymer Laboratory (NOBIPOL), Department of Biotechnology and Food Sciences, NTNU Norwegian University of Science and Technology, Sem Sælands vei 6/8, 7491 Trondheim, Norway

^c SINTEF Industry, Department of Biotechnology and Nanomedicine, Richard Birkelands veg 3 B, 7034 Trondheim, Norway

* Corresponding author: vasile.ostafe@e-uvt.ro

one of the most studied non-toxic biomaterials with ideal characteristics such as antimicrobial properties [1,2], biodegradability [3], and biocompatibility [4]. Currently, on the market, there are many wound dressings based on chitosan, mainly hemostatic dressings and the interest in chitosan as wound dressing starting material will only increase in the future [5,6] as it has become more and more difficult to treat and heal infected wounds.

While pristine chitosan possesses an antibacterial effect, as many studies have proven this over the years, its antibacterial properties are dependent on several physico-chemical characteristics, mainly molecular weight (MW) and degree of deacetylation (DDA%) [5]. The use of different polymers in combination with antibacterial agents has become a common practice, but due to the increase of antibiotic resistance, other molecules, such as antimicrobial peptides, are replacing conventional antibiotics. Antimicrobial peptides (AMPs), both synthetic or from natural sources, are small molecules, from 6 up to 100 amino acids, usually of cationic nature, with activity against a wide range of microorganisms, from bacteria, yeast, fungi, to viruses and even tumor cells [7].

Nisin, a polycyclic cationic peptide produced by *Lactococcus sp.*, is composed of 34 amino acids and is classified as a Type A (I) lantibiotic molecule. Mainly used in food preservation [8], nisin is active on both Gram-positive and Gram-negative bacteria, by interfering in the cytoplasmic membrane permeability and cell wall disruption. While nisin is FDA (Food and Drug Administration) approved and has a GRAS (Generally Regarded as Safe) status, its application has extended to biomedical fields [9], especially due to the proven activity against drug-resistant bacterial strains [10].

In this study, several types of chitosan were used to prepare chitosan and chitosan-nisin membranes. The physico-chemical characteristics of the above-mentioned membranes were investigated, as well as their antibacterial effects against Gram-positive and Gram-negative bacteria.

RESULTS AND DISCUSSION

Preparation of chitosan membranes

Different types of chitosan were used (Table 1) to prepare chitosan and chitosan-nisin membranes (Figure 1), via the solvent casting method. Membranes were dried at 37°C and peeled using 1 M NaOH. Chitosan membranes were transparent and flexible, while the addition of nisin made the membranes less flexible and brittle. The main characteristics of chitosan (Cs) and chitosan-nisin (Cs-N) membranes, based on visual observations, are described in Table 2.

PREPARATION, PHYSICO-CHEMICAL CHARACTERIZATION AND ANTIBACTERIAL PROPERTIES
OF CHITOSAN AND CHITOSAN-NISIN MEMBRANES

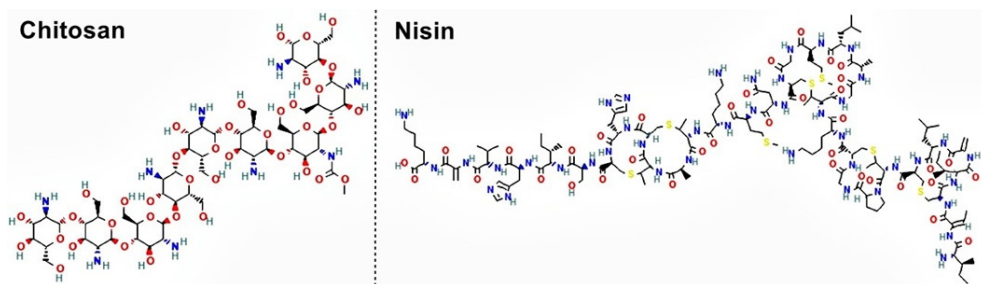


Figure 1. Chemical structure of chitosan and nisin

All chitosan membranes were peeled off easily, after 10 to 15 minutes after NaOH addition, except Cs-50 membrane, which needed more time to be removed from the Petri plate. Also, this type of membrane was more flexible, presented higher elasticity upon removal from Petri plate for neutralization, low resistance to mechanical stress, and required longer time to dry, compared to the other chitosan membranes.

Table 1. Characteristics of chitosan types used for membrane preparation

Chitosan type	Chitosan code	Molecular weight (kDa)	Fraction of acetylation (FA)/Degree of deacetylation (DDA%)
Chitopharm S	Cs-S	198	FA 0.19
Chitopharm L	Cs-L	604	FA 0.17
Chitopharm 50	Cs-50	190	FA 0.52
ChitoClear	CC	270	DDA 95%
Chitosan Low Molecular Weight	Cs-SA	50-190	DDA 74 – 85%

Chitosan-nisin membranes peeled off in a matter of seconds after adding 1 M NaOH, but were less flexible and brittle, especially CCN membrane, which shattered easily upon handling, after drying. After complete drying, Cs membranes turned out less wrinkled than Cs-N membranes (Figure 2). Cs membranes presented homogeneity and absence of insoluble particles, while the presence of nisin, in some cases, lead to a lower homogeneity of membranes, except Cs-50N membrane, which kept its homogenous appearance, and that might depend on the chitin ability to form

protein retention membranes [11]. As seen in Table 1, this type of membrane is based on chitosan with an acetylation fraction of 0.52, meaning there is at least an equal number of acetylated and deacetylated glucosamine units in the polymer backbone.

Table 2. Observed morphological characteristics of membranes

Membrane code	Observations regarding membrane properties
Cs-S	A transparent, flexible, smooth surface membrane
Cs-SN	A slightly transparent, brownish membrane, moderately flexible, smooth surface
Cs-L	A transparent, flexible, smooth surface membrane
Cs-LN	A slightly transparent, brownish membrane, moderately flexible, smooth surface
Cs-50	A transparent, very flexible, smooth surface membrane,
Cs-50N	A transparent, very flexible, smooth surface, membrane
CC	A transparent, slightly yellowish, moderately flexible, smooth surface membrane
CCN	A slightly opaque, brownish, very brittle, slightly rough surface membrane
Cs-SA	A transparent, yellowish, flexible, smooth surface membrane
Cs-SAN	A slightly transparent, brownish, moderately flexible, slightly smooth surface membrane

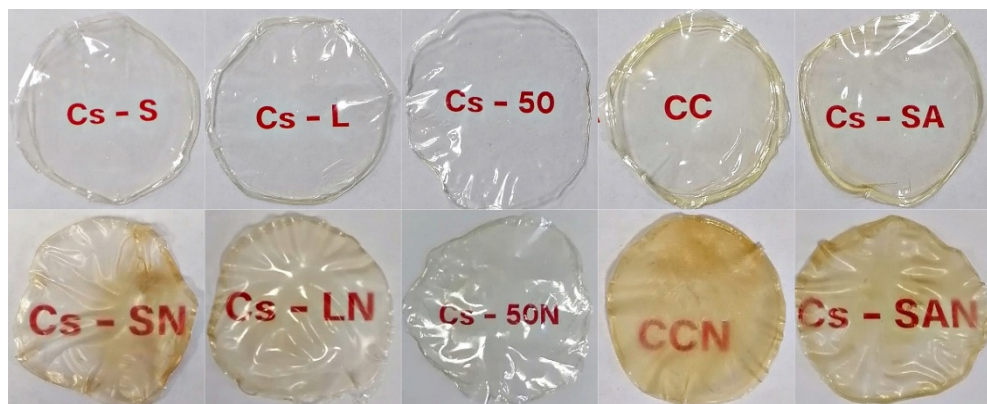


Figure 2. Digital images of the membranes

Moisture content and total soluble matter

The moisture content (right side) and total soluble matter of the membranes are shown in Figure 3 (left side). The presence of nisin in Cs membranes slightly increased the membrane moisture content. This could be explained by the fact that besides the strong hydrogen bonds, that occur between the functional groups in the chitosan chain ($-\text{OH}$, $-\text{NH}_2$) and water molecules [12], the presence of nisin, which is an amphipathic molecule (the C-terminal hydrophilic region and the N-terminal hydrophobic region) increases the hydrophilicity of membrane [13].

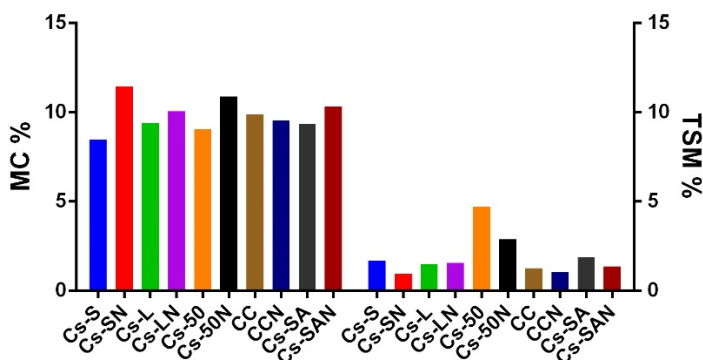


Figure 3. Moisture content (MC % - left) and total soluble matter (TSM % - right) of membranes

The values obtained from measuring total soluble matter give information for the resistance of the membranes against water, and the results obtained (Figure 3 – right side) showed that solubility of membranes decreased with the addition of nisin, which may also be due to the hydrophobic nature of the antimicrobial peptide.

The Cs-50 and Cs-50N membranes are based on a type of chitosan having FA 0.52, meaning that the chitosan backbone contains at least, an equal number of glucosamine and N-acetylglucosamine units. It is known that chitosan has a better film forming ability than chitin [14], and we observed that during the membrane preparation step, when Cs-50 membrane was difficult to handle and less resistant to mechanical stress. Therefore, the higher soluble matter in this membrane type may be caused by the less structured membrane, compared to the other Cs membranes, based on chitosan with a higher deacetylation degree.

Swelling measurements

The swelling of Cs and Cs-N membranes involves the diffusion of water molecules into the polymer matrix followed by the expansion of the polymer matrix into the surroundings [15]. As shown in Figure 4, Cs-50 and Cs-50N membranes had the highest swelling ratio (4.7 and 5.9 gram of solvent sorbed per gram of dry membrane), twice compared to the other membranes (Figure 4). This high swelling capacity of Cs-50 and Cs-50N membranes may be due to the chitin sorbent ability [16].

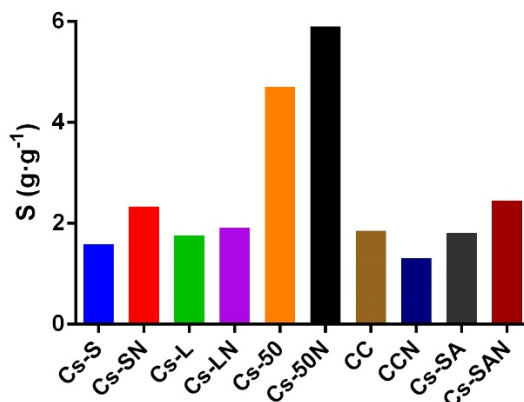


Figure 4. Swelling measurements of membranes

Swelling capacity may depend also on the deacetylation degree and molecular weight [17], as the CC and Cs-SA and Cs-L containing membranes had the highest swelling values (Figure 4), compared to the other chitosan types, which had smaller deacetylation degrees and lower molecular weight (Table 1).

Table 3. Thickness and opacity of the films

Membrane code	Thickness (μm)	O_m value
Cs-S	37.14	3.925
Cs-SN	40.05	5.405
Cs-L	44.29	2.996
Cs-LN	51.43	5.264
Cs-50	25.71	3.385
Cs-50N	52.86	5.324
CC	54.43	2.942
CCN	67.14	6.529
Cs-SA	60.01	2.340
Cs-SAN	71.02	7.266

The Cs-N membranes had high swelling capacity compared to Cs, except CC type (Figure 4). There are two ways for water to be absorbed by the membrane, by binding to the membrane itself or by being retained in the pores formed in the membrane structure [18]. On the other side, Cs-N membranes were thicker than Cs membranes, and the chitosan-nisin blend would form a denser structure, therefore they would retain more water molecules in their structure (Table 3).

Water vapor permeability

The water vapor permeability transmission rate (WVTR) showed different results based on the type of chitosan (Figure 5). Although, the swelling capacity increased slightly with the molecular weight of chitosan, it seems that the WVTR will decrease based on the same criteria [19]. Moreover, the addition of nisin decreases, even more, the WVTR, probably due to the formation of a denser structure within the membrane. If considering that the vapor rate for injured skin, the value can reach up to $5138 \text{ g}\cdot\text{m}^{-2}\cdot\text{d}^{-1}$ for a granulating wound, therefore, the results we obtained for both Cs and Cs-N membranes, between 2000 and $3000 \text{ g}\cdot\text{m}^{-2}\cdot\text{d}^{-1}$, the membranes would meet the requirements for a wound dressing material [18]. Moreover, the values we obtained are comparable to commercial wound dressings products available on the markets [20].

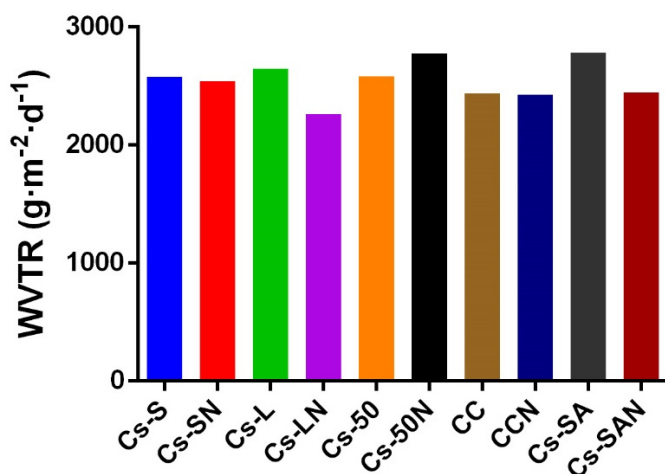


Figure 5. Water vapor permeability rate of membranes

Optical characteristics and thickness of membranes

The measurements regarding the thickness and opacity of membranes showed that the addition of nisin lead to an increase of both parameters. The opacity of the membranes doubled when nisin was added, and CCN and Cs-SAN presented the highest O_m values, while all Cs membranes showed similar opacity (Table 4).

The addition of nisin affected the transmittance rate of membranes, as shown in Table 5, where T_{800nm} is starting from a range of 66 to 76% for all membranes, and gradually decreases until zero at T_{200nm} (Figure 6). Four of the membranes exhibit lower transmittance rate compared to the other membranes, Cs-LN, CC, CCN, and Cs-SAN. The lowest transmittance rate is observed for CCN membrane, which starts from 12% at T_{800nm} and reaches 0 at T_{200nm} . Given the results obtained, we can suggest that chitosan-based membranes would provide protection against UV light to some wounds. Although the effectiveness of UV radiation in wound care, for bactericidal effect was proven [21], there are some limitations and further analysis must be employed, as UVC and UVB can damage the genetic material in the host cell [22].

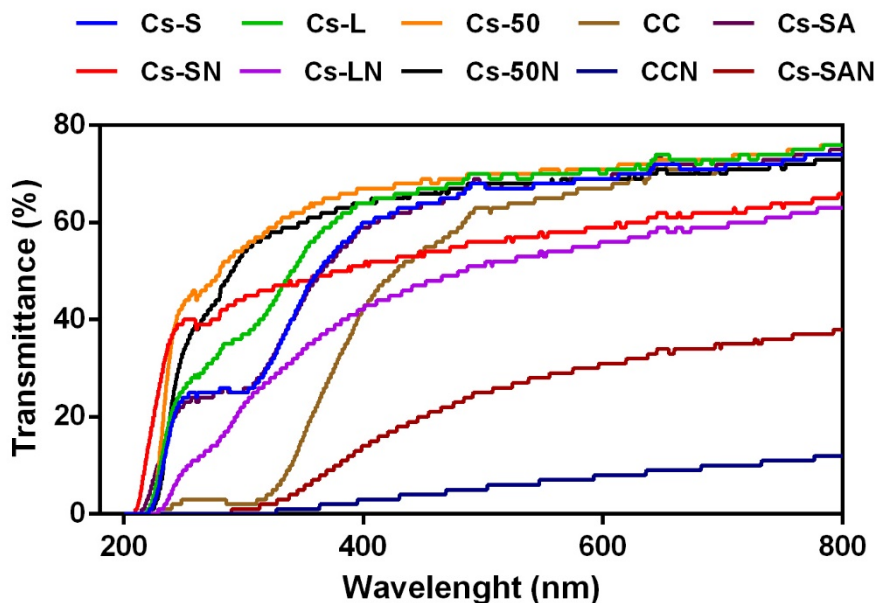


Figure 6. The transmittance of the membranes

Table 4. Light transmittance of membranes

Membrane code	Transmittance (%) at different wavelengths (nm)												
	200	250	300	350	400	450	500	550	600	650	700	750	800
Cs-S	0	24	25	45	60	64	68	68	69	72	71	73	74
Cs-SN	0	40	44	48	51	53	56	57	59	62	62	63	66
Cs-L	0	26	37	54	64	67	70	70	70	74	73	74	76
Cs-LN	0	9	22	34	42	47	51	53	56	59	59	61	63
Cs-50	0	43	55	62	67	69	70	71	71	73	73	74	76
Cs-50N	0	34	54	60	64	66	68	68	69	71	70	71	73
CC	0	3	2	16	42	54	63	65	67	72	71	72	74
CCN	0	0	0	1	3	4	5	7	8	9	10	11	12
Cs-SA	0	23	26	44	59	64	68	68	69	73	72	73	75
Cs-SAN	0	0	1	5	14	20	25	28	31	34	35	36	38

***In vitro* degradation**

Biodegradable polymers, as chitosan, desired to be used for wound treatment, are susceptible to *in vivo* oxidative and enzymatic degradation, when such molecules are secreted during the inflammatory phase [23]. Therefore, the biodegradation of membranes was determined by monitoring the weight loss, in phosphate buffered saline (PBS – used as control), lysozyme, and H₂O₂, after 24 hours at 37°C. The degradation assay revealed that there is no significant difference between PBS degradation and lysozyme degradation, for the membranes, except Cs-50 and Cs-50N membranes, that lost almost 50% of their weight, after 24 hours of incubation in lysozyme. Given the fraction of acetylation of this type of chitosan (FA 0.52), and the results obtained during the swelling measurements (Figure 4), thickness (Table 3) and *in vitro* degradation (Figure 7), confirm the weak film-forming ability of low deacetylation degree of chitosan, that can be easily degraded.

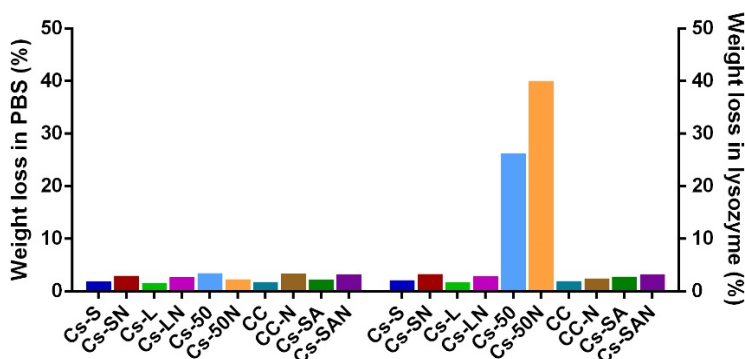


Figure 7. In vitro degradation of membranes (PBS – left and lysozyme – right)

As for the H_2O_2 degradation assay, we were not able to measure the weight loss, because, after 24 hours, all membranes were almost entirely degraded, resulting in very small pieces of membranes, and for Cs-50 and Cs-50N, remaining only a gel-like solution. Therefore, membrane resistance in oxidative environments was very low. On the other side, the long-term stability of membranes under enzymatic degradation indicates that the obtained membranes could be appropriate for external use as wound dressing materials. A controlled degradation process of polymeric matrix can be advantageous for drug release, especially in biomedical application, such as wound healing [24].

Antibacterial testing

The antibacterial effect of Cs and Cs-N membranes was tested using the disk diffusion method, which is a qualitative test that indicates the inhibitory effect of a sample. The inhibition zone diameter in susceptibility testing of conventional antibiotics indicates the sensitivity or resistance of bacteria to antimicrobial agents. Here, the measure of inhibition zone diameter is mainly a qualitative result, as there are no standards available for these new emerging antimicrobial molecules. Is possible that the zone diameter depends on the diffusion rate of the chitosan-based on its molecular weight. However, the results showed a significant difference between the chitosan-nisin membrane inhibitory effect and chitosan solutions.

As seen in Figure 8, all membrane-forming solutions showed an inhibitory effect against both bacterial strains tested (Table 5), while Cs membranes instead, showed no inhibition zone (Figure 10). It is known that the antibacterial effect of chitosan is based on its polycationic nature in an acidic environment. Therefore, in an aqueous acidic environment, the positive charge of chitosan increases, because the $-\text{NH}_2$ are converted to soluble protonated form $-\text{NH}_3^+$. The antibacterial effect of chitosan is based on its protonated form, due to electrostatic interaction between protonated amino groups and anionic structures from the bacterial cell surface [5]. This would explain the lack of inhibition zone when testing the antibacterial effect of dried and neutralized Cs membranes. One drawback observed when adapting the disk diffusion method to chitosan-based membranes was the poor adherence of membranes to agar media. Once placed on top of the agar surface and incubated at 37°C , the edges of the membranes would curl up. Therefore, to overcome this drawback, before placing them into the incubator, the Petri plates were kept at 4°C for 2 hours to ensure better adherence to the agar surface. The same step was applied to membrane-forming solutions, to prevent the drying of the solution on the filter paper disk and to allow a better diffusion of viscous chitosan to agar media.

The addition of nisin increased highly the inhibitory effect on both bacterial strains, while seemingly, the inhibitory effect against *S. aureus* MRSA was higher than against *P. aeruginosa*. Nisin is known to have a bactericidal effect against a broad spectrum of Gram-positive bacteria [25], but its inhibitory effect is lower against Gram-negative species [26]. However, our results are similar to other studies [27] and show that the nisin-chitosan blend exhibit a high inhibitory effect on both Gram-positive and Gram-negative strains, hence the synergistic effect of both antimicrobials (Figure 9).

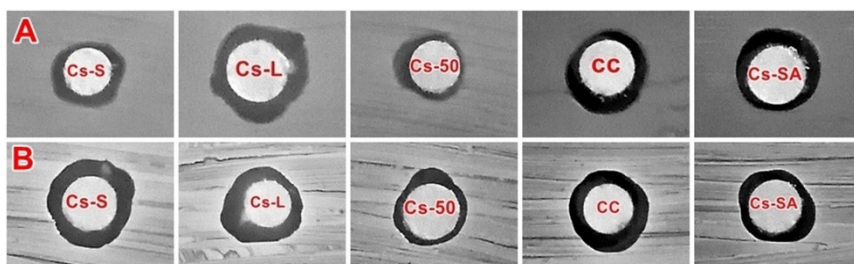


Figure 8. Disk diffusion method: Inhibition zone of Cs solutions against A) *Pseudomonas aeruginosa* (G-), B) *Staphylococcus aureus* MRSA (G+)

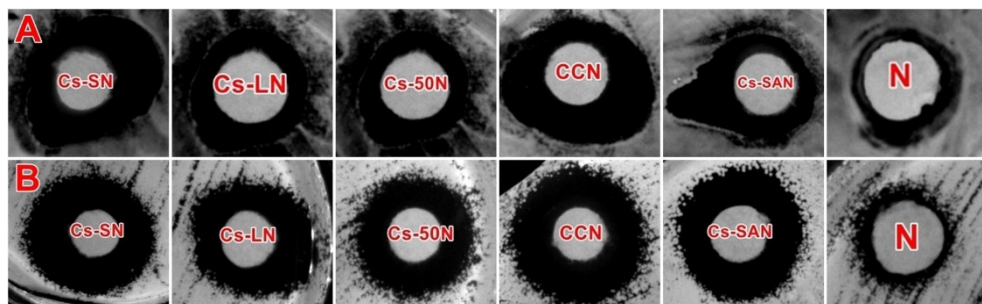


Figure 9. Disk diffusion method: Inhibition zone of Cs-N solutions against A) *Pseudomonas aeruginosa* (G-), B) *Staphylococcus aureus* MRSA (G+)

The inhibitory effect of Cs and Cs-N membranes was lower, compared to membrane-forming solutions, as explained above. As seen in Figure 10, a clear inhibitory effect, based on inhibition zone, was observed against *S. aureus* MRSA (methicillin-resistant *Staphylococcus aureus*) strain. Four types of membranes inhibited the growth of this strain, Cs-SN, Cs-LN, Cs-50N, and Cs-SAN. The other membranes (CC and CCN) did not inhibit bacterial

growth, and some of them did not adhere completely to the agar surface. This drawback could influence the inhibitory effect, due to the poor diffusion of the antimicrobials to agar media. While none of the membranes tested showed any inhibition zone against *P. aeruginosa* growth, it was observed that the bacterial cells did not grow on the surface of the membranes, compared to *S. aureus* MRSA growth, where we observed bacterial growth on the surface of Cs membranes. Our results are comparable to other studies, which show that the antibacterial effect of chitosan and nisin as well, depends on the bacterial strains [10,28,29].

Table 5. Inhibition zone diameter of membranes-forming solutions

Membrane code	Inhibition zone (mm)	
	<i>P. aeruginosa</i>	<i>S. aureus</i> MRSA
Cs-S	10	11
Cs-SN	24	24
Cs-L	11	11
Cs-LN	20	22
Cs-50	8	9
Cs-50N	20	22
CC	10	11
CCN	25	25
Cs-SA	10	10
Cs-SAN	19	24
N	11	10

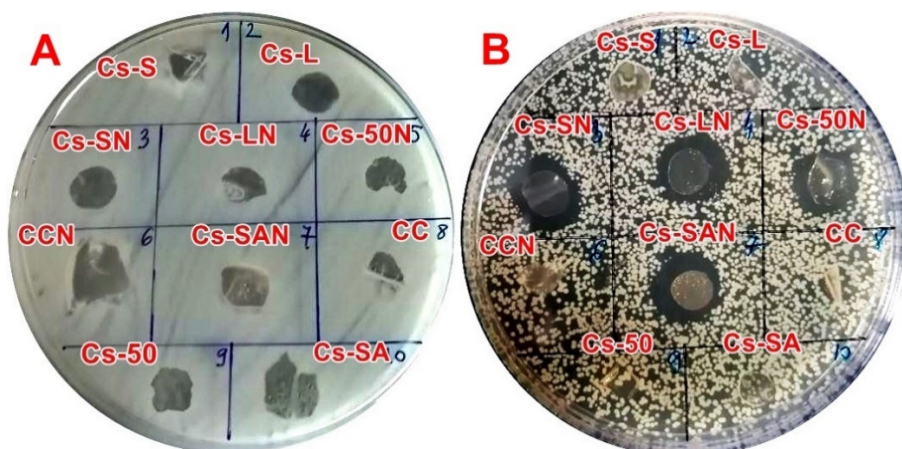


Figure 10. Disk diffusion method: Inhibition zone of Cs and Cs-N membranes against A) *Pseudomonas aeruginosa* (G-), B) *Staphylococcus aureus* MRSA (G+)

CONCLUSIONS

The use of antimicrobial peptides incorporated in the biopolymer matrix could provide better protection against bacterial colonization and infection of different wound types [30,31]. In this study, membranes were successfully prepared, via solvent casting method, from chitosan powder of different molecular weight and deacetylation degrees. The antibacterial effect of pristine chitosan was enhanced by blending nisin, an antimicrobial peptide already used in food preservation.

The physico-chemical characteristics showed that the membranes developed had a good swelling capacity and water vapor transmission rate, which could provide a suitable environment for wound healing application. The optical characteristics showed that the membranes could provide UV protection, as genetic material from host cells can be affected by ultraviolet light exposure [22]. The antibacterial effect of the membranes, tested against two bacterial strains, common to wound infections, was confirmed by both membrane-forming solutions and membrane as well. By using the chitosan-nisin blend, the inhibitory effect was higher, the two components working synergistically.

These findings are comparable to previous studies [9,27,29,32], which show the effectiveness of nisin to human pathogenic bacterial strains and the use of AMPs in combination with chitosan could become a promising derivative with intense use in biomedical and pharmaceutical applications. Moreover, based on our results, the membranes based on low molecular weight chitosan with a higher deacetylation degree are the most suitable for wound healing application.

EXPERIMENTAL SECTION

Materials

In this study, we used five types of chitosan, with different molecular weights (MW) and different deacetylation degrees (DDA%) or fraction of acetylation (FA), expressed differently due to the provider choice of describing the product. As described in literature, the fraction of acetylation of chitosan is situated in 0 to 1 range, 0 FA meaning polyglucosamine while 1 FA is considered chitin [14].

Three types of chitosan of different MW and FA were obtained from Chitinor (Chitopharm S – MW 198 kDa, FA 0.19, Chitopharm L – MW 604 kDa, FA 0.17, Chitopharm 50 – 190 kDa, FA 0.52), during one research project. One chitosan sample was obtained from Primex (ChitoClear 43010 –

MW 270 kDa, 95%DDA), and one chitosan powder was purchased from Sigma Aldrich (Chitosan low molecular weight – 50-190 kDa, 75-85% DDA). Acetic acid (CH_3COOH) p.a., sodium hydroxide (NaOH) p.a. ISO, sodium chloride (NaCl) p.a. ACS ISO, potassium chloride (KCl) p.a. ACS ISO, disodium hydrogen phosphate (Na_2HPO_4) p.a. ACS, and potassium dihydrogen phosphate (KH_2PO_4) p.a. ACS, were purchased from Carl Roth. Nisin was purchased from MP Biomedicals. Mueller Hinton Broth, Mueller Hinton Agar was purchased from Carl Roth, hydrogen peroxide (H_2O_2) 30% puriss. p.a., reag. ISO, reag. Ph. Eur. and lysozyme (~ 100000 U/mg) were purchased from Sigma Aldrich.

Preparation of chitosan membranes

All chitosan (Cs) solutions were prepared as follows: 1g of chitosan powder was added to 100 mL of 1% CH_3COOH solution (w/v). The mixtures were magnetically stirred (Witeg SMHS-3) at room temperature (RT) and 300 rpm until complete dissolution. The solutions were filtered through six layers of sterile filter gauze to remove any undissolved particles. All chitosan solutions were left overnight for deaeration. Nisin (N) was dissolved in 1% CH_3COOH solution (w/v) [27] and mixed with chitosan solution to give a final concentration of 10 mg/mL. The Cs and Cs-N membranes were prepared by the method of casting and evaporation of the solvent [26,33] with minor modifications: 10 mL of solution was cast in glass Petri plates (60 mm diameter) and dried at 37°C (Memmert UF 55 oven) overnight.

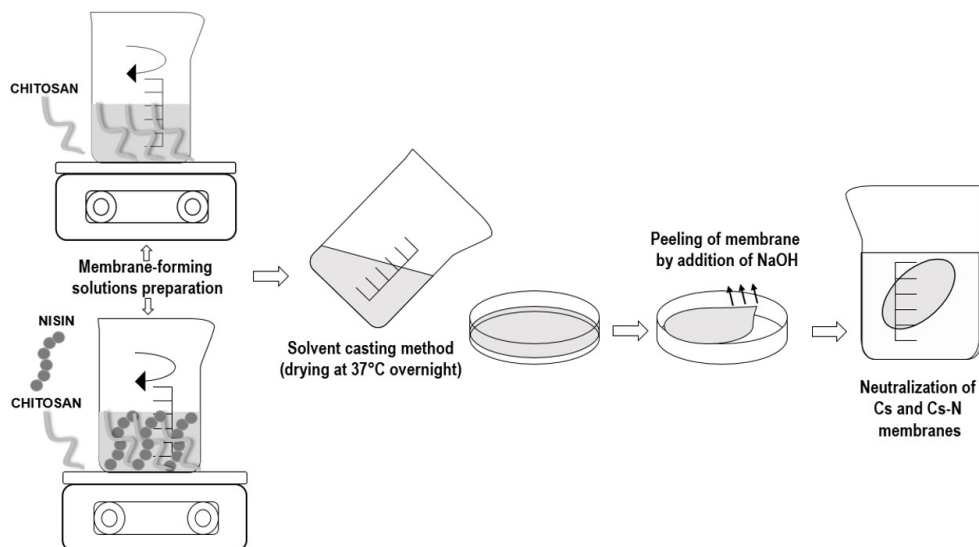


Figure 11. Schematic representation of membrane preparation process

The resulting membranes were subjected to alkali treatment by pipetting 15 mL of 1M NaOH and mixed on a rotary shaker (BIOSAN Sunflower Mini-Shaker 3D) until the membranes were peeled off easily from the Petri plate surface. Thereafter, the membranes were washed with distilled water until neutralization. pH paper was immersed in the wash water to check the neutralization state [34]. Finally, all membranes were dried at RT for 24 hours in a pressed condition to avoid wrinkle formation as much as possible [35].

Moisture content and total soluble matter

The moisture content of the Cs and Cs-N membrane was determined by the method of Yu et al. [36]. Membranes were weighed and dried overnight in a convection oven (Mettler UF 55 oven) at 105°C. The moisture content (MC%) was determined using the following formula: $MC\% = (m_1 - m_2)/m_1 \times 100$, meaning m_1 and m_2 are the initial and final dry weight (g) of the chitosan membranes.

Afterward, the same dry membranes were used for the determination of total soluble matter (TSM) according to the method reported previously in the literature [37]. Therefore, the previously dried membranes of known weight were submerged in distilled water. After incubation at RT for 24 hours, the membranes were taken out and dried overnight at 105°C. The weight of dry matter, that was not solubilized in water, was determined as follows: $TSM\% = (W_i - W_f)/W_i \times 100$, where W_i and W_f are the initial and final mass of the membranes.

Swelling measurements

Cs and Cs-N membranes, dried at a constant weight, were immersed in phosphate buffer solution at RT. Their weight was measured after 24 hours, by removing the membranes from liquid and blotting with filter paper the excess of liquid. The swelling ratio (S), after 24 hours, was determined by the following equation: $S = (M_t - M_0)/M_0$, where M_0 is represented by the mass of the dry membrane and M_t is the mass of the swollen membrane at 24 hours. The results are expressed as gram of solvent sorbed per gram of dry membrane, S ($g \cdot g^{-1}$) [15].

Water vapor permeability

Chitosan membranes were fixed over the opening of a glass bottle containing 5 mL of distilled water. The system was weighed and the water vapor permeability was measured over time, at 37°C, by measuring the weight of the system. The water vapor transmission rate (WVTR) was calculated using this formula: $WVTR = (W_0 - W_t)/(tA)$ where W_0 is the mass of the system at the initial weighing, W_t is the mass of the system at certain time t , while t is the measurement time and A represents the open area of the glass bottle. The results are expressed as grams per square meter per day ($g \cdot m^{-2} \cdot d^{-1}$) [18,33].

Optical characteristics and thickness of membranes

A Shimadzu UV-1900i UV-VIS spectrophotometer was used for measuring the transmittance and opacity of Cs and Cs-N membranes. Membranes were cut in strips and attached to the wall of the cuvette, while an empty cuvette was used as blank. Measurements were made in the wavelength range from 200 to 800 nm. The opacity of the membranes (O_m) was determined by measuring the absorbance at 600 nm. The O_m value, a parameter positively linked to film opacity, was calculated by the following equation: $O_m = A_{600nm}/N$, where A_{600nm} is the absorbance of chitosan membrane at 600 nm and N is the membrane thickness (mm), measured by Vernier digital caliper [36].

The thicknesses of chitosan membranes were measured using a Vernier digital caliper with a measuring accuracy of 0.01 mm. The thickness of each membrane was measured at six random points and the average thickness of membranes was calculated [37].

In vitro degradation

In vitro degradation of the membranes was determined according to Mishra et al. [23] and Ma et al. [18].

The degradation of Cs and Cs-N membranes at physiological conditions was made using PBS (phosphate buffered saline) solution (NaCl 8 g/L, KCl 0.2 g/L, Na_2HPO_4 1.44 g/L, KH_2PO_4 0.245 g/L, pH 7.4) and PBS solution with lysozyme and H_2O_2 . Samples of dried membranes were placed in 10 mL PBS solution (as control) and to mimic *in vivo* physiological conditions, PBS/lysozyme solution of 20,000 U/mL and 3.5% H_2O_2 in PBS were used. The samples were incubated at 37°C for 24 hours. Afterward, membranes were dried in an oven at 105°C for 24 hours and weighed again.

The degradation at physiological conditions was calculated as follows: $(W_{dry f}/W_{dry i}) \times 100$, where $W_{dry i}$ is the initial mass and $W_{dry f}$ is the final mass of membranes, after 24 hours.

Antibacterial testing

Antibacterial activity of chitosan membranes was tested using Gram-negative bacteria *Pseudomonas aeruginosa* (ATCC 27853) and Gram-positive bacteria *Staphylococcus aureus* MRSA (ATCC 43300) by agar disk diffusion method [38]. Bacterial inoculum of 0.1 a.u. (OD_{620nm}), cultivated in Mueller Hinton Broth (beef infusion solids 2.0 g/L, casein hydrolysate 17.5 g/L, starch 1.5 g/L), was spread by swabbing on Petri plates containing Mueller Hinton Agar (beef infusion solids 2.0 g/L, casein hydrolysate 17.5 g/L, starch 1.5 g/L, agar 17 g/L). Disk diffusion method was applied to both chitosan and chitosan-nisin forming solutions and membranes. The antibacterial testing of membrane-forming solutions was tested using sterilized filter paper disks

of 7 mm diameter, which were placed onto the inoculated agar surface, and 20 μ L of the solution was pipetted on each disk. The antibacterial effect of membranes was tested similarly. Therefore, sterilized disks of chitosan and chitosan-nisin membranes (7 mm diameter) were placed carefully onto the inoculated agar surface. The Petri plates were placed at 4°C for two hours prior to the incubation step, at 37°C for 24 hours.

ACKNOWLEDGMENTS

This work was supported by the ERA-Net COFASP Project “Biotechnological tools implementation for new wound-healing applications of byproducts from the crustacean seafood processing industry-Chitowound (project no. PN3-P3-284/4/2017 program H2020, financed by the Romanian National Authority for Scientific Research UEFISCDI).

REFERENCES

1. A. Matica; G. Menghiu; V. Ostafe; *New Front Chem*, **2017**, 26, 55-63.
2. A. Matica; G. Menghiu; V. Ostafe; *New Front Chem*, **2017**, 26, 39-54.
3. A. Matica; G. Menghiu; V. Ostafe; *New Front Chem*, **2017**, 26, 75-86.
4. V. Patrulea; V. Ostafe; G. Borchard; O. Jordan; *Eur J Pharm Biopharm*, **2015**, 97, 417-426.
5. M.A. Matica; F.L. Aachmann; A. Tøndervik; H. Sletta; V. Ostafe; *Int J Mol Scie*, **2019**, 20, 5889.
6. C. Moraru; M. Mincea; G. Menghiu; V. Ostafe; *Molecules*, **2020**, 25, 4758.
7. M. Mahlapuu; J. Håkansson; L. Ringstad; C. Björn; *Front Cell Infect Microbiol*, **2016**, 6, 194-194.
8. J.C.P. Santos; R.C.S. Sousa; C.G. Otoni; A.R.F. Moraes; V.G.L. Souza; E.A.A. Medeiros; P.J.P. Espitia; A.C.S. Pires; J.S.R. Coimbra; N.F.F. Soares; *Innov Food Sci Emerg Technol*, **2018**, 48, 179-194.
9. Z. Najmi; A. Kumar; A.C. Scalia; A. Cochis; B. Obradovic; F.A. Grassi; M. Leighab; M. Lamghari; I. Loinaz; R. Gracia; L. Rimondini; *Front. Bioeng. Biotechnol.*, **2020**, 8.
10. J.M. Shin; J.W. Gwak; P. Kamarajan; J.C. Fenno; A.H. Rickard; Y.L. Kapila; *J Appl Microbiol*, **2016**, 120, 1449-1465.
11. C. Schmitz; L.G. Auza; D. Koberidze; S. Rasche; R. Fischer; L. Bortesi; *Mar Drugs*, **2019**, 17, 452.
12. A. Aljawish; L. Muniglia; A. Klouj; J. Jasniewski; J. Scher; S. Desobry; *Food Hydrocoll.*, **2016**, 60, 551-558.

13. A. Jozala; L. de Lencastre Novaes; A. Pessoa. Nisin. In *Concepts, Compounds and the Alternatives of Antibacterials*, V. Bobbarala, Ed. InterchOpen: 2015; pp. 103-123.
14. J. Wattjes; S. Sreekumar; C. Richter; S. Cord-Landwehr; R. Singh; N.E. El Gueddari; B.M. Moerschbacher; *React Funct Polym*, **2020**, *151*, 104583.
15. J. Ostrowska-Czubenko; M. Gierszewska; M. Pieróg; *J. Polym. Res*, **2015**, *22*, 153.
16. F. Blind; S. Fränzle; *Polysaccharides*, **2021**, *2*, 773-794.
17. J.D. Bumgardner; V.P. Murali; H. Su; O.D. Jenkins; D. Velasquez-Pulgarin; J.A. Jennings; A. Sivashanmugam; R. Jayakumar. Characterization of chitosan matters. In *Chitosan Based Biomaterials Volume 1*, J.A. Jennings, J.D. Bumgardner, Eds. Woodhead Publishing: 2017; pp. 81-114.
18. Y. Ma; L. Xin; H. Tan; M. Fan; J. Li; Y. Jia; Z. Ling; Y. Chen; X. Hu; *Mater. Sci. Eng. C*, **2017**, *81*, 522-531.
19. M.J. Bof; V.C. Bordagaray; D.E. Locaso; M.A. García; *Food Hydrocoll.*, **2015**, *51*, 281-294.
20. J. Kingkaew; S. Kirdponpattara; N. Sanchavanakit; P. Pavasant; M. Phisalaphong; *Biotechnol Bioprocess Eng.*, **2014**, *19*, 534-544.
21. D. Yarboro; A. Millar; R. Smith; *Wound management & prevention*, **2019**, *65*, 16-22.
22. A. Gupta; P. Avci; T. Dai; Y.-Y. Huang; M. Hamblin; *Adv Wound Care*, **2013**, *2*, 422-437.
23. S.K. Mishra; S. Raveendran; J.M. Ferreira; S. Kannan; *Langmuir.*, **2016**, *32*, 10305-10316.
24. A.I. Visan; G. Popescu-Pelin; G. Socol; *Polymers*, **2021**, *13*.
25. C. Wu; T. Wu; Z. Fang; J. Zheng; S. Xu; S. Chen; Y. Hu; X. Ye; *RSC Adv.*, **2016**, *6*, 46686-46695.
26. L. Remedio; J. Santos; V. Maciel; C. Yoshida; R. Carvalho; *Food Hydrocoll.*, **2018**, *87*.
27. X. Zhu; H. Wu; J. Yang; J. Tong; J. Yi; Z. Hu; J. Hu; T. Wang; L. Fan; *React. Funct. Polym*, **2015**, *91-92*, 71-76.
28. N. Cé; C.P.Z. Noreña; A. Brandelli; *CYTA J Food.*, **2012**, *10*, 21-26.
29. J.L. Webber; R. Namivandi-Zangeneh; S. Drozdek; K.A. Wilk; C. Boyer; E.H.H. Wong; B.H. Bradshaw-Hajek; M. Krasowska; D.A. Beattie; *Sci. Rep.*, **2021**, *11*, 1690.
30. M.L. Mangoni; A.M. McDermott; M. Zasloff; *Exp Dermatol*, **2016**, *25*, 167-173.
31. H. Felgueiras; M.T. Amorim; *Colloids Surf B Biointerfaces*, **2017**, *156*.
32. L.W. Place; T. Helmonds; S.F. Filocamo. *Development and Characterization of Methods to Encapsulate Nisin for Use as an Antimicrobial Agent*; Natick Soldier Research, Development and Engineering Center: 2018.
33. L. Cui; S. Gao; X. Song; L. Huang; H. Dong; J. Liu; F. Chen; S. Yu; *RSC Advances*, **2018**, *8*, 28433-28439.
34. R.I. Nakayama; K. Katsumata; Y. Niwa; N. Namiki; *Membranes*, **2020**, *10*.
35. A.K. Azad; N. Sermsintham; S. Chandkrachang; W.F. Stevens; *Journal of biomedical materials research. Part B, Applied biomaterials*, **2004**, *69*, 216-222.
36. Z. Yu; F.K. Alsammarraie; F.X. Nayigiziki; W. Wang; B. Vardhanabhuti; A. Mustapha; M. Lin; *Food Res. Int.*, **2017**, *99*, 166-172.
37. S. Ahmed; S. Ikram; *J. Photochem. Photobiol. B, Biol.*, **2016**, *163*, 115-124.
38. A. Nouri; M.T. Yarak; M. Ghorbanpour; S. Agarwal; V.K. Gupta; *Int. J. Biol. Macromol.*, **2018**, *109*, 1219-1231.

ELECTROCHEMICAL EVALUATION OF THE RELATIONSHIP BETWEEN THE THERMAL TREATMENT AND THE PROTECTIVE PROPERTIES OF THIN SILICA COATINGS ON ZINC SUBSTRATES

TAMARA-RITA OVÁRI^a, GABRIEL KATONA^b, GABRIELLA SZABÓ^{b,*},
LIANA MARIA MURESAN^a

ABSTRACT. One of the challenges of smart and thin silica layers preparation on metallic substrates consists in the simultaneous network formation and introduction of corrosion inhibitors in it. Taking into account that both steps are affected by the temperature, it is really important to evaluate first its effect on the silica network formation. In this context, this paper aims the presentation of findings regarding the optimal heat treatment parameters in the preparation of thin silica (SiO₂) coatings on zinc. These silica layers were prepared by sol-gel method (dip-coating technique) and were tested as protective films against zinc (Zn) corrosion. After optimization of several parameters such as the drying temperature, drying duration, the corrosion resistance of the coatings was evaluated mainly by means of electrochemical methods (electrochemical impedance spectroscopy and potentiodynamic polarization). The electrochemical evaluation corroborated with morpho-structural characterization led to the conclusion that the SiO₂ coatings have better protection properties when dried at 150°C for 1h.

Keywords: *zinc; sol-gel; silica coating; electrochemical impedance spectroscopy; potentiodynamic polarization curves*

INTRODUCTION

Materials-oriented scientists manifest great interest in the last decades towards sol-gel techniques and coatings preparation on different substrates.

^a Department of Chemical Engineering, Babes-Bolyai University, Faculty of Chemistry and Chemical Engineering, 11, Arany J. St, 400028 Cluj-Napoca, Romania

^b Department of Chemistry and Chemical Engineering of Hungarian Line, Babes-Bolyai University, Faculty of Chemistry and Chemical Engineering, 11, Arany J. St, 400028 Cluj-Napoca, Romania

* Corresponding author: gabriella.szabo@ubbcluj.ro

The sol–gel route is based on the evolution of a colloidal system through the formation of an inorganic or hybrid sol followed by its gelation to form a continuous polymer network (gel) [1]. Among these, due to their versatile applications, silica thin films have a great importance. Some of them aim to obtain superhydrophobic, anti-fogging [2], antireflective and increased light transmitting [3, 4] surfaces applicable on solar cells, eyeglasses, windshields and other optical areas. The deposition of silica coatings on coked alumina refractories, units of the petrochemical industry, can modify their surface and enhance their mechanical properties [5]. Last but not least, an important application of silica layers is due to their anticorrosion protective properties.

The coatings prepared by sol-gel method showed great potential for the replacement of toxic pre-treatments and layers, like chromate conversion coatings, which have traditionally been used [6], but due to highly toxic hexavalent chromium salts, which cause DNA damage and cancer [1], they were banned [7, 8]. This method is an eco-friendly technique of metal surface protection against corrosion and offers many advantages, a few of them being the low processing temperature and the “green” coating technology, which means that the method is waste-free and excludes the stage of washing [6]. Sol-gel coatings act as barriers on the surface of the metal, blocking the access of corrosive media and enhancing the corrosion protection [9, 10]. Despite the fact that wide-ranging studies were made in the past decades, the relationship between the sol formation, gelation process parameters and the interface properties of these coatings are not very well known yet. To control and design the properties of these coatings, further studies are necessary [6]. The sol composition (molar ratio of components), the used solvent and catalyst (acid or base), the ageing and annealing temperature, and the thermal treatment duration are factors that determine the structure and subsequently the mechanical and optical properties, as well as the electrochemical resistance [2-5, 11] of the coatings.

In previous works, we reported the preparation of mesoporous silica coatings by sol-gel method and the impregnation of their pore system with corrosion inhibitors [12, 13]. In other cases, they were doped with encapsulated corrosion inhibitors and polymerizable agents and consequently they exhibited self-healing properties [14-18].

In the cases of mesoporous coatings, surfactants were added to the precursor sols in higher concentration than the critical micellar concentration. By the heat treatment, the as formed micelles were transformed into pores that could host corrosion inhibitors. However, there are several nanoparticles (e.g., graphene oxide GO) that cannot be introduced in the mesopores formed in the abovementioned way, so in those cases this procedure is useless. From this perspective there is no need for the heat treatment at 410 °C mentioned in our

previous reports which was necessary only for the combustion of the micelles. In case of Zn, a supplementary complication occurs due to its behavior at elevated temperatures, more specifically exceeding 200 °C, when horizontal and vertical cracks could appear on the metal surface [19]. It also has a melting point of 419.5 °C. This is why a reconsideration of the thermal treatment of the silica coatings is necessary.

Although it has a broad implementation, the heat treatment of silica coatings differs from one study to another [7, 9, 10] and from one metal to another. As it is of great importance to generate excellent adhesion between the Zn surface and silica coating, the influence of the temperature and its effects on the silica layers deposited on Zn needs to be further discussed. Moreover, in our previous work, aiming to develop a coating with both barrier and inhibitor carrier properties, it was reported that compact silica layers on Zn presented approximately the same anti-corrosive protection like the porous ones, which were obtained at higher temperatures [12]. This interesting and unexpected finding motivated the further investigation on how the thermal treatment affects the silica coatings properties

In this work, a detailed investigation regarding the curing process of the silica coating was made to determine the optimal conditions (drying temperature and duration) for the preparation of silica coatings on zinc substrates by sol-gel method. To the best of our knowledge, a deep electrochemical investigation able to correlate the anti-corrosion properties of the coatings with the thermal treatment parameters of silica deposits on zinc was not yet reported. For this purpose, electrochemical impedance spectroscopy (EIS) and potentiodynamic polarization measurements were used. The morphology and structure of the silica were determined by SEM, and the thickness of the layer by AFM measurements.

RESULTS AND DISCUSSION

The corrosion protective properties of silica-coated zinc samples prepared in different experimental conditions (various drying temperatures and drying times) were tested in an aqueous solution of 0.2 g/l Na₂SO₄ (pH 5) by using electrochemical investigation methods.

Influence of drying temperature

In order to choose properly the drying temperature of the silica coatings, firstly, thermogravimetric analysis was performed. During the probe heating, it was noticed a total loss of 86,6% in a single step. (TG). This was attributed

to the evaporation of the ethylic alcohol at 59°C (DTG supplementary data are available upon request from the authors). Therefore, the first annealing temperature (a little bit higher than the solvent evaporation) was chosen to be 80°C. On the other hand, in order to avoid the coating deterioration, the highest drying temperature was limited to 350°C. Next, several experiments were carried out in the interval between 80°C and 350°C in order to determine the optimal drying temperature of the silica protective coatings. All the coatings described in this study showed a glassy and transparent visual aspect.

Figure 1 presents the Nyquist diagrams obtained for the samples dried at ambient temperature, 80°C, 150°C, 200°C and 350°C for 0.5h, respectively, recorded at OCP. At first sight, the largest diameter of the capacitive loop, which can be assigned to the polarization resistance (R_p), was noticed in the case when the protective layer was dried at 150°C. An inductive loop was observed at 350°C suggesting a change of the protection mechanism offered by the coating.

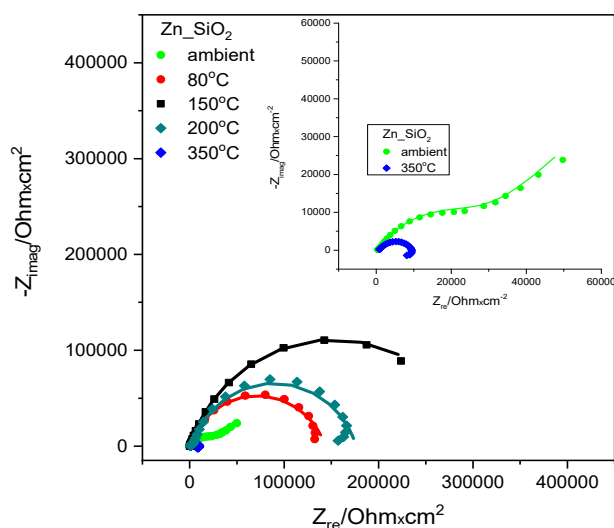


Figure 1. Nyquist impedance spectra of compact SiO₂ layers on zinc substrate dried at different temperatures for 0.5 hours. Samples were immersed in Na₂SO₄ electrolyte pH =5; spectra were recorded in 10 mHz –100 kHz frequency range.

Insets: spectra of coated Zn dried at ambient temperature and 350 °C

Impedance data were modelled using three different electrical circuits presented in **Figure 2**. The corresponding parameters obtained after fitting the experimental diagrams to an equivalent electrical circuit model are listed in **Table 1**. In all the cases, the accuracy of the fitting was estimated with the

relative standard error percent for the equivalent circuit parameters (mostly below 10%) and the chi-squared χ^2 value (around 10^{-3} or less). In **Figure 2**, R_s is the solution resistance, R_{ct} and Q_{dl} represent the charge transfer resistance and the constant phase element corresponding to the electrical double layer capacitance at the metal/solution interface, R_{coat} and C_{coat} are the coating resistance and capacitance, respectively, and L and R (**Figure 2C**) are the inductance and the resistance occurring when the coating was heated at high temperatures during drying, suggesting a structural change of the coating.

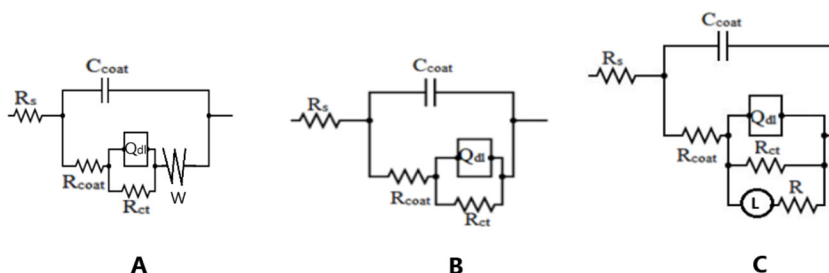


Figure 2. Equivalent electrical circuits used to model the metal/electrolyte interface when the silica coating was dried at temperatures: ambient (A), 80 °C – 200 °C (B) and at 350 °C (C)

In the case of drying at ambient temperature, the Warburg impedance in **Figure 2A** could be attributed to the diffusion of ions through the incompletely formed silica layer on zinc surface in which the polycondensation process continues taking place, as it is not finished at the moment of metal extraction from the gel and after drying it at low temperature.

Table 1. Electrochemical parameter values for Zn/SiO₂ coated samples calculated by non-linear regression of the impedance data using the equivalent electrical circuits from **Figure 2**. ($n \sim 0.79$)

Temp. °C	R_s ($k\Omega \cdot cm^2$)	C_{coat} ($\mu F/cm^2$)	R_{coat} ($k\Omega \cdot cm^2$)	Q_{dl} ($\mu S s^n/cm^2$)	R_{ct} ($k\Omega \cdot cm^2$)	$10^4 \cdot W$ ($S s^{5/2}/cm^2$)	$10^{-5} L$ ($H \cdot cm^2$)	R ($k\Omega \cdot cm^2$)	R_p ($k\Omega \cdot cm^2$)
ambient	0.35	0.154	0.25	1.67	24.61	1.213	-	-	-
80	0.14	0.328	0.16	5.55	143.10	-	-	-	143.26
150	0.17	0.268	0.202	4.83	304.8	-	-	-	305.00
200	0.61	0.085	2.61	2.67	172.80	-	-	-	175.41
350	0.69	0.036	0.24	6.66	8.80	-	4.033	17.9	9.04

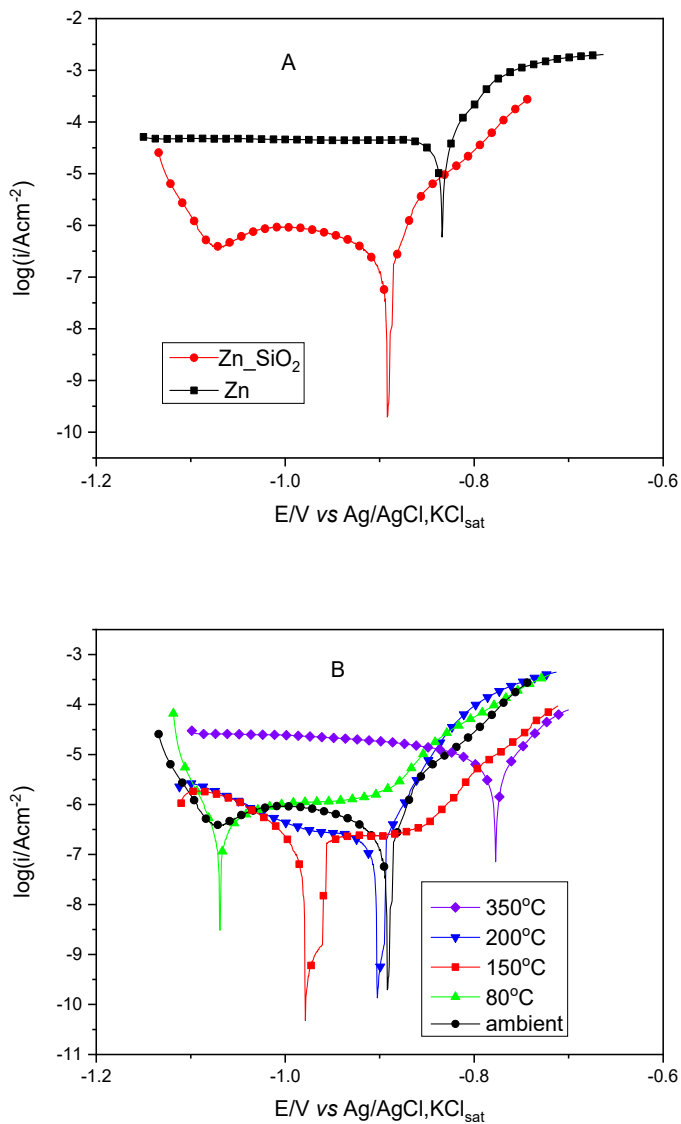


Figure 3. Potentiodynamic polarization curves recorded for bare Zn and Zn/SiO₂ samples at ambient temperature (A) and Zn/SiO₂ samples thermally treated at different temperatures (ambient, 80 °C, 150 °C, 200 °C and 350 °C) for 0.5 h (B)

The appearance of an inductive loop at high temperatures could be associated with the variation of the active surface area of the electrode and can be ascribed to an adsorbed intermediate relaxation. This type of behaviour was observed in other corroding systems too [22]. At these temperatures, also possible cracks may appear which explain the lower corrosion resistance of the coating (see also **Figure 8**). The results are similar with those reported previously in literature [1].

Further investigations were conducted by recording the potentiodynamic polarization curves of the various coated Zn samples heated at different temperatures (**Figure 3**). Bare Zn samples were used for comparison.

Some kinetic parameters like corrosion potential (E_{corr}), anodic (β_a) and cathodic (β_c) coefficients (representing the slopes of the fitted plots) were obtained by the Tafel interpretation of the polarization curves. The Tafel plots should be considered only an approximate evaluation method for the corrosion of coated metals, because the coatings themselves should be protective and are supposed to corrode only at pores. Nevertheless, the information extracted from the curves can give useful preliminary information about the corrosion resistance of the coatings [23].

$$i_{\text{corr}} = \frac{\beta_a \cdot \beta_b}{2.303 \cdot R_p \cdot (\beta_a + \beta_b)} \quad (1)$$

where β_a and β_c are the Tafel slopes determined from the polarization curves and R_p is the polarization resistance obtained from the impedance spectra.

For all samples, the kinetic parameters obtained by Tafel interpretation (the corrosion potential E_{corr} , cathodic and anodic Tafel coefficients β_c and β_a) are listed in **Table 2**. The corrosion current densities i_{corr} were calculated by Stern-Geary equation, the polarization resistance values (R_p) were determined from impedance spectra. PE represents protective efficiency.

Table 2. Corrosion parameters for coated zinc samples determined from Tafel interpretation of the polarization curves from **Figure 3**.

Sample	T °C	E_{corr} (vs. Ag/AgCl, KCl) (V)	i_{corr} ($\mu\text{A} / \text{cm}^2$)	β_c (V/dec)	β_a (V/dec)	R_p ($\text{k}\Omega \cdot \text{cm}^2$)	PE (%)
Bare Zn	ambient	-0.830	16.030	-	0.048	1.30	-
Zn/SiO ₂	ambient	-0.891	0.526	0.216	0.035	24.86	96.72
	80	-1.068	0.078	0.031	0.149	143.26	99.51
	150	-1.040	0.090	0.080	0.300	305.00	99.44
	200	-0.901	0.087	0.280	0.040	175.41	99.45
	350	-0.766	2.86	0.489	0.068	9.04	82.16

The protective efficiency of the coatings, PE, was calculated with the formula:

$$PE(\%) = 100 \cdot \frac{i_{corr}^0 - i_{corr}}{i_{corr}^0} \quad (2)$$

where i_{corr}^0 is the value of the corrosion current density for the uncoated Zn sample, while i_{corr} is the corrosion current density of the coated samples.

The random change in the Tafel constants indicates a mixed inhibition mechanism where rates of zinc dissolution (anodic process) and oxygen evolution (cathodic process) are retarded by the presence of sol-gel coatings [24].

Analyzing the polarization curves, it can be also seen that a decrease with three orders of magnitude of i_{corr} is noticed (in comparison with the bare Zn) in the case when the drying temperature was 150°C. In this case, the protection efficiency reached 99.64 % suggesting that the coating is continuous, without cracks and able to protect successfully the zinc substrate. Consequently, for further experiments, the optimal drying temperature was chosen 150°C.

Influence of heat treatment duration

After preparation, the coated samples were heated at the optimal drying temperature (150 °C) in a drying oven for 0.5 h, 1 h, 2 h and 4 h. The Nyquist impedance spectra from **Figure 4** show the largest diameter of the capacitive loop corresponding to the polarization resistance at the duration of 1h of the drying process. It is believed that at this time the silica's polycondensation is finished. After 4h, further heating of the coating could lead to structural changes that are not beneficial for the coating's resistance (cracks may appear).

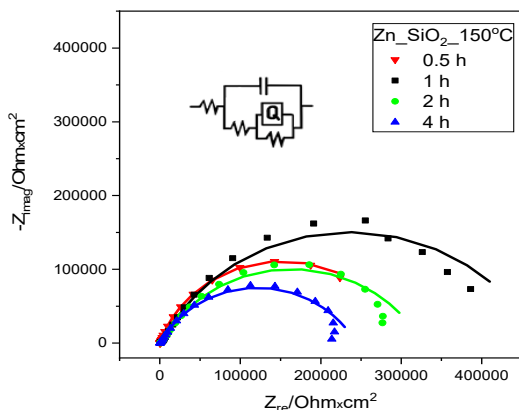


Figure 4. Nyquist impedance spectra of compact SiO₂ layers on zinc substrate prepared at 150°C with different duration of heat treatment. Samples were immersed in Na₂SO₄ electrolyte pH =5, spectra were recorded in 10 mHz –100 kHz frequency range.

The EIS spectra were fitted to the equivalent electrical circuit model from **Figure 2B** and the results are presented in **Table 3**.

Table 3. Electrochemical parameter values for Zn/SiO₂ coated samples dried at 150°C for different intervals of time calculated by non-linear regression of the impedance data. ($n \sim 0.79$)

Heat treatment duration (h)	R_s (k $\Omega \cdot \text{cm}^2$)	C_{coat} ($\mu\text{F}/\text{cm}^2$)	R_{coat} (k $\Omega \cdot \text{cm}^2$)	Q_{dl} ($\mu\text{Ss}^n/\text{cm}^2$)	R_{ct} (k $\Omega \cdot \text{cm}^2$)	$R_p = R_{\text{coat}} + R_{\text{ct}}$ (k $\Omega \cdot \text{cm}^2$)	χ^2
0.5	0.17	0.268	0.20	4.83	304.80	305.00	$1.74 \cdot 10^{-3}$
1	0.58	0.084	2.37	3.89	468.20	470.57	$7.12 \cdot 10^{-3}$
2	0.73	0.085	1.66	3.57	323.60	325.26	$5.35 \cdot 10^{-3}$
4	0.21	0.107	0.78	3.12	242.80	243.58	$3.52 \cdot 10^{-3}$

It can be observed that the highest resistance of the coating was reached after 1h. In the same time, the charge transfer resistance R_{ct} reaches a maximum, suggesting a braking of the corrosion process as compared to the coatings heated at lower or higher temperatures. This is due to better protective properties of the silica coating.

The polarization curves corresponding to the corrosion behaviour of Zn/SiO₂ samples heated at 150 °C for different intervals of time are presented in **Figure 5**.

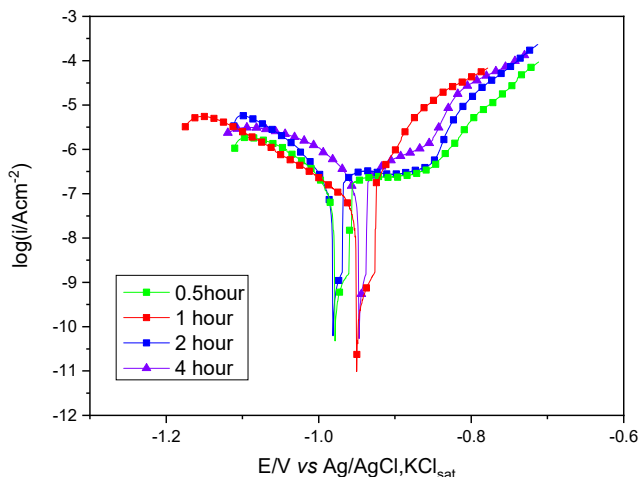


Figure 5. Potentiodynamic polarization curves recorded for zinc and Zn/SiO₂ samples heated at 150 °C for different intervals of time.

The kinetic parameters of the corrosion process obtained by the Tafel interpretation of the above-mentioned polarization curves are listed in **Table 4**. As before mentioned, E_{corr} is the corrosion potential, and β_c and β_a are the cathodic and anodic Tafel coefficients. The corrosion current densities i_{corr} were calculated by Stern-Geary equation, the polarization resistance values (R_p) were determined from impedance spectra. PE represents the protective efficiency.

Table 4. Corrosion parameters for coated zinc samples determined from Tafel interpretation of the polarization curves (**Figure 5**).

Heat treatment	Duration	E_{corr} (V vs. RE)	i_{corr} ($\mu\text{A} / \text{cm}^2$)	β_c (V/dec)	β_a (V/dec)	R_p ($\Omega \cdot \text{cm}^2$)	PE (%)
Bare Zn	-	-0.83	16.03	-	0.048	1.30	-
Zn/SiO ₂	0.5 h	-1.040	0.090	0.080	0.300	305.00	99.44
	1 h	-0.952	0.043	0.064	0.166	470.57	99.73
	2 h	-0.980	0.077	0.077	0.232	325.26	99.52
	4 h	-0.945	0.095	0.091	0.128	243.58	99.41

Analysing the parameters listed in **Table 4**, one can conclude that the best performance belongs to the coatings dried at 150 °C for 1h. This is in agreement with the results obtained with EIS method. The corrosion current densities reported in our previous works [9, 12] for compact silica coatings prepared at high temperature of 410 °C were μA order, similar to those obtained at 350 °C, but a significant current drop was achieved only by using a silylating agent. By using lower annealing temperatures, such as 150 °C it can be observed the decrease of i_{corr} with approximately two orders of magnitude without any further treatment.

Atomic force microscopy

In order to assess surface coverage and coating homogeneity, AFM analysis was conducted on Zn/SiO₂ samples. The atomic force microscopy images on the pre-treated bare zinc sample show a relatively uniform surface with only a few remaining scratches after the polishing procedure (**Figure 6 A and B**).

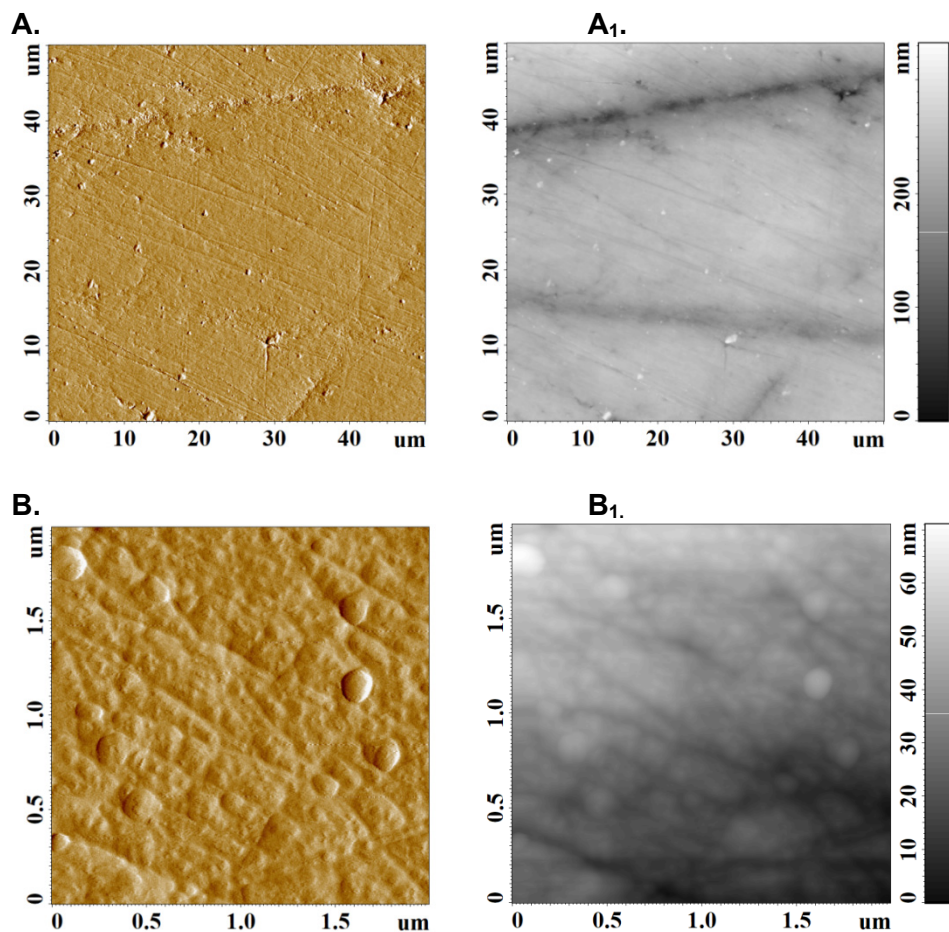


Figure 6. AFM images at two different magnifications (A, B) and high-resolution topographies (A1, B1) of Zn samples.

The high-resolution topographies prove that the depth of these surface deformities is generally below 60 nm, with only a few reaching 100 nm (**Figure 6 A1 and B1**). In the same time, from our previous studies regarding the coating thickness [9, 12] we learned that compact silica deposits are about 130 – 250 nm thin depending on the number of layers.

Similarly, AFM images of the coated surface point to a surface irregularity generally lower than 10 nm (**Figure 7 A1, B1**). Due to the effectiveness of the coating process, most surface deformities appear to be

covered by SiO_2 (**Figure 7A and B**), while only a few crevices with more significant depth remaining visible on the AFM images (**Figure 7 A**). Overall, microscopy studies point to a good coverage of the zinc surface.

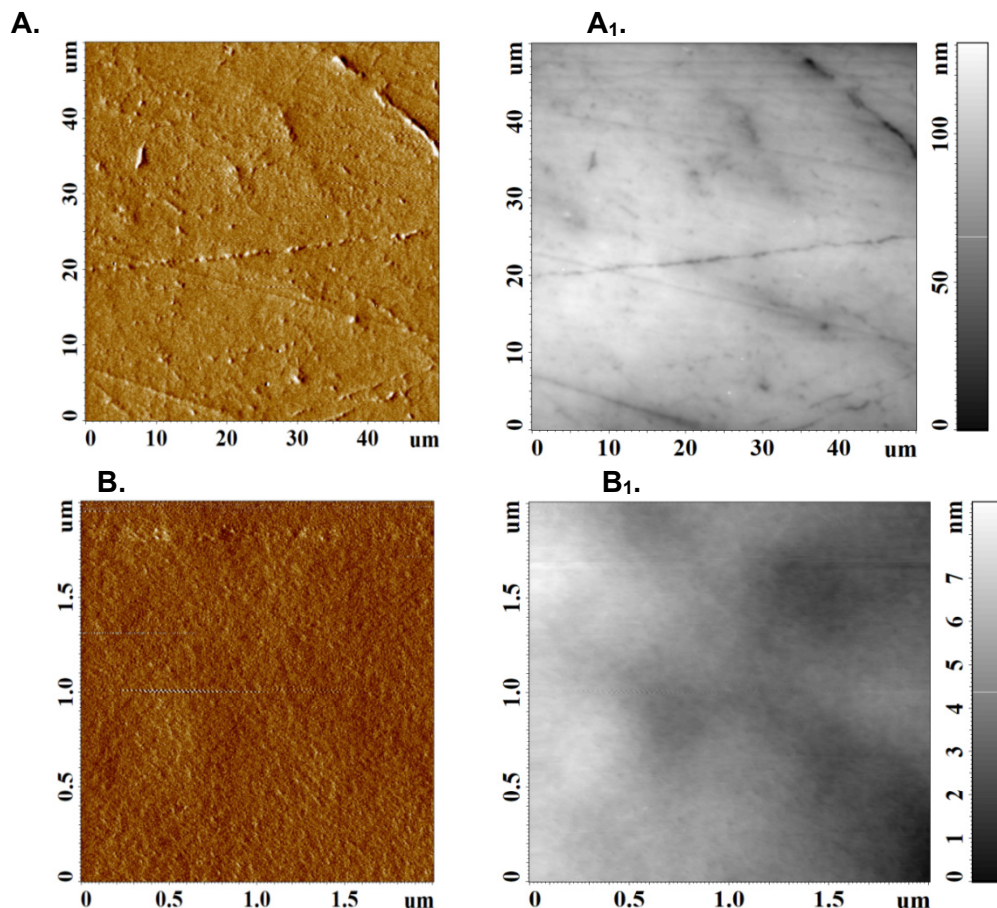


Figure 7. AFM images at two different magnifications (A, B) and high-resolution topographies (A1, B1) of Zn/SiO₂ samples dried at 150 °C during 1h.

Scanning electron microscopy

SEM images taken immediately after the silica coating deposition on zinc and after 2 weeks held in a corrosive solution of Na_2SO_4 (pH 5) clearly showed that the heat treatment at 350 °C causes the cracking of the silica coating from the beginning (**Figure 8 B and D**). These cracks explain the

lower corrosion protective efficiency of these layers (**Table 2**) [25]. On the contrary, the samples cured at 150 °C present a good coverage (**Figure 8 A**) and only few corrosion points even after 2 weeks of immersion in the corrosive medium (**Figure 8 C**).

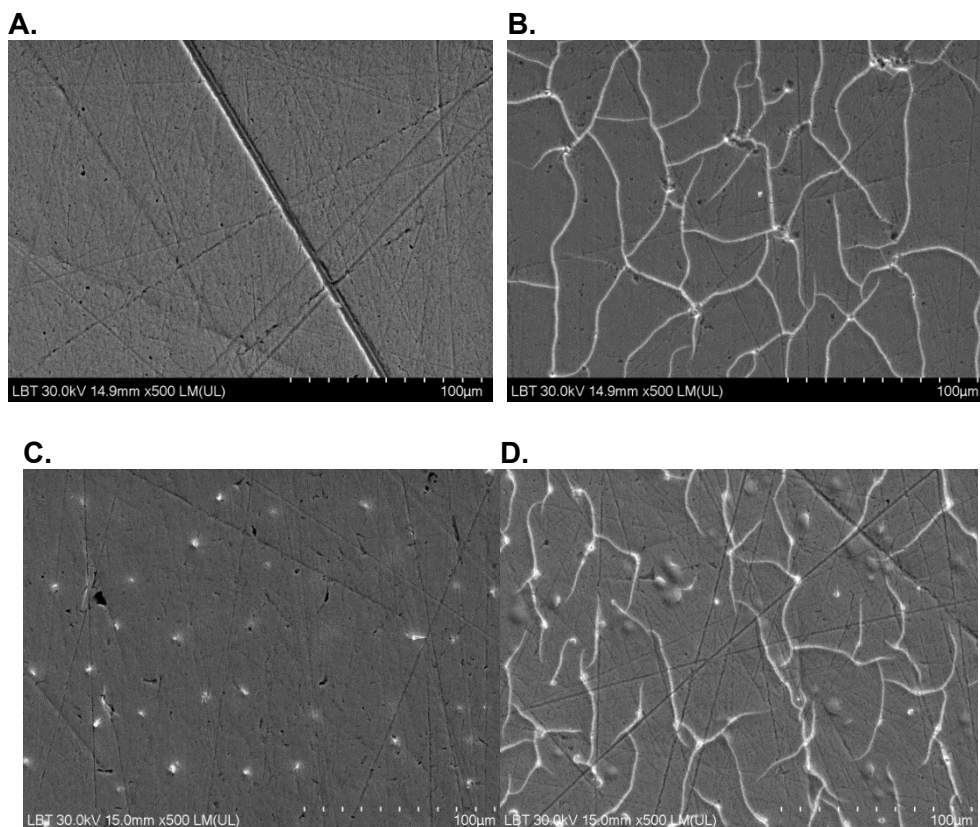


Figure 8. SEM images of silica coated Zn samples, thermal treated during 1 h after layer deposition at (A) 150 °C, and (B) 350 °C; after kept 2-weeks in 0.2 g/L Na₂SO₄ solution (pH 5) for sample treated at (C) 150 °C and (D) 350 °C.

CONCLUSIONS

The preparation of thin sol–gel silica coatings on zinc substrates was optimized in order to enhance their anti-corrosion properties. SiO₂ can improve the oxidation and acidic corrosion resistance of zinc due to its high heat and chemical resistance. After comparing the obtained results with that

of previous ones [12], one can conclude, that the heat treatment of the coatings between 80-200 °C caused an increasing anti-corrosion resistance, the corrosion current densities decreased approximately two orders of magnitude.

The duration of the heat treatment also influences the properties of layers, and it was shown that the optimal time interval is 1 hour. Results have shown to be very promising and led to the conclusion that the SiO₂ coatings have better protection properties when dried at 150°C for 1h. In these conditions can be obtained a quite compact, crack free and very good coverage of the Zn surface.

Nevertheless, the electrochemical measurements have shown that the investigated system, even when prepared in optimized conditions, exhibit only limited barrier properties and after a while the pitting corrosion appears. This drawback could be diminished by hydrophobization, multi-layer deposition and/or doping.

EXPERIMENTAL SECTION

Materials

Tetraethyl-orthosilicate (TEOS, for synthesis, >99%, Merck), hydrochloric acid (HCl, purum, 37%, Fluka), ethanol (EtOH, a. r., >99.7%, Reanal), and distilled water were used for preparing the precursor sol. The electrochemical measurements were done in aqueous solution of sodium sulfate (Na₂SO₄, 99%, Riedel-de Haen).

The Zn substrate (7x2cm) was polished emery paper (grade 1200, 2000, 3000), then ultrasonicated in 2-propanol (2-PrOH, a. r., > 99.7%, Reanal), cleaned with 0.1M aqueous HCl solution and with 2-propanol before layer deposition. The active surface of the sample in electrochemical measurements was limited to 2 cm².

Precursor sol synthesis

Silica precursor sols were prepared by acid catalysed, controlled hydrolysis of TEOS in ethanolic media. 0.1M aqueous HCl solution was used as a catalyst. The molar ratios for TEOS:EtOH:H₂O:HCl were 1:18.6:5.5:1 10⁻³ M. The solution was stirred for 60 min at ambient temperature. The precursor sols were stored at 25°C for 24 h prior to use [12].

Preparation of the coatings

Before layer deposition, in order to remove any scratches from the surface of the Zn substrate, it was polished with emery paper. In the subsequent step, the substrate was ultrasonicated in 2-propanol solution for

2 minutes, then treated with 0.1M aqueous HCl solution followed by 2-propanol solution and dried.

The sol-gel silica films on Zn were prepared from the above-mentioned precursor sol by dip-coating method (home-made dip-coater). The procedure consisted in the immersion of the cleaned and dried substrates in the precursor sol with a constant speed of withdrawal of 10 cm/min. The coated Zn was annealed at different temperatures (ambient temperature, 80°C, 150°C, 200°C, 350°C) for 0.5h or at 150°C at different drying durations (0.5h, 1h, 2h, 4h) with the aim of finding the optimal parameters to obtain favourable results consisting their anticorrosion properties.

Electrochemical characterization

The electrochemical measurements were carried out in a three-electrode cell containing a working electrode (the bare or coated Zn sample, $S = 2 \text{ cm}^2$), a counter electrode (platinum wire) and a reference electrode (Ag/AgCl/KCl_{sat}). All measurements were performed in 0.2 g/L Na₂SO₄ solution (pH = 5.0) with a computer-controlled potentiostat (PARSTAT 2737). First of all, the open circuit potentials (OCP) were recorded during 1 h and after that, electrochemical impedance spectroscopy (EIS) measurements were performed in the frequency range 10 mHz – 100 kHz, with a sinusoidal current of 10 mV amplitude, at OCP. Further, the polarization curves ($E = \pm 200 \text{ mV}$ vs. OCP) were recorded with a scan rate of 0.166 mV/s.

Atomic force microscopy analysis

The high-resolution topographies were recorded with an MFP-3D atomic force microscope (Asylum Research, Santa Barbara CA; driving software written in IgorPro 6.34A, Wavemetrics), using rectangular silicon cantilevers with a tetrahedral tip of a radius below 10 nm (AC240, Olympus, Optical Co. Ltd. Tokyo, Japan). The spring constant for each cantilever used was calibrated prior to measurements, according to standard built-in procedures [20, 21]. The images were recorded in a 50X50 μm and 2X2 μm surface area, respectively. All height images were first order flattened and plane-fitted in order to correct any sample tilt.

Scanning electron microscopy analysis

To study the morphological and structural properties of the coatings a Hitachi SU8230 ultra-high resolution scanning electron microscope was used. SEM measurements were conducted to investigate the surface morphology of the samples treated at high temperature such as 350 °C, compared with the samples cured on 150 °C for 1h.

Thermogravimetric investigation

In order to establish the right working temperature interval, thermogravimetric analysis of the silica gel was carried out on a TGA/SDTA 851e-METTLER, TOLEDO apparatus. The samples were placed in an Alumina 900 μ L sample holder. The measurements were carried out in a 60mL/min flow rate fed air atmosphere.

ACKNOWLEDGMENTS

The present work has received financial support through the project: Entrepreneurship for innovation through doctoral and postdoctoral research, POCU/380/6/13/123886 co-financed by the European Social Fund, through the Operational Program for Human Capital 2014- 2020. The authors thank Dr. Ioana Perhaița for the thermogravimetric analysis.

REFERENCES

1. M. Zheludkevich; I.M. Salvado; M. Ferreira; *J. Mater. Chem.*, **2015**, *15*, 5099-5111.
2. L. Ye; Y. Zhang; C. Song; Y. Li; B. Jiang; *Mater. Lett.*, **2017**, *188*, 316-318.
3. F. Chi; Y. Zeng; C. Liu; D. Liang; Y. Li; R. Xie; N. Pan; C. Ding; *Results Phys.*, **2020**, *18*, 103315.
4. F. Chi; Y. Zeng; C. Liu; *Optik*, **2020**, *224*, 165501.
5. K.S. Campos; G.F.B. L. e Silva; E.H.M. Nunes; A.M.A. Silva; G.A. Bestard; W.L. Vasconcelos; *Ceram.*, **2019**, *45*, 8626-8633.
6. D. Wang; G. P. Bierwagen; *Prog. Org. Coat.*, **2009**, *64*, 327-338.
7. S. Dalbin; G. Maurin; R.P. Nogueira; J. Persello; N. Pommier; *Surf. Coat. Technol.*, **2005**, *194*, 363-371.
8. A.S.H. Makhoulouf; *Qatar Foundation Annual Research Forum*, **2013**, Volume Issue 1, HBKU Press.
9. E. Volentiru; M. Nyári; G. Szabó; Z. Hórvölgyi; L. M. Mureșan; *Period. Polytech. Chem. Eng.*, **2014**, *58*, 61-66.
10. N. Cotolan; S. Varvara; E. Albert; G. Szabó; Z. Hórvölgyi; L.M. Mureșan; *Cor. Eng. Sci. Technol*, **2016**, *51*, 373-382.
11. A.S. Hamdy; F. Alfossail; Z. Gasem; *Electrochim. Acta*, **2013**, *107*, 518-524.
12. E. Albert; N. Cotolan; N. Nagy; Gy. Sáfrán; G. Szabó; L.M. Mureșan; Z. Hórvölgyi; *Microporous Mesoporous Mater.*, **2015**, *206*, 102-113.
13. G. Szabó; E. Albert; J. Both; L. Kócs; Gy. Sáfrán; A. Szöke; Z. Hórvölgyi; L.M. Mureșan; *Surf. Interfaces*, **2019**, *15*, 216-223.

14. A.A. Nazeer; M. Madkour; *J. Mol. Liq.*, **2018**, 253, 11-22.
15. X. Wang; W. Wang; A. Liu; W. Fan; R. Ding; H. Tian; P. Han; W. Li; *Colloids Interface Sci. Commun.*, **2018**, 27, 11-17.
16. M. Montemor; *Surf. Coat. Technol.*, **2014**, 258, 17-37.
17. C.I. Idumah; C.M. Obele; E.O. Emmanuel; A. Hassan; N. Azikiwe; *Surf. Interfaces*, **2020**, 100734.
18. N.Y. Abu-Thabit; A.S. Hamdy; *Surf. Coat. Technol.*, **2016**, 303, 406-424.
19. J. Votava; V. Kumbár; A. Polcar; M. Fajman; *Acta Technol. Agric.*, **2020**, 23, 7-11.
20. J.L. Hutter; J. Bechhoefer; *Rev. Sci. Instrum.*, **1993**, 64, 1868-1873.
21. J.E. Sader; J.W. Chon; P. Mulvaney; *Rev. Sci. Instrum.*, **1994**, 70, 3967-3969.
22. M.P. Gomes, I. Costa; N. Pébère; J.L. Rossi; B. Tribollet; V. Vivier; *Electrochim. Acta*, **2019**, 306, 61-70.
23. M. Stern; A.L. Geary; *J. Electrochem. Soc.*, **1957**, 104, 56.
24. R.B. Vignesh; T.N.J.I. Edison; M. G. Sethuraman; *Mater. Sci. Technol.*, **2014**, 30, 814-820.
25. B. Xue; M. Yu; J. Liu; J. Liu; S. Li; L. Xiong; *J. Alloys Compd.*, **2017**, 725, 84-95.

RADIOCARBON INVESTIGATION OF TWO OLD ELMS FROM ROMANIA

ADRIAN PATRUT^{a,b *}, ROXANA T. PATRUT^a,
VICTOR BOCOS-BINTINTAN^c, ILEANA-ANDREEA RATIU^{a,b},
LASZLO RAKOSY^d, GEORGE ZDROB^e, EUFROSINA VANCA^f,
KARL F. VON REDEN^g

ABSTRACT. The paper reports the AMS (accelerator mass spectrometry) radiocarbon investigation results of two superlative elms from Romana, the very large field elm of Calafat, with a wood volume of 85 m³, and the wych elm of Sadova. Two wood samples were extracted from each elm and were analysed by AMS radiocarbon. The oldest dated sample from the elm of Calafat had a radiocarbon date of 350 ± 19 BP, which corresponds to a calibrated age of 415 ± 25 years, while the oldest sample from the elm of Sadova had a radiocarbon date of 188 ± 24 BP, corresponding to a calibrated age of 260 ± 25 years. These values indicate high ages for the two elms, namely 430 ± 25 years or the elm of Calafat and 400 ± 25 years for the elm of Sadova.

Keywords: AMS radiocarbon dating, *Ulmus minor*, *Ulmus glabra*, dendrochronology, age determination, Romania.

^a Babeş-Bolyai University, Faculty of Chemistry and Chemical Engineering, 11 Arany Janos, RO-400028, Cluj-Napoca, Romania.

^b Babeş-Bolyai University, Raluca Ripan Institute for Research in Chemistry, 30 Fantanele, RO-400294 Cluj-Napoca, Romania.

^c Babeş-Bolyai University, Faculty of Environmental Science and Engineering, 30 Fantanele, RO-400294 Cluj-Napoca, Romania.

^d Babeş-Bolyai University, Faculty of Biology and Geology, 44 Republicii, RO-400015, Cluj-Napoca, Romania.

^e Campulung Moldovenesc City Hall, 22 Decembrie 1989, RO-72510 Campulung Moldovenesc, Romania

^f Independence High School, 4 Horia, Closca si Crisan, RO-205200 Calafat, Romania

^g NOSAMS Facility, Dept. of Geology & Geophysics, Woods Hole Oceanographic Institution, Woods Hole, MA 02543, U.S.A.

* Corresponding author: apatrut@gmail.com

INTRODUCTION

Elms are deciduous flowering trees, which belong to the genus *Ulmus* L., in the Ulmaceae family. *Ulmus* species are widespread in the temperate regions of the northern hemisphere, i.e., in Northern America, Europe and Asia. In Europe, including Romania, three species are the most common, namely the European white elm (*Ulmus laevis* Pall.), the wych elm (*Ulmus glabra* Huds.) and the field elm (*Ulmus minor* Mill.). Elms grow in broadleaved cool forests, which are found especially near rivers and floodplains [1,2].

The story of elms is strongly marked by two destructive pandemics, determined by the introduction in the 20th century of the highly contagious fungal pathogen *Ophiostoma*. The two pandemics, caused in the 1920s by the micro-fungus *O. ulmi* and in the 1970s by *O. novo-ulmis*, are generally known as the Dutch Elm Disease (DED). The DED, which is one of the deadliest tree diseases, has devastated the elm populations from all over Europe and Northern America. The disease is transmitted by two species of the *Scolytus* elm-bark beetle or throughout the root network, leading to the death of elm trees in 2-3 years [1,2].

In 2005, we started a complex research project focused on elucidating several controversial problems regarding the architecture, growth and age of the African baobab and other baobab species. The research is based on an original method, which is not limited to deceased or fallen trees, but also allows to investigate and date live trees. The method consists of AMS radiocarbon dating of tiny wood samples extracted from different areas of such trees [3-9]. We extended our research by dating trees that belong to other tree species, including specimens from Romania.

Romania hosts several monumental trees, which have large dimensions and/or old ages. Thus, we investigated and dated by AMS radiocarbon some remains of the historic pedunculate oak of Țebea (deceased in 2005) [10], the large pedunculate oaks of Cajvana, Botoșana and Mercheașa [11-13], the old black poplar of Mocod (deceased in 2017), the very big grey poplar of Rafaila (deceased in 2015) [14] and the old ash of Aiton [15].

Here we present the investigation and AMS radiocarbon dating results of two old Romanian elms, namely the field elm of Calafat and the wych elm of Sadova.

RESULTS AND DISCUSSION

The field elm of Calafat and its area. The huge historic field elm (*Ulmus minor*) was located on the left shore of the Danube River, at only 5 m from the pier, in the place called Baba Lupa from Calafat, a town in Dolj county, Romania.

The GPS coordinates are 43°59.971' N, 022°56.232' E and the altitude is 33 m. The mean annual rainfall is 360 mm (Craiova Airport station).

The elm was already a very large tree in the 19th century, during the Independence War (1877–1878). Standing right next to the elm, on May 8, 1877, when a Turkish shell exploded at his feet, the future King Carol I of Romania uttered the memorable words: "This is the music I like!" [16].



Figure 1. General view of the very large field elm of Calafat

In the early 1970s, the elm was investigated and measured by Stoiculescu. The tree had a height of 43 m and the circumference at breast height (cbh; at 1.30 m above mean ground level) was 6.63 m. The trunk was twisted forming clockwise spirals along its entire length. It forked at the height of 4 m into two large branches, with diameters of 1.5 and 1.2 m (**Figure 1**). The canopy, which was asymmetrical, with a lean of over 30° towards the Danube, had a maximum diameter of 28 m and a projected floor area of 616 m². The calculated overall wood volume was 85 m³ (**Figure 2**). The elm grew on alluvial clay-sandy soil, with the groundwater table at a depth of just 2 m [16].

In 2011, the circumference of the big elm was measured again and had a value cbh = 6.70 m.



Figure 2. The photograph shows the twisted trunk of the elm of Calafat

Unfortunately, in February 2015, the historic elm from Baba Lupa was cut down at the order of a local businessman and with the consent of the city's mayor. This irresponsible act on a protected Natural Monument was motivated by the fact that its crown had begun to dry up. The remaining stump, mutilated by the blade of a bulldozer, was completely removed after a few months (**Figure 3**). Ultimately, the elm was used as firewood. Thus ended the dramatic history of one of the largest trees of Romania.



Figure 3. Image of the mutilated stump of the elm of Calafat

The wych elm of Sadova and its area. The multi-centennial wych elm (*Ulmus glabra*) is located in the Sadova village, a suburb of Campulung Moldovenesc city, Suceava county, Romania [17]. It can be found in a private garden, on a slope with south-eastern exposure, at a distance of around 50 m from a stream called Pârâul Morii, very close to its confluence with the Sadova stream. The GPS coordinates are 47°32.619' N, 025°31.573' E and the altitude is 659 m. The mean annual rainfall is 626 mm (Suceava station).

The elm, which has a new canopy with young branches, has a current height $h = 13.8$ m and a circumference $cbh = 6.77$ m (**Figure 4**). Its state is degraded, with the trunk mostly empty inside. The very large hollow extends from the ground up to the maximum height of the trunk, i.e., 5.3 m. The main entrance to the cavity has a height of 1.53 m and a variable width, which does not allow a man to enter inside. The thickness of the dry and partially rotten wood left in the walls of the cavity varies between 0.10 and 0.40 m (**Figure 5**). Only three branches of the original canopy are still standing. They have diameters up to 0.70–0.80 m. The horizontal dimensions of the restored canopy are 18.2 m (WE) x 17.6 m (NS). The current overall wood volume (including the hollow parts) is around 18 m³.



Figure 4. General view of the wych elm of Sadova

Another large hollow elm with a circumference $cbh = 5.03$ can be found at only 24 m toward the north. During the Second World War, in the hollows of the two elms, archival documents of the Cămpulung Moldovenesc Military Circle, a number of 25 weapons, carpets and other valuables were stored. Both elms are protected and have been declared Natural Monuments in 1934.

Wood samples. Two tiny samples, labelled CL-1 and CL-2, were extracted with a sharp instrument from the remaining stump of the elm of Calafat, shortly after it was felled, from an area close to the calculated pith.

One wood sample, labelled SA-1, with the length of 0.15 m was collected with an increment borer from the elm of Sadova, at the height of 1.61 m above ground. Two pieces/segments, each 10^{-3} m long (marked a and b), were extracted from determined positions of the sample SA-1. Another tiny sample, labelled SA-2, was extracted with a sharp instrument from the cavity, at the height of 1.45 m.

AMS results and calibrated ages. Radiocarbon dates of the 5 sample segments are listed in Table 1. The radiocarbon dates are expressed in ^{14}C yr BP (radiocarbon years before present, i.e., before the reference year 1950). Radiocarbon dates and errors were rounded to the nearest year.

Calibrated (cal) ages, expressed in calendar years CE (CE, i.e., common era), are also displayed in Table 1. The 1σ probability distribution (68.3%) was selected to derive calibrated age ranges. For two segments (CL-1, CL-2), the 1σ distribution is consistent with two ranges of calendar years, while for the other two sample segments (SA-1b, SA-2) it corresponds to three and four ranges of calendar years. In all these cases, the confidence interval of one range is considerably greater than that of the other(s); therefore, it was selected as the cal CE range of the segment for the purpose of this discussion.

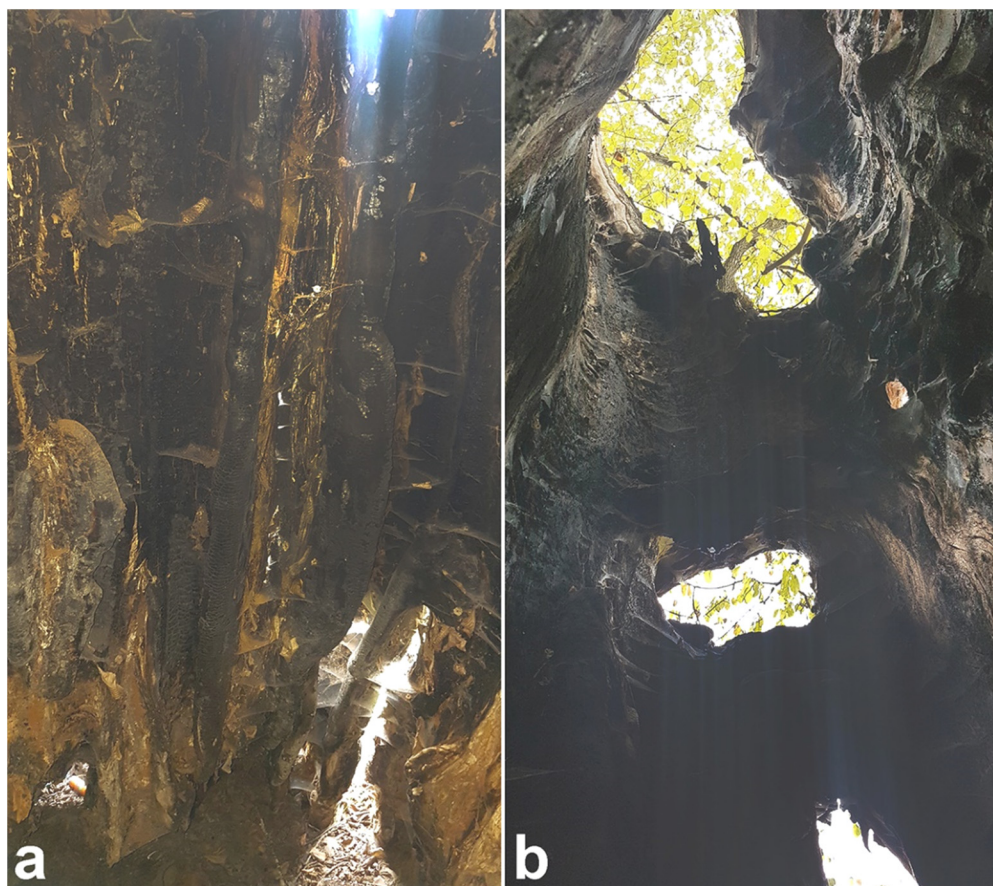


Figure 5a and b. The image shows the lower (a) and upper part (b) of the large inner cavity of the wych elm

Table 1. AMS Radiocarbon dating results and calibrated ages of samples collected from the elm of Calafat (CL) and from the elm of Sadova (SA).

Sample code	Depth ¹ [height ²] (m)	Radiocarbon date [error] (¹⁴ C yr BP)	Cal CE range 1σ [confidence interval]	Assigned year [error] (cal CE)	Sample age [error] (cal CE)
CL-1	1.05 [0.80]	345 [± 20]	1490-1524 [25.7%] 1572-1630 [42.6%]	1601 [± 29]	415 [± 30]
CL-2	1.25 [0.80]	350 [± 19]	1486-1521 [30.0%] 1578-1624 [38.3%]	1601 [± 23]	415 [± 25]
SA-1a	0.05 [1.61]	-	-	> 1950	> Modern
SA-1b	0.12 [1.61]	105 [± 18]	1696-1724 [21.7%] 1812-1838 [19.3%] 1878-1915 [27.2%]	1896 [± 18]	125 [± 18]
SA-2	0.40 [1.45]	188 [± 24]	1664-1682 [14.9%] 1736-1785 [37.9%] 1794-1802 [6.0%] 1936-... [9.5%]	1760 [± 25]	260 [± 25]

¹ Depth in the wood from the sampling point.

² Height above ground level.

For obtaining single calendar age values of sample segments, we derived a mean calendar age of each sample segment, called assigned year, from the selected range (marked in bold). Sample/segment ages represent the difference between the year 2016 CE (for samples CL-1 and CL-2, when the elm of Calafat died) or the current year 2022 CE (for samples SA-1 and SA-2) and the assigned year, with the corresponding error. Sample ages and errors were rounded to the nearest 5 yr. We used this approach for selecting calibrated age ranges and single values for sample ages in our previous articles on AMS radiocarbon dating of large and old angiosperm trees [3-15,18-21].

Dating results of samples (segments). For the elm of Calafat, the two samples extracted from the mutilated stump, i.e., CL-1 and CL-2, had very close radiocarbon dates of 345 ± 20 BP and 350 ± 19 BP. These values correspond to quasi-identical calibrated ages of 415 ± 30 and 415 ± 25 calendar yr.

For the elm of Sadova, the oldest dated sample SA-2 had a radiocarbon date of 188 ± 24 BP, which corresponds to a calibrated age of 260 ± 25 calendar yr. The deepest end of sample SA-1, namely SA-1b, had a radiocarbon date of 105 ± 18 BP, corresponding to a calibrated age of 125 ± 18 calendar yr. The negative radiocarbon date and the age of segment SA-1a shows that the elm of Sadova grew the last 0.05 m in radius in less than 72 years.

Age of the field elm of Calafat. The two samples CL-1 and CL-2, which have practically identical ages, namely 415 years (in 2016), were collected from an area which includes the calculated pith of the stump, at a distance of 0.20 m from each other. These results suggest that the true pith was positioned between the two sampling points. All these data indicate an age of 430 ± 25 years for the elm of Calafat in 2016, when it was cut down. It should be noted the excellent state of vegetation of the field elm of Calafat, whose stump did not have hollow parts. Typically, very large and old elms have their trunk mostly hollow, with little wood left in the cavities. It is worthful to mention that for almost 40 years, between the measurements of Stoiculescu and our measurements, the elm of Calafat increased in circumference by only 0.07 m, i.e., from 6.63 to 6.70 m. This value indicates a very old age.

Age of the wych elm of Sadova. The oldest sample SA-2 was extracted from the large inner cavity, at a depth in the wood of 0.40 m from the bark and at a height of 1.45 m above ground. At this height, the diameter of the tree is 2.10 m, which corresponds to a radius of 1.05 m. Taking into account that young elms grow fast, while old elms grow very slowly, we estimate that the age of sample SA-2, namely 260 years, represents around 65% of the true age of the tree. Therefore, we consider that the wych elm of Sadova is 400 ± 25 years old.

CONCLUSIONS

Our research discloses the AMS radiocarbon dating results of the giant field elm of Calafat, with a wood volume of 85 m^3 , and of the wych elm of Sadova. Two samples were extracted from each elm. The radiocarbon date of the oldest sample collected from the elm of Calafat was $350 \pm 19 \text{ BP}$, which corresponds to a calibrated age of 415 ± 25 calendar years. The oldest sample from the elm of Sadova had a radiocarbon date of $188 \pm 24 \text{ BP}$, corresponding to a calibrated age of 260 ± 25 calendar years. These results, combined with the original positions of the dated samples in the trees, indicate an age of 430 ± 25 years for the elm of Calafat and 400 ± 25 years for the elm of Sadova.

EXPERIMENTAL SECTION

Sample collection. The sample SA-1 was collected with a Hagl f CH 800 increment borer (0.80 m long, 0.0108 m inner diameter). A number of two tiny pieces/segments were extracted from predetermined positions along

the sample. The other three small samples, i.e., CL-1, CL-2 and SA-2, were extracted from predetermined positions with a sharp instrument. The sample/segments were processed and investigated by AMS radiocarbon dating.

Sample preparation. The α -cellulose pretreatment method was used for removing soluble and mobile organic components [22]. The resulting samples were combusted to CO₂, which was next reduced to graphite on iron catalyst [23,24]. The resulting graphite samples were analysed by AMS.

AMS measurements. AMS radiocarbon measurements were performed at the NOSAMS Facility of the Woods Hole Oceanographic Institution (Woods Hole, MA, U.S.A.) by using the Pelletron® Tandem 500 kV AMS system [25]. The obtained fraction modern values, corrected for isotope fractionation with the normalized $\delta^{13}\text{C}$ value of -25 ‰, were ultimately converted to a radiocarbon date.

Calibration. Radiocarbon dates were calibrated and converted into calendar ages with the OxCal v4.4 for Windows [26], by using the IntCal20 atmospheric data set [27].

ACKNOWLEDGMENTS

The research was funded by the Romanian Ministry of Education CNCS-UEFISCDI under grant PN-III-P4-ID-PCE-2020-2567, No. 145/2021.

REFERENCES

1. R.H. Richens, "Elm", Cambridge University Press, Cambridge, **1983**.
2. G. Caudullo, D. de Rigo, *Ulmus*: elms in Europe: distribution, habitat, usage and threats. In: "European Atlas of Forest Tree Species", **2016**, Publication Office of the European Union, Luxembourg, pp.186-188.
3. A. Patrut, K.F. von Reden, D.A. Lowy, A.H. Alberts, J.W. Pohlman, R. Wittmann, D. Gerlach, L. Xu, C. Mitchell, *Tree Phys.*, **2007**, 27, 1569-1574.
4. A. Patrut, K.F. von Reden, R. Van Pelt, D.H. Mayne, D.A. Lowy, D. Margineanu, *Ann. Forest Sci.*, **2011**, 68, 993-1003.

5. A. Patrut, S. Woodborne, K.F. von Reden, G. Hall, M. Hofmeyr, D. Lowy, R.T. Patrut, *PLoS ONE*, **2015**, *10*(1), e0117193.
6. A. Patrut, S. Woodborne, K.F. von Reden, G. Hall, R.T. Patrut, L. Rakosy, P. Danthu, J-M. Leong Pock-Tsy, D.A. Lowy, D. Margineanu, *Radiocarbon*, **2017**, *59*(2), 435-448.
7. A. Patrut, S. Woodborne, R.T. Patrut, L. Rakosy, D.A. Lowy, G. Hall, K.F. von Reden, *Nat. Plants*, **2018**, *4*, 423-426.
8. A. Patrut, R.T. Patrut, L. Rakosy, D.A. Lowy, D. Margineanu, K.F. von Reden, *Studia UBB Chemia*, **2019**, *LXIV*, 2 (II), 411-419.
9. A. Patrut, S. Woodborne, R.T. Patrut, G. Hall, L. Rakosy, C. Winterbach, K.F. von Reden, *Forests*, **2019**, *10*, 983-994.
10. A. Patrut, K.F. von Reden, D.A. Lowy, S. Pasca, L. Kekedy-Nagy, I. Sovago, *Studia UBB Chemia*, **2010**, *LV*, 1, 113-120.
11. A. Patrut, K.F. von Reden, V. Savu, D.A. Lowy, R. Mitea, I. Barbul, *Studia UBB Chemia*, **2011**, *LVI*, 1, 145-155.
12. A. Patrut, N. Robu, V. Savu, R.T. Patrut, L. Rakosy, I.A. Ratiu, D.A. Lowy, D. Margineanu, K.F. von Reden, *Studia UBB Chemia*, **2018**, *LXIII*, 4, 7-13.
13. A. Patrut, L. Rakosy, R.T. Patrut, V. Bocos-Bintintan, I.A. Ratiu, J. Bodis, S. Woodborne, *Studia UBB Chemia*, **2021**, *LXVI*, 3, 255-263.
14. A. Patrut, K.F. von Reden, D.A. Lowy, R.T. Patrut, D.L. Vaida, D. Margineanu, *Nucl. Instrum. Methods Phys. Res. Sect. B.*, **2013**, *294*, 616-621.
15. A. Patrut, R.T. Patrut, L. Rakosy, I.A. Ratiu, D.A. Lowy, J. Bodis, K.F. von Reden, *Studia UBB Chemia*, **2018**, *LXIII*, 3, 41-48.
16. C.D. Stoiculescu, *Ocrot. nat. med. inconj.*, **1978**, *22*(1), 55-58.
17. Primăria Sadova, „Legenda ulmilor secolari”,
<https://sadova.ro/en/2021/08/12/legenda-ulmilor-secolari/2021>.
18. A. Patrut, D.H. Mayne, K.F. von Reden, D.A. Lowy, S. Venter, A.P. McNichol, M. L. Roberts, D. Margineanu, *Radiocarbon*, **2010**, *52*(2-3), 727-734.
19. A. Patrut, K.F. von Reden, P. Danthu, J-M. Leong Pock-Tsy, L. Rakosy, R.T. Patrut, D.A. Lowy, D. Margineanu, *Nucl. Instrum. Methods Phys. Res. Sect. B*, **2015**, *361*, 591-598.
20. A. Patrut, R.T. Patrut, P. Danthu, J-M. Leong Pock-Tsy, L. Rakosy, D.A. Lowy, K.F. von Reden, *PLOS One*, **2016**, *11*(1): e0146977.
21. A. Patrut, A. Garg, S. Woodborne, R.T. Patrut, L. Rakosy, I.A. Ratiu, *PLOS One*, **2020**, *15*(1): e0227352.
22. N.J. Loader, I. Robertson, A.C. Barker, V.R. Switsur, J.S. Waterhouse, *Chem. Geol.*, **1997**, *136*(3), 313-317.
23. Z. Sofer, *Anal. Chem.*, **1980**, *52*(8), 1389-1391.
24. J.S. Vogel, J.R. Southon, D.E. Nelson, T.A. Brown, *Nucl. Instrum. Methods Phys. Res. Sect. B*, **1984**, *5*, 289-293.
25. M.L. Roberts, J.R. Burton, K.L. Elder, B.E. Longworth, C.P. McIntyre, K.F. von Reden, B.X. Han, B.E. Rosenheim, W.J. Jenkins, E. Galutschek, A.P. McNichol, *Radiocarbon*, **2010**, *52*, 228-235.
26. C. Bronk Ramsey, *Radiocarbon*, **2009**, *51*, 337-360.

27. P.J. Reimer, W.E.N. Austin, E. Bard, A. Bayliss, P.G. Blackwell, C. Bronk Ramsey, M. Butzin, H. Cheng, R. Lawrence Edwards, M. Friedrich, P.M. Grootes, T.P. Guilderson, I. Hajdas, T.J. Heaton, A.G. Hogg, K.A. Hughen, B. Kromer, S.W. Manning, R. Muscheler, J.G. Palmer, C. Pearson, J. van der Plicht, R.W. Reimer, D.A. Richards, E.M. Scott, J.R. Southon, C.S.M. Turney, L. Wacker, F. Adolphi, U. Büntgen, M. Capano, S.M. Fahrni, A. Fogtmann-Schulz, R. Friedrich, P. Köhler, S. Kudsk, F. Miyake, J. Olsen, F. Reinig, M. Sakamoto, A. Sookdeo, S. Talamo, *Radiocarbon*, **2020**, 62(4), 727-757.

RECENT RESEARCH RELATED TO LI-ION BATTERY RECYCLING PROCESSES – A REVIEW

IOANA ALINA POPESCU^a, SORIN-AUREL DORNEANU^{a,b,*},
ROXANA MARIA TRUȚĂ^a, PETRU ILEA^{a,b}

ABSTRACT. Recycling Li-ion batteries (LIBs) is a globally discussed issue in relation with waste management and environmental protection. This review reports the recent research and industrial progresses in LIBs recycling. After a brief introduction concerning the importance of LIBs recycling, and their structure and applications, the main aspects dedicated to LIBs recycling (pre-treatment, pyrometallurgical and hydrometallurgical processes) are presented. Greater attention has been paid to the hydrometallurgical processes due to their complexity but also because they can lead to the production of valuable products without a high ecological impact (compared to pyrometallurgical ones). Given that today, worldwide, only about 5% of spent LIBs are recycled, the data presented in our review can inspire the design and implementation of competitive technologies that fit into a sustainable circular economy that preserves the primary resources and ensures the environmental protection.

Keywords: *Li-ion batteries recycling, pre-treatment, pyrometallurgy, hydrometallurgy, environmental protection.*

INTRODUCTION

Spent LIBs recycling challenge

In the coming decades, the global production of LIBs will increase significantly due to the growing demand from the electric vehicles (EV) and portable electronics (PE) [1, 2]. At the same time, there is a growing concern about the supply of raw materials, especially rare metals such as Co. In this context, LIBs recycling provides crucial solutions for: (i) securing the supply

^a Babeș-Bolyai University, Faculty of Chemistry and Chemical Engineering, Department of Chemical Engineering, 11 Arany Janos Street, Cluj Napoca, RO-400028, Romania

^b Babeș-Bolyai University, Interdisciplinary Research Institute on Bio Nano Sciences, 42 Treboniu Laurian Street, Cluj Napoca, RO-400271, Romania

* Corresponding author: sorin.dorneanu@ubbcluj.ro

of raw materials, (ii) compensating of price fluctuations, (iii) reducing pollution and (iv) preserving of mineral resources [3, 4]. According to literature, China is the largest market for LIBs recycling and, by 2040, more than 50% of spent LIBs (equivalent to 4.3 million tonnes) will be recycled in China. Although, at the beginning of 2020, most of the available LIBs for recycling came from consumer electronics, starting from 2025, the EV sector will significantly dominate the LIBs recycling market [5].

LIBs structure and advantages

LIBs are mainly composed of housing, anode, cathode, separator, electrolyte, and other components [6, 7]. The cathode is made of metal oxides (including Li), the anode is a porous structure of carbon (graphite) that contains Li atoms, and the electrolyte solution consists in a solvent (organic or aqueous) containing a Li salt and additives. LIBs are manufactured in different geometries according to their beneficiaries' requests.

Considering LiCoO_2 and graphite as typical electrode materials, as presented in Figure 1, the charging/discharging of LIBs consists in the Li oxidizing/reducing processes, simultaneously with the transport of Li^+ ions between the two electrodes. The corresponding electrochemical reactions are [5, 8, 9]:

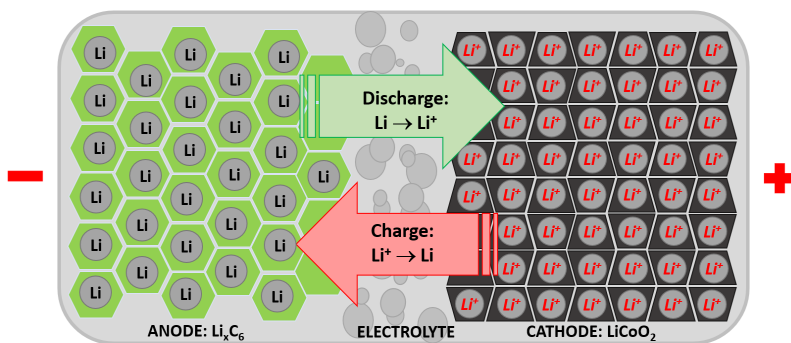
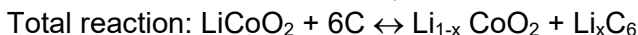


Figure 1. Schematic presentation of the LIBs charging - discharging processes

Among other aspects, the efficient energy storage is the key factor for the future of decarbonisation [9]. Due to the included components,

operation mode, advantages, and their role in a sustainable future, LIBs play an important role in the energy storage, being currently the most competitive type of battery [5, 10, 11].

The efficiency and low cost of LIBs favour the development and the number increase of EVs and hybrids. The high gravimetric and volumetric energy density of LIBs and their mass production has brought the price of electric vehicles closer to the classical ones. In terms of operating costs, the price of electricity for the operation of EVs is lower than the cost of fuel for internal combustion engines [11, 12].

Types of LIBs and their recycling assessment

Due to its complexity, the cathode material represents an essential element of LIBs, and, depending on its composition, several types were developed. The most known 6 models of LIBs are presented in Table 1, along with some specific parameters.

Table 1. Types of LIBs depending on the cathode material [5, 13]

Cathode material (Battery type)	Cost	Thermal stability	Life cycles	Applications	Safety
LiCoO ₂ (LCO)	High	Low 150°C	Short (500÷1000)	Mobile Phones, Cameras, Laptops	Poor
LiMn ₂ O ₄ (LMO)	Low	High 250°C	Short (300÷700)	EV, power tools, medical instruments	Moderate
LiNiMnCoO ₂ (NMC)	High	Moderate 210°C	Moderate (1000÷2000)	Power tools, e-bikes, EV, home energy storage	Moderate
LiNiCoAlO ₂ (LCA)	Low	Moderate 150°C	Moderate (2000)	Medical devices, industrial applications, EV	Poor
LiFePO ₄ (LFP)	High	High 270°C	Long (3000÷7000)	Starter Batteries, high current applications	Excellent
Li ₄ Ti ₅ O ₁₂ (LTO)	Very Low	Excellent	Long	Electric powertrains, solar streetlights	Excellent

From the types of LIBs included in Table 1, LCOs, NMCs and LFPs are the most used, and, therefore, they will present the largest percentage of recycled spent LIBs. Related to these 3 types, Table 2 presents the mass percentage of the different components of LIBs, and Table 3 details the elementary mass composition of cathode materials [14].

Table 2. Composition of different types of LIBs [14]

Battery type	LIBs composition [%]						
	Al cathode current collector	Cathode active Material	Cu anode current collector	Anode active material	Electrolyte	Housing	Sepa-rator
LCO	4	41	7	18	10	17	3
NMC	7	26	17	15	10	22	3
LFP	6	25	10	13	16	27	3

Table 3. Composition of active cathode material [14]

Battery type	Cathode composition [%]						
	O	Co	Li	Mn	Ni	Fe	P
LCO	33	60	7	-	-	-	-
NMC	21	39	5	17	18	-	-
LFP	41	-	4	-	-	35	20

Given the high ratio of valuable metals in LCO and NMC cathodes and the popularity of these models in many consumer applications, their recovery will become increasingly important. The recovered materials could be used to produce new batteries, reducing the manufacturing costs. At present, these materials represent more than half from the batteries cost [15].

The price of Co reached the highest level in 2018, due to its increased demand for EVs production. The growth appeared because the cars' manufacturers tried to secure the long-term supplies of Co to be used in LIBs [16, 17]. The concentrations of valuable metals in LIBs (Li, Co, Ni, Mn) can exceed their concentrations in the natural ores. If these metals can be widely recovered from spent LIBs in a more economical way than the extraction from natural ores, the price of PE, and EVs should decrease [15]. In Table 4, the estimated values of the recycled metals from LIBs are presented.

Table 4. Estimated values of the recycled metals from LIBs [18]

Battery type	Price/ton of spent LIBs [USD]							
	Co	Li	Mn	Ni	Fe	Cu	Al	Total
LCO	20100	473	-	-	-	472	72	21117
NMC	13065	338	153	2698	-	1146	126	17526
LFP	-	270	-	-	43	674	108	1095

As it can be seen from Table 4, the recycling of LCO LIBs is the most advantageous due to the high Co value, followed by NMC batteries. At opposite, the LFP batteries recycling is economically unattractive due to the lack of valuable metals.

Assuming a LIBs collection rate of 65% and a Li recycling efficiency of 57%, the value of the recovered materials (Co, Ni, Al and Li) could reach \$ 408 million in 2030, contributing to the preservation of these materials into EU economy and the creation of 2,618 jobs [19]. In terms of the LIBs recycling contribution to the supply chain security, it could reduce the globally demand for both Li and Co from ores [20-22]. Countries with the highest battery recycling rates include Belgium, Finland, France, the UK, the USA, Canada, and China. Most of these countries are based on European battery recycling initiatives [8]. Among the listed countries, the relevant common features of the recycling systems include: (i) collection and recycling systems with clear objectives; (ii) development of visually attractive containers for collecting of spent batteries; (iii) involvement of producers and traders in the collection process; (iv) efficient transport regulations for LIBs; (v) partial taxation of the producers and traders for the recycling process; (vi) application of hydrometallurgical treatments for metal refining; (vii) green tax. Incorporating these features is essential to the success of LIBs recycling systems.

LIBs RECYCLING PROCESSES

The waste management of LIBs includes a series of steps, starting with collection, sorting, and transport of the waste, followed by recycling using pre-treating, and pyrometallurgical (PMP) and/or hydrometallurgical (HMP) processes [23].

Pre-treating processes

The pre-treating processes (PP) involved in the LIBs waste recycling are based on the physical properties of the materials (density, magnetic susceptibility, electrical conductivity, etc.) and they include “Discharging-Shredding-Crushing-Sieving-Separation” [24]. The products resulting from PP are metallic and non-metallic fractions. The metallic fraction represents a mixture of various metal: Mn, Li, Co, Ni, Al, Cu, etc. [25, 26].

In addition to the previous invoked phases, PP may also include drying steps [27-29]. Most of the spent LIBs PP includes a first discharging step [30-33] by immersion in a solution of NaCl 5% and then drying [34]. The cells are discharged or short-circuited to reduce the electric-shock hazard, to recover the remaining energy, and allow safe disassembly and grinding [35-37].

After the complete discharge, LIBs are disassembled manually or mechanically. Depending on the type of the recycled LIBs, the obtained parts after disassembling can be divided into metal or plastic housings, cables, battery management units, anode, cathode, and organic compounds [38]. The housing and organic membranes can be treated in a centralized mode due to their high purity and value in the market [39]. The active anode and cathode materials represent a mixture of oxides (LiCoO_2 , $\text{LiNi}_x\text{Co}_y\text{Mn}_z\text{O}_2$, LiMn_2O_4 , LiNiO_2 and LiFePO_4), a small amount of conductive agent, and a polyvinylidene fluoride binder (PVDF). Due to the complex structure and composition of those materials, the recovery of the cathode material has become the most studied in this field [14, 39-45].

The separation of cathodic and anodic materials from the Al or Cu foils represents the first step to recover the electrode materials. The bonding strength between graphite and Cu foil is relatively weak, making it easy to break. After the battery disassembling, some graphite can be separated from the Cu foil and recycled. The industrial recovery of waste graphite is necessary, but the existing methods for graphite recycling are not feasible for large-scale industrial processes due to excessively high costs [29]. The cathode material is more difficult to separate due to the strong adhesion onto the Al foil substrate and need to follow a separation process [46, 47].

The mechanical separation includes the shredding, drying, and sieving of the electrode materials to obtain a powder fraction (black mass), followed by hydraulic (flotation), magnetic or pneumatic separation.

The drying step aims to remove the electrolyte. At temperatures above $100\text{ }^\circ\text{C}$ and low pressure, the organic electrolytes are vaporized. The organic solvents from the electrolyte present in LIBs are a mixture of carbonates such dimethyl-, ethyl-, methyl-, diethyl-, propylene-, and ethylene-carbonate. The vapours can be recovered by condensation or burned for energy recovery [48]. Elimination of the electrolyte leads to an improved separation process and minimizes the possibility of obtaining impure products. Sieving process allows to separate the rests of plastic, paper, Cu, Al from the black mass, leading to a fraction that contains only valuable materials like Li, Ni, Co and Mn, that can be recovered in a further process.

Pyrometallurgical process

The pyrometallurgical process (PMP), representing a branch of extractive metallurgy or metals recycling from spent LIBs, includes stages of incineration, melting in electric arc or plasma discharge furnaces, sintering, and gas phase reactions at high temperatures [49-51]. For LIBs recycling using PMP, the

waste is heated up to 1000°C or more [52], to recover the Li salt and other materials from the electrodes [53, 54].

For LIBs recycling, the physical-chemical properties of the batteries are crucial for the choice of PMP conditions because, unlike the ore, LIBs contain various materials such as plastic, metals, oxide, carbon, salts, and organic solvents. Some of them are volatile, flammable, sensitive to water, toxic and unstable at high temperatures [55].

PMP for recycling of spent LIBs involves pyrolysis. The electrolyte solvents are first removed [56, 57] at temperatures above boiling point, of approx. +250 ° C. In spent LIBs is also present the carbon (graphite) which, in mixture with the active materials of the electrodes, can act in PMP as a reducing agent or is burned in the calcination stage. The binders used in LIBs for the preparation of electronic materials (for example, PVDF) can generate CO₂, PF₅, HF etc. [51, 58, 59] therefore for these toxic gases must be ensured their capture and treatment to avoid air contamination [59]. On the other hand, binders may be dissolved in an organic solvent [60].

Sometimes, the removal of organic materials and graphite from spent LIBs is done by roasting [61], optionally with the addition of inorganic salts [40, 62]. After that, most residual materials are Li metal oxides and some metal scraps from current collectors [63]. Separation of Li metal oxides is possible at high temperatures, having the disadvantage of high-energy consumption. Separation of Li₂O and metal oxides encounters difficulties in the extraction process [63]. Mn oxides can be reduced to MnO with C, CO and H₂, but it is difficult. Al can reduce LiCoO₂ to generate Co and LiAlO₂, but Li is difficult to separate from LiAlO₂ [51].

Another PMP for treating spent LIBs is the reductive melting (RT) [64] in furnace using reducing agents as carbon, CO, and natural gas. After RT, the heavier liquid metals accumulate in the lower part of the furnace and the Li oxide remains in the upper layer of the slag. Impurities present in the two molten phases can be removed by typical refining treatments such as metal-slag, metal-metal, and metal-gas phases [40, 65]. Due to their high economic values, the most recovered metals by PMP are Co, Li and Ni. For example, Li et al. [66] managed through PMP to recover 95.72% of Co and 98.93% of Co, and Guoxing et al. [67] recovered, by pyrolysis, a Co-Ni-Cu alloy with recovery degrees of 81.6%, 93.3% and 90.7% for Co, Ni and Cu, respectively, but also Li in slag in proportion of 82.4%.

Worldwide, the companies are applying mainly PMPs for recycling waste LIBs [51, 68]. The process developed by Accurec GmbH use high temperature furnaces to melt pre-briquetted cathodic materials, resulting a Co-Mn alloy and a Li containing slag [55]. The Sony/Sumitomo process includes the burning of flammable components and the magnetic separation

of metals, which are then processed hydrometallurgically [55]. In the Umicore process, the flammable components are burned firstly, and the metals are melted to generate Ni, Co, Cu, and Fe alloys, which are subsequently separated hydrometallurgically [51].

Due to the high costs of recycling by PMP, the companies that use this technique do not recover all materials from LIBs [63-65]. The main disadvantages of PMP are high-energy consumption and the generation of highly toxic and volatile products. Due to high environmental hazard, the resulting gases must be carefully treated [62].

Hydrometallurgical process

The hydrometallurgical process (HMP) is based on the: (i) leaching of the grinded spent LIBs in acidic or alkaline aqueous solutions, (ii) possibly purification of leaching solutions, (iii) separation of valuable components by solvent extraction, chemical precipitation, electrodeposition, etc., and (iv) treatment/regeneration of the solutions to be recirculated in process [69, 70].

Leaching process of the metals from spent LIBs

Leaching aims the transfer of metals, oxides and salts that are part of the anode and cathode materials of LIBs into a liquid phase. The leaching step of spent LIBs is done after the removing of some battery components. This approach helps to minimize the volume of aqueous leaching solutions and the number of the subsequent purification and separation steps.

The rate and degree of the metals recycling from LIBs depend on the leaching efficiency and rate [70], which are influenced by the used leaching reagent, concentration of chemicals, solid/liquid ratio (S/L), temperature, duration, ultrasound support, mechanical agitation, and other factors [24]. In this context, in Table 5, we present summarized literature data concerning the specific leaching parameters for different types of LIBs. As it can be seen, the researchers use widely mineral acids (H_2SO_4 , HCl , HNO_3 and H_3PO_4 [71-74]), but also organic acids, as citric acid ($\text{C}_6\text{H}_8\text{O}_7$), oxalic acid ($\text{C}_2\text{H}_2\text{O}_4$), lactic acid ($\text{C}_3\text{H}_6\text{O}_3$), malic acid ($\text{C}_4\text{H}_6\text{O}_5$), tartaric acid ($\text{C}_4\text{H}_6\text{O}_6$) and aspartic acid ($\text{C}_4\text{H}_7\text{NO}_4$) [75-79]. To accelerate the leaching process of metal compounds, various reducing agents have been used, as H_2O_2 [80], Na_2SO_3 [81], NaHSO_3 [82], and carbohydrates, including D-glucose [83] and ascorbic acid ($\text{C}_6\text{H}_8\text{O}_6$) [84]. The reducing agents are added to convert Co^{3+} to Co^{2+} and Mn^{4+} to Mn^{2+} , which are easier to be dissolved in the solutions [85].

The acidic leaching has been shown to be highly efficient [69, 77, 78] even more efficient than the alkaline one [86].

Table 5. Leaching specific parameters for different types of spent LIBs

Battery type	Leaching agents	S/L ratio [g/L]	Temp. [°C]	Time [min]	Leached metals / Leaching rate [%]	Ref.
Mixed	0.5 N C ₆ H ₈ O ₆	10	65	90	Co: 52.19; Li: 59.23; Mn: 57.98	[76]
	1.5 M H ₂ SO ₄ 30% H ₂ O ₂ 5 g C ₅ H ₈ O ₄	10	90	120	Co: 87.85; Li: 99.91; Ni: 91.46	[77]
	2.0 M H ₂ SO ₄ 4.0% H ₂ O ₂	10	70	180	Al: 97.8; Cu: 64.7; Co: 99.6; Li: 98.8; Ni: 99.6; Mn: 97.4	[80]
	0.5 M H ₂ SO ₄ 0.1 M Na ₂ SO ₃	20	120	360	Ni: 93.11; Co: 92.84; Mn: 90.18	[81]
	1 M H ₂ SO ₄ 0.075 M NaHSO ₃	50	95	240	Li: 91.6; Co: 96.4; Ni: 87.9; Mn: 83.69	[82]
	1M H ₂ SO ₄	20	95	240	Li: 96.7; Co: 91.6; Ni: 96.4; Mn: 87.9	[87]
	1M H ₂ SO ₄	50	95	240	Li: 93.4; Co: 66.2; Ni: 96.3; Mn: 5.02	[88]
	15% H ₂ O ₂ 0.5 M C ₆ H ₈ O ₇	20	90	60	Li: 99.1; Co: 99.8; Ni: 98.7; Mn: 95.2	[89]
	28% NH ₃	10	80	120	Co: 100; Cu: 100; Ni: 100	[90]
	1 M H ₂ SO ₄ 0.5 M HNO ₃	25	75	60	Li: 93.2; Co: 90.5; Ni: 82.8; Mn: 77.7	[91]
	2M H ₂ SO ₄	240	20-23	500	Co: >96; Ni: >96; Mn: >96; Li: >96	[92]
	2 M H ₂ SO ₄ 6 % H ₂ O ₂	10	75	90	Co: 100	[93]
NMC	0.5 M C ₆ H ₈ O ₆ 1M HNO ₃	20	85	10	Li: ~100; Mn: ~100; Co: ~100; Ni: ~100	[41]
	4 M NH ₃ 1 M (NH ₄) ₂ CO ₃ 0.3 M Na ₂ SO ₃	50	80	300	Li: 79.1; Co: 86.4; Ni: 85.3	[95]
LCO	2M HCl	50	60–80	90	Li: ~100; Co: ~100	[72]
	1.5 M H ₃ PO ₄ 0.02 M C ₆ H ₁₂ O ₆	50	80	120	Li: 100; Co: 98	[74]
	1 M C ₆ H ₈ O ₇	20	80	60	Co: 90	[75]

Battery type	Leaching agents	S/L ratio [g/L]	Temp. [°C]	Time [min]	Leached metals / Leaching rate [%]	Ref.
	2 M H ₂ SO ₄ 4 M HCl 10% H ₂ O ₂ 10% C ₅ H ₈ O ₄	20	80	300	Co: 100; Li: 95.1; Ni: 100	[78]
	1.5 M C ₄ H ₄ O ₄ 0.5% H ₂ O ₂	20	70	20	Ni: 98.27; Co : 98.06; Mn : 98.54; Li: 95.74	[79]
	1M C ₆ H ₈ O ₇ 0.2 M C ₆ H ₈ O ₆	20	80	360	Co: 80; Li: 100	[84]
	1 M C ₄ H ₄ O ₄ 0.3 M SnCl ₂	20	60	40	Li: 98.67; Co: 97.5	[96]
	1.5 M H ₃ Cit 6% H ₂ O ₂	15	90	90	Co: 99.5; Li: 97	[97]
	2 M H ₃ Cit, H ₂ O ₂	50	70	80	Co: 98; Li: 99	[98]
	0.9% H ₂ O ₂	20	90	35	Li: 90; Co: 80	[99]
	1.5 M C ₆ H ₈ O ₇ 2% H ₂ O ₂	20	20	95	Al: 93; Co: 90; Li: 96; Mn: 94; Ni: 94	[100]
	99.8% Na ₂ CO ₃	60	80	60	Li: 92.82	[101]
	2M H ₂ SO ₄ 10% H ₂ O ₂	33	70	120	Co: 98.5; Li: 99.8; Ni: 98.6	[102]
LFP	0.3 M H ₂ SO ₄ 2 M H ₂ O ₂	100	60	120	Li: 96.85	[103]
LCA	4 M HCl	5	90	1080	Li: 100; Ni: 100; Co: 100; Al: 100	[104]

Data from Table 5 indicates that the mineral acids (2M H₂SO₄ and 4M HCl) are the most efficient for solubilizing metals from LIBs, and the presence of hydrogen peroxide increases their efficiency [77-78, 95, 97, 104]. However, toxic gases such as Cl₂, SO₃ and NO_x are released in the process of extracting metal ions with mineral acids, determining serious threats to environment [79]. Generally, the leaching temperature is between +60°C and +95°C, and the leaching rate of the targeted metals is close to 100%.

Compared to inorganic acids, the organic ones are considered green leaching agents, which could effectively recover the precious metals, while avoiding secondary contamination [75-76, 98, 105]. Compared to acid leaching, the dissolution of the cathodic materials in alkaline solutions have been rarely reported. However, the alkaline leaching with an ammonia-based system is relatively selective for specific elements, such as Ni, Co, and Li, due to the formation of stable complexes [29, 105].

From an economic point of view, HCl proved to be the most effective due to its relatively strong reductive capacity, assuring the complete dissolution of the cathodic material without the addition of additives [105].

Recovery of metals from the leaching solutions of spent LIBs

After the metals leaching from the spent LIBs, they can be separated from the solution in form of pure metals or chemical compounds by solvent extraction (SE), chemical precipitation (CPP), electrodialysis (EDy), and electrodeposition (EDP). In this context, Table 6 summarizes the efficient HMP for the recovering of the metals/compounds from the leaching solutions of grinded spent LIBs.

SE is based on the different solubility of metal compounds in two immiscible solvents, usually water and an organic solvent doped with a selective extractant. At the equilibrium of the extraction system, each liquid phase contains different concentrations of metal ions, assuring they separation. By mixing the charged organic phase with a stripping solution, such as H_2SO_4 , the extractant can be regenerated and reused [105,106]. The SE efficiency is influenced by the extraction yield and the phase separation capacity. This method has been widely used in various HMP and has proven to be an effective method for separating valuable metal ions or removing impurities from the aqueous leaching solution. The commercially available selective extractants such as Cyanex 272, D2EHPA or PC88A have been widely used to separate the metal ions from the leaching solutions of spent LIBs [93]. Extraction with PC88A and Cyanex 272 is very efficient in separating Co against other metals from the leaching solution [106, 107], and D2EHPA has been studied for the separation of Mn [106, 108].

The most used technique for the metals recovering from LIBs leaching solutions is CPP, based on the different solubility of metal compounds relative to pH. Lithium hydroxide and oxalate are much more soluble than similar compounds of other metals. Thus, Fe^{3+} , Al^{3+} and Cu^{2+} ions precipitate at a relatively lower pH [109, 110]. For the Li precipitation, the two commonly used chemical agents are Na_2CO_3 [27, 111-113] and Na_3PO_4 [98, 114, 115], resulting high purity Li salts. As examples, Natarajan et al. [116] obtained 99.7% purity Li_2CO_3 and Chen et al. [117] precipitated Li_3PO_4 with a purity of 93%. For the precipitation of transition metals, $\text{H}_2\text{C}_2\text{O}_4$ is widely used [99, 117], and Mn can be also precipitated as hydroxides [94].

EDP has the advantage of obtaining high purity products due to the small amount of impurities included in deposits, but has a relatively high electricity consumption. For example, Quintero-Almanza et al. [93] obtained Co with a purity of 99%. In electrodeposition, pH is a very important factor that can strongly influence the energy efficiency. The pH variations can be

minimized by addition of H_3BO_3 in solutions, determining higher current efficiencies [93, 118, 119]. Co oxide obtained by electrodeposition can be used as material for supercapacitors [105].

Table 6. HMP for the separation and recovery of products from the cathodic materials of spent LIBs

Battery type	Recovery method	Additives	Recovery products/ Recovery rate [%]	Ref.
NMC	CPP	Na_2CO_3 , EDTA	Li_2CO_3 : 99; Co_3O_4 : 98	[27]
		NaOH	Li_3PO_4 : 88; CoC_2O_4 : 98.7	[74]
		$\text{H}_2\text{C}_2\text{O}_4$	CoC_2O_4 : 80; Li_3PO_4 : 90	[99]
		$\text{H}_2\text{C}_2\text{O}_4$; H_3PO_4	$\text{CoC}_2\text{O}_4 \cdot 2\text{H}_2\text{O}$: 99; Li_3PO_4 : 93	[117]
		$\text{C}_2\text{H}_2\text{O}_4$	CoC_2O_4 : 98	[123]
		$\text{C}_4\text{H}_6\text{O}_6$	$\text{C}_4\text{H}_4\text{O}_6\text{Co}$: 98	[124]
		Na_2CO_3	Li_2CO_3 : 99.93	[125]
		Na_3PO_4	$\text{Al}(\text{OH})_3$: 90~95	[126]
Mixture	CPP	Na_2CO_3	Li_2CO_3 : 99.4	[112]
		Na_2CO_3 $(\text{NH}_4)_2\text{S}$	Li_2CO_3 : 99.7; Co_xS_y : 99; MnCO_3 : 98.7	[116]
		$\text{H}_2\text{SO}_4 + \text{H}_2\text{O}_2$	Co: 100; Ni: 100; Mn: 100	[127]
LCO	EDy / CPP	Na_2CO_3	Li_2CO_3 : 88.3	[113]
Mixture	SE / CPP	D2EHPA, Cyanex 272, DMG, Na_2CO_3	$\text{Co}(\text{OH})_2$: ~99.5; $\text{Ni}(\text{OH})_2$: ~99.5; $\text{Mn}(\text{OH})_2$: 90; Li_2CO_3 : ~99.5	[108]
NMC	SE / CPP	D2EHPA, Cyanex 272, NaOH	$\text{Co}(\text{OH})_2$: 95	[128]
LCO	SE / CPP	$\text{Na}_2\text{S}_2\text{O}_5$ Na_2CO_3	Co: 60-70; Ni: 60-70; Mn: 60-70; Li_2CO_3 : 60; Al: 81; Cu: 91; Fe: 98	[129]
		Acorga M5640, Cyanex 272, Na_2CO_3 , $(\text{NH}_4)_2\text{C}_2\text{O}_4$	Li_2CO_3 : 80; CuSO_4 : 98; $\text{CoC}_2\text{O}_4 \cdot 2\text{H}_2\text{O}$: 90	[130]
Mixture	SE	D2EHPA TBP	Fe: 98.5; Co: 99.8; Mn: 99.8; Al: 99.7; Cu: 97.8; Ni: 98.6	[116]
		D2EHPA	Mn: 84; Co: 8.6; Ni: 6.2	[119]
LCO	SE	D2EHPA	Mn : 100; Co: 94; Ni: 90	[45]
NMC	SE	D2EHPA, MnSO_4	Mn: 84	[104]
NMC	SE	D2EHPA PC88A	Li_2CO_3 : 84.7; NiSO_4 : 99; CoSO_4 : 99; MnSO_4 : 99	[107]
LFP	CPP	Na_3PO_4	Li_3PO_4 : 95.56	[100]
		NaOH, Na_3PO_4	LiOH : 99.9; FePO_4 : 99.97	[114]
		Na_2CO_3	Li_2CO_3 : 99	[130]
Mixture	SE / EDP	Cyanex 272	Co: 97-99	[93]
Mixture	EDy	EDTA	Ni: 99.3; Co: 87.3; Li: 99	[110]

Recently, the regeneration technique for the recycling of the cathodic materials has become a new direction that refers to the resynthesis of the materials directly from the leaching solutions. This method, although sophisticated, has proven to be energy efficient as it is integrated into the synthesis of the cathodic materials [105]. The sol-gel and co-precipitation methods are two main ways of regenerating the cathodic materials. Before regeneration, the content of each metal ion must be accurately analysed and then adjusted to the desired value by the addition of certain chemical compounds [120, 121, 122].

The leaching solution of organic acids is usually removed by the sol-gel method because the existing organic products can serve as chelates. After the addition of acetic salts or nitrates to regulate the ratio of metal ions, sols are obtained by the increasing of the solution pH and the gel by drying. The cathodic materials are synthesized by calcination of the gel [131].

In cases of co-precipitation, sulphates are used to adjust the ratio of metal ions when the spent cathodic material is leached into H_2SO_4 [132].

By adding NaOH or NH_3 to increase the pH of the leaching solutions, the transition metal hydroxides (precursors) could be co-precipitated. Then, by calcination of the stoichiometric mixture of Li_2CO_3 and precursors, resynthesized cathodic materials are obtained [133].

INDUSTRIAL RECYCLING TECHNOLOGIES FOR SPENT LIBs

The industrial recycling technologies (IRTs) of the spent LIBs focus mainly on the recovering of valuable or critical metals such as Co, Cu, Li, Mn, and Ni [8]. Most often, the IRTs are based on the above-mentioned processes (PMP and HMP), combined with mechanical (MP) and thermal (TP) processing. For the recovery of valuable materials, these technologies are used successively [41], as follows: (i) Direct PMP, with optional HMP pre-sorting and refining; (ii) Thermal pre-treatment by pyrolysis, with MP processing in several stages and PMP or HMP refining; (iii) Treatment at low temperatures, by electrical and/or cryogenic depollution, with multi-stage processing and HMP refining.

From the quantitative point of view, only 5% of spent LIBs have been reported as recycled by 2019. However, several institutions, as Circular Energy Storage [134], claim that this value is inaccurate and that the overall recycling rate is around 50%. The recycling potential in Asia and Europe is far ahead of the other continents. According to recent data [135], China and Europe's recycling capacity accounts for about 80% of the spent LIBs world's recycling. The manufacture of LIBs is largely concentrated in China, South

Korea, and Japan. Consequently, their recycling is also highly developed in Asia due to the large amounts of spent LIBs generated in this region [136, 137]. American and European recycling industries show a wide variety of technologies, although the available volume of spent LIBs is too small for a profitable operation [85, 138].

In this context, representative examples of LIBs recycling companies around the world and the used processes are presented in Table 7.

Table 7. Worldwide representative examples of spent LIBs recycling companies

Country	Company	Processes	Capacity [t/year]	Ref.
ASIA				
Japan	DOWA Eco-Systems Co. Ltd.	TP + PMP + HMP	>1000	[139, 135]
	KYOEI Steel	PMP	>1000	[139]
	Nippon Recycle Center Corp	PMP	<1000	[140]
	Sony Corp. & Sumitomo Metals and Mining Co	PMP	150	[135]
	4R Energy Corp	PMP + HMP	n.d.	[68]
	Mitsubishi	PMP	n.d.	[135]
Indonesia	DOWA Eco-Systems Co. Ltd	TP + PMP + HMP	n.d.	[139]
China	DOWA Eco-Systems Co. Ltd.	TP + PMP + HMP	n.d.	[139]
	Anhua Taisen Recycling Technology Co. Ltd.	MP + HMP	> 5000	[140]
	Fuoshan Bangpu Ni/Co High-Tech Co	n.d.	n.d.	[44]
	GHTECH	n.d.	n.d.	[68]
	Highpower International Inc	MP + PMP + HMP	> 1000	[139]
	Huayou Co New Material Co Ltd	MP + HMP	> 1000	[139]
	JX Nippon Mining and Metals Co.	TP + MP + HMP	<1000	[139]
	Shenzhen BAK Battery Co	Disassembly	n.d.	[68]
	Shenzhen Green Eco Manufacturer Hi-Tech. Co., Ltd.	MP + HMP	<5000	[42]
	Shenzhen Tele Battery Recycling Co	HMP	3000	[68, 139]
	Soundon New Energy Tech. Co. Ltd.	n.d.	n.d.	[68]
	TES-AMM	MP (inert gas)	<1000	[139]

Country	Company	Processes	Capacity [t/year]	Ref.
Singapore	DOWA Eco-Systems Co. Ltd	TP + PMP + HMP	n.d.	[45]
	JX Nippon Mining & Metals Co	TP + MP + HMP	<1000	[139]
Hong Kong	GHTECH	n.d.	n.d.	[68]
	Highpower International Inc	MP + PMP + HMP	> 1000	[139]
Thailand	DOWA Eco-Systems Co. Ltd	TP + PMP + HMP	n.d.	[139]
South Korea	SungEel Hitech Ltd	MP + (T +) HMP	>1000	[139]
	JX Nippon Mining and Metals Co.	TP + MP + HMP	<1000	[139]
	SK Innovation Co	n.d.	n.d.	[68]
EUROPE				
Spain	Pilagest	MP + HMP	<1000	[68]
Belgium	REVATECH	n.d.	n.d.	[68]
	Umicore	PMP + HMP	>1000	[139]
France	AFE Group (Valdi)/ ERAMET	PMP	n.d.	[68]
	Euro Dieuze Industrie/ SARP	HMP	200	[135]
	Recupyl S.A.S	HMP	110	[135]
	S.N.A.M. AFE Group (Valdi)/ ERAMET	MP + (TP) + HMP	n.d.	[68]
Germany	Accurec Recycling GmbH	TP + MP + PMP + HMP	>1000	[139]
	AERC Recycling Solutions	PMP	n.d.	[68]
	Brunp Recycling Technology Co	TP + MP + HMP	3000	[139]
	Chemetall	n.d.	n.d.	[68]
	DK Recycling und Roheisen GmbH	PMP	n.d.	[45]
	Düsenfeld GmbH	MP + PMP	n.d.	[68]
	NIHÜTTE AUE GMBH	TP + PMP + HMP	>1000	[139]
	GRS Batterien	PMP		[68]
	PROMESA GmbH & Co. KG	MP (aqueous shred) + unknown	<1000	[139]
	JX Nippon Mining and Metals Co	TP + MP + HMP	<1000	[139]
	Primobius	PMP + HMP	n.d.	[141]
	REDUX GmbH	TP + MP + unknown	<1000	[139]
UK	AEA Technology Batteries	HMP	n.d.	[135]
	Cawleys	n.d.	n.d.	[68]
	Ecobat Technologies Ltd	PMP + HMP	n.d.	[68]
	Metal-Tech Ltd.	n.d.	n.d.	[68]

Country	Company	Processes	Capacity [t/year]	Ref.
Sweden	SAFT. AB	PMP	n.d.	[68]
	Erasteel Kloster AB Vikmanshyttan	n.d.	n.d.	[68]
Finland	AkkuSer	MP	4000	[135]
Switzerland	Batrec Industrie AG	MP +HMP + TP + PMP	200	[135, 68]
Norway	Xstrata/ Glencore	PMP + HMP	7000	[135]
NORTH AMERICA				
Canada	Earthtech	Disassembly	n.d.	[135]
	Lithion Recycling	HMP	n.d.	[68]
	Li-Cycle	MP + HMP	5000	[65]
USA	American Mn	HMP	n.d.	[68]
	Battery Resources LLC	n.d.	n.d.	[68]
	Battery Safety Solutions	Collection + Discharge + Disassembly	n.d.	[68]
	Euro Dieuze Industrie/ SARP	Disassembly+ PMP + HMP	>5000	[68, 139]
	Inmetco	PMP	6000	[135]
	OnTo Technology Oregon US	Direct recycling	n.d.	[135]
	Salesco Systems	PMP	n.d.	[68]
	Toxco/ Retriev Tech.	MP (aqueous shred) + HMP	n.d.	[139]
	DOWA Eco-Systems Co. Ltd	TP + PMP + HMP	n.d.	[139]
	JX Nippon Mining and Metals Co.	TP + MP + HMP	<1 000	[139]
AUSTRALIA				
West Perth	Neometals Ltd	MP +HMP	Lab Scale	[135]

(n.d. = no data)

As it can be seen from Table 7, most companies around the world mainly use PMPs to recycling the spent LIBs. Overall, recycling efficiency decreases if it is operated at high temperatures due to the decomposition of organic components [141]. On the other hand, HMP can recover a greater number of materials.

Another important aspect of companies is the maximum focus on the supply chain with spent LIBs and on the key stakeholders that are important for the supply of spent LIBs. The feed profile of spent LIBs must be central into the process development. The inherently heterogeneous nature of spent LIBs must be closely considered as part of any recycling process [142, 143].

Generally, the recycling companies recover Co, Cu, Li and Mn due to their high value, but, also, Fe, Ni and Al are often recovered. Even if Fe is the lowest value component from the battery, its extraction process is simplistic, as it can be magnetically separated if MPs are used in the first stage of the recycling process.

The MP steps allow the recovery of the solid parts, such as materials from the housing, modules and cells, electrical conductors, and steel screws. Zigzag sieving allows the separation of materials according to their density. A vibrating sieve can be also used to separate the electrode black mass from the separator and the current collector foils. Finally, the composition of the obtained fractions is determined after the manual or automatic screening and sorting. The fragments from the modules can be dried at temperatures between 100-140 °C [144] to remove the electrolyte, and the evaporated solvents can be recovered by condensation.

To support the efficient recycling of LIBs, state-of-the-art technologies are recommended to improve the flexibility and recovery rate of all materials from the spent devices. These technologies must consider a combination of safe and ecological MP and HMP with low costs, able to recycle all types and models of spent LIBs. As example, a combined process for the spent LIBs recycling was successfully implemented by the Li-Cycle® Canadian company [142], based on a safe MP size reduction and dedicated HMP, allowing a recovery rate of the recycled materials up to 100%.

Concerning the economic aspects of the IRTs, American Manganese Company Inc. [145] presents a business plan developed to recover valuable metals from spent LIBs cathodes, using combined MP and HMP. The study shows that, at a 3 tons/day processing capacity of NMC type spent LIBs, with a recovery rate of 95%, and working 350 days/year, annual revenues of \$14.3 million can be obtained at production costs of \$7.9 million. We can conclude that the processing of Li batteries can generate generous profits, of \$6.4 million in this case. Implementation of the combined technology processes could also: (i) to remove Li-ion batteries waste from landfills; (ii) to diminish the manufacturing costs by the materials recycling from spent LIBs and reusing them in the manufacturing process of batteries; (iii) to significantly reduce the CO₂ emissions.

In the future, the recycling of spent LIBs is expected to be one of the main sources of Li supply. Unlike oil, where the price fluctuations only lead to the increased car operating costs, the potential Li price fluctuations will

have an impact on the total purchase price of the car. Therefore, the recycling will be one of the means of mitigating the amplitude of the possible fluctuations due to the geo-political or other barriers.

CONCLUSIONS AND PERSPECTIVES

Worldwide, the lithium-ion battery will be for at least medium term, the most important and widely used electrochemical source of energy. However, the exponential increase in the production of LIBs also generates a huge amount of scrap. Their recycling is necessary for at least two reasons: (i) to avoid pollution and (ii) to reintroduce valuable and deficient materials (on the world market) from these batteries into the economic circuit [10].

The research on the spent LIBs recycling has been mainly focused on the recovery of metals from the cathodic material, especially Co, which is deficient on the world market. As the volume of spent LIBs increase, the interest in the complete valorisation of all materials also increase. Thus, more recent research is focused on the recovery of other metals such as Mn, Ni and, of course, Li.

A promising direction is the recent research aimed to reintroduce (direct recycling routes) in batteries the recovered cathodic material after a minimal processing [4, 146,147].

There are also concerns to develop processes for all-components recycling from the spent LIBs, based mainly on the: (i) discharging of spent LIBs, (ii) dismantling and classification of components, (iii) separation of electrode materials, and (iv) refining and value-adding technologies for the cathodic materials and graphite [148]. Future recycling strategies will need to be redefined so they can adapt to the large diversity of the spent LIBs and capitalize as many of their recoverable components.

The achieving of a reasonable economic profitability for the spent LIBs recycling is also conditioned by the responsibility of manufacturers to develop and implement innovative processes in the factory design to make the batteries more capable to fit into the circular economy [149].

For the future, to facilitate and make more efficient the recycling of the spent LIBs, it is essential their selectively collection (SC), followed by the robotization of the physical processes (RPP) of dismantling and sorting to minimize the need for labor. The SC and RPP processes can be significantly facilitated by intelligent and standardized labeling, which will allow the facile identification of spent LIBs from type, composition, lifetime, etc. Further, the spent LIBs pretreatments at low temperature and pressure, in inert atmosphere, will diminish the pollution with toxic products, as HF, PF₅, etc.

ACKNOWLEDGMENTS

The present work has received financial support through the project: Entrepreneurship for innovation through doctoral and postdoctoral research, POCU/360/6/13/123886 co-financed by the European Social Fund, through the Operational Program for Human Capital 2014- 2020.

REFERENCES

1. Y. Yang; E. G. Okonkwo; G. Huang; S. Xu; W. Sun; Y. He; *Energy Storage Mater.*, **2021**, 36, 186-212.
2. A. Islam; S. Roy; M. A. Khan et al.; *J. Mol. Liq.*, **2021**, 338, 116703.
3. Y. Zhao; O. Pohl; A. I. Bhatt; G. E. Collis; P. J. Mahon; T. R  ther; A. F. Hollenkamp; *Sustain. Chem.*, **2021**, 2, 167-205.
4. H. Pinegar; Y. R. Smith; *J. Sustain. Metall.*, **2019**, 5, 402-416.
5. C. Zu; Y. Ren, F. Guo, H. Yu, H. Li; *Adv. Energy Sustainability Res.*, **2021**, 2(10), 2100062.
6. C. M. Costa; J. C. Barbosa; R. Gon  alves; H. Castro; F. J. Del Campo; S. Lanceros-M  ndez; *Energy Storage Mater.*, **2021**, 37, 433-465.
7. Y. Zhao; L. -Z. Fang; Y. -Q. Kang; L. Wang; Y. -N. Zhou; X. -Y. Liu, T. Li, Y. -X. Li, Z. Liang, Z. -X. Zhang; B. -H. Li; *Rare Met.*, **2021**, 40(6), 1431-1436.
8. Y. Wu; *Lithium-Ion Batteries: Fundamentals and Applications*, Taylor & Francis Group, 1st ed., Boca Raton, FL, **2015**, pp. 3-24.
9. Z. A. Kader; A. Marshall; J. Kennedy; *Emerg. Mater.*, **2021**, 4, 725-735.
10. S. Windisch-Kern; E. Gerold; T. Nigl; A. Jandric; M. Altendorfer; B. Rutrecht; S. Scherhauer; H. Raupenstrauch; R. Pomberger; H. Antrekowitsch; F. Part; *Waste Manage.*, **2022**, 138, 125-139.
11. M. Walter; M. V. Kovalenko; K. V. Kravchyk; *New J. Chem.*, **2020**, 44, 1677-1683.
12. H. E. Melin; *State-of-the-art in reuse and recycling of lithium-ion batteries - A research review*, The Swedish Energy Agency, London, UK, **2019**.
13. K. Kishore; A. AlFantazi; A. T. Mayyas; *Energy Fuels*, **2021**, 35, 18257–18284.
14. J. Chung-Yen; P. -C. Sui; J. Zhang; *J. Energy Storage*, **2021**, 35, 102217.
15. C. Stollery; A. Holland; *Li-ion Battery Recycling Market 2022-2042*, IDTech Ex Research, **2021** (Research-report).
16. <https://www.ft.com/content/1e6303f6-2386-11e8-add1-0e8958b189ea> Accessed 18.12.2021.
17. <https://www.reuters.com/article/us-umicore-recycling-idUKKBN1KN1ZO> Accessed 02.02.2022.
18. <https://www.lme.com/> Accessed 18.12.2021.
19. <https://www.ceps.eu/ceps-publications/prospects-end-life-electric-vehicle-batteries-circular-economy/> Accessed 05.02.2022.
20. P. Alves Dias; D. Blagoeva; C. Pavel; N. Arvanitidis; *JRC*, **2018**, 112285, doi:10.2760/97710.

21. M. Kamran; M. Raugei; A. Hutchinson; *Resour. Conserv. Recy.*, **2021**, 167, 105412.
22. S. Bobba; M. F. Gian; A. Blenginiab; *Resour. Conserv. Recy.*, **2019**, 145, 279-291.
23. E. G Pinna; N. Toro; S. Gallegos; M. H. Rodriguez; *Materials*, **2022**, 15, 44.
24. G. Zhang; X. Yuan; Y. He; H. Wang; T. Zhang; W. Xie; *J. Hazard. Mater.*, **2021**, 406, 124332.
25. D. Yu; Z. Huang; B. Makuza; X. Guo; Q. Tian; *Miner. Eng.*, **2021**, 173, 107218.
26. C. Yang; J. Zhang; Q. Jing; Y. Liu; Y. Chen; C. Wang; *Int. J. Miner. Metall.*, **2021**, 28(9), 1478.
27. S. Kim; J. Bang; J. Yoo; Y. Shin; J. Bae; J. Jeong; K. Kim; P. Dong; K. Kwon; *J. Clean. Prod.*, **2021**, 294, 126329.
28. J. Liu; H. Shi; X. Hua; Y. Geng; L. Yang; P. Shao; X. Luo; *Sci. Total Environ.*, **2021**, In Press, <https://doi.org/10.1016/j.scitotenv.2021.151621>.
29. R. Sommerville; J. Shaw-Stewart; V. Goodship; N. Rowson; E. Kendrick; *Sustain. Mater. Technol.*, **2020**, 25, e00197.
30. R. Zheng, W. Wang, Y. Dai, et al.; *Green Energy Environ.*, **2017**, 2, 42-50.
31. J. Liu; X. Bai; J. Hao; H. Wang; T. Zhang; X. Tang; S. Wang; Y. He; *J. Environ. Chem. Eng.*, **2021**, 9, 106017.
32. H. Al-Shammari; S. Farhad; *Resour. Conserv. Recycl.*, **2021**, 174, 105749.
33. S. Pindar; N. Dhawan; *J. Therm. Anal. Calorim.*, **2021**, 146, 1819-1831.
34. J. Yu; Y. He; Z. Ge; H. Li; W. Xie; S. Wang; *Sep. Purif. Technol.*; **2018**, 190, 45-52.
35. C. Tokoro; S. Lim; K. Teruya; M. Kondo; K. Mochidzuki; T. Namihira; Y. Kikuchi; *Waste Manage.*, **2021**, 125, 58-66.
36. Y. Kikuchi; I. Suwa; A. Heiho; Y. Dou; S. Lim; T. Namihira; K. Mochidzuki; T. Koita; C. Tokoro; *Waste Manage.*, **2021**, 132, 86-95.
37. X. Chen; C. Guo; H. Ma; J. Li; T. Zhou; L. Cao; D. Kang; *Waste Manage.*, **2018**, 75, 459-468.
38. Y. Chen; N. Liu; F. Hu; L. Ye; Y. Xia; S. Yanga; *Waste Manage.*, **2018**, 75, 469-476.
39. S. Zhao; W. He; G. Li; *Springer, Cham*, **2019**, pp. 1-26.
40. O. C. Barrios; Y. C. Gonzalez; L. I. Barbosa; P. Orosco; *Miner. Eng.*, **2022**, 176, 107321.
41. H. Chen; S. Gu; Y. Guo; X. Dai; L. Zeng; K. Wang; C. He; G. Dodbiba; Y. Wei; T. Fujita; *Hydrometallurgy*, **2021**, 205, 105746.
42. H. Ali; H. A. Khan; M. G. Pecht; *J. Energy Storage*, **2021**, 40, 102690.
43. J. Zhu; G. Guo; J. Wu; X. Cheng; Y. Cheng; *Ionics*, **2022**, 28, 241-250.
44. S. Windisch-Kern; A. Holzer; C. Ponak; T. Hochsteiner, H. Raupenstrauch; *Carbon Resources Conversion*, **2021**, 4, 184-189.
45. Y. Li; Q. Fu; H. Qin; K. Yang; J. Lv; Q. Zhang; H. Zhang; F. Liu; X. Chen; M. Wang; *Korean J. Chem. Eng.*, **2021**, 38(10), 2113-2121.
46. Y. Zhao; Y. Kang; M. Fan; T. Li; J. Wozny; Y. Zhou; X. Wang; Y. -L. Chueh; Z. Liang; G. Zhou; J. Wang; N. Tavajohi; F. Kang; B. Li; *Energy Storage Mater.*, **2022**, 45, 1092-1099.

47. H. Gomaa; M. A. Shenashen; H. Yamaguchi; *Green Chem.*, **2018**, 20, 1841-1857.
48. B. Ebin; M. Petranikova; C. Ekberg; *J. Mater. Cycles Waste Manag.*, **2018**, 20, 2018-202758.
49. L. Zhu; M. Chen; *Sustainability*, **2020**, 12, 9164.
50. A. Holzer; S. Windisch-Kern; C. Ponak; H. Raupenstrauch; *Metals*, **2021**, 11 (1),149.
51. H. Yin; P. Xing; *Recycling of Spent Lithium-Ion Batteries*, Springer Nature Switzerland AG, **2019**, pp. 57-83.
52. Y. Shi; G. Chen; Z. Chen; *Green Chem.*, **2018**, 20, 851-862.
53. Y. Jian; Z. Zongliang; Z. Gang; J. Liangxing; L. Fangyang; J. Ming; L. Yanqing; *Hydrometallurgy*, **2021**, 203, 105638.
54. M. Zhou; B. Li; J. Li; Z. Xu; *ACS EST Eng.* **2021**, 1, 1369–1382.
55. D. Mu; Y. Liu; R. Li; Q. Ma; C. Dai; *New J. Chem.*, **2017**, 41, 7177-7185.
56. Y. Liu; D. Mu; R. Li; Q. Ma; R. Zheng; C. Dai; *J. Phys. Chem.*, **2017**, C 121, 4181-4187.
57. B. Makuza; Q. Tian; X. Guo; K. Chattopadhyay; D. Yu; *J. Power Sources*, **2021**, 491, 229622.
58. S. Yu; J. Xiong; D. Wu; X. Lü; Z. Yao; S. Xu; J. Tang; *Environ. Sci. Pollut. Res.*, **2020**, 27, 40205-40209.
59. X. Zhang; L. Cai; E. Fan; J. Lin; F. Wu; R. Chen; L. Li; *J. Hazard. Mater.*, **2021**, 1, 100003.
60. O. Kwon; I. Sohn; *Resour. Conserv. Recycl.*, **2020**, 158, 104809.
61. Y. Yueshan; W. Dahui; C. Huaijing; Z. Xiaodong; X. Li; Y. Lixin; *Chem. Res. Chinese Universities*, **2020**, 36(5), 908-914.
62. J. Lin; C. Liu; H. Cao; L. Li; R. Chen; Z. Sun; *Progress Chem.*, **2018**, 30, 1445-1454.
63. J. Mao; J. Li; Z. Xu; *J. Cleaner Prod.*, **2018**, 205, 923-929.
64. B. Wrålsen; V. Prieto-Sandoval; A. Mejia-Villa; R. O'Born; M. Hellstrom; B. Faessler; *J. Cleaner Prod.*, **2021**, 317, 128393.
65. S. Chu; Y. Cui; N. Liu; *Nat. Mater.*, **2016**, 16, 16.
66. J. Li; G. Wang; Z. Xu; *J. Hazard. Mater.*, **2016**, 302, 97-104.
67. R. Guoxing; X. Songwen; X. Meiqiu; P. Bing; F. Youqi; F. Wang; X. Xing; *Advances in Molten Slags, Fluxes, and Salts: Proceedings of the 10th International Conference on Molten Slags, Fluxes and Salts*, Springer, Cham, **2016**, pp. 211-218. https://doi.org/10.1007/978-3-319-48769-4_22
68. D. Werner; U. A. Peuker; T. Mütze; *Metals*, **2020**, 10, 316.
69. H. Pinegar; R. Y. Smith; *J. Sustain. Met.*, **2020**, 6,142-160.
70. Y. Yao; M. Zhu; Z. Zhao; B. Tong; Y. Fan; Z. Hua; *ACS Sustainable Chem. Eng.*, **2018**, 6(11), 13611-13627.
71. Y. Liu; W. Lv; X. Zheng; D. Ruan; Y. Yang; H. Cao; Z. Sun; *ACS Sustainable Chem. Eng.*, **2021**, 9, 3183-3194.
72. Z. Takacova; T. Havlik; F. Kukurugya; D. Orac; *Hydrometallurgy*, **2016**, 163, 9-17.

73. P. Meshrama; A. Abhilasha; B. D. Pandey; T. R. Mankhand; H. Devecic; *J. Ind. Eng. Chem.*, **2016**, 43, 117-126
74. E. G. Pinna; M. C. Ruiz Ojeda; M. W. Rodriguez; *Hydrometallurgy*, **2016**, 167, 66-71.
75. Y. A. Nurqomariah; R. S. Fajaryanto; *E3S Web of Conferences*, **2018**, 67, 03036.
76. H. Chu; J. Lie; J. -C. Liu; *Sustain. Metall.*, **2021**, 7, 630-641.
77. W. Urbanska; *Minerals*, **2020**, 10, 555.
78. M. Aaltonen; P. Peng; B. P. Wilson; M. Lundström; *Recycling*, **2017**, 2, 20.
79. E. Fan; J. Yang; Y. Huang; J. Lin; F. Arshad; F. Wu; L. Li; R. Chen; *ACS Appl. Energy Mater.*, **2020**, 3, 8532-8542.
80. A. A. Nayl; R. A. Elkhatab; S. M. Badawy; M. A. El-Khateeb; *Arab. J. Chem.*, **2015**, 10(2), S3632-S3639.
81. X. Tanga; W. Tangb; J. Duana; W. Yanga; R. Wanga; M. Tanga; J. Lia; *J. Alloys Compd.*, **2021**, 874, 159853.
82. P. Meshram; B. D. Pandey; T. R. Mankhand; H. Deveci; *JOM*, **2016**, 68, 2613-2623.
83. E. Mossalia; N. Picone; L. Gentilinic; O. Rodriguez; J. Manuel; P. M. Colledani; *J. Environ. Manage.*, **2020**, 264, 110500.
84. G. P. Nayaka; J. Manjanna; K. V. Pai; R. Vadavi; S. J. Keny; V. S. Tripathi; *Hydrometallurgy*, **2015**, 151, 73-77.
85. H. Pinegar; R. S. York; *J. Sustain. Met.*, **2020**, 6, 142-160.
86. M. Pagliaro; F. Meneguzzo; *Heliyon*, **2019**, 5, e01866.
87. P. Meshram; B. D. Pandey; T. R. Mankhand; *Chem. Eng. J.*, **2015**, 281, 418-427.
88. P. Meshram; B. D. Pandey; T. R. Mankhand; *Waste Manage.*, **2015**, 45, 306-313.
89. L. Li; Y. Bian; Y. Guan; E. Fan; F. Wu; R. Chen; *Waste Manage.*, **2018**, 71, 362-371.
90. H. Ku; Y. Jung; M. Jo; S. Park; S. Kim; D. Yang; K. Rhee; E. M. An; J. Sohn; K. Kwon; *J. Hazard. Mater.*, **2016**, 313, 138-146.
91. P. Meshrama; A. Abhilasha; B. D. Pandey; T. R. Mankhand; H. Devecic; *J. Ind. Eng. Chem.*, **2016**, 43, 117-126.
92. L. A. Diaz; M. L. Strauss; B. Adhikari; *Resour. Conserv. Recycl.*, **2020**, 161, 104900.
93. D. Quintero-Almanza; Z. Gamíño-Arroyo; L. Sánchez-Cadena; *Batteries*, **2019**, 5, 44.
94. Z. Xu; Y. Dai; D. Hua; H. Gu; N. Wang; *ACS Sustainable Chem. Eng.*, **2021**, 9, 3979-3984.
95. C. Wanga; S. Wang; F. Yan; Z. Zhang; X. Shen; Z. Zhang; *Waste Manage.*, **2020**, 114, 253-262.
96. L. Sun; B. Liu; T. Wu; G. Wang; Q. Huang; Y. Su; F. Wu; *Int. J. Miner. Metall.*, **2021**, 28(6), 991.
97. M. Xu; S. Kang; F. Jiang; X. Yana; Z. Zhua; Q. Zhaoa; Y. Tenga; Y. Wang; *RSC Adv.*, **2021**, 11, 27689-27700.

98. M. -M. Wang; C. -C. Zhang; F. -S. Zhang; *Waste Manag.*, **2016**, 51, 239-244.
99. B. Fan; X. Chen; T. Zhou; J. Zhang; B. Xu; *Waste Manag. Res.*, **2016**, 34(5), 74-81.
100. T. Punt; G. Akdogan; S. Bradshaw; P. van Wyk; *Miner. Eng.*, **2021**, 173, 107204.
101. J. Li; Y. He; Y. Fu; W. Xie; Y. Feng; K. Alejandro; *Waste Manage.*, **2021**, 126, 517-526.
102. W. -S. Chen; H. -J. Ho; *Key Eng. Mater.*, **2018**, 775, 419-426.
103. H. Li; S. Xing; Y. Liu; F. Li; H. Guo; G. Kuang; *ACS Sustainable Chem. Eng.*, **2017**, 5, 8017-8024.
104. M. Joulié; R. Laucourt; E. Billy; *J. Power Sources*, **2014**, 247, 551-555.
105. J. Wang; Z. Guo; *Recycling of Spent Lithium-Ion Batteries*, Springer Nature Switzerland AG, **2019**, pp 27-55.
106. S. Lei; W. Sun; Y. Yang; *J. Hazard. Mater.*, Part D, **2022**, 424, 127654.
107. J. Hu; J. Zhang; H. Li; Y. Chen; C. Wang; *J. Power Sources*, **2017**, 351, 192-199.
108. W. -S. Chen; H. -J. Ho; *Metals*, **2018**, 8(5), 321.
109. J. Kozak; A. Townshend; *Encyclopedia of Analytical Science*, Elsevier, 3rd ed., **2019**, pp. 111-120.
110. Z. Liang; C. Cai; G. Peng; J. Hu; H. Hou; B. Liu; S. Liang; K. Xiao; S. Yuan; J. Yang; *ACS Sustainable Chem. Eng.*, **2021**, 9, 5750-5767.
111. W. Gao; J. Song; H. Cao; X. Lin; X. Zhang; X. Zheng; Y. Zhang; Z. Sun; *J. Clean. Prod.*, **2018**, 178, 833-845.
112. A. Higuchi; N. Ankei; S. Nishihama; K. Yoshizuka; *JOM*, **2016**, 68, 10.
113. Y. Song; Z. Zhao; *Sep. Purif. Technol.*, **2018**, 206, 335-342.
114. J. Yu; X. Wang; M. Zhou; Q. Wang; *Energy Environ. Sci.*, **2019**, 12, 2672-2677.
115. D. Kaiser; S. Pavón; M. Bertau; *Chem. Ing. Tech.*, **2021**, 93(11), 1840-1850.
116. S. Natarajan; A. B. Boricha; H. C. Bajaj; *Waste Manage.*, **2018**, 77, 455-465.
117. X. Chen; C. Luo; J. Zhang; J. Kong; T. Zhou; *ACS Sustainable Chem. Eng.*, **2015**, 3(12), 3104-3113.
118. D. Kaiser; S. Pavón; M. Bertau; *Chem. Ing. Tech.*, **2021**, 93(11), 1833-1839.
119. H. Nadimi; N. J. Karazmoudeh; *J. Sustain. Metall*, **2021**, 7, 653-663.
120. S. Li; X. Wu; Y. Jiang; T. Zhou; Y. Zhao; X. Chen; *Waste Manage.*, **2021**, 136, 18-27.
121. L. Yuan; J. Wen; P. Ning; H. Yang; Z. Sun; H. Cao; *ACS Sustain. Chem. Eng*, **2022**, In press., DOI: 10.1021/acssuschemeng.1c06307.
122. W. Xuan; A. de Souza Braga; A. Chagnes; *ACS Sustainable Chem. Eng.*, **2021**, In press. DOI: 10.1021/acssuschemeng.1c07109.
123. Q. Meng; Y. Zhang; P. Dong; *Waste Manag.*, **2017**, 64, 214-218.
124. X. Chen; D. Kang; L. Cao; J. Li; T. Zhou; H. Ma; *Sep. Purif. Technol.*, **2019**, 210, 690-697.
125. W. Gao; J. Song; H. Cao; X. Lin; X. Zhang; X. Zheng; Y. Zhang; Z. Sun; *J. Clean. Prod.*, **2018**, 178, 833-845.

126. T. Sieber; J. Dücke; A. Rietig; T. Langner; J. Acker; *Nanomaterials*, **2019**, 9, 246.
127. K. H. Chan; J. Anawati; M. Malik; G. Azimi; *ACS Sustainable Chem. Eng.*, **2021**, 9, 4398-4410.
128. A. Amato et al.; *Recovery of critical metals from LCDs and Li-Ion batteries*, ELECTRONICS GOES GREEN 2016+ (EGG), Berlin, Germany, **2016**, pp. 1-5.
129. N. Vieceli; C. A. Nogueira; C. Guimarães; M. F. C. Pereira; F. O. Durão; F. Margarido; *Waste Manage.*, **2018**, 71, 350-361.
130. J. Zhang; J. Hu; Y. Liu; Q. Jing; C. Yang; Y. Chen; C. Wang; *ACS Sustainable Chem. Eng.*, **2019**, 7(6), 5626-5631.
131. A. Mohanty; S. Sahu; L. B. Sukla; N. Devi; *Materials Today: Proceedings*, **2021**, 47, 1203-1212.
132. J. Zhu; G. Guo; J. Wu; X. Cheng; Y. Cheng; *Ionics*, **2022**, 28, 241-250.
133. W. Lv; D. Ruan; X. Zheng; L. Li; H. Cao; Z. Wang; Y. Zhang; Z. Sun; *Chem. Eng. J.*, **2021**, 421, 129908.
134. J. Chen; H. Zhang; Z. Zeng; Y. Gao; C. Liu; Xiaoqi Sun; *Hydrometallurgy*, **2021**, 206, 105768.
135. R. D. Perraud; *The Recycling of Lithium-Ion Batteries: A Strategic Pillar for the European Battery Alliance*, Center for Energy, IFRI, Paris, France, **2020** (Annual report).
136. H. Bae; Y. Kim; *Mater. Adv.*, **2021**, 2, 3234-3250.
137. Jiang J; Zeng X; Li J; *Appl. Mech. Mater.* **2015**, 768, 622-626.
138. R. Sommerville; P. Zhu; M. A. Rajaeifar; O. Heidrich; V. Goodship; E. Kendrick; *Resour. Conserv. Recycl.*, **2021**, 165, 105219.
139. M. Kaya; *REWAS 2019 Manufacturing the Circular Materials Economy*, Minerals, Metals & Materials Series, 1st ed., Cham, Switzerland, **2019**, pp. 277-288.
140. R. Sojka; Q. Pan; L. Billmann; *Comparative study of Li-ion battery recycling processes*, ACCUREC Recycling GmbH, Krefeld, Germany, **2020** (Report).
141. L. Gaines; *ACS Annual Meeting March 23*, **2020**.
142. A. Mielea; J. Aksen; M. Wolinetz; E. Mainec; Z. Longa; *Transp. Res. D. Transp. Environ.*, **2020**, 81, 102275.
143. A. Boyden; V. K. Soo; M. Doolan; *Procedia CIRP*, **2016**, 48, 188-193.
144. C. Scheller; K. Schmidt; T. S. Spengler; *J. Bus. Econ.*, **2021**, 91, 253-282.
145. https://americanmanganeseinc.com/wp-content/uploads/2019/10/AMY_BP-8_28_2019.pdf, Accessed 05.02. **2022**
146. L. -P. Yue; P. Lou; G. -H. Xu; H. Xu; G. Jin; L. Li; H. Deng; Q. Cheng; S. Tang; Y. -C. Cao; *Ionics*, **2020**, 26, 2757-2761.
147. B. Gangaja; S. Nair; D. Santhanagopalan; *ACS Sustainable Chem. Eng.*, **2021**, 9, 4711-4721.
148. W. Zhang; C. Xu; W. He; G. Li; J. Huang; *Waste Manag. Res.*, **2018**, 36(2), 99-112.
149. W. Lv; Z. Wang; H. Cao; Y. Sun; Y. Zhang; Z. Sun; *ACS Sustainable Chem. Eng.*, **2018**, 6, 1504-1521.

ANTIMICROBIAL ACTIVITY OF GRAPHENE OXIDE-COATED POLYPROPYLENE SURFACES

LUCIAN CRISTIAN POP^{a,c}, GABRIEL BARTA^b,
LIVIU COSMIN COTET^{a,c}, KLARA MAGYARI^{c,e}, MONICA BAIA^{c,d},
LUCIAN BARBU TUDORAN^{f,g}, RODICA UNGUR^h, DAN VODNAR^b,
LUCIAN BAIA^{c,d,e}, VIRGINIA DANCIU^{a,c*}

ABSTRACT. Due to its optical, chemical and electronic properties, graphene oxide (GO), among others subtypes of graphene-based materials, has been broadly studied over the past decade. Thanks to its contact-based antimicrobial activity GO represents a good candidate for the construction of materials with antimicrobial properties. Thus, GO's capability to interact with microbes delivers a prospect to improve textiles designed for usage as personal protective equipment. This paper presents the results concerning the obtain of the GO-impregnated SFM-1 polypropylene membrane, its morpho-structure and antimicrobial activity and adherence on two gram-negative bacteria (*E. coli*, *S. typhimurium*), a gram-positive bacterium (*S. aureus*) and a yeast (*C. albicans*). The investigations on the GO-impregnated polypropylene membrane, through Raman spectroscopy, Scanning and Transmission electron microscopy (SEM, TEM), Energy Dispersive X-Ray Analysis (EDX), X-ray diffraction (XRD), and Fourier-transform infrared spectroscopy (FTIR) suggested the successful polypropylene impregnation with GO. The antibacterial tests have shown that all but one of the microorganisms (*S. typhimurium*) displayed

^a Faculty of Chemistry and Chemical Engineering, Department of Chemical Engineering, Babes-Bolyai University, 11 Arany Janos str., RO-400028, Cluj-Napoca, Romania

^b Department of Food Science, University of Agricultural Sciences and Veterinary Medicine, 3-5 Calea Mănăştur str., RO-400372, Cluj-Napoca, Romania

^c Institute of Research-Development-Innovation in Applied Natural Sciences, Babes-Bolyai University, 30 Fântânele str., RO-400294, Cluj-Napoca, Romania

^d Faculty of Physics, Babes-Bolyai University, 1 M. Kogălniceanu str., RO-400084 Cluj-Napoca, Romania

^e Interdisciplinary Research Institute on Bio-Nano-Sciences, Nanostructured Materials and Bio-Nano-Interfaces Center, Babes-Bolyai University, 42 T. Laurian str., RO-400271, Cluj-Napoca, Romania

^f Electron Microscopy Center, Faculty of Biology and Geology, Babes-Bolyai University, 1 M. Kogălniceanu str., RO-400084 Cluj-Napoca, Romania

^g Integrated Electron Microscopy Laboratory, National Research and Development Institute for Isotopic and Molecular Technologies, 67-103 Donat str., RO-400293 Cluj-Napoca, Romania

^h Department of Medical Rehabilitation, Faculty of Medicine, Iuliu Hatieganu University of Medicine and Pharmacy, Louis Pasteur str., RO-400349 Cluj-Napoca, Romania

* Corresponding author: virginia.danciu@ubbcluj.ro

to be susceptible to the antimicrobial activity of the GO material. Bacterial adhesion was also checked to simulate their affinity for the polypropylene surface immediately after impregnation, in this case the best results were observed on the *S. aureus* strains.

Keywords: *graphene materials; polymer; composite; bacterial adherence, antimicrobial activity.*

1. INTRODUCTION

The increasing resistance of pathogens to antibiotics [1] due to their excessive use has led to the need to find alternative ways to destroy bacteria and fungi based on materials with antibacterial properties such as fullerenes, carbon nanotubes, and graphene [2].

Graphene materials (GM) are crystalline structures formed of carbon nanolayers composed of sp^2 hybridized carbon atoms packed in a honeycomb network [3], creating a 2D crystal [4]. The best-known method of obtaining graphene oxide is the modified Hummers method which is based on the oxidation of graphite with $KMnO_4$ in the presence of H_2SO_4 , $NaNO_3$, and H_2O_2 [5]. Recent research has shown that the morpho-structural, optical, and electrical properties of graphene oxide (GO) depend on both the reaction conditions used and the graphite source [6-11].

It has been shown that the antimicrobial activity of GM depends on the presence of various network defects, morphology, number of graphene layers, their lateral size, particle shape, and dispersibility [12], [13]. Thus, Perreault et al. observed that a higher number of defects, respectively smaller GO nanosheets cause an increased antimicrobial activity on *Escherichia coli* [14]. Furthermore, the rise of the number of layers leads to the increase of the GM thickness, which causes a decrease of the nano-knife effect and an increase of the aggregation tendency of the particles. As a result, the contact between graphene and pathogen is reduced [12]. The graphene surfaces angle orientations [15] and the number of free basal planes [16] are also significant parameters influencing the graphene materials' antimicrobial activity. Another important parameter that influences the antifungal activity of graphene material is the shape of the nanoparticles. Sharp-corner protruded particles having a low energy barrier can penetrate more easily through the membrane of the pathogen [17]. According to the literature, there are three main mechanisms by which the antimicrobial activity of GM is manifested, namely:

- the mechanism of nano-knives (cell membrane stress) through which graphene penetrates the cell membrane of the pathogen due to the sharp edges of graphene nanosheets [18]

- the mechanism of oxidative stress that may be dependent or independent on the production of highly reactive species (HRS) [19], [20]

- the mechanism of wrapping/clamping the bacterial cell membrane [21].

The mechanism of oxidative stress independent of the production of highly reactive species is based on the oxidation and destruction of the pathogenic cell by the transfer of charge from the cell membrane to graphene. Initially, oxygen adsorption takes place at the edges of the graphene sheets and in the defective areas, then the reduction occurs through a variety of enzymatic reactions [22-24]. The oxidative stress mechanism, dependent on HRS production, occurs through the intracellular accumulation of OH^\bullet , H_2O_2 , $^1\text{O}_2$, and $\text{O}_2^{\bullet-}$ which cause the deterioration of the cell membrane, lipid peroxidation, impairment in the mitochondrial function, and cell necrosis. The mechanism of wrapping / trapping the cell membrane can occur due to graphene's thin and very flexible film structure that surrounds and isolates the pathogen from the nutrient environment, leading, in the end, to the death of the cell [20]. Some researchers have shown that the physicochemical interaction between graphene material and pathogen depends not only on the morpho-structural properties of graphene but also on the structure of the pathogen, the presence or absence of the cell envelope, bacterial cell age, environmental stress conditions, cell metabolism, factors that influence the sensitivity of the bacterium in the presence of GM [25].

In this study, we investigated the antimicrobial activity of the GO obtained by a patented process. We deposited the obtained GO on a polypropylene membrane and then we tested its antimicrobial activity on *Escherichia coli*, a gram-negative bacterium, *Staphylococcus aureus*, a gram-positive bacterium, *Salmonella thyphimurium*, a pathogenic gram-negative bacterium, and *Candida albicans*, an opportunistic pathogenic yeast.

2. RESULTS AND DISCUSSIONS

2.1. Morpho-structural characterization

The structure and properties of graphite oxide depend strongly on method of preparation and degree of oxidation (the quantity of oxygen groups existing on the surface or on the edges). Graphene oxide (Figure1) is the result of liquid phase exfoliation, a procedure in which a single layer or several layers of graphene are exfoliated from graphite in a liquid environment. With attached uncharged but polar oxygen groups such as hydroxyl (-OH) and

epoxide (-O-) and carboxylate groups (-COOH) on the edge and irremediable basal plane defects, the electronic properties of graphene oxide are reduced when related to graphene [18], [25]. The outcome is a huge 2D molecule that has both hydrophilic and lipophilic properties [19] that may behave like a surfactant possetting thus a certain degree of cytotoxicity [20], [21].

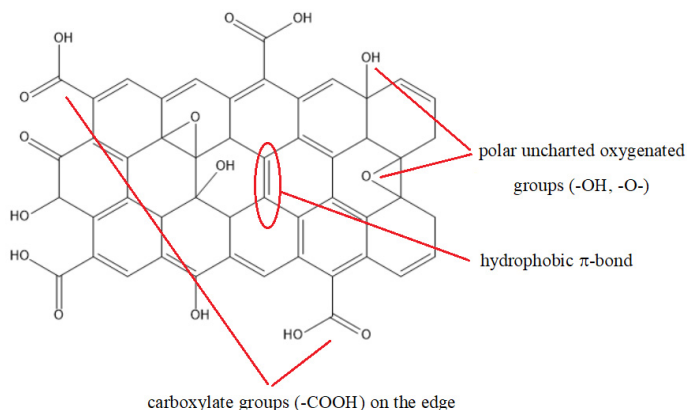


Figure 1. Schematic structure of GO

Raman spectrum of GO-based sample (GO mixed with H₂O: EtOH 1:1) and the spectra of SFM1-PP and SFM1-PP-GO samples were recorded and illustrated in Figure 2. The Raman spectrum of SFM1-PP sample exhibits both the polymer characteristic vibrational bands but also those of the soy flour. Thus, the band at 858 cm⁻¹ is due to the stretching vibration of CC and the rocking vibration of CH₂ whereas the bands from 1091 and 1100 cm⁻¹ are given by the stretching vibration of the CC bonds and the bending vibrations of the CH₃. The medium intense band at 1289 cm⁻¹ is assigned to the in-plane deformation vibrations of the CH₂ groups.

The most intense Raman bands from 1610 and 1722 cm⁻¹ are due to the amide I band stretching in the protein secondary structure and carbonyl bond stretching vibrations of the soy flour [26]. The spectrum of GO-based sample exhibits two well-known features: the D band, about 1350 cm⁻¹, due to the structural disorder in graphitic structure, and the G band, at about 1600 cm⁻¹, assigned to the first-order scattering of E_{2g} phonons from sp² carbon bonds of the graphite plane [27], [28]. In our spectrum, the D band is located at 1344 cm⁻¹, whereas the maximum of the G band is at 1599 cm⁻¹. The intensity of the D band is correlated with the number of defects in the graphene plan [29]. In the spectrum of SFM1-PP-GO sample one can notice both the presence of bands due to the PP vibrations and the D and G bands specific to GO vibrations, proving the formation of the new composite based on SFM1-PP and GO components.

Considering that the ID/IG intensity ratio can offer information concerning defects in graphene material, we propose evaluating the ratio for the SFM1-PP-GO and GO-based samples. Results previously reported in the literature suggest a link concerning the GO reduction and the rise of the ID/IG intensity ratio [30]. Thus, in order to do this a deconvolution of the spectral range between 1200 and 1700 cm^{-1} of the SFM1-PP-GO spectrum was performed and the obtained bands are illustrated in the inset from Figure 2.

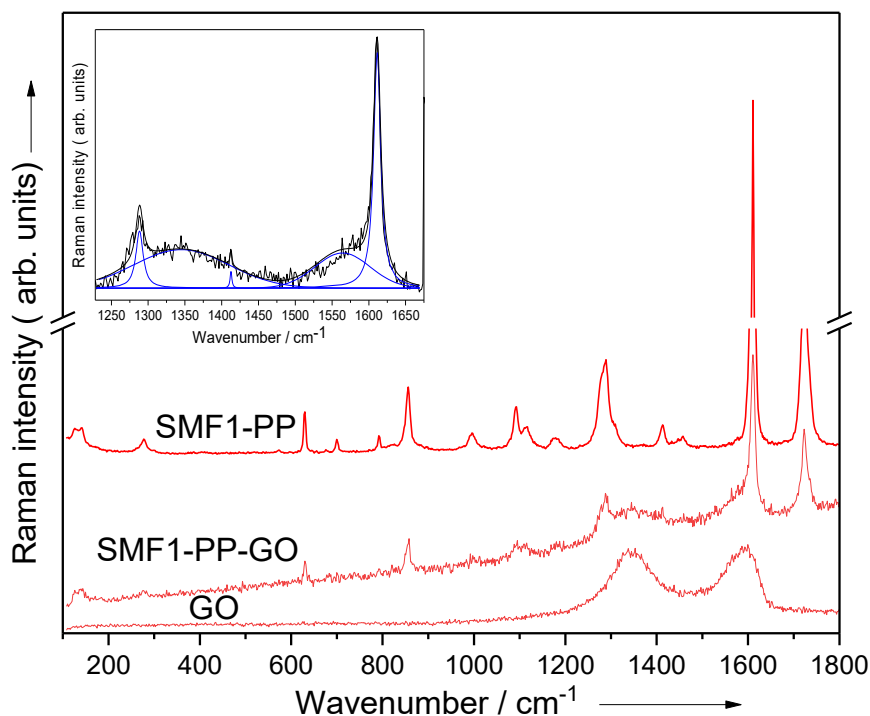


Figure 2. Raman spectra of GO, SFM1-PP and SFM1-PP sample with GO as indicated

Moreover, the ID/IG intensity ratios were calculated, and the same value of 1 was obtained. Thus, in this case, the analysis of the Raman spectra cannot provide detailed information related to the changes of the GO structure that may occur in the SFM1-PP-GO sample as compared to the GO-based one.

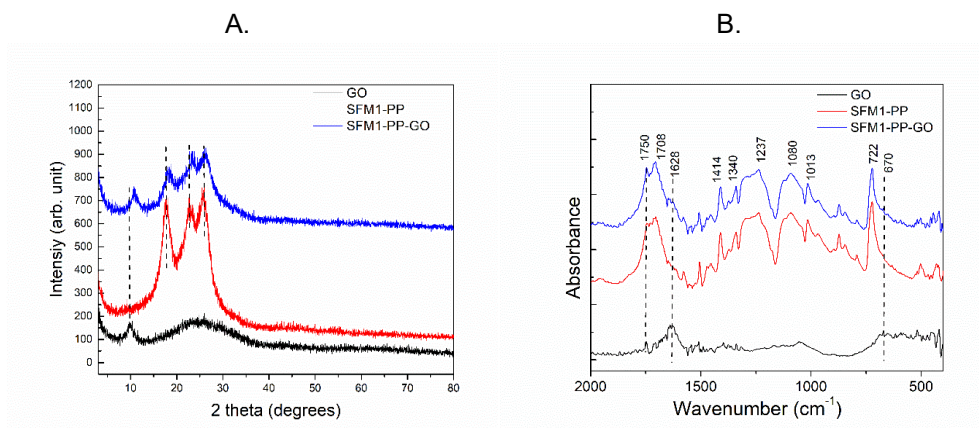


Figure 3. A. XRD analysis of GO, SFM1-PP, and SFM1-PP GO samples, **B.** FTIR spectra of GO, SFM1-PP, and SFM1-PP GO samples

The SFM1-polypropylene presents a semicrystalline structure with diffraction peaks coming from (110), (045) and (130) planes (Fig. 3A) [31]. It can be observed that after polypropylene impregnation with GO, the specific GO diffraction peak shift from 9.8° to 10.7° indicating the modification of interlayer spacing which is proportional to the degree of oxidation [32]. This change confirms the binding between the polypropylene material and the GO.

The FTIR spectra of GO and SFM1-PP material, before and after impregnation with GO, were presented in Fig. 3B. The SFM1-PP has characteristic FT-IR spectrum of polyethylene [33] and shows peaks positioned around the following value: 1650 cm^{-1} (carbonyl stretching vibration of the primary amide), 1414 cm^{-1} (bending deformation), 1340 and 1414 cm^{-1} (CH_3 symmetric deformation), 1080 cm^{-1} (C-O stretching), 722 cm^{-1} (rocking deformation) [34], [35]. The spectrum of GO presents the following spectral features: C=O stretching (around 1750 cm^{-1}), C=O stretching vibrations from carbonyl group (around 1628 cm^{-1}) and C-O functional group (at 1070 cm^{-1}). After the impregnation of the PP with GO, the FT-IR spectra show all the representative bands of GO, which suggest the successful polypropylene impregnation.

SEM investigations proved a similar diameter of SFM1-PP fibbers $\sim 10\text{ }\mu\text{m}$ (Fig. 4.A) with smooth surfaces and variable sizes of GO sheets spread between polypropylene fibres (Fig. 4.B). The EDX spectra confirmed the presence of GO by differences in S percentage, from the synthesis reactions of GO (Fig. 4 C and D). Side views of GO sheets (Fig. 5.A) and transversal sections (Fig. 5.B) demonstrate a 600-700 nm thickness.

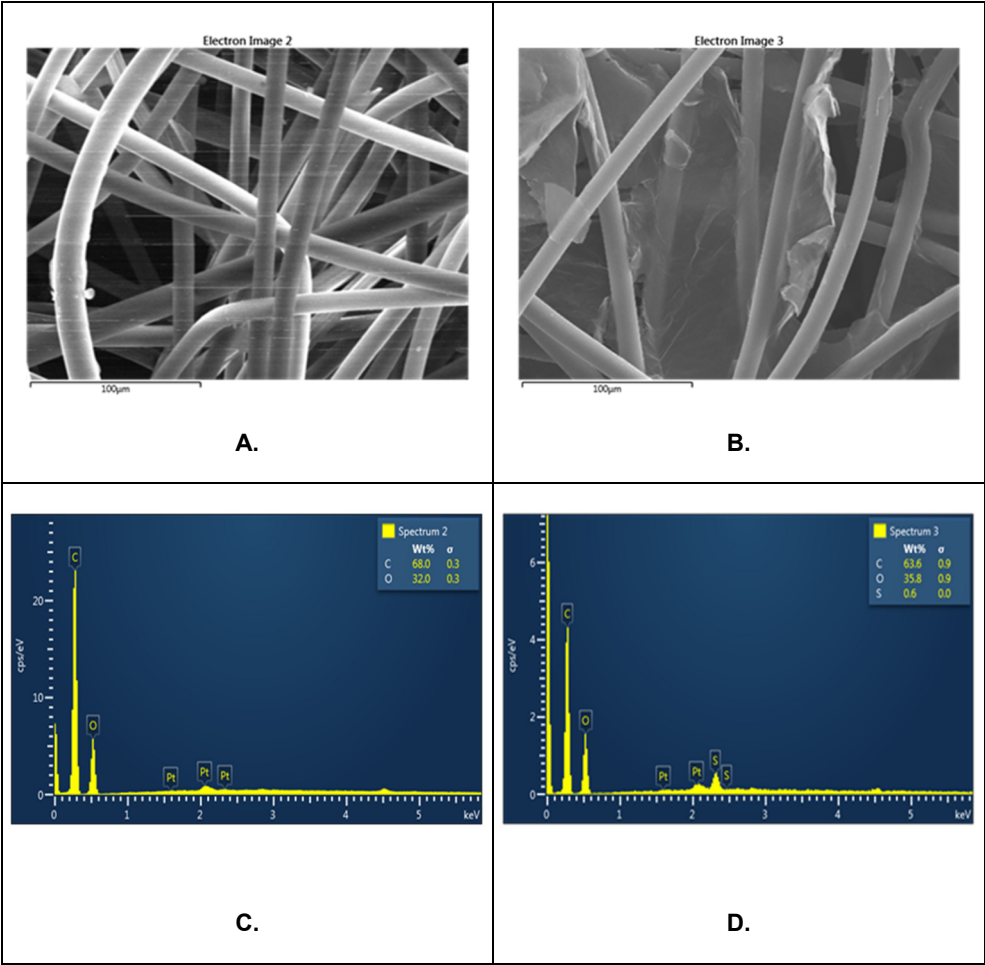


Figure 4. SEM images of the SFM1-PP (A) and SFM1-PP-GO (B), and their EDX spectra (C and D)

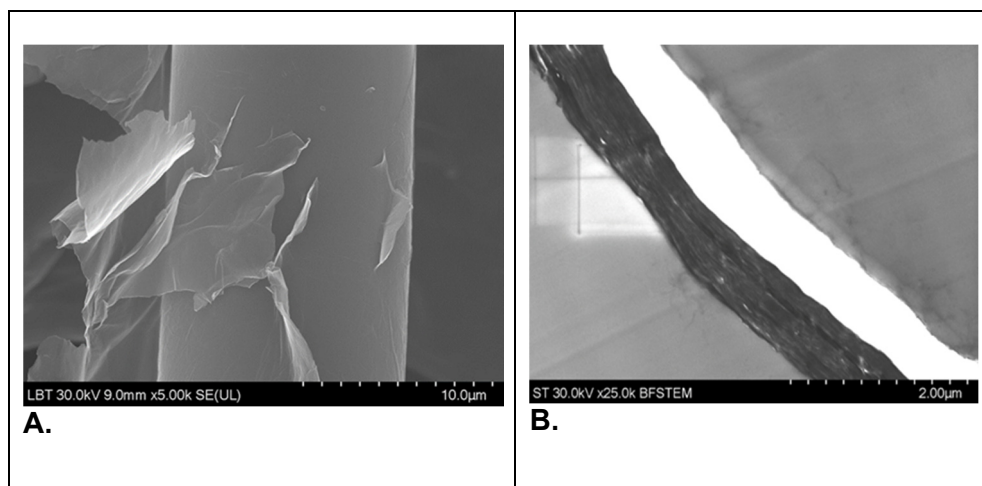


Figure 5. Determination of GO membrane thickness – A. SEM and B. TEM – 600-700 nm

2.2. Antibacterial activity

According to the results determined after counting the number of colonies present on the agar dishes, the activity of the tested samples expressed an antibacterial effect against 3 of the four analysed strains. Initially, the microbial concentrations were at $7 \log_{10}$ CFU/ml. However, after exposure to the GO-coated polypropylene surface, the final microbial concentrations decreased to $6.11 \log_{10}$ CFU/ml in case of *E. coli*, $5.84 \log_{10}$ CFU/ml for *S. aureus*, and $3.54 \log_{10}$ CFU/ml for *C. albicans*. But in the case of the *S. typhimurium* strain, the samples tested could not inhibit strain development as the number of colonies could not be counted on the agar plates; they did not decrease.

Table 1. Microbial viability after GO exposure

Microorganism	Viability [\log_{10} CFU/ml]
<i>S. aureus</i> ATCC 25923	5.84
<i>E. coli</i> ATCC 25922	6.11
<i>C. albicans</i> ATCC 102310	3.54
<i>S. typhimurium</i> ATCC 14028	-

E. coli and *S. typhimurium* are both gram-negative bacteria having the shape of a rod. The first one has adhesive fimbriae and a cell wall consisting of an exterior membrane having lipopolysaccharides, a periplasmic space with a peptidoglycan sheet, and an internal cytoplasmic membrane [36]. The second one contains characteristics that separate it from other kinds of bacteria. It has 2 membranes (one outside and one inside), periplasm, and a lipopolysaccharide (LPS) [37].

The outer shell of bacteria is negatively charged thanks to the existence of teichoic or lipoic acid in the gram-positive (CW) cell wall or due to LPS and phospholipids in the outer membrane of gram-negative (OM) bacteria [38]. The cytoplasmic membrane (CM) is also negatively charged due to the existence of incorporated phospholipids and proteins. As a result, for adhesion to the surface of the negatively charged cell and subsequent penetration and permeability of the membrane (CM and OM), the graphene material must possess cationic groups and a certain degree of hydrophobicity [39]. The bacterial envelope of the CM and CW membrane functions as an external barrier for the permeability of bacteria. In the case of gram-negative bacteria, the key component of the cell wall is the outer membrane - an asymmetric double lipid layer comprising of proteins, LPS in the outer layer and phospholipids in the inner layer [39].

According to the zeta potential results, the bacterial surface charge of *E. coli* and *S. typhimurium* obtained by T. Arasoglu et al. is $-17.9 \pm 0.62\text{mV}$ and $-13.1 \pm 0.57\text{mV}$ [40]. So, it was thought that their interaction with graphene-based material having a positive surface charge is stronger. Furthermore, the pore size of the cell membrane is also important because it is stated in the literature that due to the small pore structure of bacteria, penetration of active substances into the cell is limited [41]. Furthermore, in a recent article, citric acid-coated Fe_3O_4 and Ag nanoparticles had a better antibacterial effect on *E. coli* than on *S. typhimurium* [42], which was also observed in this study, as the GO-coated surface had no significant antibacterial effect on *S. typhimurium*.

S. aureus is a gram-positive cocci-shaped bacterium. One of the primary infection reasons globally is that it can infest diverse host cell types, where it can survive (autophagy and apoptosis) and replicate [43]. At minimal inhibitory concentration (MIC) analysis showed an antibacterial effect similar to *E. coli* strain which was also observable in similar studies but with different antimicrobial polymers/hydrogels. This antibacterial effect was given by the polymers with lower molecular weight (polymethacrylates/polyacrylate, poly- β -lactams, polymaleimides, polycarbonates), which can hinder microbial growth even at reduced concentrations [44].

C. albicans is a fungus that is present in various parts of the human organisms and microbiota. Regardless it can also transform in a pathogen, generating life threatening aliment [45]. Because this microorganisms is able to develop in various human tissues it also implies morphological and metabolically alterations related with the manifestation of divergent virulence circumstances (morphogenesis, host recognition biomolecules, secreted phospholipases and proteases) [46]. The highest antibacterial activity in this study was observed with *C. albicans*, which can be bestowed to the membrane integrity disruption and permeabilization given by the GO. The same effect could be observed in a corresponding research with two types of antibacterial peptides on this fungi, which could hinder efficiently the expansion of fungal resistance [47].

2.3. Bacterial adherence

The best bacterial adherence was recorded on the strains *S. aureus*, a gram-positive, round-shaped bacterium, common member of the body microbiota [48], habitually present in the superior respiratory system and on the skin surface. Although *S. aureus* is generally non-pathogenic and living in close association with *Homo sapiens* microbiota, it may occasionally become an opportunistic pathogen, triggering skin and respiratory infections and food poisoning [49]. Pathogenic strains often spread diseases by producing virulence factors.

Table 2. Bacterial adherence to GO-polypropylene sample

Microorganism	Viability [\log_{10} CFU/ml]
<i>E. coli</i> ATCC 25922	uncountable
<i>S. aureus</i> ATCC 25923	4.81
<i>S. thyphimurium</i> ATCC 14028	4.66
<i>C. albicans</i> ATCC 102310	uncountable

The results of this research may have a positive impact against this bacteria's negative effect. Also, positive results were obtained against *S. thyphimurium* on the bacterial adherence tests. Even if the other two bacteria (*E. coli* and *C. albicans*) generated negative effects at adherence, the tested samples showed a slight resistance. Furthermore, the findings of this determination are comparable to those obtained when the sample's minimal inhibitory capacity was examined, as provided with the MIC analysis.

3. CONCLUSIONS

The research presented in this paper supports the further advance of the incorporation of graphene oxide in textiles, taking into account the inhibition effect towards microorganisms. The GO-coated SFM1-PP surfaces developed after an oxidative-exfoliation patented method presented enhanced antimicrobial effect, presumably provided by the small surface size that inhibits the bacterial development and disrupts the bacterial cell membrane. The morpho-structural analyses showed that the graphene oxide sheets having a thickness of 600-700 nm and variable size are spread between the polypropylene fibres. The GO-coated SFM1-PP composite proved effective on 3 of the 4 strains tested, the most affected being the yeast (*C. albicans*).

4. EXPERIMENTAL

4.1. Materials

Reagents were used as received without further purification. Sulfuric acid (H_2SO_4 , 98%), phosphoric acid (H_3PO_4 , 85%), hydrochloric acid (HCl, 37% aq.), absolute ethanol ($\text{C}_2\text{H}_5\text{OH}$, 99.5%) were obtained from Nordic Invest, Cluj-Napoca, graphite powder (diameter < 0.15 mm), was purchased from Fluka, potassium permanganate (KMnO_4 , 99%) was obtained from Merck, hydrogen peroxide (H_2O_2 , 3%) was purchased from Hipocrate 2000 based in Bucharest. The microorganisms *E. coli* (ATCC 25922) (gram-negative), *S. aureus* (gram-positive) (ATCC 25923), *S. typhimurium* (ATCC 14028, a pathogenic gram-negative bacterium), and *C. albicans* (ATCC 102310) were procured from Food Biotechnology Laboratory, Life Sciences Institute, University of Agricultural Sciences and Veterinary Medicine, Cluj-Napoca, Romania.

4.2. Methods

4.2.1. Preparation of GO-coated polypropylene sample

The GO suspension was obtained by the patented oxidative-exfoliation method as described previously [50]. In short, a solution of H_2SO_4 and H_3PO_4 (9:1) was added to graphite powder, followed by KMnO_4 . After the reaction was performed, H_2O_2 was slowly added. Afterward, a few centrifugation-decantation-washing-sonication in H_2O , HCl, and ethanol procedures were carried out. The obtained black-dark product was dispersed in 1:1 volume per volume H_2O /ethanol solution. The installation, shown in Figure 6, was used to obtain the GO-coated polypropylene samples. A 23 mm diameter

disk with an approximate surface of 4.15 cm^2 was made from melt-spun soy flour/polypropylene fibres (SFM1-PP) used to make medical masks. The obtained disk was inserted into a filter funnel, then a few drops of ethanol were poured into moistening the entire surface. Next, 1 ml of a 10 mg/ml GO hydroalcoholic solution (1:1 v/v) was applied uniformly on this surface. After 60 seconds, the water tap vacuum pump was turned on for 60 seconds so that the pores of the material to be filled with GO suspension. The impregnated disk was dried under ambient conditions for 48h yielding a black composite (5.8 mg GO/cm^2). The as-prepared sample was used to test the bacterial adherence and antibacterial activity.

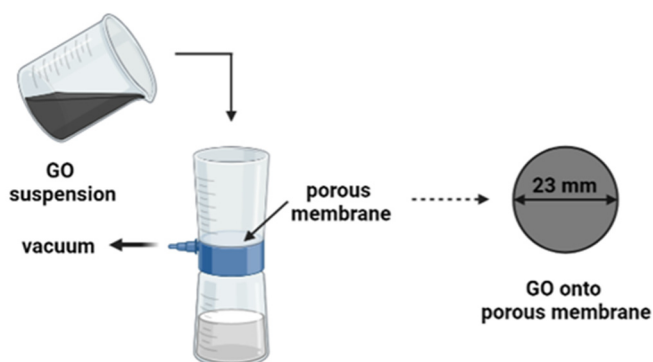


Figure 6. The device used for GO deposition on the SFM1-PP membrane

4.2.2. Morpho-structural characterizations

The FT-IR absorption spectra for all samples were recorded with a Jasco 6200 (Jasco, Tokyo, Japan) spectrometer in reflection configuration, at room temperature, in the range of $400 - 4000 \text{ cm}^{-1}$, with a 4 cm^{-1} spectral resolution; employing the well-established KBr pellet technique.

The X-ray diffraction (XRD) was carried out on a Shimadzu XRD 6000 diffractometer (Kyoto, Japan) using $\text{CuK}\alpha$ radiation ($\lambda = 1.54 \text{ \AA}$), with Ni-filter. The diffractograms were recorded in 2θ range from 3° to 80° with a speed of $2^\circ/\text{min}$.

Raman spectra were recorded with a Renishaw in Via Reflex Raman Microscope (Wotton-under-Edge, England) equipped with a Ren Cam charge-coupled device (CCD) detector. The 532 nm laser line was used for

excitation, and the spectra were collected with a 0.85 NA objective of 100× magnification. Typical integration times were 10 s, and the laser power was 0.5 mW. The Raman spectra were recorded with a spectral resolution of 4 cm⁻¹.

Morphology and structure of GO and PP fibers were determined by electron microscopy (EM): for scanning electron microscopy (SEM), samples were deposited onto double sticky carbon tape and sputter-coated with 7 nm of Pt/Pd in an Automatic Sputter Coater (Agar Inc. UK). Images were recorded in a cold field-emission SEM operated at 30 kV (Hitachi SU8320 STEM, Hitachi, Japan), while qualitative and semi-quantitative compositional analysis were obtained using an energy dispersive X-ray spectrometer (EDX) from Oxford Instruments (UK). For transmission electron microscopy (TEM) GO was embedded in Epon 812 (VWR, USA) resin and sectioned at 70–80 nm with a Leica UC7 (Austria) ultramicrotome. Images were recorded in a cold field-emission TEM operated at 200 kV (Hitachi HD2700 STEM, Hitachi, Japan).

4.2.3. Antibacterial activity

To determine the antibacterial activity of the GO-coated polypropylene samples, the guidelines in conformity with the Clinical Laboratory Standards Institute (CLSI) [51] were applied, employing the microdilution method for bacteria that develop aerobically, with minor adaptations [52]. In summary, the microorganisms were cultured in Muller-Hinton Broth (MHB)/Tryptic Soy Broth (TSB), and the cultures were stored at 4 °C and sub-cultured once a month. Preceding antibacterial persistence, *C. albicans* (ATCC 102310) was cultured in MHB at 30 °C, and *E. coli* (ATCC 25922), *S. aureus* (ATCC 25923), and *S. typhimurium* were cultivated in TSB at 37 °C for 24 h. These cells were washed 3 times with a sterile 0.9% NaCl solution and then diluted to a final density of 7 log₁₀ colony-forming units (CFU) ml⁻¹ in sterile saline solution.

The final density was confirmed by measuring the optical density with the NanoDrop 1000 spectrophotometer (NanoDrop Technologies, Wilmington, DE, USA) at 600 nm (OD₆₀₀) within the values of 0.009 and 0.011. Then, the cells were brought into contact with the GO-coated SFM1-PP surface for 3 hours. After this incubation period the cell suspension was removed and the GO-coated SFM1-PP filters were washed with sterile 0.9% sodium chloride solution in order to eliminate the unattached cells. After that, the probes were introduced into a 50 ml Falcon vial containing 10 ml of 0.9% NaCl solution followed by a 10-minute sonication period having in mind to remove the cell from the surface. After this operation the cells were immediately placed on agar plates (MHB/TSB) and incubated for the duration of a night at 30/37 °C for the final cell viability determination. Bacteria viability was assessed using plate counting method (viable cell determination within

30 and 300 colonies/plate) and the values were displayed in logarithmic counts of CFU/ml of sample (\log_{10} CFU/ml). The counting process is described at this reference [53].

4.2.4. Bacterial adherence

The bacterial adherence tests were performed to determine the affinity of microbes to the PP surface straight after impregnation. A procedure modified from Tanner and Nganga [54] has been applied for all the microorganisms tested on coated samples. Each bacterium was precultured from a frozen glycerol preparation and inoculated in a volume of 45 ml MHB over a period of 16 h at 37 °C, respectively, in TSB for 16 h at 30 °C. After this period the bacteria were centrifuged for 10 minutes at 10000 rpm (4 °C), then washed two times with a sodium chloride solution (0.9%). At that point the cells were resuspended in the same solution having a concentration of approximately 0.035 at A550, which corresponded to $\sim 1 \times 10^7$ CFU. This suspension was then sonically treated and gently vortexed to homogenize the contents after which was introduced in a 15 ml vial containing 5 ml of the bacterial suspension. Afterward, the samples were washed three times with NaCl solution at ambient temperature followed by a gentle drying procedure so that the surface is not touched. Then, the bacterial samples on the surface of the specimens were collected to perform the viability tests.

Bacterial cells attached to the surface of the samples were collected using micro brushes in tubes with a volume of 2 millilitres containing 0.9 millilitres of MHB/TSB/ with 10% glycerol. Thereafter, the bacterial suspension was homogenized, serially diluted in NaCl 0.9% solution (10 μ l of 1:10, 1:100, and 1:1000), and cultured on MHB/TSB agar dishes. CFU measurements were performed after 24 h of culturing at 37/30 °C.

ACKNOWLEDGMENTS

This research was funded by the Romanian Ministry of Research and Innovation—UEFISCDI, project number PN-III-P1-1.2-PCCDI-2017-0350/01.03.2018 (Graphene4Life), within PNCDI III.

REFERENCES

1. World Health Organization. Global action plan on antimicrobial resistance. *World Health Organization*, **2017**, 1–28
2. A. Al-Jumaili, S. Alancherry, K. Bazaka, M. V. Jacob, *Materials (Basel)*, **2017**, *10*, 1–26

3. B. L. Dasari, J. M. Nouri, D. Brabazon, S. Naher, *Energy*, **2017**, 140, 766–778
4. K. S. Novoselov, *et al.*, *Nature*, **2012**, 490, 192–200
5. A. T. Smith, A. M. LaChance, S. Zeng, B. Liu, L. Sun, *Nano Mater. Sci.* **2019**, 1, 31–47
6. M. S. Junior, M. C. Terence, J. A. G. Carrió, *J. Nano Res.*, **2016**, 38, 96–100
7. N. I. Zaaba, *et al. Procedia Eng.*, **2017**, 184, 469–477
8. H. Yu, B. Zhang, C. Bulin, R. Li, R. Xing, *Sci. Rep.*, **2016**, 6, 1–7
9. A. Romero, M. P. Lavin-Lopez, L. Sanchez-Silva, J. L. Valverde, A. Paton-Carrero, *Mater. Chem. Phys.*, **2018**, 203, 284–292
10. G. Santamaría-Juárez, *et al.*, *Mater. Res. Express*, **2019**, 6, 125631
11. L. Richtera, *et al.*, *Key Engineering Materials*, **2014**, 592–593, 374–377
12. X. Zou, L. Zhang, Z. Wang, Y. Luo, *J. Am. Chem. Soc.*, **2016**, 138, 2064–2077
13. Y. Zhang, *et al.*, *Nanotechnology*, **2014**, 25 (13), 135301
14. F. Perreault, A. F. De Faria, S. Nejati, M. Elimelech, *ACS Nano*, **2015**, 9, 7226–7236
15. V. T. H. Pham, *et al.*, *ACS Nano*, **2015**, 9, 8458–8467
16. J. D. Mangadlao, *et al.*, *Chem. Commun.*, **2015**, 51, 2886–2889
17. Y. Li, *et al.*, *Proc. Natl. Acad. Sci. U.S.A.*, **2013**, 110, 12295–12300
18. S. Liu, *et al.*, *ACS Nano*, **2011**, 5, 6971–6980
19. J. D. West, L. J. Marnett, *Chem. Res. Toxicol.*, **2006**, 19, 173–194
20. J. Li, *et al.*, *Sci. Rep.*, **2014**, 4, 4359
21. I. E. Mejías Carpio, C. M. Santos, X. Wei, D. F. Rodrigues, *Nanoscale*, **2012**, 4, 4746–4756
22. X. Lu, *et al.*, *Proc. Natl. Acad. Sci. U. S. A.*, **2017**, 114, E9793–E9801
23. C. Lu, Z. Lu, Z. Li, C. K. Y. Leung, *Constr. Build. Mater.*, **2016**, 120, 457–464
24. S. Gurunathan, J. W. Han, A. Abdal Dayem, V. Eppakayala, J. H. Kim, *Int. J. Nanomedicine*, **2012**, 7, 5901–5914
25. V. C. Sanchez, A. Jachak, R. H. Hurt, A. B. Kane, *Chem. Res. Toxicol.*, **2012**, 25, 15–34
26. O. Guzman, A. A. Ogale, *Fibers*, **2019**, 7 (10), 83
27. M. T. H. Aunkor, I. M. Mahbubul, R. Saidur, H. S. C. Metselaar, *RSC Adv.*, **2016**, 6, 27807–27825
28. A. C. Ferrari, D. M. Basko, *Nat. Nanotechnol.*, **2013**, 8, 235–246
29. L. G. Cançado, *et al. Nano Lett.*, **2011**, 11, 3190–3196
30. S. Pei, H. M. Cheng, *Carbon N. Y.*, **2012**, 50, 3210–3228
31. C. A. Stackhouse, S. Yan, L. Wang, K. Kisslinger, R. Tappero, A. R. Head, K. R. Tallman, E. S. Takeuchi, D. C. Bock, K. J. Takeuchi, A. C. Marschilok, *Applied Materials & Interfaces* **2021**, 13 (40), 47996–48008
32. L. C. Cotet, K. Magyari, M. Todea, M. C. Dulescu, V. Danciu, L. Baia, *J. Mater. Chem. A*, **2017**, 5, 2132–2142
33. C. Akarsu, Ö. Madenli, E. Ü. Deveci, *Environmental Science and Pollution Research*, **2021**, 28, 47517–47527
34. J. V. Gulmine, P. R. Janissek, H. M. Heise, L. Akcelrud, *Polymer Testing*, **2002**, 21, 557–563
35. T. A. Aragaw, B. A. Mekonnen, *Environ. Syst. Res.*, **2021**, 10:8
36. N. Dasgupta, C. Ramalingam, *Environ. Chem. Lett.* **2016**, 14, 477–485

37. H. Kita, H. Nikaido, *J. Bacteriol.*, **1973**, *113*, 672–679
38. M. Caroff, A. Novikov, LPS Structure, Function, and Heterogeneity, in *Endotoxin Detection and Control in Pharma, Limulus, and Mammalian Systems*, K. L. Williams, Springer, Cham., **2019**, Chapter 3, 53–93
39. L. Izzo, S. Matrella, M. Mella, G. Benvenuto, G. Vigliotta, *ACS Appl. Mater. Interfaces*, **2019**, *11*, 15332–15343
40. T. Arasoğlu, *et al.*, *Turkish J. Biol.*, **2017**, *41*, 127–140
41. D. Sun, *et al.*, *J. Nanoparticle Res.*, **2016**, *18*, 1–21
42. L. Gabrielyan, H. Badalyan, V. Gevorgyan, A. Trchounian, *Sci. Rep.*, **2020**, *10*, 1–12
43. K. E. Watkins, M. Unnikrishnan, *Adv. Appl. Microbiol.*, **2020**, *112*, 105–141
44. M. M. Konai, B. Bhattacharjee, S. Ghosh, J. Haldar, *Biomacromolecules*, **2018**, *19*, 1888–1917
45. C. Tsui, E. F. Kong, M. A. Jabra-Rizk, *Pathog. Dis.*, **2016**, *74*, ftw018
46. R. A. Calderone, W. A. Fonzi, *Trends Microbiol.*, **2001**, *9*, 327–335
47. D. do Nascimento, *et al.*, *Sci. Rep.*, **2020**, *10*, 1–14
48. C. Kumpitsch, K. Koskinen, V. Schöpf, C. Moissl-Eichinger, *BMC Biol.*, **2019**, *17*, 1–20
49. K. Szabo, Z. Diaconeasa, A. Catoi, D. C. Vodnar, *Antioxidants*, **2019**, *8*, 1–11
50. M. Stroe, *et al.*, *Molecules*, **2020**, *25*, 1–11
51. M. P. Weinstein, J. B. Patel, C.-A. Burnhman, B. L. Zimmer, Approval CDM-A.; *M07 Methods dilution Antimicrob. Susceptibility Tests Bact. That Grow Aerob.*, **2018**, 91
52. B. E. Ștefănescu, *et al.*, *Antioxidants*, **2020**, *9*(6), 495
53. https://users.aber.ac.uk/hlr/mpbb/index_files/Page299.html
54. J. Tanner, P. K. Vallittu, E. A. Söderling, *J. Biomed. Mater. Res.*, **2000**, *49*, 250–256.